Hydrogen Interactions in an Additively Manufactured Martensitic Stainless Steel

Presented by:

Lauren Singer

A Dissertation

Presented to the Faculty of the School of Engineering and Applied Science
University of Virginia

In partial fulfillment of the Requirements for the Degree of Doctor of Philosophy in
Materials Science and Engineering

Supervisor:
Dr. John R. Scully

Abstract

Additive manufacturing (AM) has emerged as a compelling avenue for producing metallic components, offering several promising advantages over conventional manufacturing methods of alloys such as stainless steels. Despite numerous studies examining the mechanical behavior and corrosion properties of additively manufactured stainless steels, there is a notable lack of research on hydrogen behavior within these alloys. Given the substantial microstructural differences between additively manufactured and conventionally manufactured materials, as well as the often pivotal role of these features in hydrogen interactions (i.e., uptake, absorption, trapping, and diffusion), identical hydrogen behavior in additively manufactured and wrought materials cannot be assumed. Additionally, increased susceptibility to hydrogen environmentally-assisted failure has been observed in AM alloys such as 17-4 PH stainless steels compared to their wrought counterparts. However, a mechanistic understanding of the role of hydrogen in this increased susceptibility is lacking.

The primary objective of this work is to provide insight into hydrogen behavior in additively manufactured 17-4 PH stainless steel compared to its compositionally equivalent matched-strength wrought counterpart. This investigation employs a comprehensive set of corroborating analysis methods to elucidate the impact of microstructure on hydrogen-metal interactions, as well as to assess the contribution of these interactions towards the enhanced susceptibility to environmentally-assisted cracking in AM 17-4 PH. This overarching goal has been realized through a scientific inquiry into the following key areas: (1) analysis of bulk hydrogen behavior in the wrought and AM alloys, involving the determination of effective hydrogen diffusivity and assessments of diffusible and total hydrogen concentration; (2) characterization and comparison of microstructural trap states influencing bulk hydrogen behavior in wrought and AM 17-4 PH; and (3) elucidation and modeling of the relationship between selected hydrogen materials parameters, such as the critical diffusible hydrogen concentration and effective hydrogen diffusivity, and subsequent environmentally-assisted cracking kinetics. The fulfillment of these three objectives contributes significantly towards addressing the knowledge gaps regarding hydrogen in additively manufactured stainless steels.

Bulk hydrogen behavior of wrought and AM 17-4 PH is assessed through characterization of effective hydrogen diffusivity as well as total hydrogen concentration, diffusible hydrogen concentration, and the critical threshold hydrogen concentration required for cracking. Effective hydrogen diffusivity of wrought and AM 17-4 PH in the peak-aged and over-aged conditions is determined through both electrochemical and thermal methods. AM alloys in both heat treatments display increased effective hydrogen diffusivities compared to their wrought counterparts. Additionally, analysis of electrochemical permeation and thermal desorption data indicates that reversible trapping has a significant impact on hydrogen diffusion in both wrought and AM alloys.

Diffusible and total hydrogen concentrations are established as a function of hydrogen overpotential, and likely metallurgical trap states are identified. Microstructural characterization is used to provide a systematic comparison of the microstructural attributes responsible for hydrogen trapping in each alloy. Results indicate that, though the vast majority of hydrogen is trapped in low-temperature reversible trap sites in all alloys, there is a significant increase in reversibly trapped hydrogen in the wrought alloys. These reversible sites likely correspond to high-angle grain boundaries, which are more numerous in the wrought specimens due to finer grain size, as well as Cu-rich precipitates originating from the aging process.

This trapping analysis indicates that grain size may have the highest contribution to the difference in bulk hydrogen behavior in AM and wrought 17-4 PH. Given the strong correlation discovered between grain size and effective diffusivity, an Oriani-type trapping model is employed as a framework to scrutinize the impact of grain boundary density and binding energy on effective diffusivity. The Hashin-Shtrikman upper bound two-phase composite diffusion model is then used to examine grain boundary diffusion behavior in wrought and AM 17-4 PH, revealing a slight increase in grain boundary diffusivity in the AM specimens; possible origins are discussed.

The influence of such hydrogen behavior in determining hydrogen environmentally assisted cracking (HEAC) kinetics is investigated by assessing the relationship between crack growth kinetics and diffusible hydrogen concentration. The agreement of concentration-dependent HEAC behavior with an existing crack growth rate kinetics model is analyzed, and the impact of effective hydrogen diffusivity and critical diffusible hydrogen concentration on the heightened HEAC susceptibility of AM 17-4 PH in both peak-aged and over-aged conditions is discussed. Results suggest that the increased crack growth kinetics in AM alloys can be attributed, at least in part, to the increased diffusivity as well as a reduction in the critical diffusible hydrogen concentration necessary for cracking.

In summary, this thesis contributes to the scientific understanding of hydrogen behavior in additively manufactured alloys, establishing assessment methodologies and providing clarification as well as insight into the interplay between microstructure and hydrogen behavior in complex AM microstructures. The development of a methodology to appraise the potential ramifications of hydrogen interactions on environmentally-assisted crack growth kinetics contributes to the current understanding of hydrogen-assisted failure criteria. The conclusions presented in this thesis emphasize the importance of understanding hydrogen behavior in AM materials and provide a basis for future studies aimed at developing reliable and durable additively manufactured alloys for widespread usage.

Acknowledgements

This thesis represents the collective efforts and support of a remarkable group of individuals, and for that, I am truly grateful. First and foremost, I would like to extend my appreciation to my advisor, Dr. John Scully, whose support, guidance, and expertise have been invaluable throughout this research journey. I am also profoundly thankful to my thesis committee members, Dr. James Burns, Dr. Ji Ma, Dr. Chris Li, and Dr. Sebastian Thomas, for their valuable insights, constructive feedback, and dedicated commitment to the advancement of my work.

I want to give heartfelt acknowledgement to Zachary Harris and Trevor Shoemaker—I cannot thank either of you enough for your generosity with both your time and knowledge, as well as your willingness to talk through my endless questions.

Special thanks are due to the members of the Scully group, both past and present. In particular, I would like to thank Katie Lutton, Carol Glover, Angela Gerard, Elena Romanovskaia, Alen Korjenic, Sam Inman, Deb Sur, and Lun Chan for assistance, friendship, advice, and many listening ears over the past years. I would also like extend my appreciation to several members of the third floor for their invaluable help and support, especially Carly Cocke, Sarah Blust, Armando Shehi, and Alex Jennion.

The staff at UVA has been indispensable to the realization of this thesis. I am particularly grateful to Helge Heinrich, Richard White, Tanner Fitzgerald, Tonya Reynolds, Bryana Amador, and Sherri Sullivan. Additionally, I would like to thank the Commonwealth Center for Advanced Manufacturing for their role in producing the materials used in this work. Financial support from the Office of Naval Research under Grant No. N00014-18-1-2427 with Dr. David Shifler as the Scientific Officer is gratefully acknowledged.

I am also especially grateful to Samantha Jaszewski, Kristyn Ardrey, and Kallie Whritenour for their unwavering support and friendship, as well as consistently waking up at 6 am to watch me try to send a V2. And to Kate Quiambao, for being one of my first friends at UVA and for remaining one of my best.

Most of all, I would like to thank my family. To Mom and Dad: I am so lucky to have

you as parents. I could not have asked for better role models, and nothing makes me prouder than being your daughter. Thank you for always picking up the phone.

And to Ryan Iaquinto, my biggest supporter, I can't begin to express my love and gratitude for standing by my side.

Contents

List of Tables

List of Figures

Nomenclature

List of Abbreviations

AM	Additive manufacturing or additively manufactured
BCC	Body-centered cubic
BCT	Body-centered tetragonal
BT	Breakthrough
CSL	Coincident site lattice
E	Elasticity/Young's modulus
EAC	Environment-assisted cracking
EBSD	Electron backscatter diffraction
EDS	Energy dispersive spectroscopy
EL	Percent elongation
EP	Electrochemical permeation
FCC	Face-centered cubic
GB	Grain boundary
GND	Geometrically necessary dislocation
H	Hydrogen
HAADF	High-angle annular dark-field
HAGB	High angle grain boundary
HEAC	Hydrogen environment-assisted cracking
HIP	Hot isostatic pressing

HRC	Rockwell hardness C
IG	Intergranular
IPF	Inverse pole figure
KAM	Kernel average misorientation
L-PBF	Laser powder bed fusion
LAGB	Low angle grain boundary
MMSE	Mercury-mercury sulfate electrode
OA	Over-aged
OIM	Orientation imaging microscopy
PA	Peak-aged
PAG	Prior austenite grain
PAGB	Prior austenite grain boundary
PBF	Powder bed fusion
PH	Precipitation hardening
RA	Retained austenite
SA	Solution annealing; less commonly, surface area
SCC	Stress corrosion cracking
SCE	Saturated calomel electrode
SLM	Selective laser melting
TDS	Thermal desorption spectroscopy
TEM	Transmission electron microscopy
TG	Transgranular
UTS	Ultimate tensile strength
W	Wrought
YS	Yield strength

List of Symbols

A	Material constant in Kissinger's desorption model
a	Crack length
a_{L}	H activity in normal lattice sites
A_r	Atomic weight
a_{T}	H activity in trapping sites
α	Scaling factor for localized hydrogen concentration at a crack tip
α''	Cracking constant derived from dislocation structure near crack tip
B	Trap site-sepcific constant in Lee's desorption model
b	Constant associated with first-term approximate solution to permeation transient
$\bar{b}$	Burgers vector
β	Number of interstitial sites per atom in a unit cell
β'	Cracking constant derived from dislocation structure near crack tip
β_i	Scaling factor for effects of trace impurity i along fracture path interface
C	Hydrogen concentration
C_0	Fixed hydrogen concentration at charging side of specimen
$C_{\mathrm{H,diff}}$	Diffusible hydrogen concentration
$C_{\mathrm{H,diff\text{-}crit}}$	Critical diffusible hydrogen concentration required for crack propagation
$C_{\mathrm{H,irr}}$	Hydrogen concentration in irreversible trap sites
$C_{\mathrm{H,L}}$	Hydrogen concentration in the bulk lattice
$C_{\mathrm{H,rev}}$	Hydrogen concentration in reversible trap sites
$C_{\mathrm{H}\sigma}$	Stress-enhanced hydrogen concentration at crack site
$C_{\mathrm{H}\sigma\text{-crit}}$	Critical stress-enhanced hydrogen concentration required for crack propagation
$C_{\mathrm{H,T}}$	Hydrogen concentration in all trap sites
$C_{\mathrm{H,tot}}$	Total hydrogen concentration

C_{i}	Local concentration of trace impurity i
$\bar{d}$	Average grain size
D_0	Pre-exponential term in Arrhenius relationship between temperature and hydrogen diffusivity
D_{eff}	Effective hydrogen diffusivity
D_{gb}	Hydrogen diffusivity along a grain boundary network
D_{L}	Ideal lattice diffusivity
$\left(\frac{\mathrm{d}a}{\mathrm{d}t}\right)_{\mathrm{II}}$	Stage II crack growth rate
E_{act}	Activation energy for bulk hydrogen diffusion
E_{b}	Binding energy required for hydrogen trapping
E_{d}	Activation energy for hydrogen desorption
E_{L}	Activation energy required for interstitial diffusion of H in the bulk lattice
F	Faraday's constant
f_{gb}	Area or volume fraction of grain boundaries
i	Current density
i_0	Initial steady-state current density at time $t = 0$
i_1	Steady-state permeation current density initially present at rise transient
i_2	Steady-state permeation current density initially present at decay transient
i_∞	Final steady-state current density
J_t	Hydrogen current density at time t
K	Equilibrium constant for H activity in trapping and in lattice sites
k	Trapping rate parameter
k_0	Pre-exponential value in the Arrhenius temperature dependency relationship of the trapping rate parameter
k_{B}	Boltzmann constant
k_{IG}	Critical Griffith stress intensity factor for cleavage fracture without hydrogen

K_{TH}	Apparent threshold stress intensity for onset of subcritical crack growth
L	Specimen thickness
m	Slope of linear permeation transient plot
n	Number of electrons transferred during oxidation
N_{A}	Avogadro's number
N_{L}	Lattice site density
$N_{\mathrm{T},i}$	Site density of trap state i
η_{ch}	Hydrogen charging overpotential
p	Detrapping rate parameter
p_{σ}	Pressure tensor of a stress field
p_0	Pre-exponential value in the Arrhenius temperature dependency relationship of the detrapping rate parameter
ϕ	Ramp rate TDS heating rate
R	Ideal gas constant
ρ	Density of a species
ρ_{SA}	Surface area density of a species
s	Concentration-based segregation coefficient for grain boundary diffusion
s_0	Pre-exponential factor for the Arrhenius-type relationship between temperature and grain boundary diffusion segregation
σ_{H}	Hydrostatic stress
σ_{YS}	Yield strength
T	Temperature
t	Time
$t_{1/2}$	Half-time of hydrogen egression from TDS
θ_i	Fractional coverage of hydrogen in any site i
t_{bt}	Breakthrough time, or time at which current density is 10% of steady-state

t_{lag}	Lag time, or time at which current density is 63% of steady-state
T_{max}	Temperature at which a hydrogen desorption peak occurs in the TDS spectrum
θ_{L}	Fractional coverage of hydrogen in lattice sites
$\theta_{\mathrm{T},i}$	Fractional coverage of hydrogen in trap site i
U	Interaction controlling solute segregation in a stress field
V	Atomic volume of a solute atom
$\bar{V}_{\mathrm{H}}$	Partial molar volume due to hydrogen
x	Distance
x_{crit}	Critical distance ahead of fracture process zone
x_{H}	Fraction of hydrogen released during desorption
z	Number of electrons transferred during oxidation

Chapter 1

Introduction

1.1 Background

1.1.1 Additive Manufacturing of Metallic Alloys

Additive manufacturing (AM) has emerged as a promising pathway for fabricating metallic components, offering distinct advantages over traditional manufacturing methods.[1–5] One notable benefit is the ability of AM processes to produce intricate and complex geometries at near-net shape while maintaining tight tolerances, thereby minimizing material wastage and the number of required machining steps.[6–8] This results in a substantial decrease in overall manufacturing costs. These advantages are especially relevant for components employed in harsh operating environments, which are often geometrically unique with limited supply and long production lead times.[9–11]

The strengths of AM have driven recent discussions regarding the potential impact of additive manufacturing in major industries such as aerospace,[9, 12] construction,[13, 14] healthcare,[15, 16] electronics,[17] and oil and gas;[18] companies such as Airbus,[19] Volkswagen,[20] Toyota,[21] and Samsung[22] have already made advancements towards commercial implementation of AM technology. Additionally, in 2022, seven large manufacturers (GE

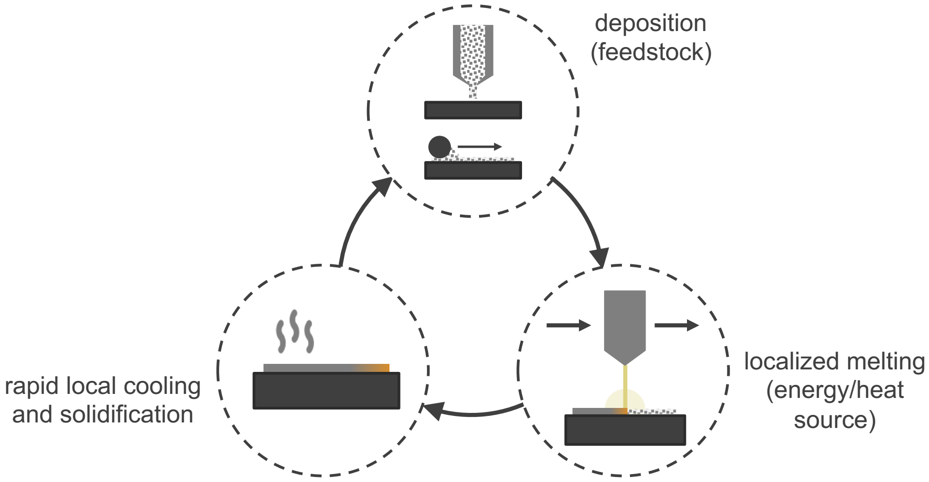

Figure 1.1: A schematic summarizing the basic mechanisms involved in different types of metal additive manufacturing.

Aviation, Raytheon, Siemens Energy, Lockheed Martin, Honeywell, Boeing, and Northrup Grumman) announced their participation in the United States federal program AM Forward, aimed towards providing support for increased adoption of AM technologies among smaller U.S.-based manufacturers and suppliers.[23] Market reports predict that interest will only increase in the coming years; estimates of the 2022 global additive manufacturing and material market valuation range from \$20-27 billion, and future predictions vary from a worldwide market valuation of \$74.6 billion by 2030, to \$183 billion by 2032.[24–26]

Common metal AM techniques include powder bed fusion (PBF) processes, in which thin layers of atomized powder are melted and solidified layer-by-layer to form the required part; and directed energy deposition (DED), in which atomized powder is laser melted simultaneously while being fed to the build surface.[6, 7] Though each manufacturing technique is unique, the general process underlying each method is similar: a repeated sequence of material deposition via powder layers or feedstock, localized melting using laser energy or some equivalent heat source, and subsequent rapid local cooling and solidification, as shown in Figure 1.1.

The microstructures of AM alloys tend to be markedly different from their traditionally produced counterparts, as the melting and remelting processes and fast cooling rates in additive manufacturing often produce complex solidification microstructures.[1] A variety of processing parameters can impact microstructure as well; studies have demonstrated that AM microstructure varies with scan speed, scan strategy, powder layer thickness, feed rate, laser power, powder atomization environment, and build atmosphere.[27–41] Additionally, the AM process can lead to defects and discontinuities such as increased porosity, delamination or lack of fusion between adjacent layers, and unmelted or partially melted particles.[42] The type of substrate and the role of the substrate as a heat sink may also affect properties, which is particularly relevant for materials with quench sensitivities. Furthermore, build direction must be considered due to inherent anisotropy from the AM process—the complex thermal cycles that take place often induce different local ranges of temperature throughout the part, causing inhomogeneity and microstructural anisotropy.[2]

As the microstructure and composition of AM materials often differs from that of their conventional counterparts, it is reasonable to assume that the hydrogen interactions in the materials may differ as well, leading to changes in hydrogen embrittlement and hydrogen-assisted cracking behavior.

1.1.2 State of Literature on Additively Manufactured 17-4 PH

17-4 PH is the most commonly used grade of precipitation-hardened stainless steel due to its excellent mechanical properties, though it is highly susceptible to hydrogen embrittlement, particularly in high-strength conditions.[43, 44] Wrought 17-4 PH is usually fully martensitic and contains approximately 15-17.5 wt% Cr, lending the alloy good corrosion resistance due to the formation of a passivation layer.[45] The presence of Ni, an austenite stabilizer, often leads to the occurrence of retained austenite in the microstructure. The relatively high hardness of the alloy originates from the growth and precipitation of coherent Cu precipitates during the aging process.[46]

Due to the low carbon content in 17-4 PH stainless steel, there is minimal lattice distortion of body-centered tetragonal (BCT) martensite from expansion along the c-axis, making it difficult to distinguish from the body-centered cubic (BCC) ferrite phase using diffraction techniques.[47, 48] The open BCT structure and the similarity between phases allows for faster diffusion compared to FCC austenitic stainless steels.[48]

There are several commonly used heat treatments for 17-4 PH. The first is the H900 heat treatment, otherwise known as the peak-aged condition, which involves aging for 1 hour at 482°C and results in a high-strength specimen with adequate ductility. The second is the H1025 heat treatment, otherwise known as the over-aged condition, which involves aging for 4 hours at 552°C and results in a specimen with reduced strength but increased ductility.[49]

Due to its good weldability, 17-4 PH stainless steel is considered amenable to manufacturing via AM processes, which has motivated numerous studies on the mechanical behavior of AM 17-4 PH,[1, 40, 41, 48, 50–66] as well as recent contributions exploring fatigue,[50, 51, 67–73] corrosion resistance,[74, 75] and stress corrosion cracking.[76] However, hydrogen behavior in AM 17-4 PH and the role of hydrogen in environment-assisted cracking has not been sufficiently explored in existing literature. The following section serves as a brief review of significant recent advancements concerning AM 17-4 PH.

The structure of as-built AM 17-4 PH is highly dependent on printing technique and processing parameters, leading to considerable diversity in the microstructural features and material properties reported in literature. Most as-built AM 17-4 PH specimens exhibit an anisotropic, dendritic structure with elongated grains along the building direction.[48, 52, 53, 63] Phase composition is significantly influenced by the atomization and build environments, with argon-atomized and argon-built specimens often displaying martensitic or δ-ferritic structures with small amounts of retained austenite, whereas their nitrogen-atomized and nitrogen-built counterparts contain high amounts of austenite due to the austenite-stabilizing properties of nitrogen.[40, 48, 52, 52, 53, 59, 63, 64, 67, 77] In a study by Murr et al. comparing Ar and N_2 atomization and build environments, all specimens either built or atomized in Ar were primarily body-centered cubic (BCC) in structure, whereas the specimen that was both built and atomized in N_2 consisted of primarily face-centered cubic (FCC) austenite.[40]

A significant distinguishing characteristic of AM 17-4 PH compared to its wrought counterpart is the widespread presence of small, spherical pores with micron- or sub-micron-level diameters,[50, 51, 57, 61, 67–71, 74–86] commonly attributed to partially melted particles as well as entrapped gas from the argon atomization or build process.[50, 57, 74] Porosity has also been observed in nitrogen-atomized and nitrogen-built specimens, but the pores were eliminated through a hot isostatic pressing (HIP) treatment.[87]

A focal point of many studies on AM 17-4 PH is the effect of powder characteristics and process parameters on microstructure and mechanical properties. Various investigations have explored the effects of powder density; Poudel et al.[83] compared specimens fabricated using two different powder suppliers but the same processing parameters, noting that powder with lower bulk density produced specimens with increased tensile strength but higher porosity levels and lower ductility. However, Weaver et al.[86] found similar density, hardness, and strength properties in specimens fabricated using fine and coarse powders, with an improvement in hardness, yield stress, and ultimate tensile strength in an intermediate-density powder. A dependence of ductility on powder density was also reported.[86]

The effect of laser parameters on microstructure has also been explored in recent literature. Laser power has been linked to microstructure coarseness due to the impact on cooling; thick δ-ferrite stringers were observed at increased laser power due to slower cooling rates.[88] Sun et al. found that decreasing laser scan length led to a transition from coarse, ferritic columnar grains to finer grains with increased austenite fraction.[89] Increased scanning speed has been connected to an increase in microhardness[90] and a decrease in porosity;[80] additionally, the inter-layer time intervals have been shown to affect austenite content, with shorter time intervals leading to increased austenite due to lower cooling rates.[61] Although changes in scanning strategy have been accompanied by slight changes in hardness,[91] post-processing heat treatments have proven effective in mitigating such variations in some cases.[92] However, work by Kudzal et al. indicates that scan strategy can affect the type of porosity (entrapped gas, lack of fusion, or interlayer de-bonding) found in the AM specimen.[57] It has been argued that energy density has little effect on porosity in L-PBF specimens,[93] though this does not align with other literature showing variations in porosity based on slice thickness and scanning speed.[80]

Various optimization studies compared the effects of select processing parameter combinations, though optimal parameters also depend strongly on the desired benefits. For example, Ponnusamy et al. recommend a -6 mm defocus distance as part of a set of printing parameters for optimized microhardness and compressive strength,[94] but also found that this value leads to high porosity and recommend a -4 mm defocus distance in a separate study aimed at improving surface characteristics.[95]

Beyond processing parameters, the choice of part design, location, and even spatter during building can impact the characteristics of AM specimens. Part geometry has been shown to affect porosity and melt pool depth, with an increase in porosity and shorter melt pool dimensions found in dog-bone-shaped specimens than in large block specimens.[84] Additionally, Ali et al.[78] studied the morphology and effects of spatter particles during the L-PBF process, concluding that parts printed in a non-spatter-rich region display increased ductility and smaller pores than those printed in a spatter-rich region.

Differences in build parameters lead to a high degree of variation in pertinent microstructural features. For example, varying amounts of retained austenite have been observed after post-processing, depending on the build and heat treatment procedures. Solution annealing has been shown to result in a lath microstructure that is nearly entirely martensitic,[48] with austenite reversion occurring during subsequent aging treatments.[96] Carneiro et al. observed 21% retained austenite after annealing and aging of selective laser melted (SLM) 17-4 PH.[50] Direct metal laser sintered (DMLS) 17-4 PH showed much smaller fractions of retained austenite in the peak-aged condition and was fully martensitic in the over-aged conditions.[97] Meredith et al.[62] observed a maximum of 3% retained austenite in Ar-atomized as-built specimens, whereas N_2-atomized specimens showed up to 81% retained austenite in the as-built condition, depending on the printing system. After examining a variety of solutionizing and aging treatments, the maximum retained austenite found in Ar-atomized specimens was 9%, whereas the maximum value in N_2-atomized specimens was 30%. Guennouni et al. observed 12.6% retained austenite in a peak-aged specimen, attributed to reversion during the aging step post-solution annealing; the authors also argued that this may be an underestimate, as surface preparation procedures could induce martensite transformation.[55]

Precipitation hardening occurs through the precipitation of Cu-rich regions. This results in the formation and growth of nanoscale incoherent copper precipitates after peak-aging heat treatments,[40, 52, 65, 73] which then coarsen and become incoherent upon over-aging.[73] Murr et al. observed metastable coherent Cu-rich precipitates less than 5 nm in diameter in the peak-aged condition, as well as stable incoherent Cu spheres above 5 nm.[40] Additional precipitates found in AM specimens include nano-scale oxide inclusions as well as carbides; Sun et al. postulated that these oxides suppress grain boundary migration upon heat treatment, leading to a more refined grain structure in AM than in wrought.[65, 85]

The mechanical properties of AM 17-4 PH have also been widely discussed. Depending on build parameters and post-processing, the yield strength, elastic modulus, and hardness of AM specimens mostly range from markedly worse to slightly improved compared to their wrought counterparts.[50, 52, 66, 95, 96, 98–100] As-built specimens also often display anisotropic mechanical properties due to anisotropy in the microstructure, though this can be eliminated with homogenization treatments.[61] It should be noted that high-throughput tensile testing has revealed variability in mechanical properties within single builds in as-built AM 17-4 PH.[101]

Peak-aging heat treatments in AM 17-4 PH are often used to increase yield and ultimate tensile strength,[61, 66] while over-aging provides lower strength but enhanced ductility.[102] Shot peening treatments have also proven effective in improving surface roughness, hardness, compressive yield strength, and wear resistance in DMLS 17-4 PH through a grain refinement and work-hardening effect.[103]

The choice of atomization and build environment can drastically affect mechanical properties; while argon is often chosen to avoid the austenite-stabilizing properties of nitrogen and subsequent inferior mechanical properties associated with a high percentage of austenite, it should be noted that the porosity due to entrapped gas resulting from an Ar atomization and build environment persists through post-processing heat treatments and leads to a consistent reduction of ductility in AM 17-4 PH.[59, 60, 76, 78, 83] Additionally, Ar-built specimens show increased capability for precipitation hardening due to the martensitic microstructure and therefore have higher hardness upon aging than N_2-built specimens, even when those specimens are Ar-atomized.[104] Attempts have been made to reduce the retained austenite in N_2-atomized AM 17-4 through a series of heat treatments; Lass et al.[45] developed a post-processing heat treatment consisting of homogenization, solutionization, and controlled cooling to reduce the amount of retained austenite down to around 5%, producing an AM alloy with a tensile yield strength that was over 90% of the wrought strength. This was a vast improvement from the as-built condition, which had a high amount of retained austenite and a yield strength of about 55% of that of the wrought.

Fracture along prior austenite grain boundaries has been observed in the AM specimens.[52] In the as-built specimens, quasi-cleavage failure has been shown to occur through the weld line overlap, melt pool boundary, or cleavage of ferrite.[57] Additionally, crack initiation often occurs at pores, which are features specific to AM.[57]

AM 17-4 PH has exhibited decreased fatigue resistance compared to its wrought counterpart in several studies; this has been attributed to internal defects and poor surface finish.[46, 50, 70–73, 99] Internal defects, such as pores and un-melted regions, are speculated to be crack initiation sites for fatigue cracking in the AM material; this was seen even after HIP processing, which improved fatigue behavior under axial loading but not in torsion.[71] N_2-built AM 17-4 PH has shown slightly improved fatigue performance compared to its Ar-built counterpart, attributable to grain refinement as well as the porosity caused by the Ar shield gas.[67] Yadollahi et al. and Nezhadfar et al. both observed similar fatigue crack growth behavior from peak-aged AM and wrought specimens in the Paris regime,[68, 72] but the latter study found cracking along δ-ferrite/martensite interfaces in over-aged specimens with a transition from transgranular in mode I to mixed transgranular and intergranular crack propagation in mode II.[72] In a separate study, Yadollahi et al. reported that post-processing solution annealing and peak aging led to improved low-cycle fatigue behavior but worsened high-cycle fatigue behavior.[51]

Additionally, part geometry has been shown to affect high-cycle fatigue due to changes in porosity based on specimen shape.[84] Soltani-Tehrani et al. observed improved high-cycle fatigue behavior when powder is recycled and re-used, due to the reduction of agglomerates in the powder.[69] The authors also found that, with increased re-use of the powder, the degree of fatigue dependence on the position of the part in the build plate was reduced; this was attributed to improved flowability.[69]

Limited research into wear behavior has also been conducted; AM 17-4 PH showed improved wear behavior in dry conditions, but had a higher wear rate in the lubricated condition. These differences were attributed to increased hardness and surface roughness of the AM specimen, which improved adhesion resistance but enhanced abrasion and surface fatigue.[47]

Though several studies have been published regarding the corrosion behavior of AM 17-4 PH, little consensus has been reached. Schaller et al. found reduced corrosion resistance in L-PBF 17-4 PH after heat treatment, credited to the presence of pores which may act as tight crevices causing occluded cell corrosion.[74] Active corrosion was observed near larger pores near the surface instead of the passive corrosion found near smaller pores and in the wrought specimen. However, superior general corrosion resistance was observed by Alnajjar et al. in L-PBF 17-4 PH compared to wrought after a re-austenitizing heat treatment, attributed to the absence of MnS inclusions in the AM specimen that often destabilize the passive film.[52] Beyond any effect of powder and build parameters, the disparity in these two findings may be due to difference in post-processing—both studies solution heat treated specimens at 1050°C for 60 minutes, but Schaller et al. performed a subsequent peak-aging heat treatment in order to precipitation harden the alloy. This likely caused a coarsening of the existing pores, leading to the large pores near which active corrosion was observed. Corrosion performance has also been shown to improve with the powder fineness, depending on energy density values; at the highest energy density value, the AM specimens showed better polarization resistance than their wrought counterparts.[49]

In terms of localized corrosion, Stoudt et al.[41] found higher pitting potentials in nitrogen-atomized, heat-treated AM 17-4 PH compared to the wrought alloy, attributed to finer grain size, more homogeneous distribution of carbides, and increased stability in the passive film due to the nitrogen from the build process.

Though the depth of the existing literature on AM 17-4 PH provides valuable insight into the influence of AM processes on microstructure as well as mechanical and corrosion properties, the variability evident across these studies underscores the need for further examination of AM alloys to ensure safety and reproducibility for commercial applications.

1.1.3 Significance of Hydrogen Interactions in AM 17-4 PH

Hydrogen has a significant deleterious effect on the mechanical properties of 17-4 PH stainless steel, particularly due to the material's high strength, which has been demonstrated to correlate to low hydrogen embrittlement resistance.[105] Though few studies have been published on the behavior of hydrogen in AM 17-4 PH, Alnajjar et al.[52] and Guennouni et al.[56] both observed increased susceptibility to hydrogen embrittlement in

L-PBF 17-4 PH compared to wrought, partially attributed to the increased grain size in the AM specimens. Alnajjar et al. also noted that AM 17-4 PH displayed transgranular cleavage instead of the brittle intergranular fracture mode seen in the wrought specimens. These differences in hydrogen embrittlement susceptibility between AM 17-4 PH and their wrought counterparts necessitate the study of H interactions in AM 17-4 PH to fully understand and mitigate the deleterious effects of hydrogen.

Additionally, both in-service component failures[106–116] and laboratory studies[116–126] demonstrate that wrought 17-4 PH is susceptible to environment-assisted cracking (EAC) when immersed in marine environments. In this context, EAC susceptibility is highly dependent on potential. This has been explored in related alloys through cathodically-driven hydrogen production uptake and trapping at cathodic potentials. At anodic potentials, cracking is enabled by metal dissolution, cation hydrolysis, and crack tip acidification followed by proton reduction, hydrogen uptake, and trapping. In both cases, hydrogen susceptibility is traced to a large negative hydrogen overpotential.[127]

Despite this well-documented EAC susceptibility in conventionally manufactured 17-4 PH, research on EAC behavior of AM 17-4 PH is limited,[8, 128] particularly from a fracture mechanics standpoint.[76] However, these limited efforts have already highlighted significant differences in EAC behavior between AM and wrought 17-4 PH. For instance, Shoemaker et al.[76] measured 5- to 10-fold increases in crack growth rate for peak-aged and over-aged AM 17-4 PH compared to wrought 17-4 PH with comparable strengths. Additionally, variations in fracture morphology were observed between the AM and wrought specimens and between different heat treatment conditions. However, the microstructural origins of the reduced EAC resistance of AM 17-4 PH remain unclear. Literature indicates that EAC in conventional alloys is sensitive to subtle microstructural variations[129–131] and it is well-established that AM microstructures can be markedly different from conventional materials.[2, 4, 27–31, 33, 34, 37, 41] Shoemaker et al., for example, reported widespread sub-micrometer porosity and oxide inclusions in “matched-strength” AM 17-4 PH that were not present in wrought 17-4 PH.[76] It was postulated that these unique features could increase EAC susceptibility in AM 17-4 PH by degrading the fracture toughness (k_{IG}) of the fracture pathway. Moreover, such microstructural differences between AM and conventional 17-4 PH may influence their respective hydrogen-metal interactions (e.g., uptake, trapping, and diffusion), which strongly affect EAC behavior. For example, the threshold stress intensity for the onset of EAC (K_{TH}) in high-strength steels has a demonstrated dependency on the diffusible hydrogen concentration ($C_{\mathrm{H,diff}}$).[132–134]

Literature also establishes a strong correlation between the effective hydrogen diffusivity D_{eff}, hydrogen concentration, and stage II crack growth rate $\left(\frac{\mathrm{d}a}{\mathrm{d}t}\right)_{\mathrm{II}}$ in various structural materials.[129] To illustrate, consider the HEAC stage II crack growth rate model outlined by Lee and Gangloff:[135]

$$\left(\frac{\mathrm{d}a}{\mathrm{d}t}\right)_{\mathrm{II}} = \frac{4D_{\mathrm{eff}}}{x_{\mathrm{crit}}}\left[\mathrm{erf}^{-1}\left(1 - \frac{C_{\mathrm{H}\sigma-\mathrm{crit}}}{C_{\mathrm{H}\sigma}}\right)\right]^2, \tag{1.1}$$

where x_{crit} is a critical length parameter (related to the material microstructure and fracture process control dimensions), $C_{\mathrm{H}\sigma-\mathrm{crit}}$ is a critical stress-enhanced hydrogen concentration required for EAC propagation, and $C_{\mathrm{H}\sigma}$ is the stress-enhanced hydrogen concentration adjacent to the crack tip and is highly dependent on applied potential, particularly hydrogen overpotential. The critical stress-enhanced hydrogen concentration $C_{\mathrm{H}\sigma-\mathrm{crit}}$ is an intrinsic property based on alloy composition, strength, and grain boundary nanochemistry. This model also takes into consideration the influence of hydrogen diffusivity and concentration on stage II crack growth rate. In situations where decohesion cracking adheres to this model, it becomes apparent that the determination of diffusivity, critical length parameter, stress-affected H concentration, and critical stress-affected H concentration becomes vital, and the relationship of these parameters to microstructural features is paramount. Additionally, there is a lack of investigation into assigning a refined hydrogen diffusivity value to the crack-affected zone, should diffusion be slowed by trapping or increased by rapid diffusion along amenable pathways near the crack tip. This is particularly crucial

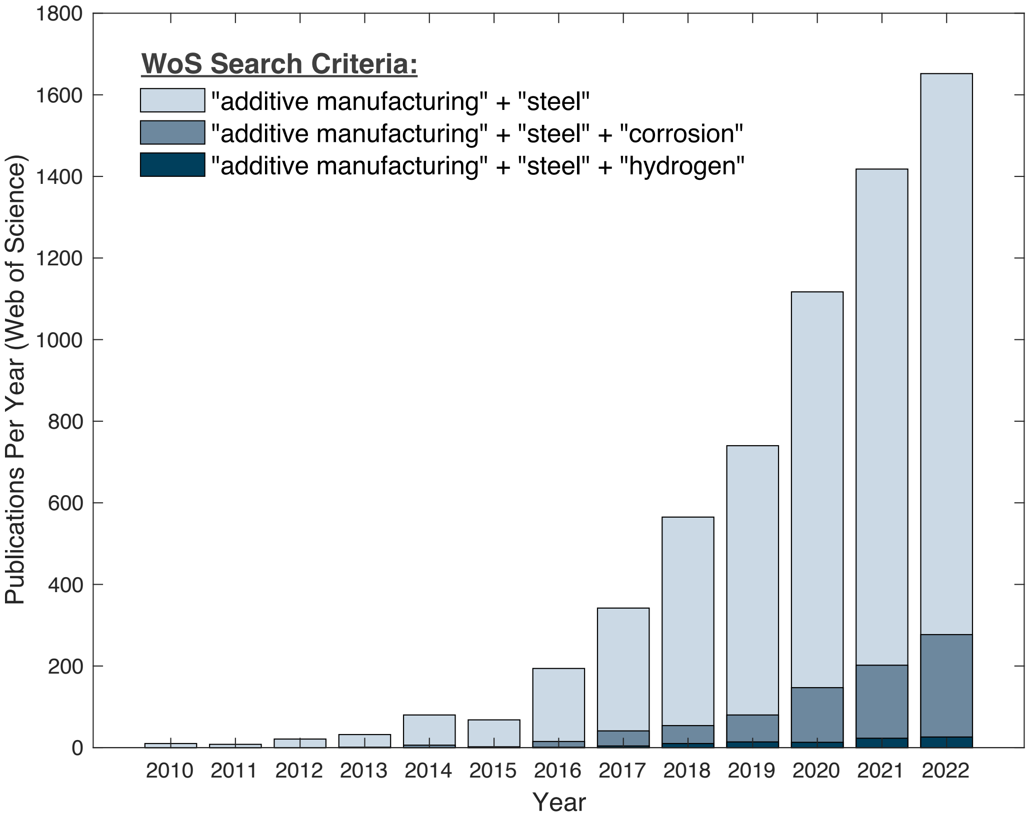

Figure 1.2: The number of publications per year discussing additively manufactured steels between 2010 and 2022, overlaid with the number of publications that mention corrosion and hydrogen (based on data from Web of Science).

concerning diffusion along grain boundaries, given the lack of consensus in literature regarding fast transport behavior along grain boundaries. These issues must be held in consideration when comparing wrought and AM alloys, along with a strong understanding of grain boundary character.

1.2 Critical Unresolved Issues

Despite a wealth of mechanical behavior and corrosion studies featuring additively manufactured stainless steels, there has been little investigation into the behavior of hydrogen in these alloys, as evidenced by the review of literature published between 2010 and 2022 shown in Figure 1.2.

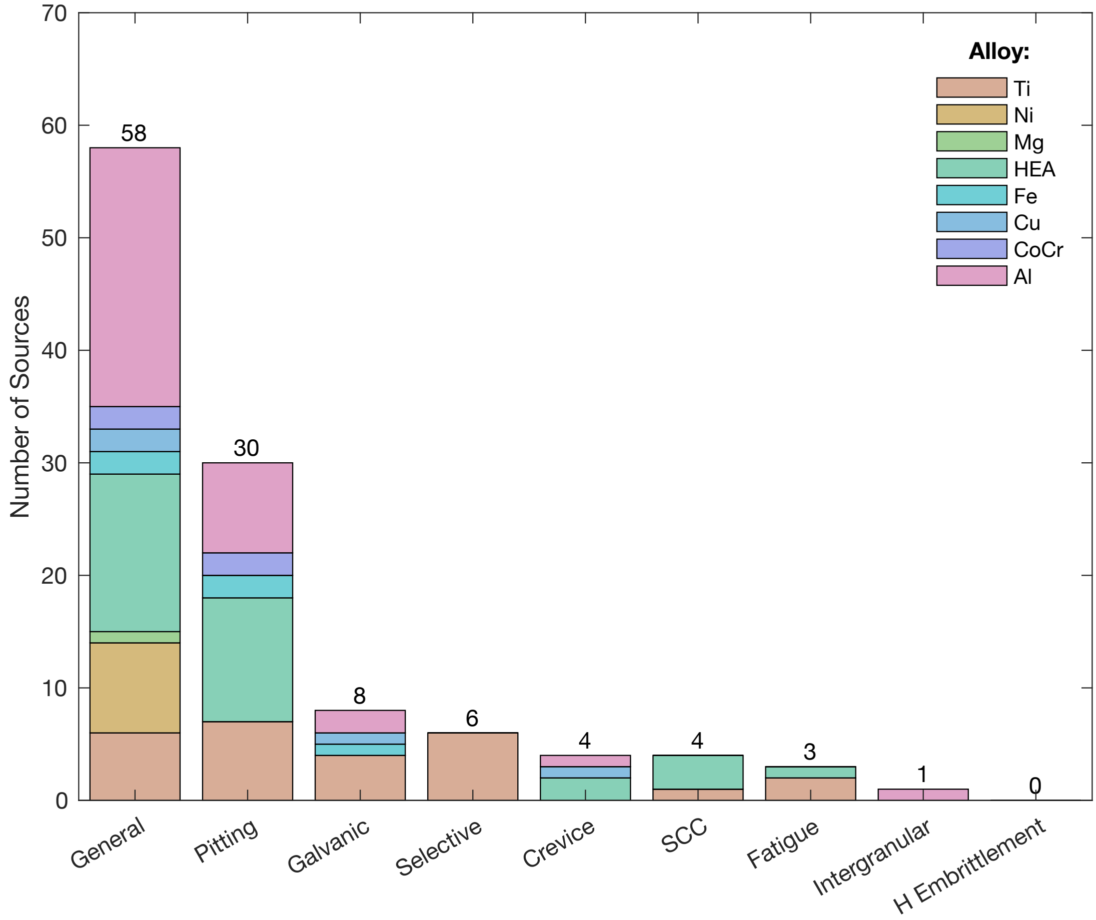

Figure 1.3: A summary of the corrosion mechanisms addressed in the literature cited in the 2018 review article by Sander et al.[8] discussing the corrosion of additively manufactured metallic alloys. The primary element or elements of each alloy are indicated.

Even within the context of corrosion-related literature, exploration into hydrogen is often limited, as illustrated in Figure 1.3 summarizing the studies cited in the 2018 review article by Sander et al. about corrosion in AM alloys.[8] However, as additively manufactured materials display considerably different microstructural features than traditionally manufactured materials and those microstructural features are key to hydrogen interactions, the assumption of identical hydrogen behavior in AM and wrought materials cannot be made. For example, AM 17-4 PH and wrought 17-4 PH alloys have shown differences in prior austenite grain size and the formation of Cu-rich precipitates, both of which have been linked to embrittlement susceptibility.[40, 44, 52]

The behavior of hydrogen is frequently assessed through either solely electrochemical or thermal techniques, which can be used to determine bulk diffusivity and diffusible hydrogen concentration and to provide insight into microstructural trapping. While each method is well-established, there are inherent assumptions or shortcomings in each technique that may influence the resulting data. Most permeation analyses rely on several assumptions that may skew results if not verified, such as entirely diffusion-controlled permeation and the lack of any mobile H in the initial microstructure before testing. The most common thermal desorption spectroscopy (TDS) analysis method assumes entirely one-dimensional diffusion and does not account for retrapping. In essence, relying solely on a single method to characterize hydrogen behavior can introduce technique-specific biases in the results. To address the assumptions and simplifications inherent in each method, this thesis employs a comprehensive approach by supplementing commonly used techniques such as permeation and TDS with others based on different physical principles, including the barnacle cell method and LECO H testing.

Additionally, a comprehensive exploration of potential microstructural trap states in AM 17-4 PH compared to its wrought counterpart has not been published in existing literature. This establishes a crucial framework for evaluating the differences in bulk hydrogen behavior and enables analysis across various length scales.

Integrating these techniques to assess hydrogen uptake, diffusion, and trapping will offer insight into the impact of AM microstructure on hydrogen behavior, serving as a foundation for further study of hydrogen-assisted failure mechanisms in AM materials.

Lastly, there have been no previous studies relating stage II crack growth rate to hydrogen diffusion, critical stress-affected hydrogen concentration, and the critical length parameter x_{crit} in AM or wrought 17-4 PH. Moreover, comparisons of hydrogen-metal interactions in AM and wrought 17-4 PH are minimal, hindering mechanistic understanding of the increased EAC susceptibility of AM 17-4 PH. This provides an impetus for the hydrogen analysis described in the upcoming chapters of this thesis, where a broad assessment of hydrogen-metal interactions in AM and wrought 17-4 PH is presented with the aim of enhancing comprehension of the mechanisms driving the increase in EAC susceptibility.

1.3 Objectives

The work presented in this thesis aims to characterize hydrogen behavior in additively manufactured 17-4 PH stainless steel through a series of corroborating analysis methods, and to explore the role of hydrogen-microstructure interactions in the increased stress corrosion cracking susceptibility in AM 17-4 PH. These objectives have been accomplished through an investigation into the following areas of interest, comparing the AM 17-4 PH to matched-strength wrought 17-4 PH:

1. Analysis of bulk hydrogen behavior through the determination of effective hydrogen diffusivity, diffusible hydrogen concentration, and total hydrogen concentration;
2. Characterization of microstructural trap states and assessment of their impact on bulk hydrogen behavior in wrought and AM specimens; and
3. Evaluation of the relationship between hydrogen and environment-assisted cracking kinetics.

These goals were achieved through the establishment of a methodology for studying hydrogen behavior that employs diverse approaches to address multiple length scales and mitigate reliance on any assumptions inherent to each technique. The completion of these objectives assists in bridging the knowledge gaps outlined in the previous section, offering crucial insights into the interactions and impact of hydrogen in AM 17-4 PH.

1.4 Dissertation Overview

The following dissertation comprises eight chapters. The current introductory chapter outlines the gaps and unresolved issues in the existing research and establishes the overview and goals of this work. Chapter 2 introduces the relevant AM and wrought 17-4 PH alloys and presents a multi-pronged approach to microstructural characterization, laying vital groundwork for analyses in subsequent chapters. The objectives outlined in the previous section are addressed in the ensuing chapters as follows:

Objective #1: Bulk Hydrogen Behavior Analysis

- Chapter 3 compares bulk effective hydrogen diffusivity in wrought and AM 17-4 PH, quantified using thermal and electrochemical techniques.
- Chapter 4 focuses on analysis of bulk diffusible and total hydrogen concentration in wrought and AM 17-4 PH, and addresses the potential impact of hydrogen concentration on diffusion.

Objective #2: Linking Microstructural Features to Hydrogen Behavior

- Chapter 5 provides an analysis of potential microstructural hydrogen trap states in AM 17-4 PH compared to its wrought counterpart, and models the impact of microstructural differences on the previously characterized bulk hydrogen behavior.
- Chapter 6 summarizes the state of literature addressing grain boundary-hydrogen interactions, and uses the Hashin-Shtrikman upper bound framework to model and compare the diffusivity along grain boundaries in AM and wrought 17-4 PH.

Objective #3: Relationship to Environment-Assisted Cracking Kinetics

- Chapter 7 couples the bulk hydrogen behavior analysis explored in the first objective to the increased stress corrosion cracking susceptibility observed in AM 17-4 PH, using the Lee-Gangloff framework to model stage II crack growth rate and provide insight into intrinsic properties that influence cracking, such as critical stress-affected hydrogen concentration and critical length parameter.

The dissertation culminates with Chapter 8, which details a summary of the major conclusions of the work as well as suggestions for future research directions.

References

[1] P. Bajaj, A. Hariharan, A. Kini, P. Kürnsteiner, D. Raabe, and E. A. Jägle, "Steels in additive manufacturing: A review of their microstructure and properties," *Materials Science and Engineering: A*, vol. 772, p. 138633, 2020.

[2] T. DebRoy, H. L. Wei, J. S. Zuback, T. Mukherjee, J. W. Elmer, J. O. Milewski, A. M. Beese, A. Wilson-Heid, A. De, and W. Zhang, "Additive manufacturing of metallic components – Process, structure and properties," *Progress in Materials Science*, vol. 92, pp. 112–224, 2018. ISBN: 9188720411.

[3] W. E. Frazier, "Metal additive manufacturing: A review," *Journal of Materials Engineering and Performance*, vol. 23, pp. 1917–1928, 2014. ISBN: 1059-9495.

[4] S. Gorsse, C. Hutchinson, M. Gouné, and R. Banerjee, "Additive manufacturing of metals: a brief review of the characteristic microstructures and properties of steels, Ti-6Al-4V and high-entropy alloys," *Science and Technology of Advanced Materials*, vol. 18, no. 1, pp. 584–610, 2017.

[5] D. Herzog, V. Seyda, E. Wycisk, and C. Emmelmann, "Additive manufacturing of metals," *Acta Materialia*, vol. 117, pp. 371–392, 2016.

[6] K. S. Prakash, T. Nancharaih, and V. V. Rao, "Additive Manufacturing Techniques in Manufacturing -An Overview," in *Materials Today: Proceedings*, 2018. ISSN: 22147853.

[7] W. J. Sames, F. A. List, S. Pannala, R. R. Dehoff, and S. S. Babu, "The Metallurgy and Processing Science of Metal Additive Manufacturing," *International Materials Reviews*, 2016.

[8] G. Sander, J. Tan, P. Balan, O. Gharbi, D. Feenstra, L. Singer, S. Thomas, R. Kelly, J. Scully, and N. Birbilis, "Corrosion of additively manufactured alloys: A review," *Corrosion*, vol. 74, no. 12, 2018.

[9] B. Blakey-Milner, P. Gradl, G. Snedden, M. Brooks, J. Pitot, E. Lopez, M. Leary, F. Berto, and A. du Plessis, "Metal additive manufacturing in aerospace: A review," *Materials and Design*, vol. 209, p. 110008, 2021. Publisher: The Author(s).

[10] G. A. Pacillo, G. Ranocchiai, F. Loccarini, and M. Fagone, "Additive manufacturing in construction: A review on technologies, processes, materials, and their applications of 3D and 4D printing," *Material Design and Processing Communications*, vol. 3, no. 5, pp. 1–7, 2021.

[11] A. Saboori, A. Aversa, G. Marchese, S. Biamino, M. Lombardi, and P. Fino, "Application of directed energy deposition-based additive manufacturing in repair," *Applied Sciences (Switzerland)*, vol. 9, no. 16, 2019.

[12] S. Singamneni, Y. Lv, A. Hewitt, R. Chalk, W. Thomas, and D. Jordison, "Additive Manufacturing for the Aircraft Industry: A Review," *Journal of Aeronautics & Aerospace Engineering*, vol. 8, Feb. 2019.

[13] A. Paolini, S. Kollmannsberger, and E. Rank, "Additive manufacturing in construction: A review on processes, applications, and digital planning methods," *Additive Manufacturing*, vol. 30, p. 100894, Dec. 2019.

[14] A. Pajonk, A. Prieto, U. Blum, and U. Knaack, "Multi-material additive manufacturing in architecture and construction: A review," *Journal of Building Engineering*, vol. 45, p. 103603, Jan. 2022.

[15] Y. Wang, Q. Tan, F. Pu, D. Boone, and M. Zhang, "A Review of the Application of Additive Manufacturing in Prosthetic and Orthotic Clinics from a Biomechanical Perspective," *Engineering*, vol. 6, pp. 1258–1266, Nov. 2020.

[16] E. Rezvani Ghomi, F. Khosravi, R. E. Neisiany, S. Singh, and S. Ramakrishna, "Future of additive manufacturing in healthcare," *Current Opinion in Biomedical Engineering*, vol. 17, p. 100255, Mar. 2021.

[17] N. Divakaran, J. P. Das, A. K. P V, S. Mohanty, A. Ramadoss, and S. K. Nayak, "Comprehensive review on various additive manufacturing techniques and its implementation in electronic devices," *Journal of Manufacturing Systems*, vol. 62, pp. 477–502, Jan. 2022.

[18] M. Sireesha, J. Lee, A. S. Kranthi Kiran, V. J. Babu, B. B. T. Kee, and S. Ramakrishna, "A review on additive manufacturing and its way into the oil and gas industry," *RSC Advances*, vol. 8, no. 40, pp. 22460–22468, 2018.

[19] D. Simmons, "Airbus had 1,000 parts 3D printed to meet deadline," *BBC News*, May 2015.

[20] "Volkswagen plans to use new 3D printing process in vehicle production in the years ahead."

[21] C. Kerkau, "Toyota to Buy First Stratasys F3300 3D Printer," Nov. 2023.

[22] "Samsung Electronics Selects Optomec's Aerosol Jet for Next-Generation Electronics Production," June 2019.

[23] “AM Forward.”

[24] S. Saha, “Additive Manufacturing and Material Market Outlook (2022 to 2032),” Tech. Rep. REP-GB-16825, Future Market Insights, Mar. 2023.

[25] “Additive Manufacturing Market - Global Forecast to 2030,” tech. rep., MarketDigits, Richmond, VA, Nov. 2023.

[26] “Additive Manufacturing Materials Market Size & Share Analysis - Growth Trends & Forecasts (2023 - 2028),” tech. rep., Mordor Intelligence, 2023.

[27] K. G. Prashanth, S. Scudino, T. Maity, J. Das, and J. Eckert, “Is the energy density a reliable parameter for materials synthesis by selective laser melting?,” *Materials Research Letters*, 2017.

[28] Y. Shang, Y. Yuan, D. Li, Y. Li, and J. Chen, “Effects of scanning speed on in vitro biocompatibility of 316L stainless steel parts elaborated by selective laser melting,” *International Journal of Advanced Manufacturing Technology*, 2017.

[29] R. Li, J. Liu, Y. Shi, M. Du, and Z. Xie, “316L stainless steel with gradient porosity fabricated by selective laser melting,” *Journal of Materials Engineering and Performance*, vol. 19, pp. 666–671, 2010.

[30] G. Sander, S. Thomas, V. Cruz, M. Jurg, N. Birbilis, X. Gao, M. Brameld, and C. R. Hutchinson, “On The Corrosion and Metastable Pitting Characteristics of 316L Stainless Steel Produced by Selective Laser Melting,” *Journal of The Electrochemical Society*, 2017.

[31] M. K. Alam, A. Edrisy, J. Urbanic, and J. Pineault, “Microhardness and stress analysis of laser-cladded AISI 420 martensitic stainless steel,” *Journal of Materials Engineering and Performance*, vol. 26, pp. 1076–1084, 2017.

[32] Y. Sun, A. Moroz, and K. Alrbaey, “Sliding wear characteristics and corrosion behaviour of selective laser melted 316L stainless steel,” *Journal of Materials Engineering and Performance*, 2014.

[33] R. I. Revilla, J. Liang, S. Godet, and I. De Graeve, “Local Corrosion Behavior of Additive Manufactured AlSiMg Alloy Assessed by SEM and SKPFM,” *Journal of The Electrochemical Society*, 2017.

[34] T. M. Chiu, M. Mahmoudi, W. Dai, A. Elwany, H. Liang, and H. Castaneda, “Corrosion assessment of Ti-6Al-4V fabricated using laser powder-bed fusion additive manufacturing,” *Electrochimica Acta*, vol. 279, pp. 143–151, 2018.

[35] R. M. Mahamood and E. T. Akinlabi, “Types of Functionally Graded Materials and Their Areas of Application,” in *Topics in Mining, Metallurgy and Materials Engineering*, Springer, 2017. ISSN: 23643307.

[36] K. M. Mantrala, M. Das, V. K. Balla, C. Srinivasa Rao, and V. V. Kesava Rao, “Laser-deposited CoCrMo alloy: Microstructure, wear, and electrochemical properties,” *Journal of Materials Research*, vol. 29, no. 17, pp. 2021–2027, 2014.

[37] J. J. Marattukalam, A. K. Singh, S. Datta, M. Das, V. K. Balla, S. Bontha, and S. K. Kalpathy, “Microstructure and corrosion behavior of laser processed NiTi alloy,” *Materials Science and Engineering C*, vol. 57, pp. 309–313, 2015.

[38] H. Ibrahim, A. R. Jahadakbar, A. Dehghan, N. S. Moghaddam, A. Amerinatanzi, and M. Elahinia, “In vitro corrosion assessment of additively manufactured porous NiTi structures for bone fixation applications,” *Metals*, vol. 8, no. 3, p. 164, 2018.

[39] H. S. Klapper, N. Molodtsov, M. Burns, and C. Wangenheim, “Critical factors affecting the pitting corrosion resistance of additively manufactured nickel alloy in chloride containing environments,” in *NACE - International Corrosion Conference Series*, 2017. ISSN: 03614409.

[40] L. E. Murr, E. Martinez, J. Hernandez, S. Collins, K. N. Amato, S. M. Gaytan, and P. W. Shindo, “Microstructures and properties of 17-4 PH stainless steel fabricated by selective laser melting,” *Journal of Materials Research and Technology*, vol. 1, no. 3, pp. 167–177, 2012. ISBN: 2238-7854.

[41] M. R. Stoudt, R. E. Ricker, E. A. Lass, and L. E. Levine, “Influence of Postbuild Microstructure on the Electrochemical Behavior of Additively Manufactured 17-4 PH Stainless Steel,” *JOM*, vol. 69, no. 3, pp. 506–515, 2017. ISBN: 1047-4838.

[42] P. C. Collins, D. A. Brice, P. Samimi, I. Ghamarian, and H. L. Fraser, “Microstructural Control of Additively Manufactured Metallic Materials,” *Annual Review of Materials Research*, vol. 46, pp. 63–91, July 2016. Publisher: Annual Reviews Inc.

[43] W. C. Chiang, C. C. Pu, B. L. Yu, and J. K. Wu, “Hydrogen susceptibility of 17-4 PH stainless steel,” *Materials Letters*, vol. 57, no. 16-17, pp. 2485–2488, 2003.

[44] S. Shen, X. Li, P. Zhang, Y. Nan, G. Yang, and X. Song, “Effect of solution-treated temperature on hydrogen embrittlement of 17-4 PH stainless steel,” *Materials Science and Engineering A*, 2017.

[45] E. A. Lass, M. R. Stoudt, and M. E. Williams, “Additively Manufactured Nitrogen-Atomized 17-4 PH Stainless Steel with Mechanical Properties Comparable to

Wrought," *Metallurgical and Materials Transactions A*, vol. 50, pp. 1619–1624, Apr. 2019.

[46] A. Yadollahi, N. Shamsaei, S. M. Thompson, A. Elwany, L. Bian, and M. Mahmoudi, "Fatigue behavior of selective laser melted 17-4 PH stainless steel," in *Proceedings of the 26th Annual International Solid Freeform Fabrication Symposium*, University of Texas at Austin, 2015.

[47] K. Sanjeev, P. Nezhadfar, C. Phillips, M. Kennedy, N. Shamsaei, and R. Jackson, "Tribological behavior of 17–4 PH stainless steel fabricated by traditional manufacturing and laser-based additive manufacturing methods," *Wear*, vol. 440-441, p. 203100, Dec. 2019.

[48] A. Caballero, J. Ding, S. Ganguly, and S. Williams, "Wire + Arc Additive Manufacture of 17-4 PH stainless steel: Effect of different processing conditions on microstructure, hardness, and tensile strength," *Journal of Materials Processing Technology*, vol. 268, pp. 54–62, 2019.

[49] H. Irrinki, T. Harper, S. Badwe, J. Stitzel, O. Gulsoy, G. Gupta, and S. V. Atre, "Effects of powder characteristics and processing conditions on the corrosion performance of 17-4 PH stainless steel fabricated by laser-powder bed fusion," *Progress in Additive Manufacturing*, vol. 3, pp. 39–49, June 2018.

[50] L. Carneiro, B. Jalalahmadi, A. Ashtekar, and Y. Jiang, "Cyclic deformation and fatigue behavior of additively manufactured 17–4 PH stainless steel," *International Journal of Fatigue*, vol. 123, pp. 22–30, 2019.

[51] A. Yadollahi, N. Shamsaei, S. M. Thompson, A. Elwany, and L. Bian, "Effects of building orientation and heat treatment on fatigue behavior of selective laser melted 17-4 PH stainless steel," *International Journal of Fatigue*, vol. 94, pp. 218–235, 2017.

[52] M. Alnajjar, F. Christien, C. Bosch, and K. Wolski, "A comparative study of microstructure and hydrogen embrittlement of selective laser melted and wrought 17–4 PH stainless steel," *Materials Science and Engineering A*, vol. 785, p. 139363, 2020.

[53] S. Cheruvathur, E. A. Lass, and C. E. Campbell, "Additive manufacturing of 17-4 PH stainless steel: post-processing heat treatment to achieve uniform reproducible microstructure," *JOM*, vol. 68, pp. 930–942, 2016. ISBN: 1047-4838.

[54] L. Facchini, N. Vicente, I. Lonardelli, E. Magalini, P. Robotti, and M. Alberto, "Metastable austenite in 17-4 precipitation-hardening stainless steel produced by

selective laser melting," *Advanced Engineering Materials*, vol. 12, no. 3, pp. 184–188, 2010.

[55] N. Guennouni, A. Barroux, C. Grosjean, D. Maisonnette, E. Nivet, E. Andrieu, D. Poquillon, L. Laffont, and C. Blanc, "Comparative study of the microstructure between a laser beam melted 17-4PH stainless steel and its conventional counterpart," *Materials Science and Engineering A*, vol. 823, p. 141718, 2021.

[56] N. Guennouni, D. Maisonnette, C. Grosjean, E. Andrieu, D. Poquillon, and C. Blanc, "Influence of hydrogen on the stress-relaxation properties of 17-4PH martensitic stainless steel manufactured by laser powder bed fusion," *Materials Science and Engineering A*, vol. 831, p. 142125, 2022.

[57] A. Kudzal, B. McWilliams, C. Hofmeister, F. Kellogg, J. Yu, J. Taggart-Scarff, and J. Liang, "Effect of scan pattern on the microstructure and mechanical properties of Powder Bed Fusion additive manufactured 17-4 stainless steel," *Materials and Design*, vol. 133, pp. 205–215, 2017.

[58] H. R. Lashgari, C. Kong, E. Adabifiroozjaei, and S. Li, "Microstructure, post thermal treatment response, and tribological properties of 3D printed 17-4 PH stainless steel," *Wear*, vol. 456, p. 203367, 2020.

[59] E. A. Lass, F. Zhang, and C. E. Campbell, "Nitrogen Effects in Additively Manufactured Martensitic Stainless Steels: Conventional Thermal Processing and Comparison with Wrought," *Metallurgical and Materials Transactions A: Physical Metallurgy and Materials Science*, vol. 51, pp. 2318–2332, 2020.

[60] T. LeBrun, T. Nakamoto, K. Horikawa, and H. Kobayashi, "Effect of retained austenite on subsequent thermal processing and resultant mechanical properties of selective laser melted 17-4 PH stainless steel," *Materials and Design*, vol. 81, pp. 44–53, 2015. Publisher: Elsevier Ltd.

[61] M. Mahmoudi, A. Elwany, A. Yadollahi, S. M. Thompson, L. Bian, and N. Shamsaei, "Mechanical properties and microstructural characterization of selective laser melted 17-4 PH stainless steel," *Rapid Prototyping Journal*, vol. 23, pp. 280–294, Mar. 2017.

[62] S. D. Meredith, J. S. Zuback, J. S. Keist, and T. A. Palmer, "Impact of composition on the heat treatment response of additively manufactured 17–4 PH grade stainless steel," *Materials Science and Engineering A*, vol. 738, pp. 44–56, 2018. Publisher: Elsevier B.V.

[63] H. K. Rafi, D. Pal, N. Patil, T. L. Starr, and B. E. Stucker, "Microstructure and Mechanical Behavior of 17-4 Precipitation Hardenable Steel Processed by Selective Laser Melting," *Journal of Materials Engineering and Performance*, 2014.

[64] T. Starr, K. Rafi, B. Stucker, and C. Scherzer, "Controlling phase composition in selective laser melted stainless steels," *Proceedings of the Solid Freeform Fabrication Symposium*, 2012.

[65] Y. Sun, R. J. Hebert, and M. Aindow, "Effect of heat treatments on microstructural evolution of additively manufactured and wrought 17-4PH stainless steel," *Materials and Design*, 2018.

[66] A. Yadollahi, N. Shamsaei, S. M. Thompson, A. Elwany, and L. Bian, "Mechanical and microstructural properties of selective laser melted 17-4 PH stainless steel," in *ASME International Mechanical Engineering Congress and Exposition, Proceedings (IMECE)*, (Houston, TX), American Society of Mechanical Engineers, 2015.

[67] P. Nezhadfar, K. Anderson-Wedge, S. Daniewicz, N. Phan, S. Shao, and N. Shamsaei, "Improved high cycle fatigue performance of additively manufactured 17-4 PH stainless steel via in-process refining micro-/defect-structure," *Additive Manufacturing*, vol. 36, p. 101604, Dec. 2020.

[68] A. Yadollahi, M. Mahmoudi, A. Elwany, H. Doude, L. Bian, and J. C. Newman, "Effects of crack orientation and heat treatment on fatigue-crack-growth behavior of AM 17-4 PH stainless steel," *Engineering Fracture Mechanics*, vol. 226, p. 106874, Mar. 2020.

[69] A. Soltani-Tehrani, J. Pegues, and N. Shamsaei, "Fatigue behavior of additively manufactured 17-4 PH stainless steel: The effects of part location and powder re-use," *Additive Manufacturing*, vol. 36, p. 101398, Dec. 2020.

[70] S. Romano, P. Nezhadfar, N. Shamsaei, M. Seifi, and S. Beretta, "High cycle fatigue behavior and life prediction for additively manufactured 17-4 PH stainless steel: Effect of sub-surface porosity and surface roughness," *Theoretical and Applied Fracture Mechanics*, vol. 106, p. 102477, Apr. 2020.

[71] R. Molaei, A. Fatemi, and N. Phan, "Multiaxial fatigue of LB-PBF additive manufactured 17–4 PH stainless steel including the effects of surface roughness and HIP treatment and comparisons with the wrought alloy," *International Journal of Fatigue*, vol. 137, p. 105646, Aug. 2020.

[72] P. Nezhadfar, E. Burford, K. Anderson-Wedge, B. Zhang, S. Shao, S. Daniewicz, and N. Shamsaei, “Fatigue crack growth behavior of additively manufactured 17-4 PH stainless steel: Effects of build orientation and microstructure,” *International Journal of Fatigue*, vol. 123, pp. 168–179, June 2019.

[73] P. Nezhadfar, R. Shrestha, N. Phan, and N. Shamsaei, “Fatigue behavior of additively manufactured 17-4 PH stainless steel: Synergistic effects of surface roughness and heat treatment,” *International Journal of Fatigue*, vol. 124, pp. 188–204, July 2019.

[74] R. F. Schaller, J. M. Taylor, J. Rodelas, and E. J. Schindelholz, “Corrosion Properties of Powder Bed Fusion Additively Manufactured 17-4 PH Stainless Steel,” *CORROSION*, vol. 73, pp. 796–807, July 2017.

[75] M. Alnajjar, F. Christien, V. Barnier, C. Bosch, K. Wolski, A. D. Fortes, and M. Telling, “Influence of microstructure and manganese sulfides on corrosion resistance of selective laser melted 17-4 PH stainless steel in acidic chloride medium,” *Corrosion Science*, vol. 168, p. 108585, May 2020.

[76] T. K. Shoemaker, Z. D. Harris, and J. T. Burns, “Comparing Stress Corrosion Cracking Behavior of Additively Manufactured and Wrought 17-4PH Stainless Steel,” *Corrosion*, vol. 78, no. 6, pp. 528–546, 2022.

[77] S. Dobson, S. Vunnam, D. Frankel, C. Sudbrack, and T. Starr, “Powder variation and mechanical properties for SLM 17-4 PH stainless steel,” in *Proceedings of the 30th Annual International Solid Freeform Fabrication Symposium – An Additive Manufacturing Conference*, University of Texas at Austin, 2019.

[78] U. Ali, R. Esmaeilizadeh, F. Ahmed, D. Sarker, W. Muhammad, A. Keshavarzkermani, Y. Mahmoodkhani, E. Marzbanrad, and E. Toyserkani, “Identification and characterization of spatter particles and their effect on surface roughness, density and mechanical response of 17-4 PH stainless steel laser powder-bed fusion parts,” *Materials Science and Engineering: A*, vol. 756, pp. 98–107, May 2019.

[79] P. Auguste, A. Mauduit, L. Fouquet, and S. Pillot, “Study on 17-4 PH stainless steel produced by selective laser melting,” *UPB Scientific Bulletin*, vol. 80, no. 4, pp. 197–210, 2018.

[80] Z. Hu, H. Zhu, H. Zhang, and X. Zeng, “Experimental investigation on selective laser melting of 17-4PH stainless steel,” *Optics & Laser Technology*, vol. 87, pp. 17–25, Jan. 2017.

[81] H. Irrinki, J. S. D. Jangam, S. Pasebani, S. Badwe, J. Stitzel, K. Kate, O. Gulsoy, and S. V. Atre, "Effects of particle characteristics on the microstructure and mechanical properties of 17-4 PH stainless steel fabricated by laser-powder bed fusion," *Powder Technology*, vol. 331, pp. 192–203, May 2018.

[82] P. G. Jerrard, L. Hao, and K. E. Evans, "Experimental investigation into selective laser melting of austenitic and martensitic stainless steel powder mixtures," *Proceedings of the Institution of Mechanical Engineers, Part B: Journal of Engineering Manufacture*, vol. 223, no. 11, pp. 1409–1416, 2009.

[83] A. Poudel, A. Soltani-Tehrani, S. Shao, and N. Shamsaei, "Effect of powder characteristics on tensile properties of additively manufactured 17-4 PH stainless steel," in *Proceedings of the 32nd Annual International Solid Freeform Fabrication Symposium*, University of Texas at Austin, 2021.

[84] R. Shrestha, N. Shamsaei, M. Seifi, and N. Phan, "An investigation into specimen property to part performance relationships for laser beam powder bed fusion additive manufacturing," *Additive Manufacturing*, vol. 29, p. 100807, Oct. 2019.

[85] Y. Sun, R. J. Hebert, and M. Aindow, "Non-metallic inclusions in 17-4PH stainless steel parts produced by selective laser melting," *Materials & Design*, vol. 140, pp. 153–162, Feb. 2018.

[86] J. S. Weaver, J. Whiting, V. Tondare, C. Beauchamp, M. Peltz, J. Tarr, T. Q. Phan, and M. A. Donmez, "The effects of particle size distribution on the rheological properties of the powder and the mechanical properties of additively manufactured 17-4 PH stainless steel," *Additive Manufacturing*, vol. 39, p. 101851, Mar. 2021.

[87] B. McWilliams, B. Pramanik, A. Kudzal, and J. Taggart-Scarff, "High strain rate compressive deformation behavior of an additively manufactured stainless steel," *Additive Manufacturing*, vol. 24, pp. 432–439, Dec. 2018.

[88] A. A. Adeyemi, E. Akinlabi, R. M. Mahamood, K. O. Sanusi, S. Pityana, and M. Tlotleng, "Influence of laser power on microstructure of laser metal deposited 17-4 ph stainless steel," *IOP Conference Series: Materials Science and Engineering*, vol. 225, p. 012028, Aug. 2017.

[89] Y. Sun, R. J. Hebert, and M. Aindow, "Effect of laser scan length on the microstructure of additively manufactured 17-4PH stainless steel thin-walled parts," *Additive Manufacturing*, vol. 35, p. 101302, Oct. 2020.

[90] A. Bayode, S. Pityana, E. T. Akinlabi, and M. B. Shongwe, "Effect of scanning speed on laser deposited 17-4PH stainless steel," in *2017 8th International Conference on Mechanical and Intelligent Manufacturing Technologies (ICMIMT)*, (Cape Town, South Africa), pp. 1–5, IEEE, Feb. 2017.

[91] R. Rashid, S. Masood, D. Ruan, S. Palanisamy, R. Rahman Rashid, and M. Brandt, "Effect of scan strategy on density and metallurgical properties of 17-4PH parts printed by Selective Laser Melting (SLM)," *Journal of Materials Processing Technology*, vol. 249, pp. 502–511, Nov. 2017.

[92] S. Giganto, P. Zapico, M. Castro-Sastre, S. Martínez-Pellitero, P. Leo, and P. Perulli, "Influence of the scanning strategy parameters upon the quality of the SLM parts," *Procedia Manufacturing*, vol. 41, pp. 698–705, 2019.

[93] H. Gu, H. Gong, D. Pal, K. Rafi, T. Starr, and B. Stucker, "Influences of Energy Density on Porosity and Microstructure of Selective Laser Melted 17- 4PH Stainless Steel," in *Proceedings of the 24th Annual International Solid Freeform Fabrication Symposium*, University of Texas at Austin, 2013. Publisher: University of Texas at Austin.

[94] P. Ponnusamy, S. H. Masood, D. Ruan, S. Palanisamy, R. A. R. Rashid, and O. A. Mohamed, "Mechanical performance of selective laser melted 17-4 PH stainless steel under compressive loading," in *Proceedings of the 28th Annual International Solid Freeform Fabrication Symposium*, University of Texas at Austin, 2017.

[95] P. Ponnusamy, S. Masood, S. Palanisamy, R. Rahman Rashid, and D. Ruan, "Characterization of 17-4PH alloy processed by selective laser melting," *Materials Today: Proceedings*, vol. 4, no. 8, pp. 8498–8506, 2017.

[96] T. Zhou, T. Zheng, A. B. Yildiz, G. Spartacus, M. Rolinska, R. Cubitt, and P. Hedström, "Microstructure control during deposition and post-treatment to optimize mechanical properties of wire-arc additively manufactured 17-4 PH stainless steel," *Additive Manufacturing*, vol. 58, p. 103047, Oct. 2022.

[97] B. AlMangour and J.-M. Yang, "Understanding the deformation behavior of 17-4 precipitate hardenable stainless steel produced by direct metal laser sintering using micropillar compression and TEM," *The International Journal of Advanced Manufacturing Technology*, vol. 90, pp. 119–126, Apr. 2017.

[98] M. R. Condruz, A. Paraschiv, and C. Puscasu, "Heat treatment influence on hardness and microstructure of ADAM manufactured 17-4 PH," *Turbo*, vol. 5, no. 2, pp. 39–45, 2018.

[99] T. M. Mower and M. J. Long, "Mechanical behavior of additive manufactured, powder-bed laser-fused materials," *Materials Science and Engineering: A*, vol. 651, pp. 198–213, Jan. 2016.

[100] B. C. Salzbrenner, J. M. Rodelas, J. D. Madison, B. H. Jared, L. P. Swiler, Y.-L. Shen, and B. L. Boyce, "High-throughput stochastic tensile performance of additively manufactured stainless steel," *Journal of Materials Processing Technology*, vol. 241, pp. 1–12, Mar. 2017.

[101] B. L. Boyce, B. C. Salzbrenner, J. M. Rodelas, L. P. Swiler, J. D. Madison, B. H. Jared, and Y. Shen, "Extreme-value statistics reveal rare failure-critical defects in additive manufacturing," *Advanced Engineering Materials*, vol. 19, p. 1700102, Aug. 2017.

[102] L. W. Tsay, W. C. Lee, R. K. Shiue, and J. K. Wu, "Notch tensile properties of laser-surface-annealed 17-4 PH stainless steel in hydrogen-related environments," *Corrosion Science*, vol. 44, no. 9, pp. 2101–2118, 2002. ISBN: 0010-938X.

[103] B. AlMangour and J.-M. Yang, "Improving the surface quality and mechanical properties by shot-peening of 17-4 stainless steel fabricated by additive manufacturing," *Materials & Design*, vol. 110, pp. 914–924, Nov. 2016.

[104] P. D. Nezhadfar, M. Masoomi, S. Thompson, N. Pham, and N. Shamsaei, "Mechanical Properties of 17-4 Ph Stainless Steel Additively Manufactured Under Ar and N2 Shielding Gas," in *Proceedings of the 29th Annual International Solid Freeform Fabrication Symposium*, University of Texas at Austin, 2018.

[105] W. M. Garrison and N. R. Moody, "Hydrogen embrittlement of high strength steels," in *Gaseous Hydrogen Embrittlement of Materials in Energy Technologies: The Problem, its Characterisation and Effects on Particular Alloy Classes*, 2012.

[106] C. F. Arisoy, G. Başman, and M. K. Şeşen, "Failure of a 17-4 PH stainless steel sailboat propeller shaft," *Engineering Failure Analysis*, vol. 10, no. 6, pp. 711–717, 2003.

[107] M. S. D. R. Coseglio, "Sulphide stress cracking of 17-4 PH for applications in oilfield components," *Materials Science and Technology (United Kingdom)*, vol. 33, no. 16, pp. 1863–1878, 2017. Publisher: Taylor & Francis.

[108] F. Fantechi and M. Innocenti, "Chloride stress corrosion cracking of precipitation hardening S.S. impellers in centrifugal compressor. Laboratory investigations and

corrective actions," *Engineering Failure Analysis*, vol. 8, no. 5, pp. 477–492, 2001. ISBN: 3905542323.

[109] T. Jiang, J. Zhong, X. Zhang, W. Wang, and K. Guan, "Hydrogen embrittlement induced fracture of 17-4 PH stainless steel valve stem," *Engineering Failure Analysis*, vol. 113, p. 104576, 2020. Publisher: Elsevier.

[110] M. Liu, F. Ma, G. Chang, F. Fu, N. S. Cheruvu, L. Yu, J. Dai, and K. Xu, "Experimental investigation of failure behavior of the cracked 17-4PH steel blades in a top gas energy recovery turbine," *Engineering Failure Analysis*, vol. 105, pp. 545–554, 2019. Publisher: Elsevier.

[111] L. Raymond and E. G. Kendall, "Failure of 17-4 PH Stainless Steel Bolts on a Titan Space Launch Vehicle," in *ASM Failure Analysis Case Histories: Mechanical and Machine Components*, ASM International, 2019.

[112] J. K. Stanley, "Stress Corrosion Cracking and Hydrogen Embrittlement of High-Strength Fasteners," Tech. Rep. TR-0073(3413-01)-1, The Aerospace Corporation, 1973.

[113] S. S. Tavares, J. M. Pardal, L. Menezes, C. A. Menezes, and C. D'Ávila, "Failure analysis of PSV springs of 17-4PH stainless steel," *Engineering Failure Analysis*, vol. 16, no. 5, pp. 1757–1764, 2009. Publisher: Elsevier Ltd.

[114] S. S. Tavares, J. S. Corte, and J. M. Pardal, "Failure of 17-4 PH stainless steel components in offshore platforms," *Handbook of Materials Failure Analysis with Case Studies from the Oil and Gas Industry*, pp. 353–370, 2016. ISBN: 9780081001264.

[115] R. M. Thompson, G. B. Kohut, D. R. Canfield, and W. R. Bass, "Sulfide stress cracking failures of 12Cr and 17-4PH stainless steel wellhead equipment," *Corrosion*, vol. 47, no. 3, pp. 216–220, 1991.

[116] J. E. Truman, "Stress-corrosion cracking of martensitic and ferritic stainless steels," *International Metals Reviews*, vol. 26, no. 1, pp. 301–349, 1981.

[117] C. S. Carter, D. Farwick, A. Ross, and J. Uchida, "Stress corrosion properties of high strength precipitation hardening stainless steels," *Corrosion*, vol. 27, no. 5, pp. 190–197, 1971.

[118] C. T. Fujii, "Stress-corrosion cracking properties of 17-4 PH steel," in *Stress Corrosion—New Approaches* (H. L. Craig, ed.), pp. 213–225, West Conshohocken, PA: American Society for Testing and Materials, 1976.

[119] W. Gerhold and E. Escalante, "NBSIR 74-560: Stress Corrosion Behavior of Selected Types of Stainless Steels and Titanium Alloys in a Marine Environment," tech. rep., Naval Air System Command, Washington, D.C., 1974.

[120] R. Ghosh, A. Venugopal, C. V. Arun Chand, P. Ramesh Narayanan, B. Pant, and R. M. Cherian, "Effect of Heat Treatment Anomaly on the Stress Corrosion Cracking Behavior of 17-4 PH Martensitic Stainless Steel," *Transactions of the Indian Institute of Metals*, vol. 72, no. 6, pp. 1503–1506, 2019. Publisher: Springer India.

[121] T. S. Humphries and E. E. Nelson, "Stress Corrosion Cracking Evaluation of Several Precipitation Hardening Stainless Steels," tech. rep., George C. Marshall Space Flight Center, Marshall Space Flight Center, AL, 1969.

[122] R. W. Judy, C. T. Fujii, and R. J. Goode, "Properties of 17-4PH Steel," tech. rep., Naval Research Laboratory, Washington, D.C., 1973.

[123] M. Karaminezhaad, S. Sharafi, and K. Dalili, "Effect of molybdenum on SCC of 17-4PH stainless steel under different aging conditions in chloride solutions," *Journal of Materials Science*, vol. 41, no. 11, pp. 3329–3333, 2006.

[124] K. Prasad Rao and K. S. Raja, "Environmental cracking behaviour of the Precipitation hardened stainless steel, 17-4 PH, under applied potential," *Materials and Corrosion*, vol. 46, no. 6, pp. 370–375, 1995.

[125] K. S. Raja and K. Prasad Rao, "On the hardness criterion for stress corrosion cracking resistance of 17-4 PH stainless steel," *Journal of Materials Science Letters*, vol. 12, no. 12, pp. 963–966, 1993.

[126] V. M. Salinas-Bravo and J. G. Gonzalez-Rodriguez, "Stress corrosion cracking susceptibility of 17-4PH turbine steel in aqueous environments," *British Corrosion Journal*, vol. 30, no. 1, pp. 77–79, 1995.

[127] B. A. Kehler and J. R. Scully, "Predicting the Effect of Applied Potential on Crack Tip Hydrogen in Low-Alloy Martensitic Steels," *Corrosion 2007*, vol. 64, no. 5, pp. 465–477, 2007.

[128] J. J. Lewandowski and M. Seifi, "Metal Additive Manufacturing: A Review of Mechanical Properties," *Annual Review of Materials Research*, vol. 46, pp. 151–186, 2016.

[129] R. P. Gangloff, H. M. Ha, J. T. Burns, and J. R. Scully, "Measurement and Modeling of Hydrogen Environment-Assisted Cracking in Monel K-500," *Metallurgical and*

Materials Transactions A, vol. 45, pp. 3814–3834, Aug. 2014. Publisher: Springer US.

[130] Z. D. Harris, J. D. Dolph, G. L. Pioszak, B. C. Rincon Troconis, J. R. Scully, and J. T. Burns, "The Effect of Microstructural Variation on the Hydrogen Environment-Assisted Cracking of Monel K-500," *Metallurgical and Materials Transactions A*, vol. 47, no. 7, pp. 3488–3510, 2016. Publisher: Springer US.

[131] Z. D. Harris and J. T. Burns, "The effect of isothermal heat treatment on hydrogen environment-assisted cracking susceptibility in Monel K-500," *Materials Science and Engineering: A*, vol. 764, p. 138249, Sept. 2019.

[132] W. Gerberich, *Modeling hydrogen induced damage mechanisms in metals.* Woodhead Publishing Limited, 2012. Publication Title: Gaseous Hydrogen Embrittlement of Materials in Energy Technologies: Mechanisms, Modelling and Future Developments.

[133] B. A. Kehler, *Modeling and experiments to explain the potential dependency of an UHSS to hydrogen environment assisted cracking.* PhD thesis, University of Virginia, Charlottesville, VA, 2008.

[134] R. L. S. Thomas, J. R. Scully, and R. P. Gangloff, "Internal Hydrogen Embrittlement of Ultrahigh-Strength AERMET 100 Steel," *Metallurgical and Materials Transactions A: Physical Metallurgy and Materials Science*, vol. 34, no. 2, pp. 327–344, 2003.

[135] Y. Lee and R. P. Gangloff, "Measurement and modeling of hydrogen environment-assisted cracking of ultra-high-strength steel," *Metallurgical and Materials Transactions A: Physical Metallurgy and Materials Science*, vol. 38, pp. 2174–2190, 2007.

Chapter 2

Wrought and AM 17-4 PH Material Characterization

2.1 Overview

This chapter provides a focused examination of the wrought and additively manufactured (AM) 17-4 PH investigated in this dissertation. Additive manufacturing build parameters and alloy composition for both wrought and AM specimens are provided, and subsequent heat treatment processes are outlined and discussed. Characterization methods including electron backscatter diffraction (EBSD), transmission electron microscopy (TEM), and energy dispersive X-ray spectroscopy (EDS) are used to compare relevant microstructural features, including phase composition, grain morphology, grain boundary characteristics, dislocation density, and precipitate behavior, between wrought and AM specimens with varying heat treatments. Noted differences in AM microstructure compared to its wrought counterpart include coarser grains, a slight decrease in dislocation density in the solution-annealed treatment, and a lower fraction of FCC phase observed through EBSD potentially linked to a decrease in the size and prominence of NbC-type carbides. Additionally, mechanical and electrochemical properties of the alloys are discussed; the AM and wrought specimens display similar behavior in both analyses, with the notable exception of slightly reduced ductility in AM 17-4 PH compared to wrought. Lastly, the increased susceptibility to stress corrosion cracking of AM 17-4 PH is discussed.

2.2 Collaborations

The following collaborations are gratefully acknowledged, all within the University of Virginia: EBSD maps collected by Dr. Zachary Harris, Kernel Average Misorientation maps generated with the assistance of Alex Jennion, TEM/EDS micrographs obtained by Dr. Helge Heinrich, and mechanical properties characterized by Dr. Trevor Shoemaker.

2.3 Background

17-4 PH is a predominantly martensitic precipitation-hardened stainless steel, with excellent corrosion resistance due to its high chromium content. Though 17-4 PH stainless steel has outstanding mechanical properties, its high strength results in an increased susceptibility to hydrogen embrittlement.[1, 2] 17-4 PH has a body-centered tetragonal (BCT) structure which allows for relatively rapid hydrogen diffusion compared to austenitic steels,[3] though its low carbon content minimizes the expansion along the c-axis.[3, 4]

The relatively high hardness of 17-4 PH is attributable to the growth and precipitation of copper-rich regions during aging processes.[5] The morphology of these precipitates is contingent on the heat treatment process.[2, 6–8] Common heat treatments include peak-aging, consisting of heating for 1 hour at 482°C; this results in increased strength and acceptable ductility along with the formation of fine, coherent copper precipitates. The second is over-aging, which involves heating for 4 hours at 552°C, resulting in lower strength but improved ductility as the precipitates grow and become incoherent. Over-aged

Cu-rich precipitates have also been observed decorating grain boundaries.[7]

Following peak-aging, Hsaio et al.[8] observed the formation of coherent copper precipitates in a Kurdujumov-Sachs orientation with the matrix, as well as a high density of dislocations. Cr- and Nb-rich precipitates, such as NbC, have also been noted in wrought 17-4 PH.[9–11] Reverted austenite content increases during aging, but shows little influence on mechanical properties such as strength and impact toughness.[12]

In contrast to its fully martensitic wrought counterpart, the microstructure and properties of AM 17-4 PH have been reported to vary widely with build parameters and initial powder conditions. In the "as-built" condition—prior to any post-processing heat treatment—AM 17-4 PH exhibits a largely ferritic structure containing martensite, austenite, or both.[4, 9, 13–19] The build atmosphere has a significant effect on microstructure, especially considering the austenite stabilization properties of nitrogen.[19] For example, AM 17-4 PH fabricated using argon gas has been shown to produce a martensitic microstructure after heat treatment regardless of the phase of the initial atomized powder, whereas AM 17-4 PH fabricated using nitrogen gas exhibits the same phase as the initial atomized powder.[13] Additionally, solution annealing has been found to eliminate the metastable austenitic phase from as-built AM 17-4 PH, though subsequent aging can lead to austenite reversion; this can vary from below 5% after H900 or H1025 heat treatment, to around 20% after H1150 heat treatment.[20] The amount of retained austenite in AM 17-4 PH can fluctuate based on AM processing parameters such as scan strategy and volumetric energy density.[21, 22]

Similar to its wrought counterpart, heat treatment will also affect the microstructure and properties of AM 17-4 PH. Peak-aged specimens have exhibited increased yield and ultimate tensile strength as well as a reduction in ductility due to the prevention of dislocation motion from precipitation hardening.[22, 23] Murr et al. found no hardness increase with aging for the N_2-fabricated austenitic AM 17-4 PH, whereas the martensitic 17-4 PH displayed significantly increased hardness after peak-aging.[13]

Fine Cu-rich precipitates have been found in peak-aged AM 17-4 PH.[4, 13, 20, 24–28] These precipitates have been observed to coarsen upon over-aging, similar to precipitation kinetics in over-aged wrought 17-4 PH.[20, 26] Guennoni et al.[29] found a higher density of Cu-rich precipitates in aged AM 17-4 PH compared to its traditionally manufactured counterpart; precipitates in the AM material were on the order of 10-15 nm in diameter, coarser than those often observed in conventionally manufactured 17-4 PH. NbC precipitates have also been observed in AM 17-4 PH, similar to its wrought counterpart.[9, 16] Additional inclusions and precipitates noted in AM 17-4 PH include MnS,[30] Mn-Si oxides,[4, 27] and a second phase at the grain boundary containing Mn, Cr, and C.[4]

Several explanations have been proposed to account for some of the variability in microstructure of AM 17-4 PH. It has been proposed that there is an increase in austenite stabilization due to Ni enrichment in interdendritic regions as a result of microsegregation, or due to nitrogen uptake during processing.[13, 31, 32] It has also been hypothesized that the increase in residual stress from the melting and remelting process combined with the small size of the solidification cell impedes the martensitic transformation process.[15]

Due to a high degree of variation in microstructure, reported mechanical properties of AM 17-4 PH can vary greatly between builds, with some studies recording similar yield and ultimate tensile strengths between AM and wrought[30, 33] and some studies reporting greatly inferior yield and ultimate tensile strengths in AM.[23, 34] Circular voids due to entrapped gas and partially or completely unmelted particles are often seen in the microstructure of AM 17-4 PH builds, which has been speculated to cause the commonly reported lower ductility and shorter fatigue life seen in AM 17-4 PH.[22, 23, 33–35] Anisotropy in tensile properties corresponding to building orientation has also been observed.[22, 23]

Table 2.1: Processing parameters for AM 17-4 PH, provided by the Commonwealth Center for Additive Manufacturing (CCAM), Disputanta, VA.

Parameter	**Value**
Powder size	45 microns
Atomization environment	Ar
Build environment	Ar
Layer thickness	0.04 mm
Laser power	220 W
Scanning speed	755.5 mm/s
Hatch distance	0.11 mm
Stripe width	12 mm
Overlap stripes	0.05 mm
Rotation angle	47°

2.4 Wrought and AM 17-4 PH Alloys

2.4.1 Specimen Information

AM 17-4 PH samples were provided by the Commonwealth Center for Additive Manufacturing (CCAM). Specimens were excised from rectangular bars (21x21x75 mm) manufactured via laser powder bed fusion (L-PBF) using an EOS M290 machine, argon-atomized powder, and standard EOS 17-4 PH build parameters, as shown in Table 2.1.[36] These bars were placed at various locations around the build plate. Argon was used for powder atomization and build environment to ensure martensitic microstructure, enabling comparison with the martensitic wrought microstructure. Electrical discharge machining (EDM) was used to remove the printed specimens from the build plate. Subsequently, specimens were polished to a minimum of 1200 grit before any experimentation to negate surface effects from building

The wrought specimens were provided as solution annealed 15.9-mm thick plates produced per ASTM A693,[37] as described by Shoemaker et al.[38] The elemental composition of both the AM and wrought specimens was characterized by Shoemaker et al.,[38] and a

Table 2.2: Chemical composition of the as-supplied wrought and as-built AM specimens, from Shoemaker et al.[38]

(wt%):	**C**	**Mn**	**P**	**S**	**Si**	**Cr**	**Ni**	**Cu**	**Nb**	**Fe**
Wrought	0.041	0.51	0.018	0.001	0.32	15.20	4.85	3.22	0.26	bal.
AM: Powder	0.020	0.46	<0.010	<0.010	0.45	16.32	4.36	4.00	0.29	bal.
AM: Build	0.014	0.42	0.009	0.006	0.53	16.10	4.51	3.73	0.28	bal.
(wppm):	**Al**	**Mo**	**N**	**O**	**V**	**Co**	**As**	**Sn**	**W**	
Wrought	10	1600	280	44	510	770	31	53	230	
AM: Powder	0	100	100	600	-	-	-	-	-	
AM: Build	12	57	140	480	26	260	17	12	7	

Table 2.3: Heat treatment conditions for wrought and AM 17-4 PH specimens, detailing the sequence of HIP, SA, and aging procedures. The hot isostatic pressing (HIP) procedure involves heating at 1125°C for four hours, followed by a furnace-cool at 310°C/hour to 300°C, then air cooling to ambient temperature. Solution annealing (SA) consists of heating at 1040°C for 30 minutes, followed by air cooling.

Type	**Condition**	**HIP**	**SA**	**Aging**
AM	HIP+SA+PA	1125°C / 4 hr	1040°C / 30 min	460°C / 1 hr
	HIP+PA	1125°C / 4 hr	-	460°C / 1 hr
	HIP+SA+OA	1125°C / 4 hr	1040°C / 30 min	552°C / 4 hr
Wrought	SA+PA (H900)	-	1040°C / 30 min	482°C / 1 hr
	SA+OA (H1025)	-	1040°C / 30 min	552°C / 4 hr

summary can be seen in Table 2.2. The primary alloying elements are reported in the top section of Table 2.2, and are all within the specifications for 17-4 PH outlined in ASTM A693.[37] Trace elements are reported in the bottom section of Table 2.2. It should be noted that the wrought built does have significantly more C than the AM build, along with trace elements Mo, N, V, Co, and W, whereas the AM build has an increase in O compared to the wrought.

2.4.2 Heat Treatment

Post-processing heat treatment procedures were employed to induce martensitic transformation in the ferritic as-built AM 17-4 PH, as well as to diminish any solidification-related

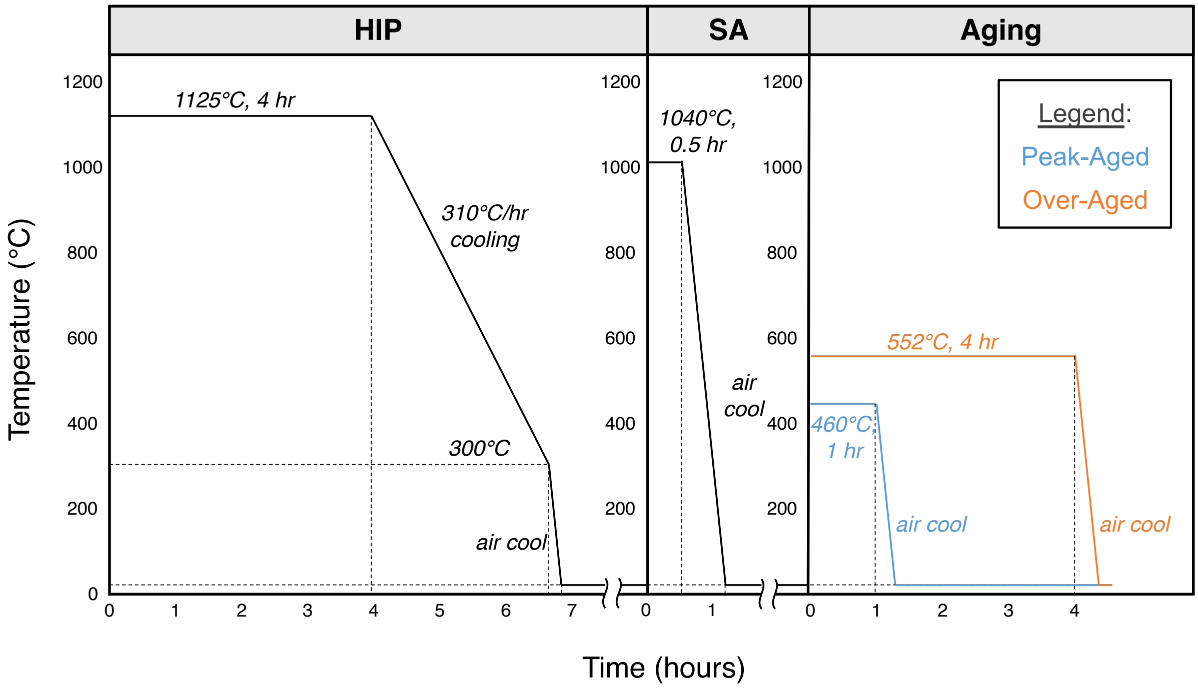

Figure 2.1: Heat treatment time versus temperature procedure for peak-aged and over-aged AM 17-4 PH.

defects and anisotropy in the material and to increase material strength. This process involves a hot isostatic pressing (HIP) heat treatment to achieve homogeneity and pore closure, followed by solution annealing (SA) to dissolve Cu and aging to subsequently precipitate Cu; a time-temperature plot outlining the heat treatment process can be found in Figure 2.1.

Each as-built "block" underwent a HIP treatment, after which the standard SA treatment for 17-4 PH[37] was performed on a subset of blocks. All blocks were then aged to either the peak-aged (PA) or over-aged (OA) conditions; pertinent parameters for each treatment are documented in Table 2.3. Experiments on wrought 17-4 PH were performed on specimens excised from a 15.9-mm thick plate procured in the SA condition; the specimens were then subjected to the standard PA (H900) and OA (H1025) treatments for 17-4 PH.[37] Shoemaker et al. demonstrated that these heat treatment protocols result in nominally similar yield strengths and coarse microstructure characteristics, though widespread sub-micrometer porosity was observed throughout the AM alloys, even after the HIP treatment.[38] Additionally, the combination of HIP and solution annealing has been shown to reduce residual stress and improve hydrogen embrittlement characteristics in alloys manufactured using L-PBF.[39]

2.5 Characterization Methods

Supplementary electron backscatter diffraction (EBSD) maps were collected at 1000x at a step size of 100 nm for each material using a FEI Helios G4 UC equipped with an Oxford Symmetry detector and operated at 20 keV with a probe current of 3.2 nA. EBSD data were analyzed to determine the grain boundary character distributions and kernel misorientation using the open-source MTeX package.[40] Parent austenite grain reconstruction was performed in MTeX using the variant graph approach outlined by Hielscher et al.[41] and Niessen et al.[42] The Nishiyama-Wasserman orientation relationship was used as the initial point of reference for parent-child reconstruction. All grains with a greater than 50% chance of belonging to a certain parent grain were automatically assigned, and the surrounding grain probabilities were then re-computed. This automatic process was repeated ten times, after which any unassigned grains were selected and assigned by hand, with iterative re-computation performed after every assignment to ensure any high-probability grains were automatically assigned. After all grains were assigned, any grains with a misorientation threshold of 0.2 below a certain pixel size were merged into their surrounding larger grains.

Additional microstructural analyses were performed using transmission electron microscopy (TEM). AM and wrought 17-4 PH foils in each heat treatment condition were prepared using focused ion beam (FIB) milling via a Ga-ion source on a Helios UC G4 Dual Beam system. Bright-field and high-angle annular dark-field imaging (HAADF) TEM micrographs were captured using a Themis 60-300 kV Transmission Electron Microscope; compositional mapping was performed using Energy Dispersive X-Ray Spectroscopy (EDS) analysis. Precipitate size and distribution were estimated from both HAADF and EDS micrographs using the open-source software ImageJ.[43] Micrographs were subjected to a rolling ball background subtraction, thresholding, watershed separation, and bulk particle analysis with a minimum particle area threshold of 10 nm^2 to reduce noise.

Lastly, nitrogen and oxygen content was examined using a LECO 836 ONH Analyzer (4500-5500 W, 1000 A). The LECO Analyzer was calibrated using three ultrahigh purity Ni baskets, and steel pins were used as a reference material. AM and wrought 17-4 PH specimens in the peak-aged and over-aged conditions, approximately 0.35 mm thick, were placed in the Ni baskets within a graphite crucible and rapidly heated until melted in the LECO Analyzer. Total oxygen and nitrogen gas content was then measured as a function of time using infrared and thermal conductivity detectors.

2.6 Microstructure

EBSD OIM maps for AM 17-4 PH in the XY and XZ direction in the as-built, HIP, and HIP+SA conditions are shown in Figure 2.2. In the initial as-built condition, a high degree of anisotropy is observable, with visible melt pools and large grains. This is similar to the relatively coarse δ-ferritic solidification microstructure reported in the as-built SLM 17-4 PH by Alnajjar et al.[24] The micrographs in Figure 2.2 depicting post-HIP heat treatment and subsequent solution annealing display grain refinement and minimization of anisotropy.

For each of the peak-aged and over-aged wrought and AM specimens, EBSD orientation imaging microscopy (OIM) maps, as well as micrographs showing reconstructed prior austenite grains (PAGs), grain boundary types, and relevant phases are displayed in Figure 2.3. All micrographs were generated by the open-source MTeX package.[40] Further analysis is discussed in the following sections.

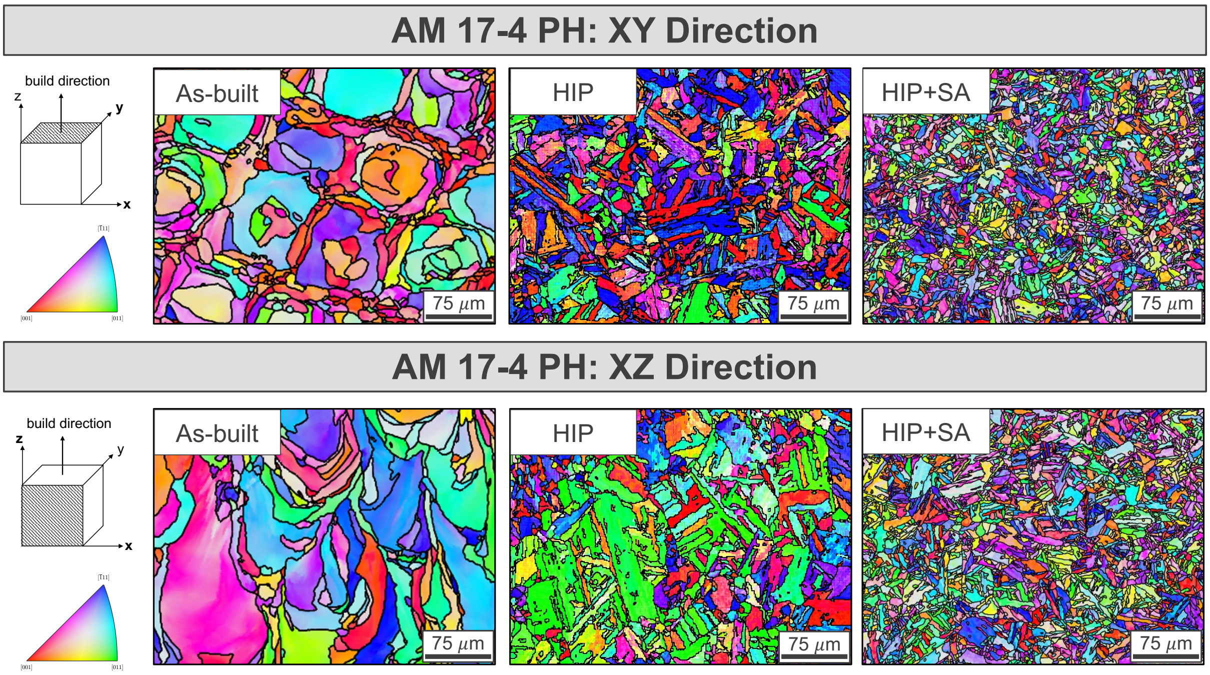

Figure 2.2: EBSD micrographs showing the microstructure of AM 17-4 PH in the as-built, HIP, and HIP+SA conditions in the XY and XZ directions. The plane relative to the build direction is illustrated.

2.6.1 Phase Determination

As seen in Figure 2.3, each specimen consists of majority martensite, with a minimal amount of FCC in all conditions. Due to the minimal carbon content, the BCT martensitic structure is indistinguishable from BCC, and therefore is denoted as BCC on the EBSD micrographs. The percentage of FCC in each condition was calculated using the MTeX open-source package and is listed in Table 2.4.[40]

Table 2.4: Percentage of FCC phase detected in each EBSD micrograph using the MTeX open-source package.[40]

Specimen	**Amount FCC (%)**
W Peak-Aged	1.05%
AM HIP+SA+PA	0.10%
AM HIP+PA	0.06%
W Over-Aged	0.66%
AM HIP+SA+OA	0.38%

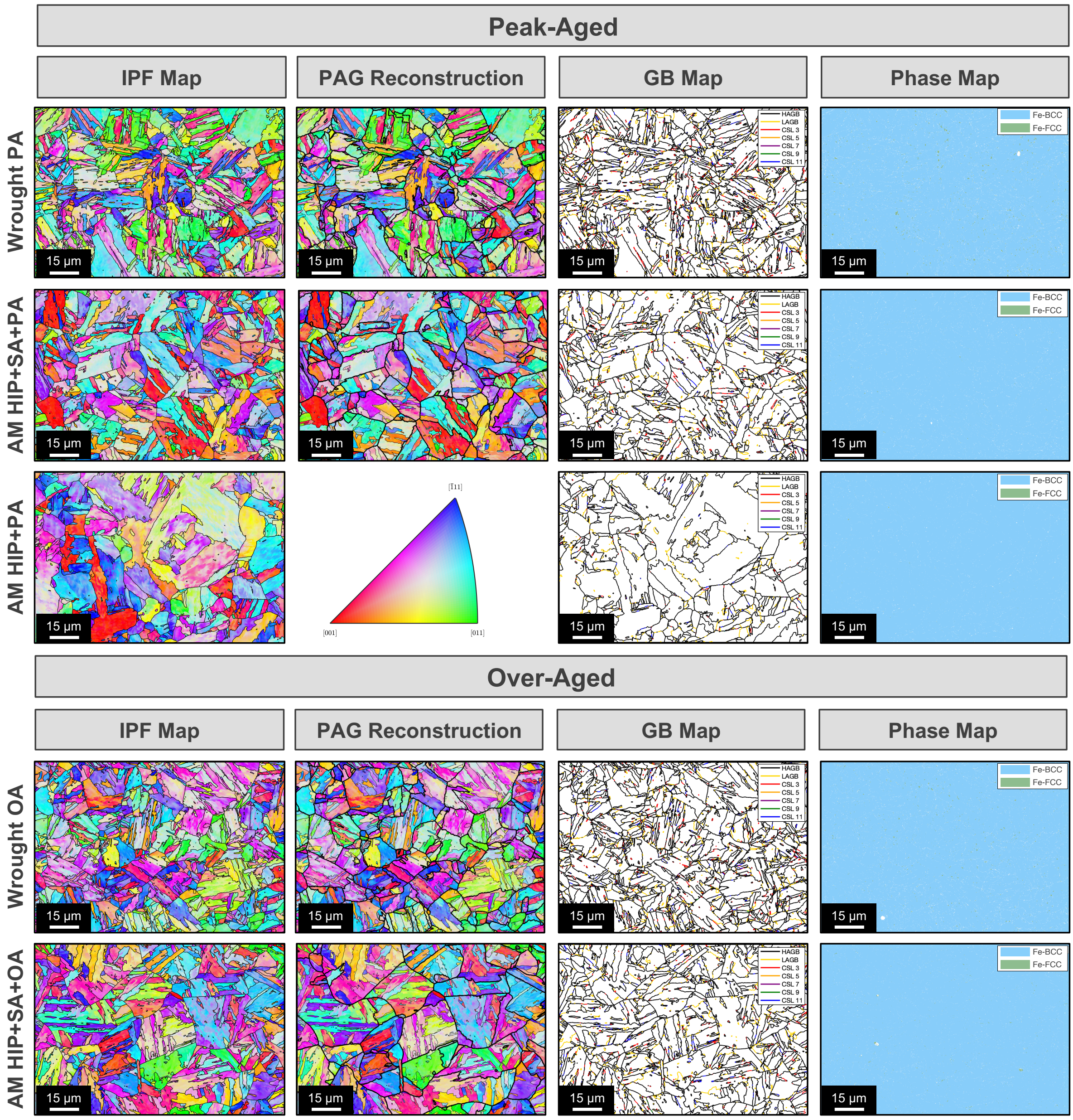

Figure 2.3: From left to right: EBSD IPF maps, IPF maps with reconstructed prior austenite grains outlined in bold, grain boundary type maps, and phase maps for each specimen. All micrographs were created using the open-source MTeX package.[40] No prior austenite grain reconstruction could be performed for the AM HIP+SA specimen due to the large grain size.

A closer look at the FCC regions in the wrought and AM peak-aged specimens can be seen in Figure 2.4. These regions are numerous and large in the wrought specimen, and can be found decorating grain boundaries as well as within the martensite lath interior. In contrast, the FCC regions are much smaller and more sparse in the AM HIP+SA+PA specimens. Similar regions were detected by Shaffer et al.[44, 45] in EBSD analysis of argon-atomized, peak-aged AM 17-4 PH and were confirmed via EDS to be niobium-rich precipitates, which have been found in both AM and wrought 17-4 PH in literature.[3, 9–11, 16] This is further explored in the precipitate analysis in Section 2.6.3.

There is little evidence of retained austenite (RA) at this length scale. Retained austenite has been linked to discontinuous yielding behavior[45] and an increase in ductility[46] in martensitic PH stainless steel. Reduction of yield and tensile strength has also been observed with increased RA,[46] though there is not universal agreement on the effect of RA on material strength.[12] Ultimately, the lack of discontinuous yielding behavior and the matched strength between wrought and AM 17-4 PH suggests that any effect of retained austenite would be similar between the two conditions.

2.6.2 Grain Boundaries

The AM 17-4 PH specimens have coarser grains compared to the wrought counterparts in both the peak-aged and over-aged conditions. Histograms of grain diameter along the widest axis of each grain can be seen in Figure 2.5; both un-weighted and area-weighted diameter measurements are included, and median grain diameter values are listed. Prior austenite grains (PAGs) are also larger in the AM specimens, and the prior austenite grain boundaries (PAGBs) are shown in bold, black outlines in Figure 2.3 for wrought and AM HIP+SA specimens in both peak-aged and over-aged conditions. The AM HIP+PA specimens have significantly larger grains than all other conditions, and parent austenite grains could not be reconstructed from this microstructure.

The difference in median grain diameter between the wrought peak-aged and AM

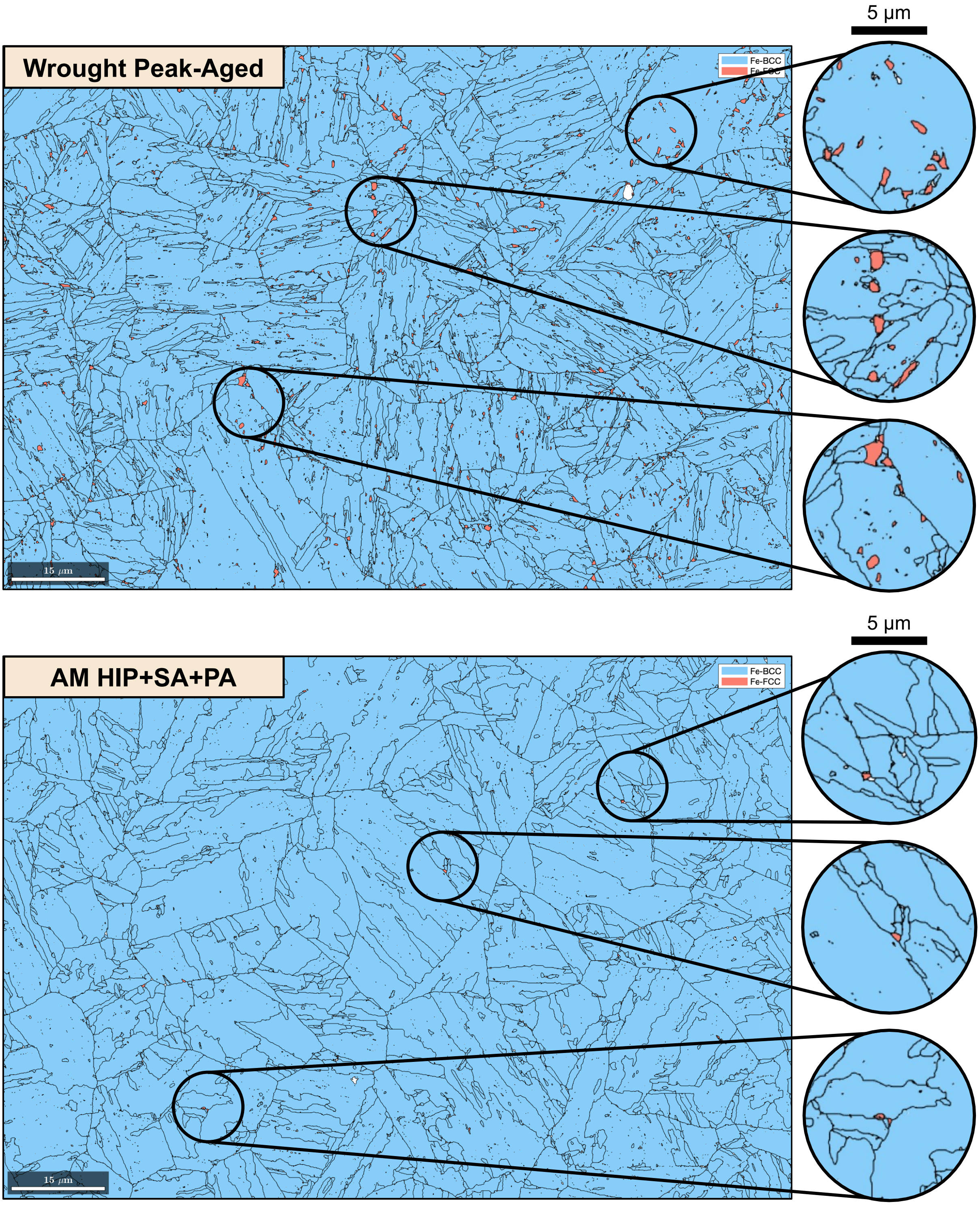

Figure 2.4: EBSD phase composition in the wrought peak-aged and AM HIP+SA+PA conditions, showing a clear increase in FCC phase density in the wrought condition.

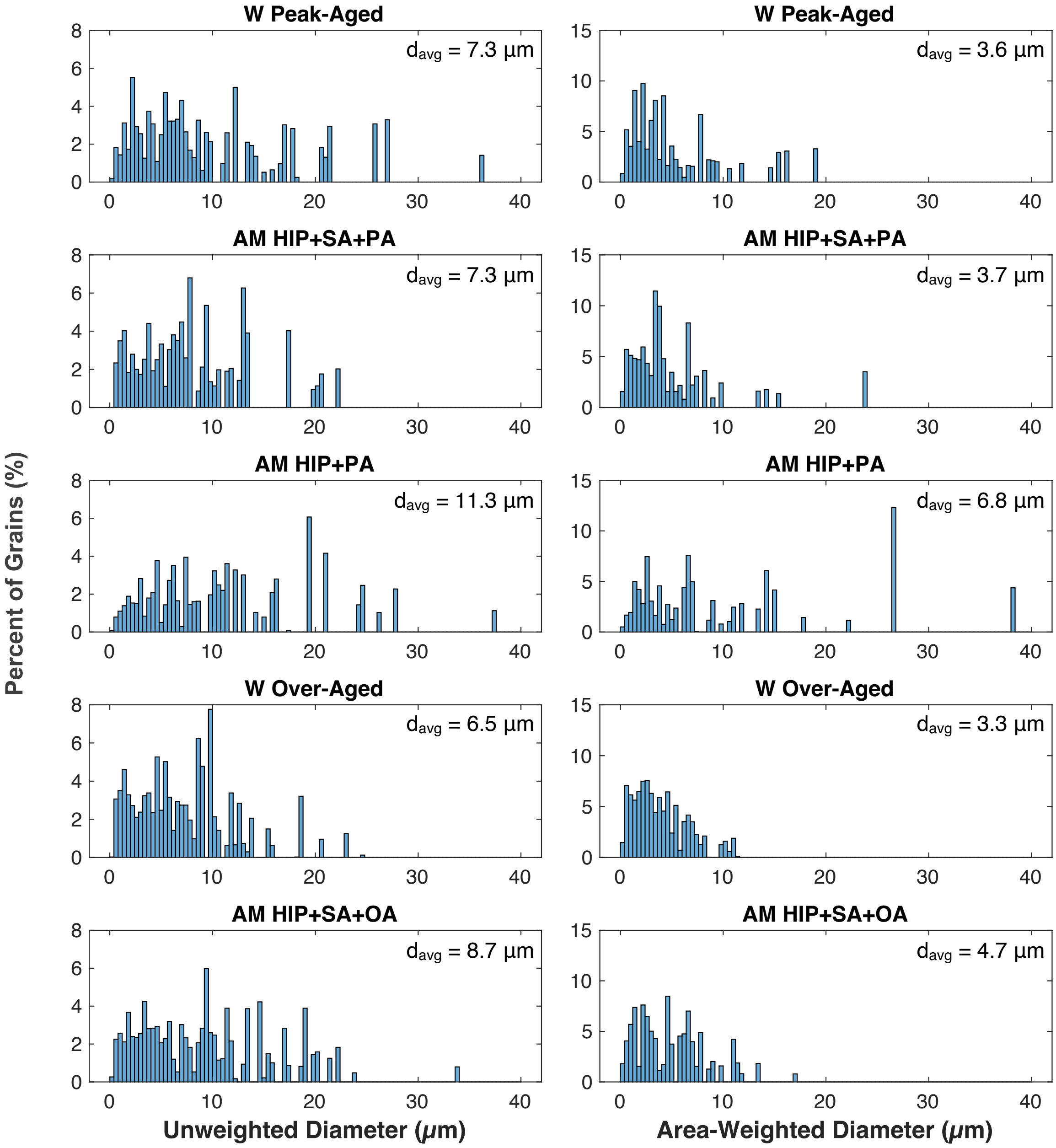

Figure 2.5: Histograms of the unweighted grain diameter (left) and the area-weighted grain diameter (right) for each specimen. Median grain diameter d_{avg} is listed on each subplot.

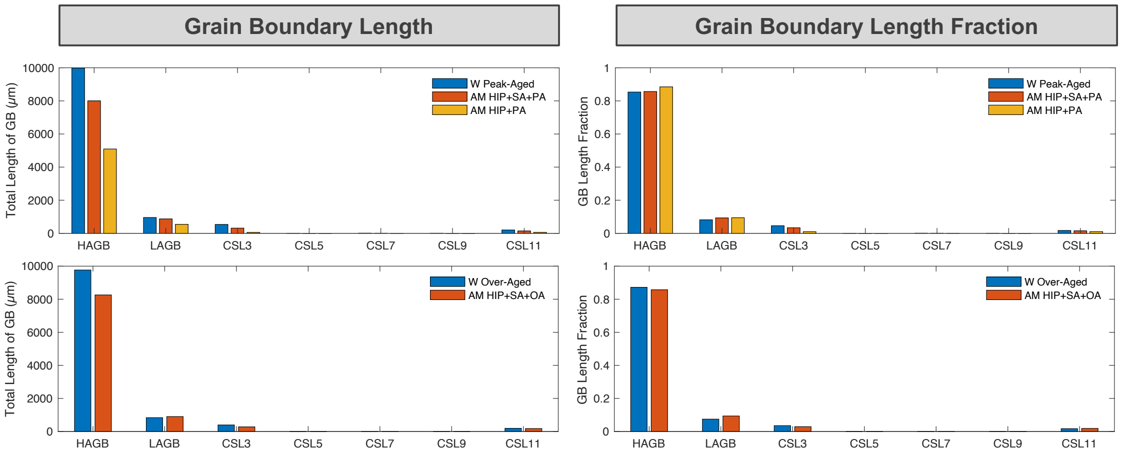

Figure 2.6: Comparison of total length (left) and length fraction (right) of the examined grain boundary types.

Table 2.5: Length fraction of prior austenite grain boundaries and each observed grain boundary type, calculated from the EBSD micrographs shown in Figure 2.3 using the open-source MTeX package.[40]

Condition	**Specimen**	**Grain Boundary Length Fraction**							
		PAGB	**HAGB**	**LAGB**	$\Sigma 3$	$\Sigma 5$	$\Sigma 7$	$\Sigma 9$	$\Sigma 11$
Peak-Aged	W PA	0.33	0.85	0.08	0.05	3.8×10^{-4}	9.2×10^{-4}	5.7×10^{-4}	0.02
	AM HIP+SA+PA	0.33	0.86	0.09	0.03	1.5×10^{-4}	7.1×10^{-4}	2.1×10^{-4}	0.02
	AM HIP+PA	-	0.89	0.09	0.01	1.9×10^{-4}	4.8×10^{-4}	9.2×10^{-5}	0.01
Over-Aged	W OA	0.30	0.87	0.08	0.04	9.9×10^{-5}	6.1×10^{-4}	3.5×10^{-4}	0.02
	AM HIP+SA+OA	0.23	0.86	0.09	0.03	2.5×10^{-4}	9.6×10^{-4}	3.2×10^{-4}	0.02

HIP+SA+PA specimen is subtle, but it should be noted that this may be an artifact of irregularly shaped grains, as diameter measurements are taken in the longest dimension of each grain and do not account for elongated structures like martensite laths. In order to more rigorously compare grain morphology between different specimens, grain boundary lengths and length fractions for each grain boundary type are compared in Figure 2.6, and a summary of the calculated grain boundary length fractions is shown in Table 2.5. This allows for a comparison of irregular grain shapes, as well as a grain size-independent analysis of grain boundary character.

The majority of the grain boundaries—between 85-89%—are classified as high-angle grain boundaries. The AM specimens have a slightly higher fraction of LAGBs and a lower fraction of Σ3, Σ5, and Σ9 grain boundaries, though it should be noted that all special grain boundaries have very low length fractions and therefore the scale of any difference is decidedly small. The over-aged specimens also have a smaller length fraction of prior austenite grain boundaries, with the AM HIP+SA+OA showing a significantly lower PAGB length fraction compared to its wrought counterpart. Conversely, the wrought and AM peak-aged specimens have a high degree of similarity in PAGB length fraction.

2.6.3 Precipitates

TEM bright-field, HAADF, and EDS micrographs for each specimen are shown in Figure 2.7. Cu-rich precipitates are apparent in the AM and wrought over-aged conditions, as well as in the AM HIP+PA specimen. Figure 2.8 shows examples of fine coherent Cu-rich precipitates in the peak-aged specimens that are visible at a higher magnification, as have been observed in peak-aged 17-4 PH in literature in wrought[2, 5, 7, 8, 47–49] and AM[4, 13, 20, 24–28] specimens. These fine, coherent precipitates have been shown to coarsen into incoherent precipitates upon over-aging in wrought[5, 8, 47, 49] and additive[20, 26] specimens, which may have contributed to the increased visibility of Cu-rich precipitates in the over-aged specimens in this study. There is also visible precipitate decoration on the grain boundaries in both AM and wrought over-aged specimens, which has been observed in literature.[7]

Cu-rich precipitate size and density of AM HIP+SA+OA and wrought over-aged specimens were characterized through ImageJ analysis of both TEM HAADF and Cu EDS micrographs. To reduce noise and background, each micrograph underwent a process of rolling ball background subtraction, auto-thresholding, despeckling, outlier removal, and binary masking with hole filling prior to the automatic particle analysis. An example of the micrograph input and the resulting particle selection from this analysis are shown in Figure 2.9. Statistical box-whisker plots of precipitate Feret diameter and area, as well as approximate precipitate count density, surface area density, and volume density, are shown

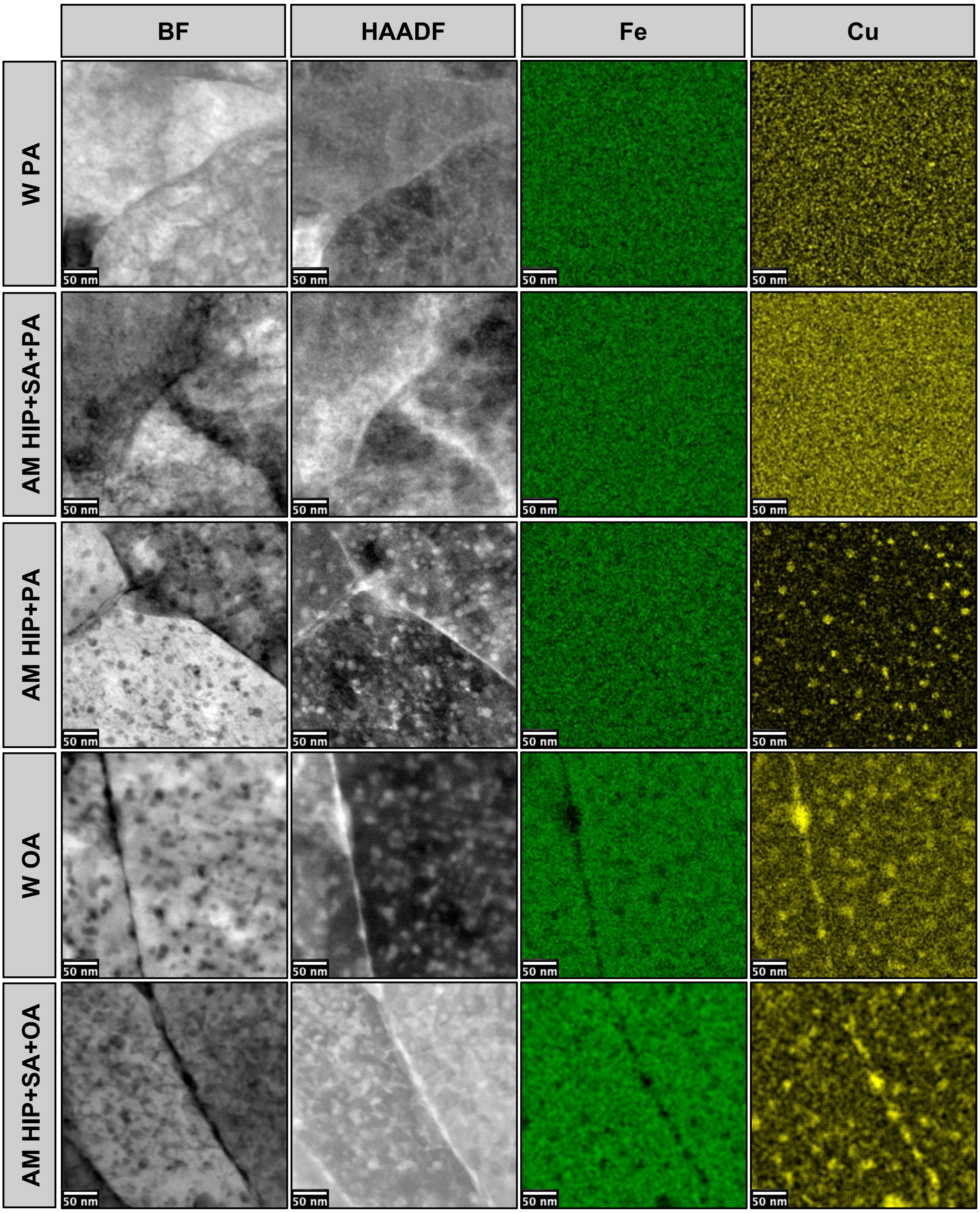

Figure 2.7: Bright field, HAADF, and EDS TEM micrographs for each specimen. Cu-rich precipitates in the bulk and along grain boundaries are visible in AM HIP+PA and both over-aged specimens. Copper is indicated by yellow intensity maps.

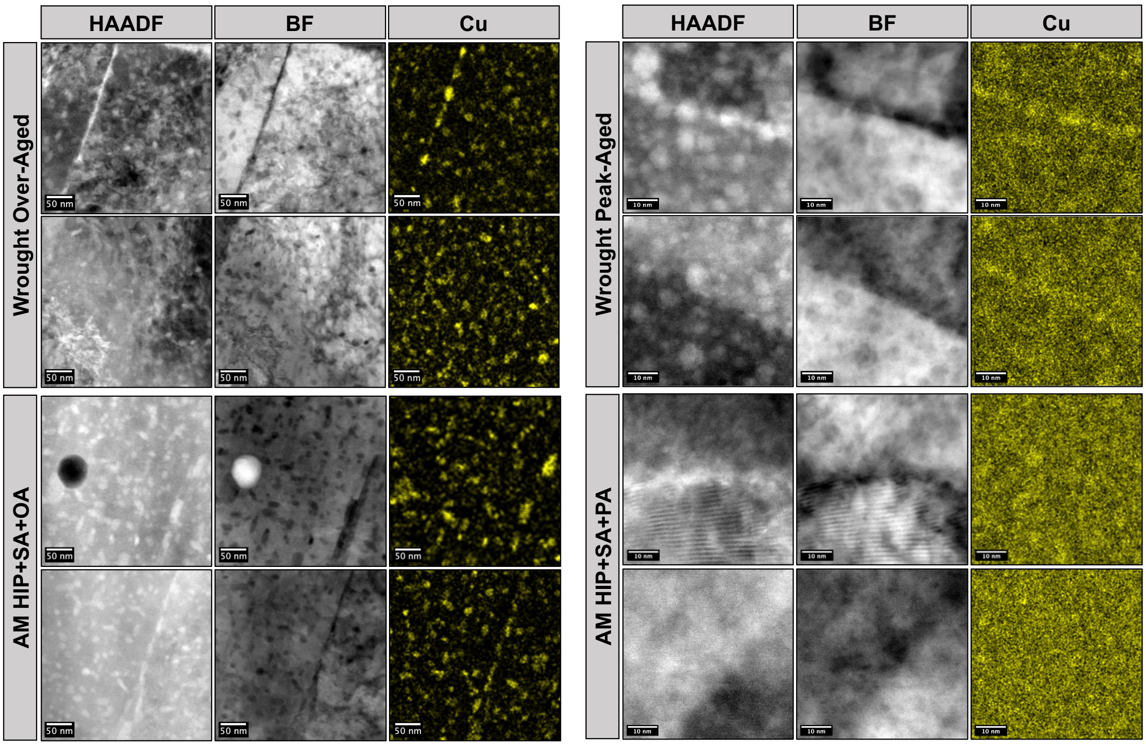

Figure 2.8: Bright field, HAADF, and EDS TEM micrographs for over-aged specimens (left, 50 nm length scale) and peak-aged specimens (right, 10 nm length scale) showing evidence of Cu-rich precipitates. Copper is indicated by yellow intensity maps.

in Figure 2.10. The results of HAADF and Cu EDS analyses were compared to account for any effects of insufficient background correction in HAADF micrographs. It should be noted that the large precipitate size outliers may be due to overlapping precipitates that could not be distinguished via watershed separation, which is likely the cause of the large-area outlier data in Figure 2.10(a)-(b). Precipitate surface area and volume were approximated from the visible precipitate area by assuming perfectly spherical precipitates, as Cu-rich precipitates in 17-4 PH have been shown to be spherical in nature;[50] however, precipitate overlap with the foil boundaries and with other precipitates may affect these results. These analyses demonstrate that the wrought over-aged specimen has very slightly finer Cu-rich precipitates than its AM counterpart, but a higher precipitate number density. Overall, the wrought and AM specimens have similar precipitate surface area per cubic nanometer, though the wrought has a marginally lower volume fraction of precipitates.

The comparable yield strengths between wrought and AM alloys[38] imply some degree

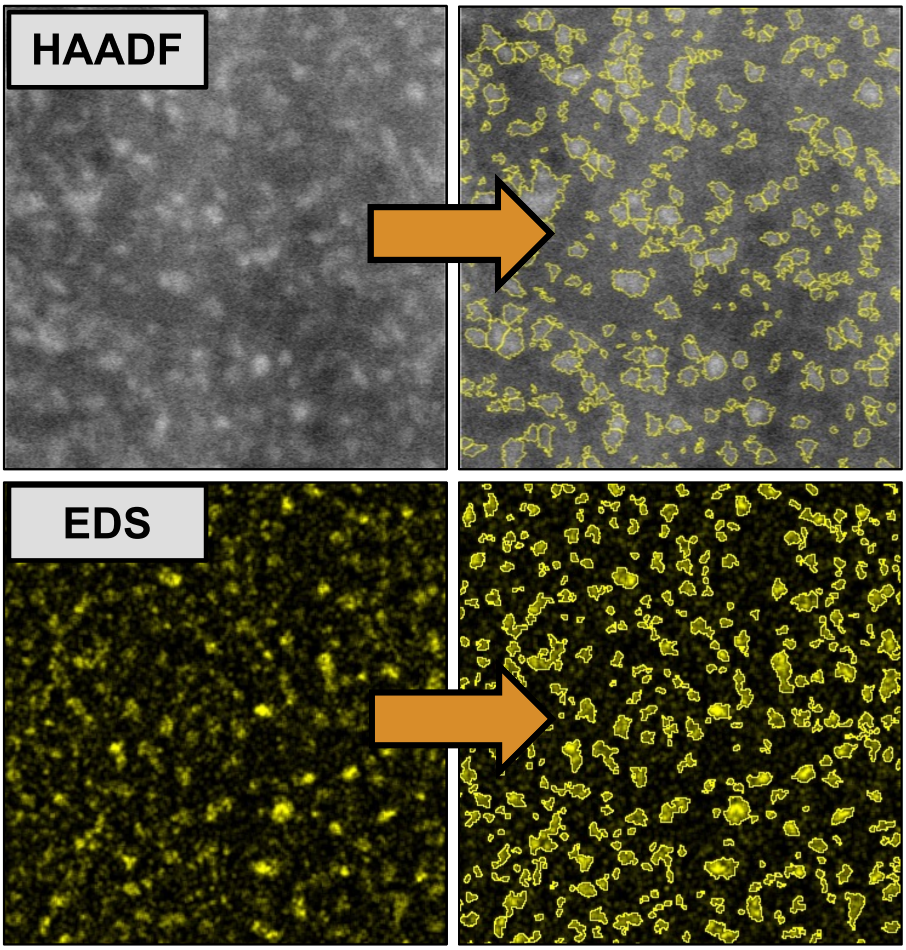

Figure 2.9: Examples of the input HAADF (top) and EDS (bottom) micrographs, as well as the subsequent detected particles outlined in yellow. Analysis performed via ImageJ. In EDS micrographs, Cu is indicated by yellow intensity maps.

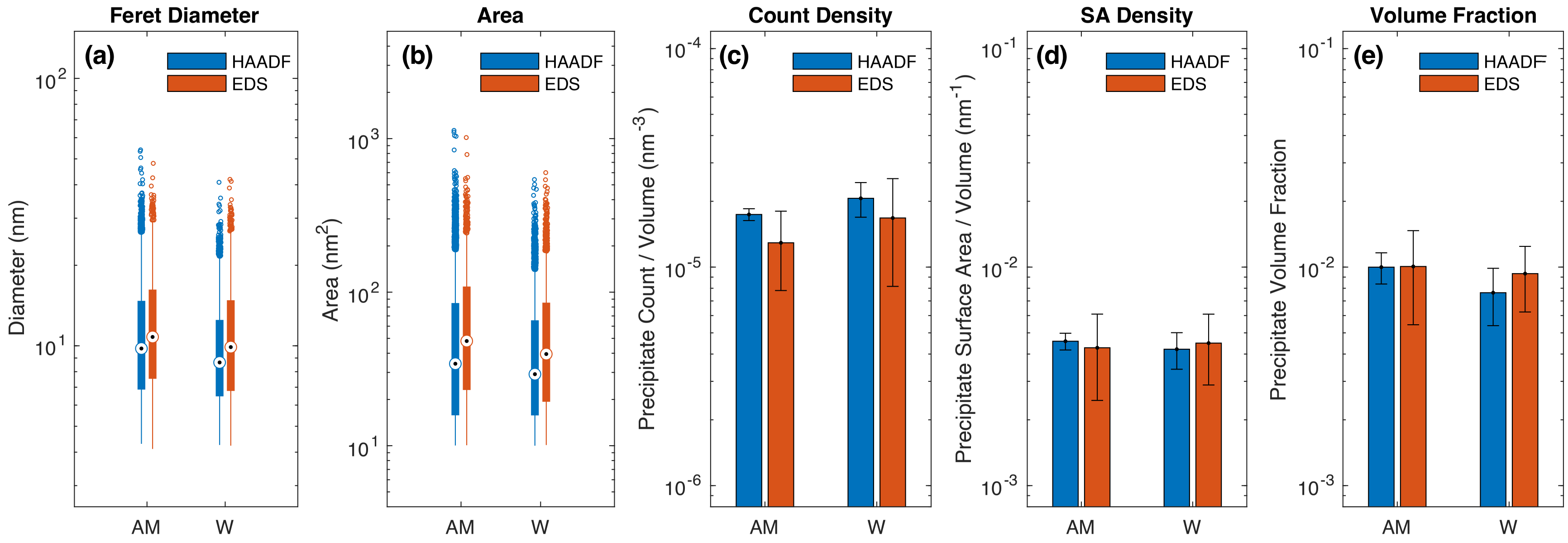

Figure 2.10: Box-whisker plot distributions of (a) precipitate area and (b) estimated precipitate surface area for both HAADF and EDS micrographs. Calculated precipitate count density, surface area (SA) density, and volume fraction for all HAADF and EDS micrographs are shown in (c), (d), and (e), respectively. Error bars on plots (c)-(d) represent the weighted standard deviation of the calculated density values from each micrograph.

Table 2.6: Statistical results for precipitate analysis for both HAADF and EDS micrographs.

Value	**AM HIP+SA+OA**		**W Over-Aged**	
	HAADF	**Cu EDS**	**HAADF**	**Cu EDS**
Single-Precipitate Statistics				
Mean area (nm^2)	65.7	82.7	51.0	66.9
Median area (nm^2)	34.2	48.0	29.2	39.5
Mean Feret diameter (nm)	11.6	12.7	10.0	11.6
Median Feret diameter (nm)	9.8	10.8	8.7	9.9
Precipitate Density Statistics				
Count density (nm^{-3})	2.54×10^{-5}	1.29×10^{-5}	2.06×10^{-5}	1.68×10^{-5}
Surface area density (nm^{-1})	4.58×10^{-3}	4.27×10^{-3}	4.21×10^{-3}	4.49×10^{-3}
Volume fraction	1.00%	1.01%	0.76%	0.93%

of similarity between AM and wrought Cu-rich precipitate characteristics since the yield strength in 17-4 PH is potently dependent on the precipitate morphology.[8] Indeed, as seen in Figure 2.10 and Table 2.6, the total Cu-rich precipitate surface area per unit volume is very similar between the AM and wrought over-aged specimens. However, the marginally finer precipitate size in the wrought specimens increases the surface area-volume ratio, leading to a slightly lower volume density of precipitates compared to the AM specimens. This could be due to the minor difference in copper content between the wrought and AM builds, with the wrought specimen having about 0.5 wt% Cu less than the AM specimen.[38]

Additionally, larger regions rich in Nb and Cu were visible in each specimen; various oxides and C, Cr, Mn, Mo, and Ni-rich regions were found in EDS micrographs of specimens of varying builds and heat treatments. Similar inclusions have been found in literature.[4, 9–11, 16, 27] An example of a NbC-type carbide, also containing Mo, is shown in the EDS micrographs in Figure 2.11; this precipitate was found in peak-aged wrought 17-4 PH. This precipitate is just over 0.5 microns in diameter along the largest dimension, which is within the range of the FCC regions observed in the wrought peak-aged specimen in Figure 2.4. This can be compared to the much smaller Nb-rich region visible in the

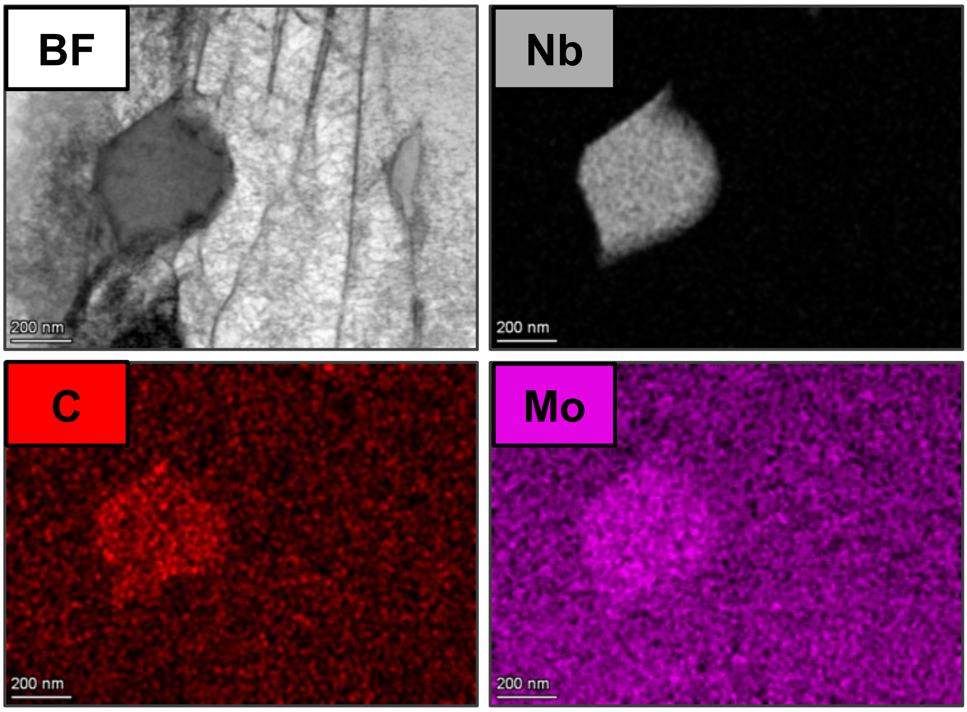

Figure 2.11: Bright-field TEM and EDS micrographs of an Nb- and C-rich region in the wrought peak-aged specimen. Nb, C, and Mo are indicated by silver, red, and pink intensity maps, respectively.

EDS micrograph of the AM HIP+SA+OA specimen, shown in Figure 2.12.

These NbC-type carbides are speculated to be the cause of the increase in FCC phase seen in EBSD phase analysis in Section 2.6.1. The decreased grain size of the wrought specimens could contribute to the increase in NbC-type carbides, as carbides have been shown to preferentially nucleate and grow along grain boundaries.[51] Similarly, Lashgari et al. reported precipitation of NbC-type carbides in AM 17-4 PH after solution annealing; large carbides were found along the grain boundaries, as well as slightly finer carbides within the lath interior.[3] Shoemaker et al.[38] also observed small secondary particles in the alloys used in this study. These particles had diameters less than 0.25 μm in AM and 0.5 μm in wrought specimens, and were speculated to be niobium carbides. This increase in length scale corresponds with the findings from the TEM and EDS analyses.

The micrographs shown in Figure 2.12 also include regions, potentially oxides, enriched with Mn and Al. Additionally, the enrichment of nickel along martensite lath boundaries

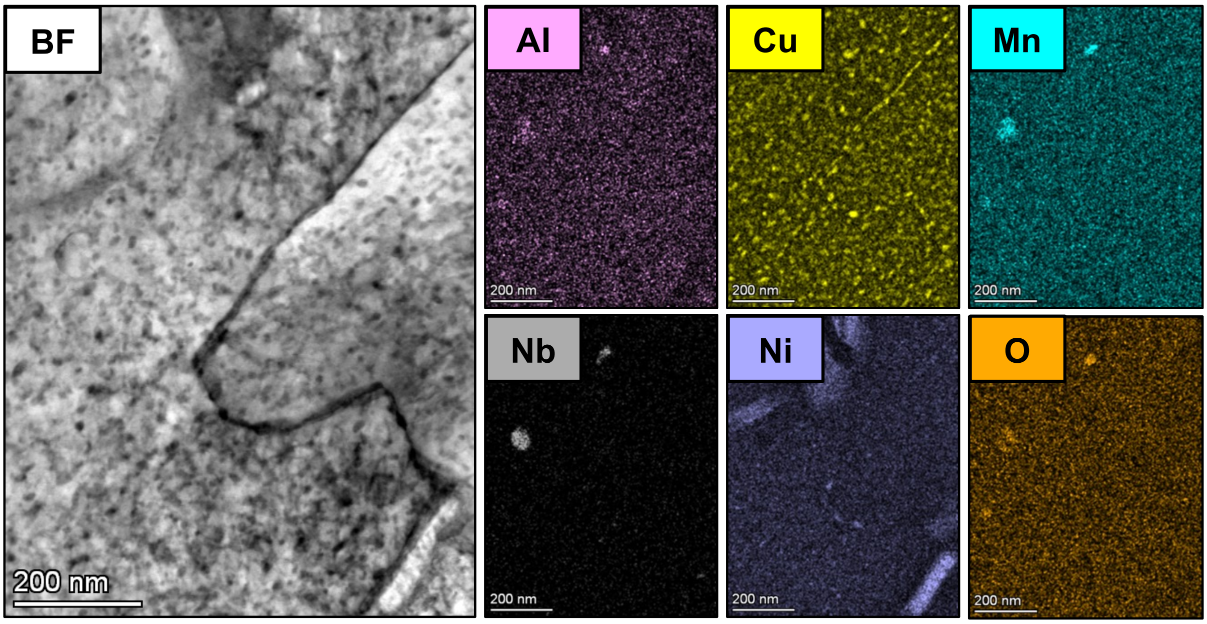

Figure 2.12: Bright-field TEM and EDS micrographs of an area in the AM HIP+SA+OA specimen containing precipitates and Ni-rich regions.

visible in Figure 2.12 has also been observed by Song et al.[52–54] However, this was attributed to carbide precipitation along the boundaries, though no carbon enrichment is present here. Though nickel is known to be a strong austenite stabilizing element and was only present in the over-aged AM and wrought 17-4 PH, there is actually a decrease in the amount of observed FCC phase in the EBSD micrographs of the over-aged specimens compared to the peak-aged. This could possibly be due to the length scale of the EBSD analysis being too large to detect thin retained austenite films along grain boundaries, or the increased density of NbC-type carbides in the peak-aged specimens counteracting any detected retained or reverted austenite.

2.6.4 Dislocations

Kernel average misorientation (KAM) maps, which can be used to estimate the prevalence of geometrically necessary dislocations (GNDs),[55] were generated from the EBSD data using MTeX.[40] KAM maps and statistical analyses for each specimen are displayed in Figure 2.13. The mean and median KAM values of both wrought specimens as well as

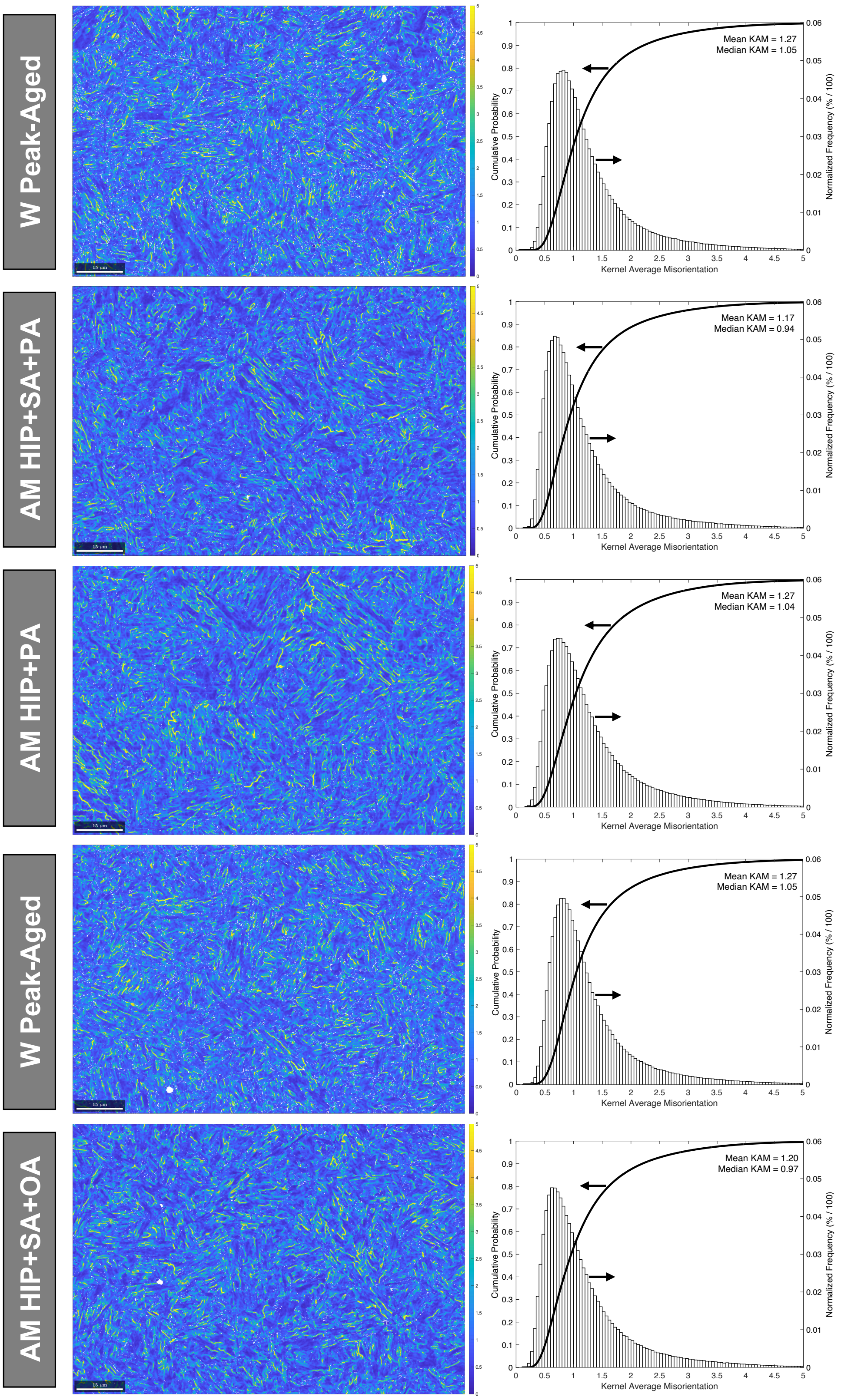

Figure 2.13: (Left) KAM maps for each condition, generated from EBSD. (Right) Cumulative probability analysis and histogram of KAM for each pixel. Mean and median KAM are recorded.

AM HIP+PA are all extremely similar, whereas AM HIP+SA+PA and AM HIP+SA+OA show a very slight decrease. This could be due to the combination of hot isostatic pressing and solution annealing; the HIP process continuously eliminates dislocation pileups, and dislocation pinning by precipitates is also reduced.[56] When combined with the solution annealing step, which has been shown to reduce dislocations as well, the AM HIP+SA specimens will have less dislocations prior to aging than the AM+HIP or wrought specimens.[39] Viswanathan et al.[49] suggest that during aging of 17-4 PH, dislocations become rearranged within the martensite laths and there is an additional reduction in dislocation density. In addition, any dislocation pinning by precipitates would likely be similar between wrought and AM alloys in the same heat treatment condition, as the precipitate morphology is largely the same.

2.6.5 Pores

A full characterization of porosity in the AM 17-4 PH alloys studied in this work has previously been performed by Shoemaker et al.[38, 57] The presence of pores is the most apparent difference in the microstructure between the wrought specimens, which show little to no porosity, and the AM specimens, which all display some degree of porosity. These pores typically range between 0.1-0.5 microns in diameter.[38] The prevalence of pores in the AM specimens in this study is by no means unique in literature; widespread porosity in L-PBF 17-4 PH has been documented in numerous studies.[4, 21, 22, 24, 33, 34, 58–72] The pores are commonly attributed to entrapped gas, particularly argon, originating from the powder atomization process.[21, 68] Notably, due to the near-zero solubility of argon in iron, these pores are resistant to elimination through hot isostatic pressing (HIP) or subsequent heat treatments.[25, 30, 64, 73, 74] However, the HIP process does serve to eliminate any much larger lack-of-fusion pores that do not contain entrapped gas.[75]

The resistance of sub-micron pores to closure via HIP processing is also noted by Shoemaker et al.[38, 57] AM 17-4 PH in the as-built condition displays small pore spacing and diameter; after the HIP treatment, both pore spacing and diameter increased. This is attributed to competition between external pressure from the HIP process acting to decrease pore density and pore size, and internal pressure from the high temperatures expanding the gas-filled pores.

However, several factors distinguish the porosity in this material from previously observed gas-entrapped pores. Gas-entrapped pores found in literature often have diameters greater than 5-10 microns, one or two orders of magnitude greater than the diameters of the pores found by Shoemaker et al. in the current material.[38] This may be due to technique resolution, which limits porosity analysis to only pores above a certain diameter.[67, 68] Additionally, gas-entrapped pores are often heterogeneously distributed in as-built AM alloys and appear near melt pool boundaries; the pores observed in this alloy are homogeneously distributed, though this may be due to post-processing homogenization of the microstructure. Ultimately, the inability of the HIP process to eliminate these pores, as well as the expansion of the pores during heat treatment, suggests the presence of some pressurized gas within the pores.

2.7 Material Properties

2.7.1 Mechanical Properties

Mechanical properties for AM and wrought 17-4 PH in the peak-aged and over-aged conditions were reported by Shoemaker et al.[38, 57] Vickers hardness and tension testing were performed in accordance with relevant ASTM standards.[37, 76, 77] The as-built AM specimens has inferior yield strength and ultimate tensile strength compared to peak-aged wrought specimens. The heat treatment process produces AM specimens in the peak-aged and over-aged conditions with yield strengths within 10% of their wrought counterparts, as shown in Figure 2.14 and by Shoemaker et al.[38, 57] However, there is a reduction in ductility in the AM specimens, attributable to the porosity in the material.[20, 38, 58, 66]

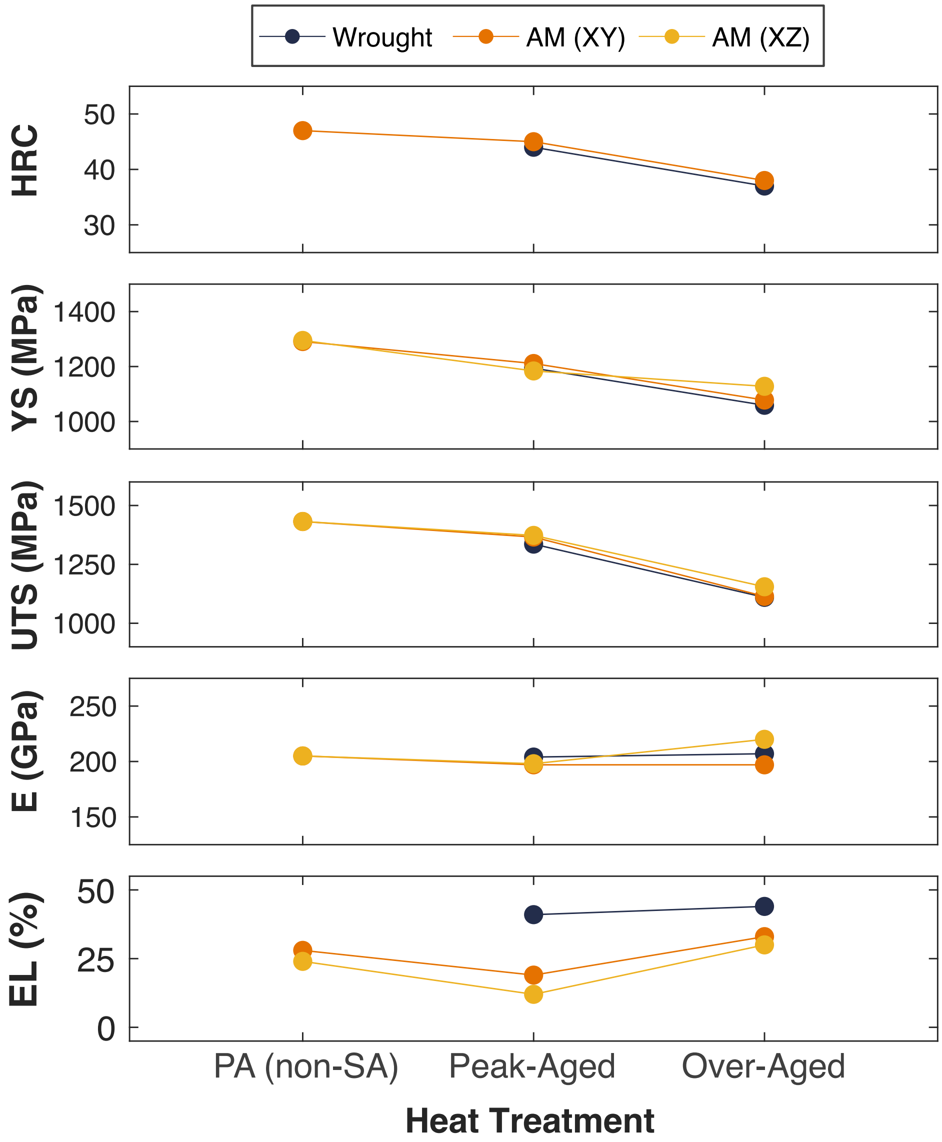

Figure 2.14: Mechanical properties of wrought and AM 17-4 PH across heat treatments. From top to bottom: Rockwell Hardness C (HRC), yield strength (YS), ultimate tensile strength (UTS), elasticity/Young's Modulus (E), and ductility (EL).[38, 57]

This reduction in ductility is less pronounced in the over-aged specimens. AM HIP+PA specimens displayed reduced strength and ductility compared to AM HIP+PA+SA, demonstrating the necessity of a solution annealing step in AM post-processing.[38] These mechanical properties of the specimens in this study are similar to high-performing AM 17-4 PH in literature.[38, 64, 78] There is also little to no anisotropy observed in the mechanical properties of the AM specimens, which is to be expected due to the heat treatment processing.

2.7.2 Electrochemical Properties

Initial potentiodynamic polarization tests were conducted on wrought and AM 17-4 PH specimens in the peak-aged heat treatment condition to determine the reversible hydrogen potential. A 30-minute OCP hold was performed to stabilize the corrosion potential of each specimen, followed by potentiodynamic polarization from -1.2V to +1.2V vs. $Hg/HgSO_4$ and back in 0.1M NaOH solution. The polarization results show a reversible H potential around -0.8V to -1.0V vs $Hg/HgSO_4$; the polarization curves can be seen in Figure 2.15. The electrochemical behavior of the AM specimens is largely independent of direction, as is expected due to the isotropic microstructure. The passive region and repassivation behavior are similar in all specimens.

2.8 Conclusions

A meticulous comparison of wrought and additively manufactured (AM) 17-4 PH microstructure and first-order properties has been undertaken. The additive manufacturing processing and post-processing parameters utilized to achieve similar mechanical behavior (with the notable exception of ductility) between the wrought and AM alloys in the peak-aged and over-aged conditions is described. Employing advanced characterization techniques such as EBSD, TEM, and EDS, a comparative analysis was conducted on key microstructural features. These features included phase composition, grain size, grain

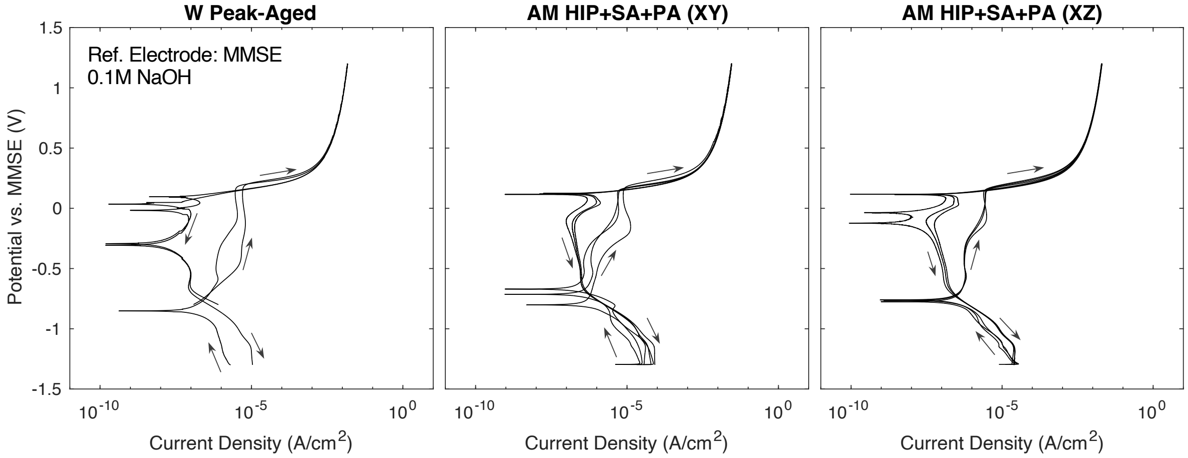

Figure 2.15: Potentiodynamic polarization curves for peak-aged wrought and additive 17-4 PH (in the XY and XZ directions), conducted between -1.2 and +1.2 V versus Hg/HgSO$_4$ in 0.1M NaOH.

boundary type, dislocation density, and precipitate morphology, revealing distinctive attributes between wrought and AM specimens across each heat treatment.

Key differences in the microstructure of AM specimens observed via EBSD include increased grain size and a slight reduction in dislocation density corresponding to the solution-annealed treatment. Additionally, a diminished fraction of FCC phase was observed in the AM specimens, correlated with a decrease in the size and prominence of NbC-type carbides found using transmission electron microscopy. TEM was also employed to examine Cu-rich precipitate morphology, showing fine coherent precipitates in the peak-aged condition and coarser incoherent precipitates upon over-aging. ImageJ analysis was used to compare Cu-rich precipitate size and density in the over-aged AM and wrought specimens; a largely similar surface area density is observed between the two conditions, though a slight increase in size and decrease in count density of precipitates in the AM specimen is seen. Collectively, these findings contribute to a better understanding of the link between additive manufacturing and microstructure in 17-4 PH, and lay the groundwork for future microstructure-property analyses in this dissertation.

References

[1] S. Shen, X. Li, P. Zhang, Y. Nan, G. Yang, and X. Song, “Effect of solution-treated temperature on hydrogen embrittlement of 17-4 PH stainless steel,” *Materials Science and Engineering A*, 2017.

[2] W. C. Chiang, C. C. Pu, B. L. Yu, and J. K. Wu, “Hydrogen susceptibility of 17-4 PH stainless steel,” *Materials Letters*, vol. 57, no. 16-17, pp. 2485–2488, 2003.

[3] H. R. Lashgari, C. Kong, E. Adabifiroozjaei, and S. Li, “Microstructure, post thermal treatment response, and tribological properties of 3D printed 17-4 PH stainless steel,” *Wear*, vol. 456, p. 203367, 2020.

[4] Y. Sun, R. J. Hebert, and M. Aindow, “Effect of heat treatments on microstructural evolution of additively manufactured and wrought 17-4PH stainless steel,” *Materials and Design*, 2018.

[5] M. Murayama, Y. Katayama, and K. Hono, “Microstructural evolution in a 17-4 PH stainless steel after aging at 400 °C,” *Metallurgical and Materials Transactions A*, vol. 30, pp. 345–353, 1999.

[6] K. C. Antony, “Aging reactions in precipitation hardenable stainless steel,” *JOM*, vol. 15, pp. 922–927, 1963.

[7] L. W. Tsay, W. C. Lee, R. K. Shiue, and J. K. Wu, “Notch tensile properties of laser-surface-annealed 17-4 PH stainless steel in hydrogen-related environments,” *Corrosion Science*, vol. 44, no. 9, pp. 2101–2118, 2002. ISBN: 0010-938X.

[8] C. N. Hsiao, C. S. Chiou, and J. R. Yang, “Aging reactions in a 17-4 PH stainless steel,” *Materials Chemistry and Physics*, vol. 74, pp. 134–142, 2002.

[9] M. R. Stoudt, R. E. Ricker, E. A. Lass, and L. E. Levine, “Influence of Postbuild Microstructure on the Electrochemical Behavior of Additively Manufactured 17-4 PH Stainless Steel,” *JOM*, vol. 69, no. 3, pp. 506–515, 2017. ISBN: 1047-4838.

[10] U. K. Mudali, A. K. Bhaduri, and J. B. Gnanamoorthy, “Localised corrosion behaviour of 17–4 PH stainless steel,” *Materials Science and Technology*, vol. 6, no. 5, pp. 475–481, 1990.

[11] C. R. Das, H. C. Dey, G. Srinivasan, S. K. Albert, A. K. Bhaduri, and A. Dasgupta, “Weldability of 17-4PH stainless steel in overaged heat treated condition,” *Science and Technology of Welding and Joining*, vol. 11, pp. 502–508, Sept. 2006.

[12] R. Bhambroo, S. Roychowdhury, V. Kain, and V. S. Raja, “Effect of reverted austenite on mechanical properties of precipitation hardenable 17-4 stainless steel,” *Materials Science and Engineering A*, vol. 568, pp. 127–133, 2013. Publisher: Elsevier.

[13] L. E. Murr, E. Martinez, J. Hernandez, S. Collins, K. N. Amato, S. M. Gaytan, and P. W. Shindo, “Microstructures and properties of 17-4 PH stainless steel fabricated by selective laser melting,” *Journal of Materials Research and Technology*, vol. 1, no. 3, pp. 167–177, 2012. ISBN: 2238-7854.

[14] L. Facchini, N. Vicente, I. Lonardelli, E. Magalini, P. Robotti, and M. Alberto, “Metastable austenite in 17-4 precipitation-hardening stainless steel produced by selective laser melting,” *Advanced Engineering Materials*, vol. 12, no. 3, pp. 184–188, 2010.

[15] H. K. Rafi, D. Pal, N. Patil, T. L. Starr, and B. E. Stucker, “Microstructure and Mechanical Behavior of 17-4 Precipitation Hardenable Steel Processed by Selective Laser Melting,” *Journal of Materials Engineering and Performance*, 2014.

[16] S. Cheruvathur, E. A. Lass, and C. E. Campbell, “Additive manufacturing of 17-4 PH stainless steel: post-processing heat treatment to achieve uniform reproducible microstructure,” *JOM*, vol. 68, pp. 930–942, 2016. ISBN: 1047-4838.

[17] S. D. Meredith, J. S. Zuback, J. S. Keist, and T. A. Palmer, “Impact of composition on the heat treatment response of additively manufactured 17–4 PH grade stainless steel,” *Materials Science and Engineering A*, vol. 738, pp. 44–56, 2018. Publisher: Elsevier B.V.

[18] S. Vunnam, A. Saboo, C. Sudbrack, and T. L. Starr, “Effect of powder chemical composition on the as-built microstructure of 17-4 PH stainless steel processed by selective laser melting,” *Additive Manufacturing*, 2019.

[19] E. A. Lass, F. Zhang, and C. E. Campbell, “Nitrogen Effects in Additively Manufactured Martensitic Stainless Steels: Conventional Thermal Processing and Comparison with Wrought,” *Metallurgical and Materials Transactions A: Physical Metallurgy and Materials Science*, vol. 51, pp. 2318–2332, 2020.

[20] T. LeBrun, T. Nakamoto, K. Horikawa, and H. Kobayashi, “Effect of retained austenite on subsequent thermal processing and resultant mechanical properties of selective laser melted 17-4 PH stainless steel,” *Materials and Design*, vol. 81, pp. 44–53, 2015. Publisher: Elsevier Ltd.

[21] A. Kudzal, B. McWilliams, C. Hofmeister, F. Kellogg, J. Yu, J. Taggart-Scarff, and J. Liang, “Effect of scan pattern on the microstructure and mechanical properties of Powder Bed Fusion additive manufactured 17-4 stainless steel,” *Materials and Design*, vol. 133, pp. 205–215, 2017.

[22] M. Mahmoudi, A. Elwany, A. Yadollahi, S. M. Thompson, L. Bian, and N. Shamsaei, “Mechanical properties and microstructural characterization of selective laser melted 17-4 PH stainless steel,” *Rapid Prototyping Journal*, vol. 23, pp. 280–294, Mar. 2017.

[23] A. Yadollahi, N. Shamsaei, S. M. Thompson, A. Elwany, and L. Bian, “Mechanical and microstructural properties of selective laser melted 17-4 PH stainless steel,” in *ASME International Mechanical Engineering Congress and Exposition, Proceedings (IMECE)*, (Houston, TX), American Society of Mechanical Engineers, 2015.

[24] M. Alnajjar, F. Christien, C. Bosch, and K. Wolski, “A comparative study of microstructure and hydrogen embrittlement of selective laser melted and wrought 17–4 PH stainless steel,” *Materials Science and Engineering A*, vol. 785, p. 139363, 2020.

[25] P. Nezhadfar, E. Burford, K. Anderson-Wedge, B. Zhang, S. Shao, S. Daniewicz, and N. Shamsaei, “Fatigue crack growth behavior of additively manufactured 17-4 PH stainless steel: Effects of build orientation and microstructure,” *International Journal of Fatigue*, vol. 123, pp. 168–179, June 2019.

[26] B. AlMangour and J.-M. Yang, “Understanding the deformation behavior of 17-4 precipitate hardenable stainless steel produced by direct metal laser sintering using micropillar compression and TEM,” *The International Journal of Advanced Manufacturing Technology*, vol. 90, pp. 119–126, Apr. 2017.

[27] T.-H. Hsu, Y.-J. Chang, C.-Y. Huang, H.-W. Yen, C.-P. Chen, K.-K. Jen, and A.-C. Yeh, “Microstructure and property of a selective laser melting process induced oxide dispersion strengthened 17-4 PH stainless steel,” *Journal of Alloys and Compounds*, vol. 803, pp. 30–41, Sept. 2019.

[28] S. Pasebani, M. Ghayoor, S. Badwe, H. Irrinki, and S. V. Atre, “Effects of atomizing media and post processing on mechanical properties of 17-4 PH stainless steel manufactured via selective laser melting,” *Additive Manufacturing*, vol. 22, pp. 127–137, Aug. 2018.

[29] N. Guennouni, A. Barroux, C. Grosjean, D. Maisonnette, E. Nivet, E. Andrieu, D. Poquillon, L. Laffont, and C. Blanc, “Comparative study of the microstructure

between a laser beam melted 17-4PH stainless steel and its conventional counterpart," *Materials Science and Engineering A*, vol. 823, p. 141718, 2021.

[30] M. Alnajjar, F. Christien, V. Barnier, C. Bosch, K. Wolski, A. D. Fortes, and M. Telling, "Influence of microstructure and manganese sulfides on corrosion resistance of selective laser melted 17-4 PH stainless steel in acidic chloride medium," *Corrosion Science*, vol. 168, p. 108585, May 2020.

[31] P. Bajaj, A. Hariharan, A. Kini, P. Kürnsteiner, D. Raabe, and E. A. Jägle, "Steels in additive manufacturing: A review of their microstructure and properties," *Materials Science and Engineering: A*, vol. 772, p. 138633, 2020.

[32] A. Caballero, J. Ding, S. Ganguly, and S. Williams, "Wire + Arc Additive Manufacture of 17-4 PH stainless steel: Effect of different processing conditions on microstructure, hardness, and tensile strength," *Journal of Materials Processing Technology*, vol. 268, pp. 54–62, 2019.

[33] L. Carneiro, B. Jalalahmadi, A. Ashtekar, and Y. Jiang, "Cyclic deformation and fatigue behavior of additively manufactured 17–4 PH stainless steel," *International Journal of Fatigue*, vol. 123, pp. 22–30, 2019.

[34] A. Yadollahi, N. Shamsaei, S. M. Thompson, A. Elwany, and L. Bian, "Effects of building orientation and heat treatment on fatigue behavior of selective laser melted 17-4 PH stainless steel," *International Journal of Fatigue*, vol. 94, pp. 218–235, 2017.

[35] R. P. Gangloff, "Hydrogen Assisted Cracking of High Strength Alloys," in *Comprehensive Structural Integrity* (I. Milne, R. O. Ritchie, and B. Karihaloo, eds.), vol. 6, pp. 31–101, New York, NY: Elsevier Science, 2003.

[36] "EOS StainlessSteel 17-4PH for EOS M 290," 2022.

[37] ASTM International, "ASTM E8/E8M-16a Standard Test Methods for Tension Testing of Metallic Materials," 2016. Place: West Conshohocken, PA.

[38] T. K. Shoemaker, Z. D. Harris, and J. T. Burns, "Comparing Stress Corrosion Cracking Behavior of Additively Manufactured and Wrought 17-4PH Stainless Steel," *Corrosion*, vol. 78, no. 6, pp. 528–546, 2022.

[39] S. Feng, Z. Ai, J. He, B. Yang, G. Gou, and L. Han, "Effect of Annealing and Hot Isostatic Pressing on the Structure and Hydrogen Embrittlement Resistance of Powder-Bed Fusion-Printed CoCrFeNiMn High-Entropy Alloys," *Metals*, vol. 13, p. 630, Mar. 2023.

[40] F. Bachmann, R. Hielscher, and H. Schaeben, "Texture Analysis with MTEX - Free and Open Source Software Toolbox," *Solid State Phenomena*, vol. 160, pp. 63–68, 2010.

[41] R. Hielscher, T. Nyyssönen, F. Niessen, and A. A. Gazder, "The variant graph approach to improved parent grain reconstruction," *Materialia*, vol. 22, p. 101399, May 2022.

[42] F. Niessen, T. Nyyssönen, A. A. Gazder, and R. Hielscher, "Parent grain reconstruction from partially or fully transformed microstructures in *MTEX*," *Journal of Applied Crystallography*, vol. 55, pp. 180–194, Feb. 2022.

[43] C. A. Schneider, W. S. Rasband, and K. W. Eliceiri, "NIH Image to ImageJ: 25 years of image analysis," *Nature Methods*, vol. 9, pp. 671–675, July 2012.

[44] D. J. Shaffer, *Role of retained austenite in mechanical response of additively manufactured 17-4 PH stainless steel.* PhD thesis, Pennsylvania State University, 2020.

[45] D. Shaffer, A. Wilson-Heid, J. Keist, A. Beese, and T. Palmer, "Impact of retained austenite on the aging response of additively manufactured 17-4 PH grade stainless steel," *Materials Science and Engineering: A*, vol. 817, p. 141363, June 2021.

[46] H. Nakagawa and T. Miyazaki, "Effect of retained austenite on the microstructure and mechanical properties of martensitic precipitation hardening stainless steel," *Journal of Materials Science*, vol. 34, pp. 3901–3908, 1999.

[47] H. J. Rack and D. Kalish, "The strength, fracture toughness, and low cycle fatigue behavior of 17-4 PH stainless steel," *Metallurgical transactions*, vol. 5, pp. 1595–1605, July 1974.

[48] Z. Wang, H. Li, Q. Shen, W. Liu, and Z. Wang, "Nano-precipitates evolution and their effects on mechanical properties of 17-4 precipitation-hardening stainless steel," *Acta Materialia*, vol. 156, pp. 158–171, 2018. Publisher: Elsevier Ltd.

[49] U. Viswanathan, S. Banerjee, and R. Krishnan, "Effects of aging on the microstructure of 17-4 PH stainless steel," *Materials Science and Engineering: A*, vol. 104, pp. 181–189, Oct. 1988.

[50] U. K. Viswanathan, P. K. K. Nayar, and R. Krishnan, "Kinetics of precipitation in 17–4 PH stainless steel," *Materials Science and Technology*, vol. 5, pp. 346–349, Apr. 1989.

[51] A. R. Jones, P. R. Howell, and B. Ralph, "The precipitation of niobium carbide at grain boundaries in an austenitic stainless steel," *Journal of Materials Science*, vol. 11, pp. 1593–1599, Sept. 1976.

[52] Y. Y. Song, X. Y. Li, L. J. Rong, D. H. Ping, F. X. Yin, and Y. Y. Li, "Formation of the reversed austenite during intercritical tempering in a Fe–13%Cr–4%Ni–Mo martensitic stainless steel," *Materials Letters*, vol. 64, pp. 1411–1414, July 2010.

[53] Y. Song, X. Li, L. Rong, and Y. Li, "The influence of tempering temperature on the reversed austenite formation and tensile properties in Fe–13%Cr–4%Ni–Mo low carbon martensite stainless steels," *Materials Science and Engineering: A*, vol. 528, pp. 4075–4079, May 2011.

[54] Y. Y. Song, X. Y. Li, L. J. Rong, Y. Y. Li, and T. Nagai, "Reversed austenite in 0Cr13Ni4Mo martensitic stainless steels," *Materials Chemistry and Physics*, vol. 143, pp. 728–734, Jan. 2014.

[55] C. Moussa, M. Bernacki, R. Besnard, and N. Bozzolo, "About quantitative EBSD analysis of deformation and recovery substructures in pure Tantalum," *IOP Conference Series: Materials Science and Engineering*, vol. 89, p. 012038, Aug. 2015.

[56] H. V. Atkinson and S. Davies, "Fundamental aspects of hot isostatic pressing: An overview," *Metallurgical and Materials Transactions A*, vol. 31, pp. 2981–3000, Dec. 2000.

[57] T. K. Shoemaker, *Fatigue and Environmentally Assisted Cracking Behavior of Wrought and Additively Manufactured 17-4PH Stainless Steel.* Doctoral dissertation, University of Virginia, 2022.

[58] U. Ali, R. Esmaeilizadeh, F. Ahmed, D. Sarker, W. Muhammad, A. Keshavarzkermani, Y. Mahmoodkhani, E. Marzbanrad, and E. Toyserkani, "Identification and characterization of spatter particles and their effect on surface roughness, density and mechanical response of 17-4 PH stainless steel laser powder-bed fusion parts," *Materials Science and Engineering: A*, vol. 756, pp. 98–107, May 2019.

[59] P. Auguste, A. Mauduit, L. Fouquet, and S. Pillot, "Study on 17-4 PH stainless steel produced by selective laser melting," *UPB Scientific Bulletin*, vol. 80, no. 4, pp. 197–210, 2018.

[60] S. Dobson, S. Vunnam, D. Frankel, C. Sudbrack, and T. Starr, "Powder variation and mechanical properties for SLM 17-4 PH stainless steel," in *Proceedings of the*

30th Annual International Solid Freeform Fabrication Symposium – An Additive Manufacturing Conference, University of Texas at Austin, 2019.

[61] Z. Hu, H. Zhu, H. Zhang, and X. Zeng, “Experimental investigation on selective laser melting of 17-4PH stainless steel,” *Optics & Laser Technology*, vol. 87, pp. 17–25, Jan. 2017.

[62] H. Irrinki, J. S. D. Jangam, S. Pasebani, S. Badwe, J. Stitzel, K. Kate, O. Gulsoy, and S. V. Atre, “Effects of particle characteristics on the microstructure and mechanical properties of 17-4 PH stainless steel fabricated by laser-powder bed fusion,” *Powder Technology*, vol. 331, pp. 192–203, May 2018.

[63] P. G. Jerrard, L. Hao, and K. E. Evans, “Experimental investigation into selective laser melting of austenitic and martensitic stainless steel powder mixtures,” *Proceedings of the Institution of Mechanical Engineers, Part B: Journal of Engineering Manufacture*, vol. 223, no. 11, pp. 1409–1416, 2009.

[64] R. Molaei, A. Fatemi, and N. Phan, “Multiaxial fatigue of LB-PBF additive manufactured 17–4 PH stainless steel including the effects of surface roughness and HIP treatment and comparisons with the wrought alloy,” *International Journal of Fatigue*, vol. 137, p. 105646, Aug. 2020.

[65] P. Nezhadfar, K. Anderson-Wedge, S. Daniewicz, N. Phan, S. Shao, and N. Shamsaei, “Improved high cycle fatigue performance of additively manufactured 17-4 PH stainless steel via in-process refining micro-/defect-structure,” *Additive Manufacturing*, vol. 36, p. 101604, Dec. 2020.

[66] A. Poudel, A. Soltani-Tehrani, S. Shao, and N. Shamsaei, “Effect of powder characteristics on tensile properties of additively manufactured 17-4 PH stainless steel,” in *Proceedings of the 32nd Annual International Solid Freeform Fabrication Symposium*, University of Texas at Austin, 2021.

[67] S. Romano, P. Nezhadfar, N. Shamsaei, M. Seifi, and S. Beretta, “High cycle fatigue behavior and life prediction for additively manufactured 17-4 PH stainless steel: Effect of sub-surface porosity and surface roughness,” *Theoretical and Applied Fracture Mechanics*, vol. 106, p. 102477, Apr. 2020.

[68] R. F. Schaller, J. M. Taylor, J. Rodelas, and E. J. Schindelholz, “Corrosion Properties of Powder Bed Fusion Additively Manufactured 17-4 PH Stainless Steel,” *CORROSION*, vol. 73, pp. 796–807, July 2017.

[69] R. Shrestha, N. Shamsaei, M. Seifi, and N. Phan, “An investigation into specimen property to part performance relationships for laser beam powder bed fusion additive manufacturing,” *Additive Manufacturing*, vol. 29, p. 100807, Oct. 2019.

[70] A. Soltani-Tehrani, J. Pegues, and N. Shamsaei, “Fatigue behavior of additively manufactured 17-4 PH stainless steel: The effects of part location and powder re-use,” *Additive Manufacturing*, vol. 36, p. 101398, Dec. 2020.

[71] J. S. Weaver, J. Whiting, V. Tondare, C. Beauchamp, M. Peltz, J. Tarr, T. Q. Phan, and M. A. Donmez, “The effects of particle size distribution on the rheological properties of the powder and the mechanical properties of additively manufactured 17-4 PH stainless steel,” *Additive Manufacturing*, vol. 39, p. 101851, Mar. 2021.

[72] A. Yadollahi, M. Mahmoudi, A. Elwany, H. Doude, L. Bian, and J. C. Newman, “Effects of crack orientation and heat treatment on fatigue-crack-growth behavior of AM 17-4 PH stainless steel,” *Engineering Fracture Mechanics*, vol. 226, p. 106874, Mar. 2020.

[73] S. Tammas-Williams, P. Withers, I. Todd, and P. Prangnell, “Porosity regrowth during heat treatment of hot isostatically pressed additively manufactured titanium components,” *Scripta Materialia*, vol. 122, pp. 72–76, Sept. 2016.

[74] G. Wegmann, R. Gerling, and F. P. Schimansky, “Temperature induced porosity in hot isostatically pressed gamma titanium aluminide alloy powders,” *Acta Materialia*, vol. 51, pp. 741–752, Feb. 2003.

[75] A. Du Plessis and E. Macdonald, “Hot isostatic pressing in metal additive manufacturing: X-ray tomography reveals details of pore closure,” *Additive Manufacturing*, vol. 34, p. 101191, Aug. 2020.

[76] ASTM International, “ASTM E384-17 Standard Test Method for Microindentation Hardness of Materials,” 2017. Place: West Conshohocken, PA.

[77] ASTM International, “ASTM E140-12b Standard Hardness Conversion Tables for Metals Relationship Among Brinell Hardness, Vickers Hardness, Rockwell Hardness, Superficial Hardness, Knoop Hardness, Scleroscope Hardness, and Leeb Hardness,” 2019. Place: West Conshohocken, PA.

[78] R. Shi, L. Chen, Z. Wang, X. S. Yang, L. Qiao, and X. Pang, “Quantitative investigation on deep hydrogen trapping in tempered martensitic steel,” *Journal of Alloys and Compounds*, vol. 854, p. 157218, 2021. Publisher: Elsevier B.V.

Chapter 3

Determination of Effective Hydrogen Diffusivity

3.1 Overview

Examination of diffusion behavior in AM alloys relative to wrought incumbents provides critical context for understanding the effect of additive manufacturing on hydrogen behavior. This study presents a comparison of effective hydrogen diffusivity, calculated using electrochemical permeation and thermal desorption spectroscopy, for wrought and additively manufactured 17-4 PH in peak-aged and over-aged conditions. The fidelity of each method is assessed, and the influence of temperature and charging potential on diffusivity in different conditions is discussed. Results consistently demonstrate that the AM alloys exhibit increased effective hydrogen diffusivity relative to analogous wrought materials in all conditions and experimental analysis methods discussed herein. Comparison between sequential permeation rise transients, as well as observation of break points in diffusivity-temperature relationships with increasing temperature, indicates a significant effect of reversible trapping, particularly in the wrought material.

3.2 Collaborations

Isothermal thermal desorption spectroscopy (TDS) experiments were performed by Emilio Martínez-Pañeda and Alfredo Zafra at Imperial College of London.

3.3 Background

Atomic hydrogen diffusion through a metal is dependent on two factors: the rate of diffusion through interstitial lattice sites, and the effect of microstructural trap sites.[1] The former can be described by the "ideal lattice diffusivity," or D_{L}, which represents the concentration gradient-driven flux of hydrogen via random walk between interstitial sites.[2] This occurs in the tetrahedral sites in body-centered cubic (BCC) metals and in the octahedral sites in face-centered cubic (FCC) metals. As BCC crystal structures have a more open structure than their FCC counterparts with a larger number of available interstitial spaces for hydrogen to occupy, hydrogen diffusion will occur more quickly in body-centered metals such as α-Fe than in face-centered metals.[3] As these interstitial sites are slightly smaller than the diameter of hydrogen, a certain activation energy is required for diffusion of hydrogen; this is often estimated to be around 4-7 kJ/mol.[4, 5]

The other factor governing hydrogen diffusion is the extent of trapping at microstructural features such as impurities, dislocations, grain boundaries, and other defects. The role of microstructural trapping on diffusivity depends on binding energy of a screened proton as well as the "depth" of the trap, or the energy required for hydrogen to de-trap.[6, 7] "Reversible" traps, which have low trapping strength in comparison to the depth of the energy well, allow for interaction between the trapped hydrogen and the hydrogen in interstitial lattice sites in order to maintain equilibrium. This increases the effective energy required for diffusion, permanently decreasing hydrogen diffusivity through the material to a trap-affected “effective” diffusivity value D_{eff}. Additionally, these reversible trap sites can act as a supply or reservoir for mobile hydrogen. When adjacent to regions with lower chemical potential, such as triaxial stress fields ahead of crack tips, diffusion from these reservoirs towards these regions is facilitated. This repartitioning may exacerbate hydrogen embrittlement effects.[8]

”Irreversible” trapping sites, which have high trapping strength compared to energy well depth, do not allow for any interaction. Therefore, irreversible sites reduce the effective diffusivity of the material only until hydrogen concentration is sufficient to fill the ”saturable” irreversible traps, at which point the diffusivity ideally reverts to D_{L}. Both reversible and irreversible traps can reduce hydrogen diffusion through the bulk lattice by introducing additional impediments to interstitial diffusion, but once irreversible traps are filled, they no longer impede hydrogen travel.[8, 9]

Effective diffusivity is influenced both by trap binding energy and trap density.[6] Low-energy reversible traps may still have a large impact on effective diffusivity if trap density is very high. The reverse is also true; a small number of traps may still influence diffusion if binding energy is large. This can be described by Oriani’s trapping model, and is further explored in Section 5.6.7.

As the microstructural features that act as traps (such as grain boundaries, inclusions, dislocations, and other defects) often increase material strength by impeding dislocation motion, there has been an observable correlation between high tensile strength and a large degree of hydrogen trapping.[10–13] The effective diffusivity value is also influenced by hydrogen “fast paths” or “short circuit paths,” microstructural features such as grain boundaries and dislocations that allow hydrogen to diffuse faster than it would through interstitial random-jump migration in an ideal lattice.[14–17] In particular, there is general disagreement in literature on the impact of grain boundaries on diffusion; several studies attribute an increase in D_{eff} to grain boundaries providing fast diffusion paths,[16, 18–29] whereas other publications report the trapping effects of grain boundaries cause a decrease in D_{eff}.[14, 30–36] This is also dependent on grain boundary type, with fast diffusion traditionally speculated to occur along a well-connected network of high-angle grain boundaries, while their low-angle or special counterparts impede diffusion.[37]

A summary of published effective diffusivity values for traditionally manufactured 17-4 PH in different heat treatment conditions is shown in Table 3.1. Each study used electrochemical permeation to determine diffusivity through lag time analysis. Typical heat treatments for wrought 17-4 PH include a solution annealing (SA) step followed by subsequent peak-aging (PA) or over-aging (OA). These diffusivity values are several orders of magnitude slower than those typically reported for BCC iron,[38] which can be used as an approximation for ideal diffusion in the nearly-identical BCT lattice in 17-4 PH due to its low carbon content. This relatively slow diffusivity can be attributed to substantial microstructural trapping. Chiang et al.[39] observed a very slight decrease in diffusivity in specimens that had been solution annealed and aged, compared to those that had only been solution annealed; this was attributed to increased reversible trapping due to the formation of coherent Cu-rich precipitates in the aging step. Tsay et al.[40] also observed a similar trend of decreased diffusivity upon aging, and also found that diffusivity decreases even further upon over-aging due to increased trapping.

Table 3.1: Literature effective diffusivity values for 17-4 PH stainless steel. The post-processing conditions are described using “SA” for solution annealed, “PA” for peak-aged, and “OA” for over-aged. Each study used electrochemical permeation in conjunction with lag time analysis to determine diffusivity.

Heat Treatment	**Method**	D_{eff} **(23°C) [m^2/s]**	**Reference**
SA	Permeation	4.60×10^{-9}	[39]
SA + PA	Permeation	2.84×10^{-9}	[39]
SA	Permeation	2.74×10^{-8}	[40]
SA + PA	Permeation	9.70×10^{-9}	[40]
SA + OA	Permeation	8.10×10^{-9}	[40]
SA + PA	Permeation	2.30×10^{-9}	[41]

In the past few years, initial explorations have been conducted into quantifying diffusivity of AM 17-4 PH. Alnajjar et al.[41] employed electrochemical permeation to examine the effective diffusivity of AM 17-4 PH manufactured using SLM and then peak-aged without a HIP or solution annealing process, leading to a ferritic microstructure; it was found that the AM 17-4 PH had slightly increased diffusivity compared to its wrought counterpart, though both were within the same order of magnitude (approximately 10^{-8} cm^2/s). The increase in diffusivity in the AM specimen was attributed to decreased reversible trapping due to coarser grains. Additionally, Guennouni et al.[42] used a finite element model to evaluate hydrogen concentration profiles for wrought and L-PBF 17-4 PH after solution annealing and peak-aging, concluding that the AM specimens likely have a diffusivity on the order of 10^{-8} cm^2/s, while hydrogen diffusion through the wrought material is an order of magnitude slower. Guennouni et al. speculated that this increase was due to the finer martensite lath sizes and a higher amount of reversed austenite leading to more austenite/martensite interfaces in the AM specimen; however, it should be noted that austenite has an FCC crystal structure and is traditionally associated with slower diffusion.[3] Additionally, the finer martensite lath sizes are likely to increase reversible trap density and slow diffusion. No experimental examination has been performed to quantify the effective diffusivity of solution-annealed or matched-strength AM 17-4 PH.

3.4 Methods

3.4.1 Permeation Analysis

Effective hydrogen diffusivity can be determined through Devanathan-Stachurski-type electrochemical permeation, as described by ASTM Standard G148-97.[43, 44] The specimen functions as a metal membrane between a charging cell, in which a cathodic current is applied to cause hydrogen charging; and an extraction cell, which is anodically polarized to enable hydrogen extraction through its oxidation without interference from other chemical reactions. The metal membrane must have parallel opposing surfaces and a cross-section larger than the microstructural repeat distance to ensure that the permeation behavior of the specimen reflects that of the bulk material. This combination of H charging and extraction allows for the quantification of hydrogen permeation across the specimen through the measurement of permeation current, or the current generated by the oxidation of hydrogen atoms, over time.

When a sufficiently large overpotential in relation to the hydrogen evolution reaction (HER) is applied to the charging cell, hydrogen permeation will increase over time in a *rise transient* until steady state is achieved. When the charging current is decreased, the rate of hydrogen permeation will also decrease until steady state is reached, resulting in a *decay transient*.

These transients can be analyzed to determine the effective diffusivity D_{eff} of a material assuming bulk diffusion control. McBreen et al.[45] derived the following solutions for rise and decay transients based on Fick's first law:

$$\frac{i - i_0}{i_\infty - i_0} = \frac{2L}{\sqrt{\pi D_{\text{eff}}}} \sum_{n=0}^{\infty} \exp\left[-\frac{(2n+1)^2 L^2}{4 D_{\text{eff}} t}\right] \qquad \text{(rise transient)} \tag{3.1}$$

$$\frac{i - i_\infty}{i_0 - i_\infty} = 1 - \frac{2L}{\sqrt{\pi D_{\text{eff}}}} \sum_{n=0}^{\infty} \exp\left[-\frac{(2n+1)^2 L^2}{4 D_{\text{eff}} t}\right] \qquad \text{(decay transient)} \tag{3.2}$$

In these models, i is the measured current density at time t, i_0 is the initial steady-state current density at $t = 0$, i_∞ is the final steady-state current density, and L is the specimen thickness. The rise transient solution is based on the following assumptions:

1. $C_{t=0} = 0$: no mobile H is present inside the specimen immediately before permeation.
2. $C_{\text{charging}} = C_{\text{o}}$: the H concentration on the charging side of the specimen is fixed at a constant value C_{o}, which is a function of the applied H overpotential or cathodic potential.
3. $C_{\text{extraction}} = 0$: the H concentration on the extraction side of the specimen is fixed at 0.

The decay transient solution is based on the following assumptions:

1. $J_{t=0} = J_\text{o}$: the hydrogen flux across the specimen is constant immediately before permeation.
2. $C_\text{charging} = 0$: the H concentration on the charging side of the specimen is fixed at 0.
3. $C_\text{extraction} = 0$: the H concentration on the extraction side of the specimen is fixed at 0.

As curve fitting using these models can be arduous, a number of simplifications have been proposed in literature. Zakroczymski outlined a simplified form of Equations 3.1 and 3.2 using a first-term approximation of each transient, as described for the rise transient in Equation 3.3 and for the decay transient in Equation 3.4:[46–48]

$$\log\left[(i - i_1)t^{0.5}\right] = C - \frac{L^2 \log e}{4D_\text{eff}} \cdot \frac{1}{t} \qquad \text{(rise transient)} \tag{3.3}$$

$$\log\left[(i_2 - i)t^{0.5}\right] = C - \frac{L^2 \log e}{4D_\text{eff}} \cdot \frac{1}{t} \qquad \text{(decay transient)} \tag{3.4}$$

in which i_1 and i_2 are the steady-state permeation current densities initially present in the rise and decay transients, C is a constant, and L is specimen thickness. Effective diffusivity can be calculated by treating Equations 3.3 and 3.4 as straight-line equations of the form $y = mx + b$ describing the linear regions of the rise and decay transients, respectively. When $\log\left[(i - i_1)t^{0.5}\right]$ (rise transient) or $\log\left[(i_2 - i)t^{0.5}\right]$ (decay transient) is plotted versus $1/t$, the slope m of the linear plot can be used to determine the effective diffusivity:[46]

$$m = -\frac{L^2 \log e}{4D_\text{eff}}. \tag{3.5}$$

In the majority of literature, diffusivity is calculated using the "lag time" or "breakthrough time" method, where additional simplifications are made to allow the calculation of diffusivity from the current density at either of two single time values as described in ASTM G148-97.[44] Equation 3.6 shows the method outlined to calculate diffusivity from the rise transient, derived from the relation of classical time lag to diffusion:[43]

$$D_{\text{eff}} = L^2/(6t_{\text{lag}}), \tag{3.6}$$

in which t_{lag} (s) is the time at which the permeation current density is 63% of the steady-state current density. The breakthrough time t_{bt}, or the time at which the permeation current density is 10% of the steady-state current density, can also be used to calculate diffusivity:[44]

$$D_{\text{eff}} = L^2/(15.3t_{\text{bt}}). \tag{3.7}$$

However, since these two methods are both based on single time values, they are more susceptible to noise or other variations in the data. For this reason, it is often useful to use the breakthrough or lag time methods in conjunction with more rigorous analysis methods such as curve fitting.

The initial permeation experiment for each specimen reflects H interactions with irreversible and reversible trap states as well as lattice and fast path diffusion. Subsequent permeation experiments on the same specimen often return increased effective diffusivity values, reflecting the occupation of irreversible trap states. Due to this phenomenon, sequential permeation runs on each specimen are useful in evaluating the degree and influence of irreversible trap states on H diffusion in a material.[43, 44] Figure 3.1 provides a summary of the different methods of sequential permeation experiments as well as examples of experimental transients from wrought 17-4 PH foil obtained through each method.

Electrochemical permeation (EP) experiments to quantify D_{eff} were performed on square specimens (thickness of 0.4-0.7 mm) using the Devanathan-Stachurski method per ASTM G148-97.[43, 44] The thickness of the foil was chosen based on average grain size of the specimen in order to ensure diffusion control. As the 0.4-0.7 mm thickness is, at minimum, 36 times the average grain size (which ranges from 3-7 microns in weighted

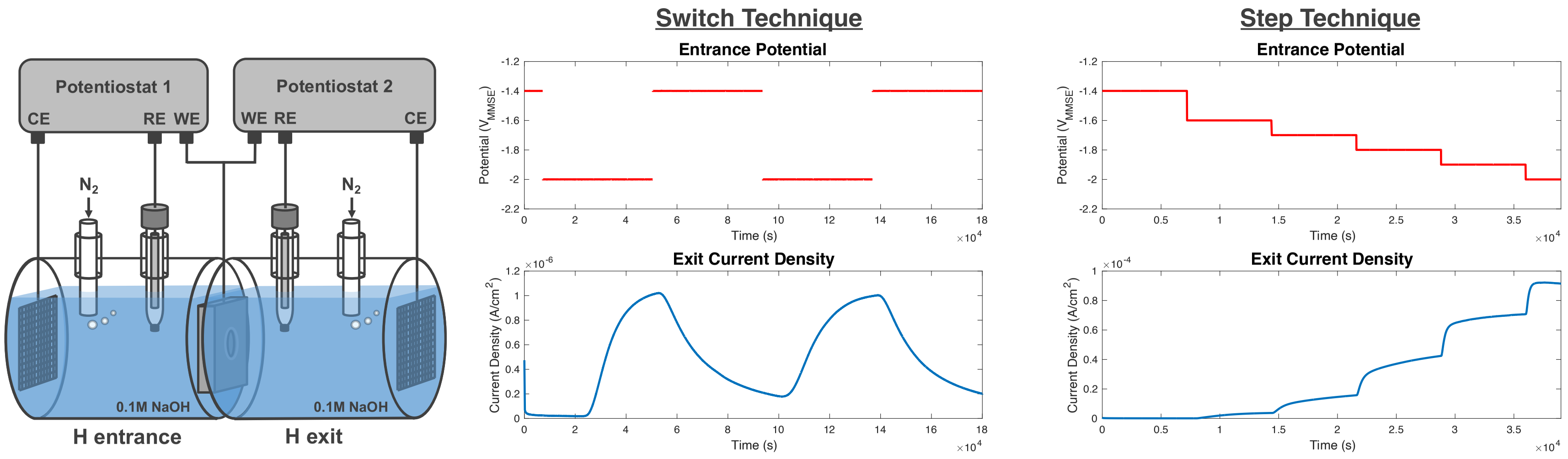

Figure 3.1: A summary of charging potential (top) and examples of exit current density data (bottom) for each of the different permeation sequences: (a) the “switch” technique, in which charging potential is consistently switched between two constant values to cause subsequent rise and decay transients; and (b) the “step” technique, in which charging overpotential is increased stepwise to cause sequential rise transients with increasing current densities. A schematic of the experimental setup is included on the left.

diameter measurements, and 6-11 microns in unweighted measurements), the permeation experiments can adequately account for grain boundary trapping. Additionally, as Cu-rich precipitates have a count density around 10^{-5} precipitates/nm^3, this thickness is sufficient to account for the trapping effects of 10^{14} precipitates for every square centimeter of the material. This allows for measured diffusivity to reflect a trap-affected bulk diffusion process in 17-4 PH, a heavily trap-rich quenched and tempered alloy.

Both sides of the EP experiment used 0.1 M NaOH solution, a Pt-coated Nb mesh as the counter electrode, and a Hg/HgSO$_4$ (MMSE) reference electrode. Each EP experiment involved a rise transient immediately followed by a decay transient. For the rise transient, the reduction side of the EP experiment was step polarized to -2.0 $\mathrm{V_{MMSE}}$, while the oxidation side was held at -0.4 $\mathrm{V_{MMSE}}$; the same oxidation side conditions were employed for the decay experiment, but the applied potential on the reduction side was increased to -1.4 $\mathrm{V_{MMSE}}$. In order to examine the effects of reversible trapping on diffusivity, this process was repeated to produce a second rise and decay transient sequence. D_{eff} was then calculated from the rise transient using three methods: curve fitting, lag time, and breakthrough time.[43, 44, 49] The decay transient was analyzed in further detail using the curve fitting method. A schematic illustrating these analysis approaches and relevant equations is shown in Figure 3.2. Multiple calculation methods were employed to eliminate any bias from the commonly used single-time methods.

In order to gain insight into the effects of temperature and charging potential on permeation in 17-4 PH, additional permeation experiments were conducted on as-received 0.076 mm-thick 17-4 PH foils. The foils were provided by McMaster-Carr in the annealed condition in accordance with ASTM A693[50] and were cut into specimens approximately 3 cm by 3 cm in area. The experimental setup is the same as previously described, with 0.1M NaOH solution, Pt-coated Nb mesh counter electrodes, and Hg/HgSO$_4$ (MMSE) reference electrodes on both sides of the permeation experimental setup. The permeation setup was placed inside a temperature-controlled chamber, and sequential rise and decay

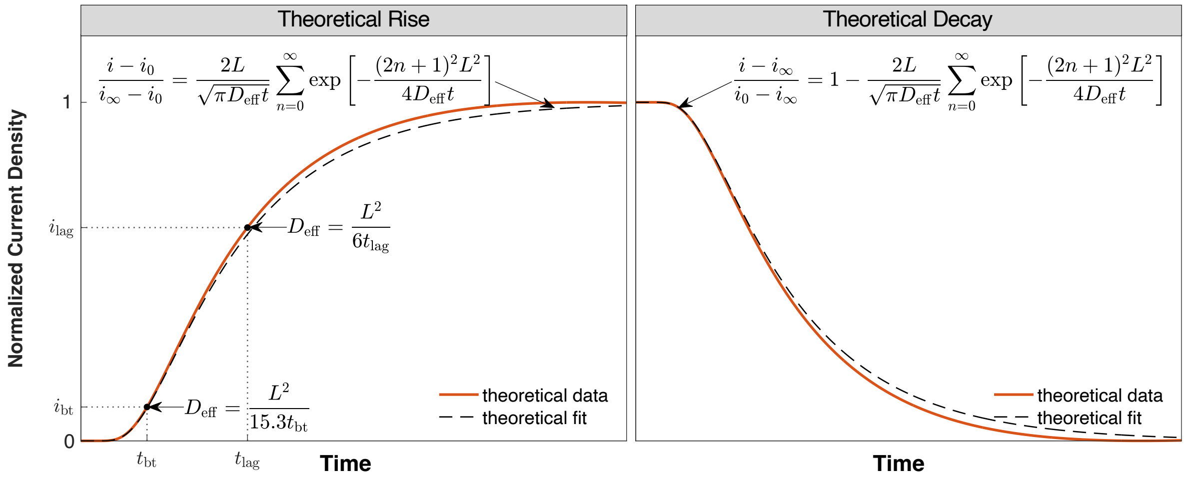

Figure 3.2: An example of the analysis methods used to determine effective diffusivity from theoretical rise and decay transients. The rise transient is analyzed through the following (from top equation to bottom equation): curve fitting, lag time, and breakthrough time. The decay transient is analyzed through curve fitting.

transients were performed and analyzed as previously described.

Another approximately 3 cm by 3 cm specimen was excised from the same 0.076 mm-thick foil to examine the effects of charging potential on diffusivity. The specimen was then used in the same electrochemical permeation setup, and underwent step-wise charging. The specimen was polarized to -0.4 V_{MMSE} on the oxidation side and underwent an initial 30-minute polarization to -1.4 V_{MMSE} on the reduction size for background, after which the applied potential on the reduction side was held for sequential 30-minute periods at -1.6, -1.7, -1.8, -1.9, and -2.0 V_{MMSE} as depicted in Figure 3.1. Each rise transient was analyzed as described in Figure 3.2.

3.4.2 Isothermal TDS

Hydrogen diffusion through a metal can be observed using thermal desorption spectroscopy (TDS), which involves controlled temperature programming in an ultrahigh vacuum environment to induce thermal desorption of adsorbed hydrogen in lattice and reversible trap sites.[51] When a pre-charged metal is held at a constant elevated temperature in a vacuum, bulk diffusion of hydrogen atoms is induced by the increase in thermal energy as

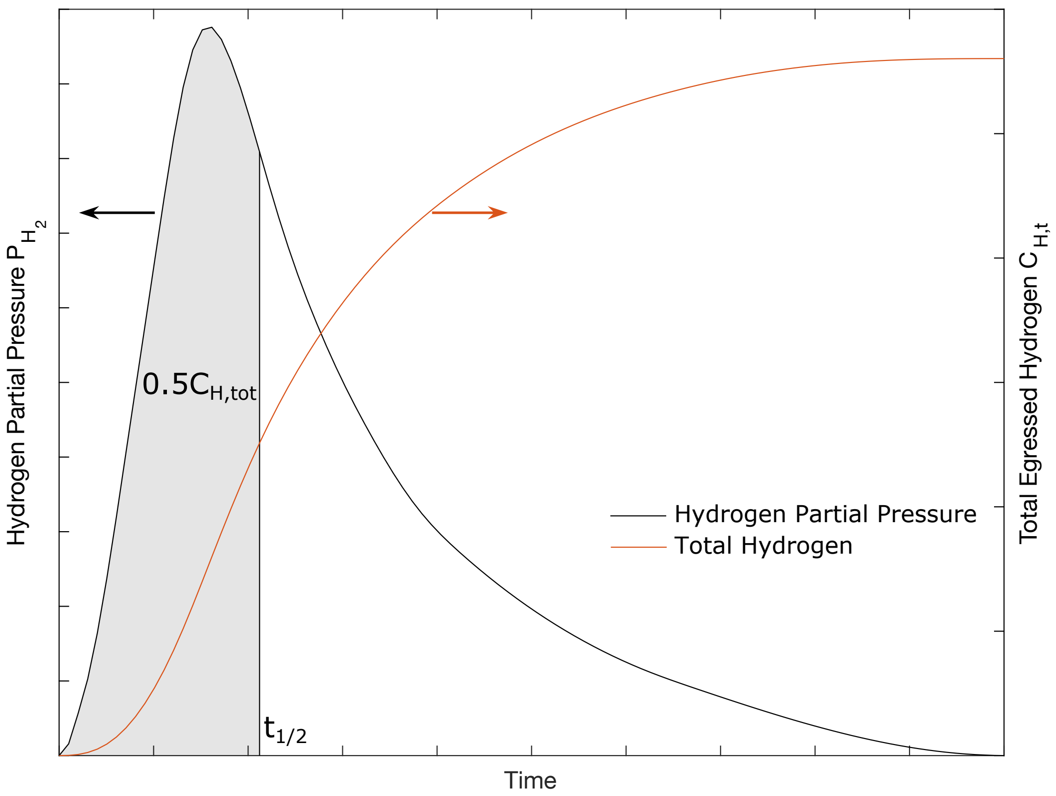

Figure 3.3: Theoretical hydrogen pressure and total hydrogen concentration for isothermal TDS.[8] The half-time $t_{1/2}$ is depicted.

well as the large concentration gradient between the sample interior and the surface, where H concentration goes to zero. This allows for characterization of the effective hydrogen diffusivity of the bulk material.[8, 52] Additionally, if the temperatures are sufficiently high that the effects of re-trapping are minimized, the effective diffusivity of hydrogen in the bulk material can be assumed to approach ideal lattice diffusivity as temperature increases.[9]

Isothermal TDS employs a quadrupole mass spectrometer to measure hydrogen partial pressure, providing a hydrogen pressure versus time curve at a constant temperature. The quantity of total hydrogen that egresses from the sample can be determined by integrating a fit of the curve or by using a trapezoidal approximation to estimate the area under the curve. The half-time of hydrogen egression ($t_{1/2}$), or the time at which half the hydrogen has egressed from the material, can be determined using this integration or approximation.

Figure 3.3 shows a theoretical example of half-time analysis in isothermal TDS data.[8]

By assuming that hydrogen diffusion coefficient is independent of hydrogen concentration, Iacoviello et al.[52] developed a model to calculate effective hydrogen diffusivity using the half-time of hydrogen egression ($t_{1/2}$). This approach is derived from a solution of Fick's equation for flat specimens, and can be simplified to Equation 3.8:

$$D_{\text{eff}} = 0.0492 L^2 / t_{1/2}, \tag{3.8}$$

in which L is sample thickness, and D_{eff} is the effective diffusivity coefficient for hydrogen in the material, taking into account the effects of trap sites in equilibrium with the lattice.

Once each high-temperature effective diffusivity value has been calculated, the room-temperature effective diffusivity value can be determined. The temperature dependence of effective diffusivity takes the form of an Arrhenius relationship:[8]

$$D_{\text{eff}} = D_{0,\text{eff}} \exp\left(-E_{\text{act}}/RT\right), \tag{3.9}$$

in which $D_{0,\text{eff}}$ is a pre-exponential factor, E_{act} is the activation temperature of bulk H diffusion, R is the gas constant, and T is absolute temperature. When multiple isothermal TDS experiments are performed at different temperatures, the effective diffusivity of hydrogen in the bulk material at room temperature can be determined using linear regression of a plot comparing $\ln D_{\text{eff}}$ to $1/T$, as seen in Figure 3.4. The activation energy of bulk H diffusion, E_{act}, can also be calculated using Equation 3.9 and can provide insight on diffusion behavior through the lattice.

As this model is derived from Fick's first law, there is an assumption of one-dimensional diffusion; therefore, this approach is valid for specimens with thickness dimensions significantly smaller than height and width dimensions. In addition, the model described by Equation 3.9 assumes that desorption is diffusion-limited; this assumption can be

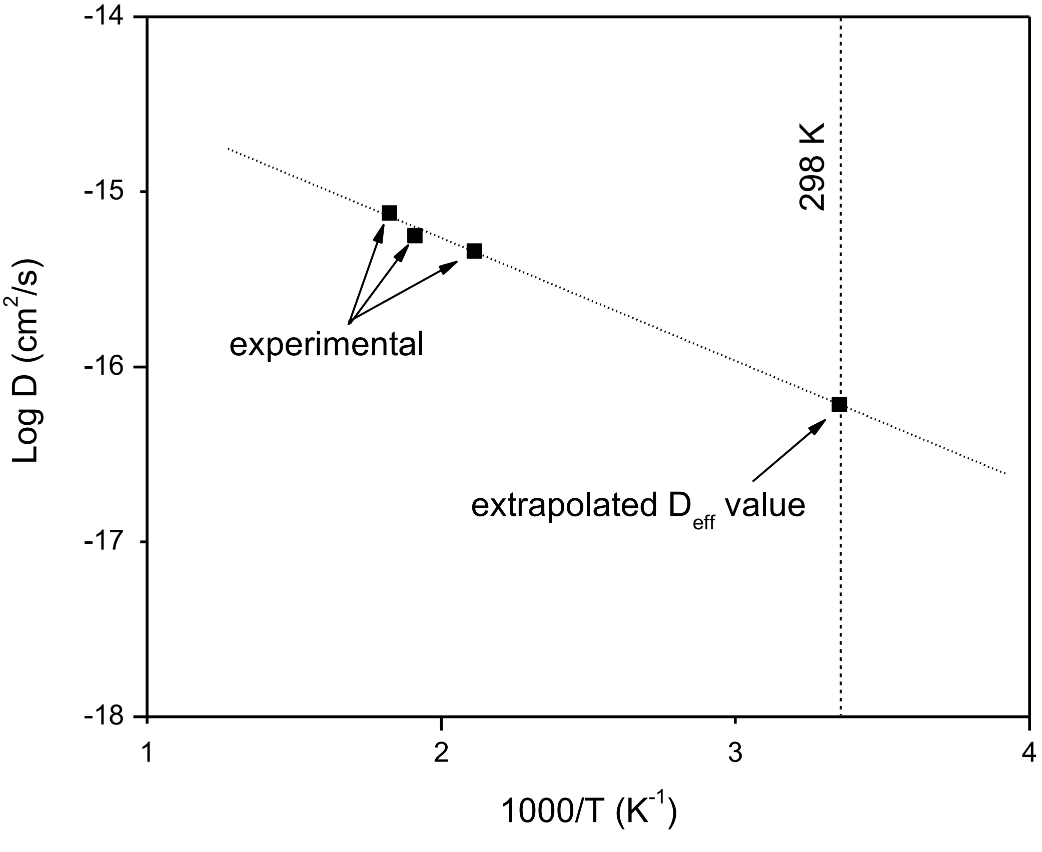

Figure 3.4: A theoretical schematic of the extrapolation method of room temperature effective diffusivity from high-temperature diffusivity values using Equation 3.9.

confirmed using Kissinger's model as detailed in Section 5.4.1.

Isothermal TDS experiments were performed in collaboration with Emilio Martínez-Pañeda and Alfredo Zafra at Imperial College of London. 0.5-mm thick specimens were charged at -1.1 V_{SCE} in deaerated 0.6M NaCl at 55°C for 24 hours to achieve saturation. After a post-charging rest period of 25 minutes to eliminate surface hydrogen, specimens were held at 22, 50, 75, and 100°C in a thermal desorption chamber until the desorption rate approached zero; the necessary time to desorb the majority of the hydrogen varied depending on temperature, from 3 hours at 100°C to around 40 hours at 22°C. Isothermal TDS results were then analyzed using Equation 3.8, and the Arrhenius-type temperature dependence was calculated.

3.5 Results

3.5.1 Bulk Effective Diffusivity

An example of the charging overpotential sequence and corresponding changes in current density can be seen in Figure 3.5, which presents rise and decay transients for the AM HIP+SA+OA specimen. It is clear that the charging overpotential is sufficiently large to induce the desired permeation behavior.

The thickness-normalized initial hydrogen flux rise and decay transients for each evaluated material condition are shown in Figure 3.6 (solid lines), along with the curve fits (dashed lines) calculated as described in Figure 3.2. These data demonstrate consistently more rapid permeation in the AM materials relative to comparable wrought alloys, suggesting an increased D_{eff}. Interestingly, the permeation behavior also depends on the post-build heat treatment, as the HIP+SA+PA AM condition reached steady state permeation more slowly than the HIP+PA AM material. These trends remained consistent through sequential rise and decay transients.

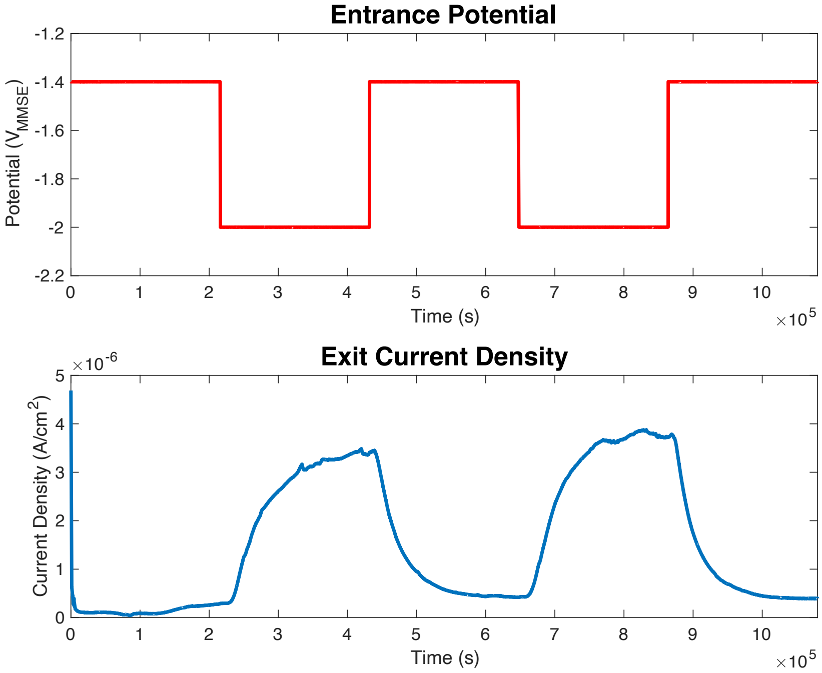

Figure 3.5: Electrochemical permeation charging potential (top) and measured exit current density (bottom) for AM HIP+SA+OA, showing rise and decay transients corresponding to large and small overpotentials, respectively.

The calculated D_{eff} for each transient/material combination using the lag time, breakthrough time, and curve fit methods (Figure 3.2) are shown in Figure 3.7 and Table 3.2. For a given material, the lag time approach generally yields increased D_{eff} values compared to the breakthrough time method; the lag time and curve fit analysis results are similar, consistent with trends reported in previous literature.[53, 54] All four employed analysis methods result in the same AM vs. wrought trends. Specifically, the AM diffusivity is increased by an average of ∼3-fold for the HIP+SA+PA and HIP+SA+OA conditions compared to their wrought counterparts, and an average of ∼5-fold for the HIP+PA condition. Literature-reported D_{eff} values[39–41, 55] for wrought 17-4 PH fall between 2.84-9.70×10^{-9} cm^2/s for both peak-aged and over-aged conditions, which is in good agreement with the D_{eff} values determined for wrought 17-4 PH in the current study. It should be noted that only one permeation sequence was performed per condition except AM HIP+SA+OA, limiting statistical analysis of the results. However, large test matrices

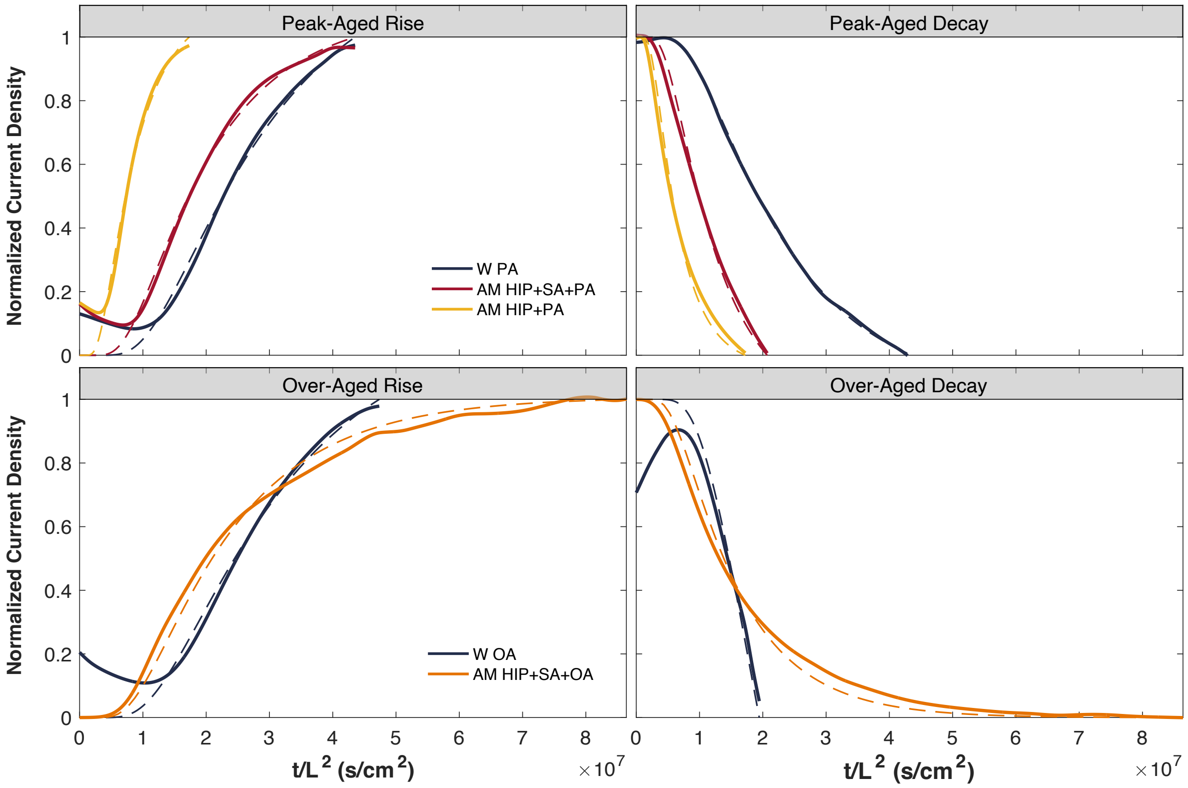

Figure 3.6: Normalized hydrogen permeation rise and decay transients for wrought (W) and additively manufactured (AM) 17-4 PH specimens in the peak-aged (top) and over-aged (bottom) conditions. Solid lines correspond to the measured permeation data, while the dashed lines represent the curve fit results. The comparatively rapid permeation behavior in AM is reproduced in both rise and decay transients for each heat treatment.

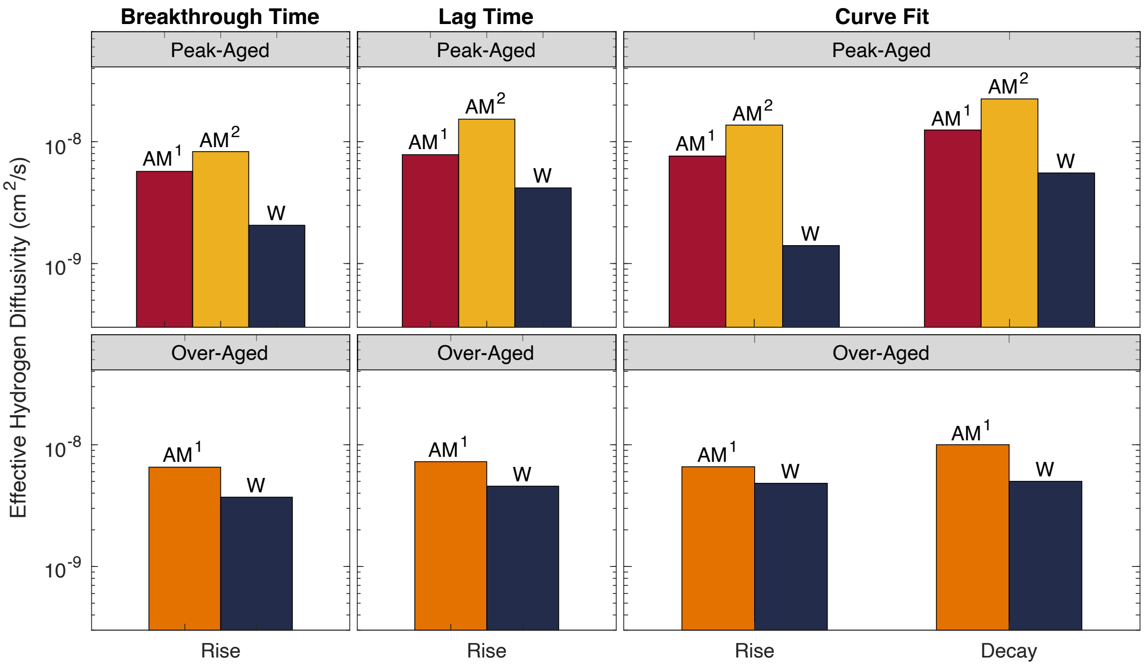

Figure 3.7: Effective diffusivity values for wrought and AM 17-4 PH across heat treatment conditions, calculated using the breakthrough time, lag time, and curve fit methods. AM^1 represents the HIP+SA conditions and AM^2 represents the non-solution annealed HIP conditions. Breakthrough and lag time methods were applied to the initial rise transient; the curve fit method was used for both initial rise and decay transients.

conducted independently on iron and steel alloys by Zafra,[56] Svoboda,[57] and Zhang[58] indicate that the error in calculated diffusivities from electrochemical permeation is between 8-14%. Therefore, given that the AM and wrought best fit effective diffusivities differ by more than 50%, these prior literature reports strongly suggest that the observed differences in Figure 3.7 are not attributable to experimental scatter.

The isothermal TDS desorption peaks for each specimen condition and temperature are shown in Figure 3.8. It is apparent that the wrought specimens have a higher global concentration of hydrogen based on increased peak height and tail width. The effective diffusivity values calculated at each temperature are displayed in Figure 3.9, and the room temperature effective diffusivity obtained from TDS is compared to the values calculated through electrochemical permeation in Table 3.3. Both methods indicate a consistent increase in effective hydrogen diffusivity in the AM specimens compared to

Table 3.2: Summary of all permeation data for each 17-4 PH specimen, with effective diffusivity calculated using breakthrough (BT) time, lag time, and curve fitting methods. Initial rise and decay are labeled “R/D 1”, and subsequent rise and decays are labeled “R/D 2”. Charging and extraction potential vs. Hg/HgSO$_4$ reference electrode is also labeled.

Specimen	**R/D**	**R/D #**	**Pot. ($\mathbf{V_{MMSE}}$)**	D_{eff} **(23°C) [cm^2/s]**		
				BT	**Lag**	**Fit**
W Peak-Aged	Rise	1	-2.0	1.50×10^{-9}	3.83×10^{-9}	1.50×10^{-9}
	Decay	1	-1.4	-	-	3.37×10^{-9}
	Rise	2	-2.0	4.96×10^{-9}	5.14×10^{-9}	6.95×10^{-9}
	Decay	2	-1.4	-	-	4.18×10^{-9}
AM HIP+SA+PA	Rise	1	-2.0	1.57×10^{-8}	7.57×10^{-9}	7.63×10^{-9}
	Decay	1	-1.4	-	-	1.25×10^{-8}
AM HIP+PA	Rise	1	-2.0	8.27×10^{-9}	1.50×10^{-8}	1.34×10^{-8}
	Decay	1	-1.4	-	-	2.25×10^{-8}
	Rise	2	-2.0	2.19×10^{-8}	1.78×10^{-8}	1.78×10^{-8}
	Decay	2	-1.4	-	-	2.36×10^{-8}
W Over-Aged	Rise	1	-2.0	3.71×10^{-9}	4.57×10^{-9}	4.82×10^{-9}
	Rise	1	-2.0	3.83×10^{-9}	5.23×10^{-9}	8.64×10^{-9}
	Decay	1	-1.4	-	-	5.00×10^{-9}
	Rise	2	-2.0	3.26×10^{-9}	4.54×10^{-9}	4.33×10^{-9}
AM HIP+SA+OA (XZ)	Rise	1	-2.0	9.87×10^{-9}	1.94×10^{-8}	8.34×10^{-9}
	Decay	1	-1.4	-	-	1.14×10^{-8}
	Rise	2	-2.0	1.42×10^{-8}	2.22×10^{-8}	1.45×10^{-8}
	Decay	2	-1.4	-	-	1.76×10^{-8}
AM HIP+SA+OA (XY)	Rise	1	-2.0	6.54×10^{-9}	7.26×10^{-9}	6.59×10^{-9}
	Decay	1	-1.4	-	-	1.00×10^{-8}
	Rise	2	-2.0	7.04×10^{-9}	7.27×10^{-9}	7.10×10^{-9}
	Decay	2	-1.4	-	-	1.03×10^{-8}

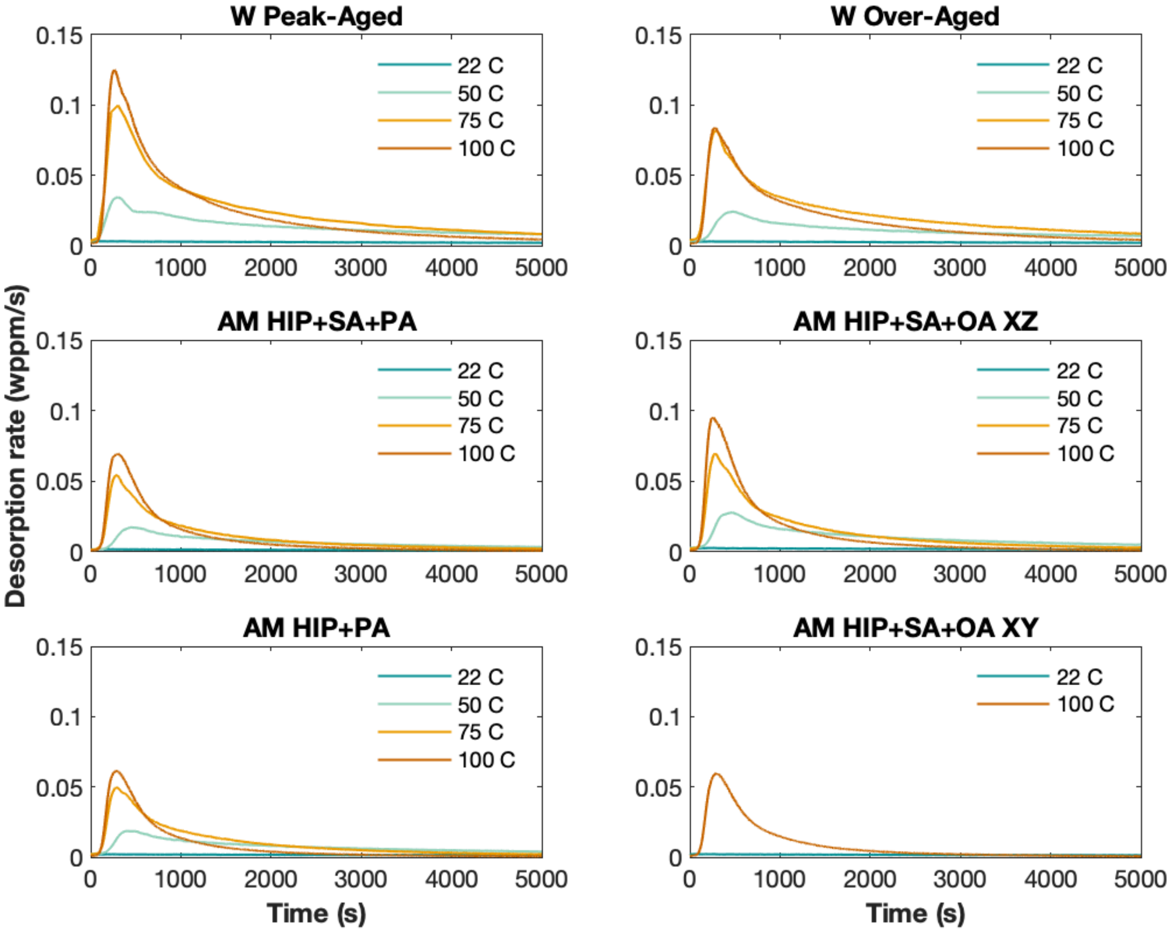

Figure 3.8: Isothermal TDS desorption rate versus time data for peak-aged (left) and over-aged (right) specimens, at temperatures between 22 and 100°C.

their wrought counterparts in both conditions; however, the difference between AM and wrought specimens is less dramatic in the TDS results than in the permeation results. Additionally, the diffusivity values calculated for the XY and XZ direction of the AM HIP+SA+OA specimens are extremely similar, indicating isotropic diffusion behavior.

The temperature dependence of diffusivity from isothermal TDS can be modeled using an Arrhenius-type relationship, as described in Equation 9. From this relationship, activation energy of diffusion E_{act} and pre-exponential material constant D_0 can be calculated, as seen in Table 3.4. As there is a break point in the fit around 80°C, the activation energy and pre-exponential constant including and excluding data beyond that break point (i.e. at 100°C) are presented. In both cases, the pre-exponential constant and

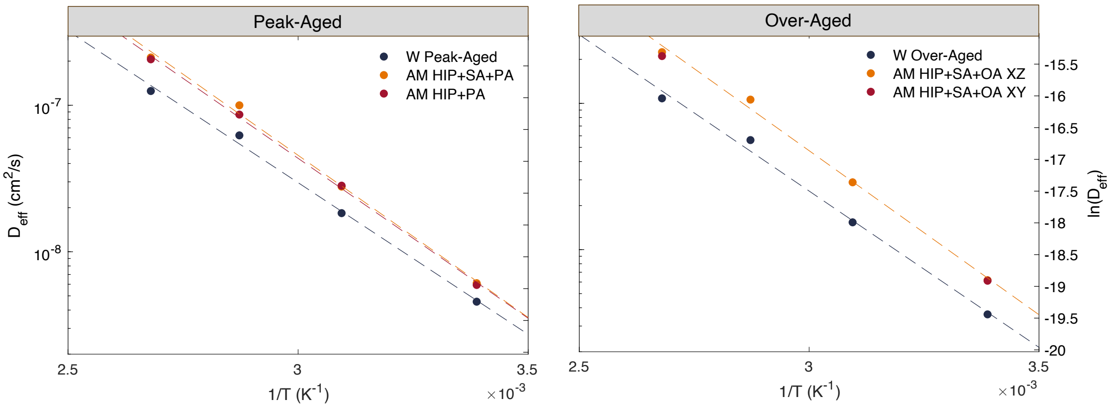

Figure 3.9: Effective diffusivity values calculated from isothermal TDS versus temperature for peak-aged (left) and over-aged (right) specimens. Linear fits are denoted by dashed lines.

Table 3.3: Comparison between diffusivity calculated using electrochemical permeation and through isothermal TDS.

Specimen	**Build**	D_{eff} (23°C) [cm^2/s]		
		Perm (Rise 1)	**Perm (Decay 1)**	**TDS**
Peak-Aged	Wrought	1.40×10^{-9}	5.54×10^{-9}	4.56×10^{-9}
	AM	7.63×10^{-9}	1.25×10^{-8}	6.10×10^{-9}
	AM (non-SA)	1.34×10^{-8}	2.25×10^{-8}	5.93×10^{-9}
Over-Aged	Wrought	4.82×10^{-9}	5.00×10^{-9}	3.61×10^{-9}
	AM	6.59×10^{-9}	1.00×10^{-8}	6.12×10^{-9}

Table 3.4: Activation energy and D_0 values for AM and wrought 17-4 PH based on Arrhenius-type evaluation of the TDS data, both including and excluding the data at 100°C to account for high-temperature trapping.

Specimen	**E_{act} (kJ/mol)**		**D_0 (cm^2/s)**	
	Incl. 100°C	**Excl. 100°C**	**Incl. 100°C**	**Excl. 100°C**
W PA	39.64	41.98	4.82×10^{-2}	1.20×10^{-1}
AM HIP+SA+PA	42.37	44.94	1.99×10^{-1}	5.39×10^{-1}
AM HIP+PA	41.78	43.22	1.53×10^{-1}	2.67×10^{-1}
W OA	40.93	44.08	6.51×10^{-2}	2.21×10^{-1}
AM HIP+SA+OA	42.95	45.72	2.56×10^{-1}	7.47×10^{-1}

the activation energy for diffusion through AM specimens are slightly higher compared to the wrought.

3.5.2 Charging Potential Dependence

The sequence of permeation rise transients resulting from step-wise charging potential increases in the 0.076 mm-thick wrought 17-4 PH foils is shown in Figure 3.10. There is a clear increase in current density with more negative charging potentials, as well a steeper and larger transient. This can be contrasted with the step-wise sequence for the 0.58 mm-thick AM 17-4 PH in the HIP+SA+OA condition shown in Figure 3.11.

Figure 3.12 shows the effective diffusivity values for the wrought 17-4 PH foil and the AM HIP+SA+OA specimen at each potential, calculated using the curve fit method. If the charging potential and the log value of the correlating effective diffusivity (calculated using the curve fit method) are assumed to be linearly related, the dependence of effective diffusivity on charging overpotential η_{ch} can be calculated using the method described by Thomas et al.[8] for the foil:

$$\log(D_{\text{eff}}) = -2.73\eta_{\text{ch}} - 9.2, \tag{3.10}$$

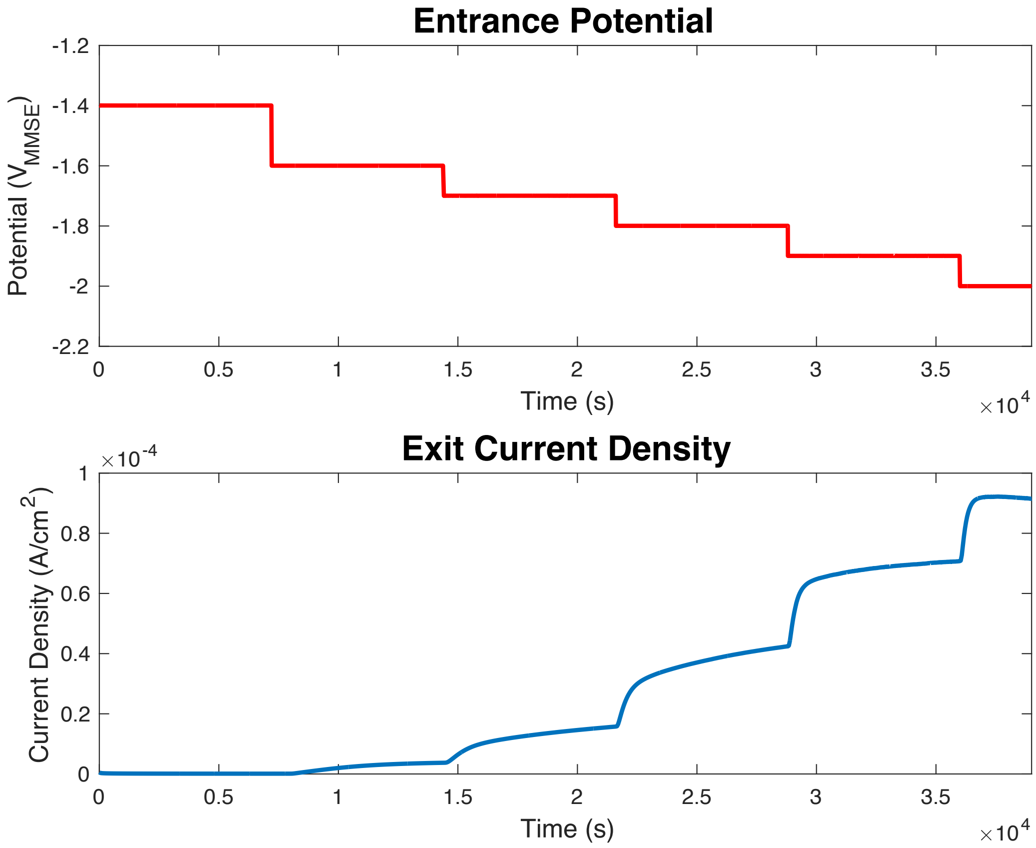

Figure 3.10: Entrance potential (top) and permeation curves (bottom) for step-wise permeation of the 0.076 mm thick wrought 17-4 PH foil in the as-received condition.

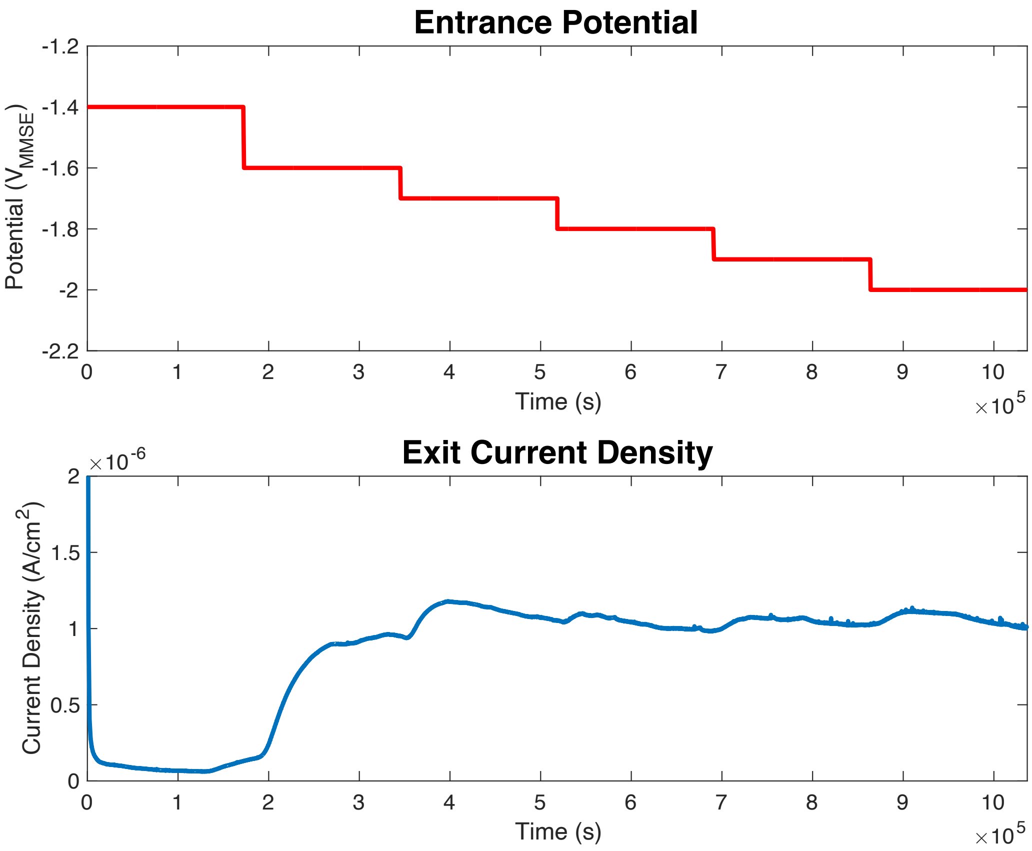

Figure 3.11: Entrance potential (top) and permeation curves (bottom) for step-wise permeation of the 0.58 mm thick AM HIP+SA+OA 17-4 PH specimen.

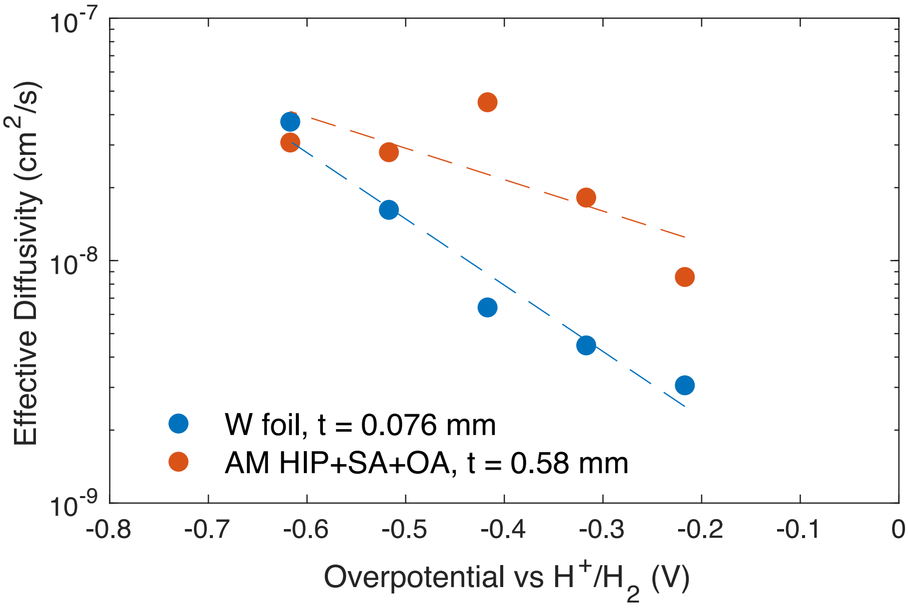

Figure 3.12: Effective diffusivity versus overpotential for wrought 17-4 PH foil of thickness 0.076 mm and AM HIP+SA+OA with thickness 0.58 mm.

and for the thicker AM HIP+SA+OA specimen:

$$\log(D_{\text{eff}}) = -1.30\eta_{\text{ch}} - 8.2. \tag{3.11}$$

Correlation between hydrogen diffusivity and charging potential has been observed in literature.[8, 59] However, the discrepancy in the behavior of the two specimens should be noted. Not only do these results follow the trend of faster diffusion in the AM specimen compared to the wrought, but this also establishes a stronger correlation between charging conditions and diffusivity for the thinner foil than for the thicker specimen. Though the exact mechanism behind this difference is unclear, it is likely due to the order-of-magnitude change in thickness, and demonstrates that the charging potentials used in this study are sufficient to fully saturate the specimens with thickness values at or greater than 0.5 mm.

3.5.3 Temperature Dependence

Each rise and decay transient for the wrought 17-4 PH foil, from 25-80°C, can be seen in Figure 3.13. The data was smoothed using the moving average and fit to Equations 3.1 and 3.2 as shown. There is an increase in slope in the permeation transients as temperature is increased, corresponding to an increase in effective diffusivity. Effective diffusivity values for each permeation transient calculated via curve fitting, breakthrough time, and lag time methods are listed in Table 3.5.

The curve fit effective diffusivities are plotted against temperature for each rise and decay transient in Figure 3.14. There is a clear break point around 40°C in both the rise and decay transients, after which the slope of the diffusivity versus temperature data becomes much less steep, nearly plateauing. This is likely due to the influence of reversible traps being eliminated as temperature increases.[60] This will cause a drastic decrease in the activation energy for diffusion; while the calculated activation energy for the decay transient below 40°C is 108-113 kJ/mol, the activation energy above 40°C is 6-8 kJ/mol. Additionally, while the first and second decay transients are very similar, there is some scatter between the first and second rise transients. This is attributable to surface effects and initial trapping effects accompanying the first rise transient.

3.6 Discussion

It is pertinent to consider the origins of the faster diffusivity and lower diffusible hydrogen concentration found in AM 17-4 PH compared to its wrought counterpart. These differences in hydrogen behavior can theoretically be credited to either a decrease in reversible trap states or the existence of a fast diffusion pathway in the AM alloys. The specific microstructural features that may influence these behaviors are addressed in subsequent chapters.

There is precedent in literature for AM alloys to display an increased effective diffusivity

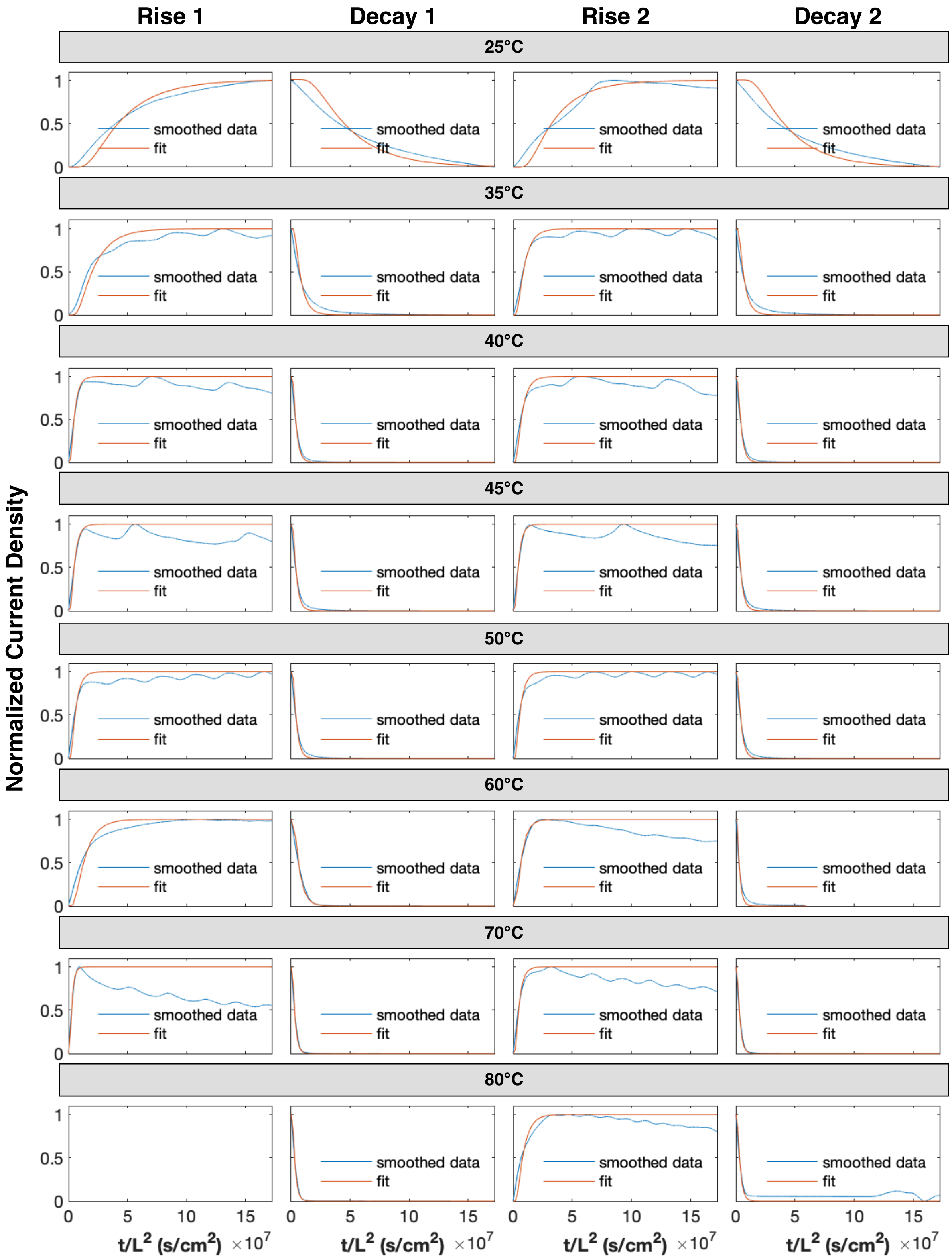

Figure 3.13: Rise and decay EP curves and curve fits for wrought 17-4 PH foil at temperatures ranging from 25-80°C.

Table 3.5: Summary of all temperature-controlled W 17-4 PH foil permeation data, with effective diffusivity calculated using breakthrough (BT) time, lag time, and curve fitting methods. Initial rise and decay are labeled "R/D #1", and subsequent rise and decays are labeled "R/D #2". Charging and extraction potential vs. Hg/HgSO$_4$ reference electrode is also labeled.

Specimen	**R/D**	**R/D #**	**Pot. (V$_{\text{MMSE}}$)**	D_{eff} **(23°C) [cm^2/s]**		
				BT	**Lag**	**Fit**
35°C	Rise	1	-2.0	1.14×10^{-8}	7.55×10^{-9}	6.94×10^{-9}
	Decay	1	-1.4	2.75×10^{-9}	3.75×10^{-8}	1.92×10^{-8}
	Rise	2	-2.0	3.19×10^{-8}	1.61×10^{-8}	1.62×10^{-8}
	Decay	2	-1.4	3.31×10^{-9}	4.30×10^{-8}	2.25×10^{-8}
40°C	Rise	1	-2.0	7.03×10^{-8}	2.74×10^{-8}	2.96×10^{-8}
	Decay	1	-1.4	6.85×10^{-9}	6.32×10^{-8}	3.65×10^{-8}
	Rise	2	-2.0	5.20×10^{-8}	2.02×10^{-8}	2.03×10^{-8}
	Decay	2	-1.4	6.60×10^{-9}	6.12×10^{-8}	3.53×10^{-8}
45°C	Rise	1	-2.0	6.90×10^{-8}	2.71×10^{-8}	2.91×10^{-8}
	Decay	1	-1.4	6.30×10^{-9}	6.37×10^{-8}	3.58×10^{-8}
	Rise	2	-2.0	7.75×10^{-8}	3.01×10^{-8}	3.32×10^{-8}
	Decay	2	-1.4	6.33×10^{-9}	6.33×10^{-8}	3.57×10^{-8}
50°C	Rise	1	-2.0	6.78×10^{-8}	2.44×10^{-8}	2.50×10^{-8}
	Decay	1	-1.4	6.20×10^{-9}	6.28×10^{-8}	3.52×10^{-8}
	Rise	2	-2.0	7.30×10^{-8}	2.50×10^{-8}	2.51×10^{-8}
	Decay	2	-1.4	6.31×10^{-9}	6.33×10^{-8}	3.57×10^{-8}
60°C	Rise	1	-2.0	3.36×10^{-8}	1.09×10^{-8}	1.09×10^{-8}
	Decay	1	-1.4	4.45×10^{-9}	3.81×10^{-8}	2.25×10^{-8}
	Rise	2	-2.0	5.27×10^{-8}	6.41×10^{-10}	2.15×10^{-8}
	Decay	2	-1.4	7.96×10^{-9}	8.96×10^{-8}	4.95×10^{-8}
70°C	Rise	1	-2.0	1.27×10^{-7}	1.73×10^{-9}	5.39×10^{-8}
	Decay	1	-1.4	9.51×10^{-9}	8.20×10^{-8}	4.81×10^{-8}
	Rise	2	-2.0	7.91×10^{-8}	2.86×10^{-8}	3.03×10^{-8}
	Decay	2	-1.4	9.35×10^{-9}	8.06×10^{-8}	4.73×10^{-8}
80°C	Decay	1	-1.4	9.49×10^{-9}	8.13×10^{-8}	4.79×10^{-8}
	Rise	2	-2.0	5.84×10^{-8}	1.62×10^{-8}	1.75×10^{-8}
	Decay	2	-1.4	4.56×10^{-10}	7.80×10^{-8}	4.42×10^{-8}

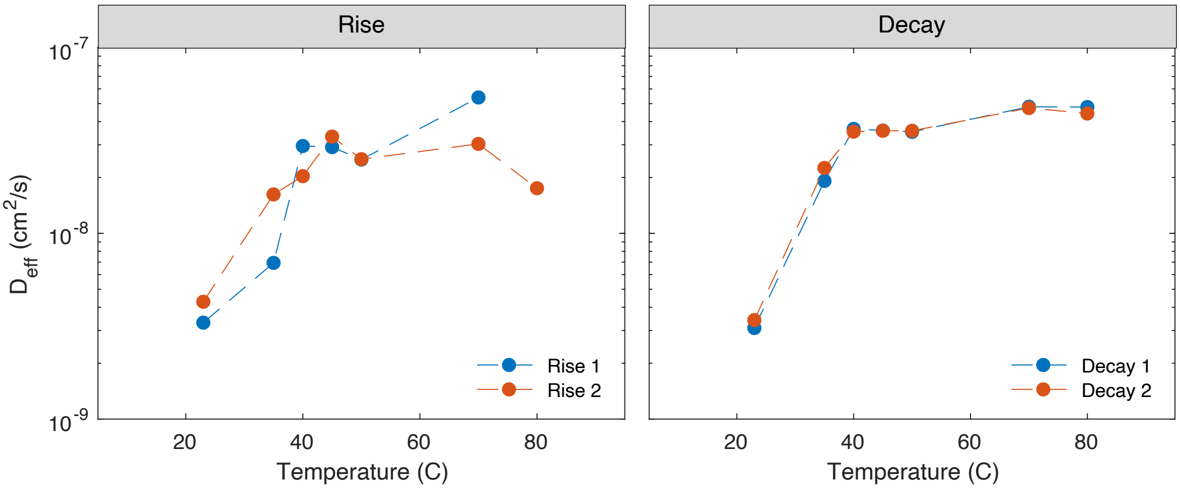

Figure 3.14: Temperature versus effective diffusivity for wrought foil permeation. Note a break in the slope continuity at around 40°C, attributable to low-temperature trapping.

relative to their wrought counterparts. Lin et al.[61] observed a four-fold increase in diffusivity in SLM 316L compared to its wrought counterpart, attributed to fast diffusion in sub-grain boundaries in the AM specimen. Studies characterizing the hydrogen diffusivity of AM 17-4 PH have shown a range of two-fold[41] to ten-fold[42] increases in effective diffusivity with varying post-processing parameters and methodology.

The increase in diffusivity observed in this work aligns well with that shown by Alnajjar et al. on SLM 17-4 PH,[41] though unlike in the study performed by Alnajjar et al., the specimens in this work underwent a HIP and solution annealing heat treatment. As the HIP and solution annealing process serves to eliminate processing defects, such as lack-of-fusion zones, and to homogenize the microstructure, this similarity may indicate that other microstructural features beyond processing defects and grain shape play a role in determining diffusivity. Alnajjar et al. speculate that this is due to additional trap sites in the wrought specimen, such as grain boundaries and precipitates.

Comparison between initial and second rise permeation transients allows for insight into the degree of irreversible trapping, as an increase in peak current density from first to second rise transient suggests that irreversible trap sites are being filled. In Figure 3.15, there is a clear increase in maximum current density between the first and the second

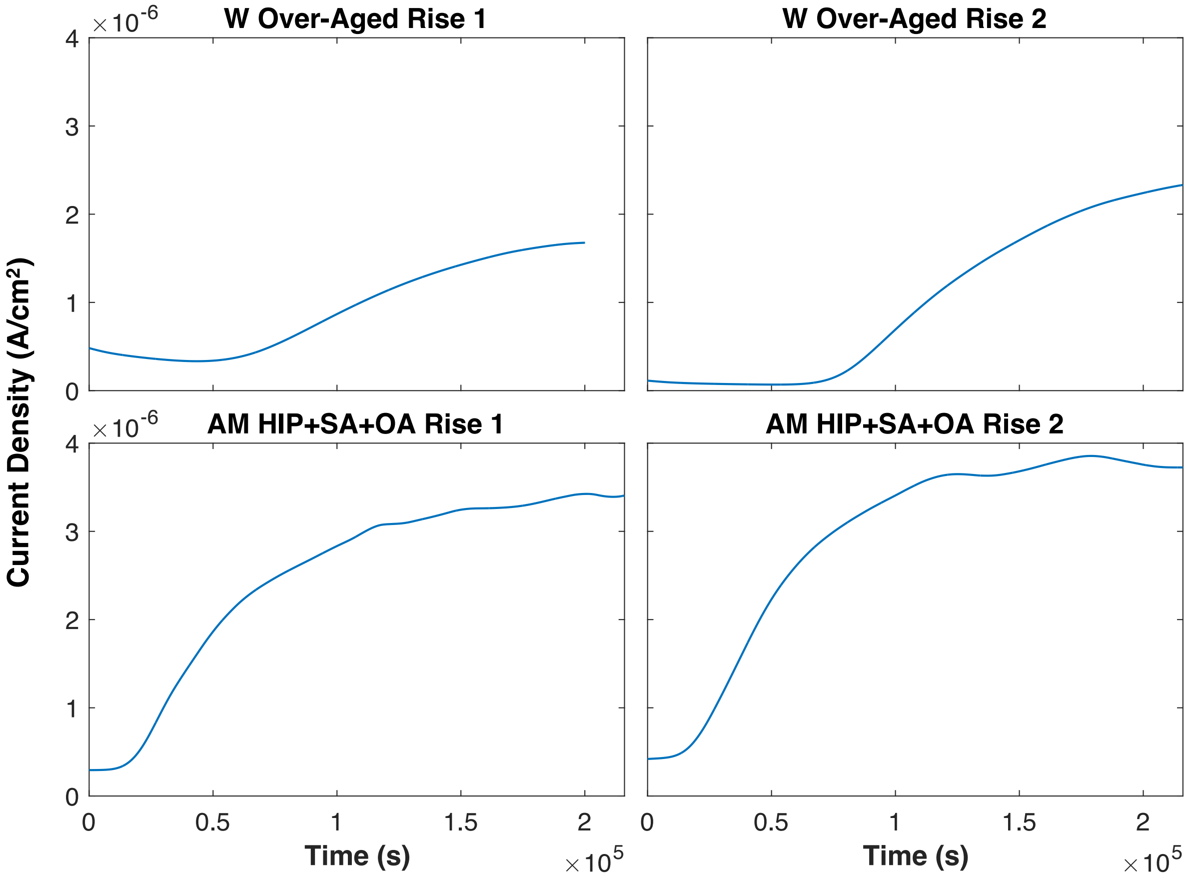

Figure 3.15: First (left) and second (right) rise transients for wrought over-aged (top) and AM HIP+SA+OA (bottom) specimens.

rise transient of both the wrought and the AM specimen, suggesting the presence of irreversible trap sites in both wrought and AM specimens that are filled upon the second rise.

The break points in the temperature-diffusivity relationships observed in isothermal TDS and variable-temperature permeation also provide insight into trapping behavior. The reduction in diffusion coefficient at lower temperatures seen in both analyses is common in literature, and has been attributed to trapping at lower temperatures.[5, 60, 62] The break point temperatures observed in permeation and TDS are both below the temperature at which the preferential occupation site for interstitial hydrogen in BCC iron transitions from tetrahedral (below 100°C) to octahedral (above 100°C).[3]

The difference in break point temperature between the isothermal TDS and foil permeation is possibly attributable to specimen post-processing and geometry. The variable-temperature permeation was conducted on foils without an aging heat treatment to enable copper precipitation, leading to a difference in trap states between the two experiments. Additionally, the thickness of the wrought permeation foils was nearly an order of magnitude lower than the thickness of the TDS specimens.

The activation energy of migration E_{act} found using isothermal TDS is slightly higher than the approximate value associated with BCC α-Fe,[62] likely due to impurities and other hydrogen traps associated with steel. When the data at 100°C after the break point are excluded from the Arrhenius fit, the activation energy value increases, as is expected due to exclusion of the high temperatures that correspond to less trapping and therefore lead to lower activation energies.

It is also important to discuss the difference between diffusivity calculated through electrochemical permeation and through thermal desorption spectroscopy. The greatest discrepancy between the two is the diffusivity in the AM HIP+PA specimen, which is markedly faster in the permeation results but similar to AM HIP+SA+PA in the TDS results. In a study comparing the variability of electrochemical permeation and TDS used to analyze the diffusivity of cold-rolled pure iron, Zafra et al. found that diffusivity values obtained using thermal desorption spectroscopy had a much lower coefficient of variance compared to the permeation values.[56] This is attributed to the influence of assumed electrochemical boundary conditions on permeation analysis. The investigation considers both first and second permeation rise transients so as to account for the effects of trapping. Though analysis of the first rise transient was highly variable, the second rise transient and TDS results were similar, and the second rise transient showed a coefficient of variation that was nearly as low as that of TDS. The study did not include an analysis of decay transients, which tend to have less variation than rise transients as seen in Figure 3.14. This may suggest that the discrepancy in diffusivities calculated using different techniques seen in the current study is due to differences in the assumed surface conditions in the electrochemical permeation analysis and the actual surface conditions.

3.7 Conclusions

This chapter provides crucial insights into the diffusion behavior of additively manufactured (AM) 17-4 PH compared to its traditional wrought incumbent. The investigation focuses on a comprehensive comparison of effective hydrogen diffusivity through electrochemical permeation and thermal desorption spectroscopy for both wrought and additively manufactured 17-4 PH alloys in peak-aged and over-aged conditions. The findings demonstrate that the AM alloys consistently exhibit increased effective hydrogen diffusivity compared to their wrought counterparts across all heat treatment conditions and analysis methods. This conclusion is in agreement with previous literature on AM alloys.

An examination of sequential permeation rise transients and the identification of a break point in the diffusivity-temperature relationship underscore a notable influence of reversible trapping in both alloys. This comparative analysis provides insight on the nuanced diffusion characteristics of AM alloys, emphasizing their distinct hydrogen behavior relative to traditional wrought materials.

References

[1] A. Turnbull, “Perspectives on hydrogen uptake, diffusion and trapping,” *International Journal of Hydrogen Energy*, vol. 40, pp. 16961–16970, Dec. 2015.

[2] A. T. Paxton, “From quantum mechanics to physical metallurgy of steels,” *Materials Science and Technology*, vol. 30, pp. 1063–1070, July 2014.

[3] F. Wei and K. Tsuzaki, “Hydrogen trapping phenomena in martensitic steels,” in *Gaseous Hydrogen Embrittlement of Materials in Energy Technologies*, pp. 493–525, Elsevier, 2012.

[4] H. Hagi, “Diffusion Coefficient of Hydrogen in Iron without Trapping by Dislocations and Impurities,” *Materials Transactions, JIM*, vol. 35, no. 2, pp. 112–117, 1994.

[5] K. Kiuchi and R. McLellan, “The solubility and diffusivity of hydrogen in well-annealed and deformed iron,” in *Perspectives in Hydrogen in Metals*, pp. 29–52, Elsevier, 1986.

[6] R. A. Oriani, “The diffusion and trapping of hydrogen in steel,” *Acta Metallurgica*, 1970.

[7] A. McNabb and P. K. Foster, “A New Analysis of the Diffusion of Hydrogen in Iron and Ferritic Steels,” *Transactions of the Metallurgical Society of AIME*, 1963.

[8] R. L. Thomas, D. Li, R. P. Gangloff, and J. R. Scully, “Trap-governed hydrogen diffusivity and uptake capacity in ultrahigh-strength AERMET 100 steel,” *Metallurgical and Materials Transactions A: Physical Metallurgy and Materials Science*, 2002.

[9] D. Li, R. P. Gangloff, and J. R. Scully, “Hydrogen Trap States in Ultrahigh-Strength AERMET 100 Steel,” *Metallurgical and Materials Transactions A: Physical Metallurgy and Materials Science*, vol. 35, pp. 849–864, 2004.

[10] J. P. Hirth, “Effects of hydrogen on the properties of iron and steel,” *Metallurgical Transactions A*, vol. 11, pp. 861–890, 1980.

[11] J. H. Ai, H. M. Ha, R. P. Gangloff, and J. R. Scully, “Hydrogen diffusion and trapping in a precipitation-hardened nickel-copper-aluminum alloy Monel K-500 (UNS N05500),” *Acta Materialia*, vol. 61, no. 9, pp. 3186–3199, 2013. ISBN: 13596454.

[12] T. Asaoka, G. Lapasset, M. Aucouturier, and P. Lacombe, “Observation of hydrogen trapping in Fe-0.15 wt% Ti alloy by high resolution autoradiography,” *Corrosion*, vol. 34, no. 2, pp. 39–47, 1978.

[13] A. J. Kumnick and H. H. Johnson, “Deep trapping states for hydrogen in deformed iron,” *Acta Metallurgica*, vol. 28, pp. 33–39, 1980.

[14] J. Yao and J. R. Cahoon, “Experimental studies of grain boundary diffusion of hydrogen in metals,” *Acta Metallurgica Et Materialia*, vol. 39, no. 1, pp. 119–126, 1991.

[15] H. Magnusson and K. Frisk, “Self-diffusion and impurity diffusion of hydrogen, oxygen, sulphur and phosphorus in copper,” tech. rep., Swedish Nuclear Fueland Waste Management Co, Stockholm, Dec. 2013. Publication Title: Swedish Nuclear Waste Management Company Technical Report.

[16] R. Kirchheim, T. Mütschele, W. Kieninger, H. Gleiter, R. Birringer, and T. D. Koblé, “Hydrogen in amorphous and nanocrystalline metals,” *Materials Science and Engineering*, vol. 99, no. 1-2, pp. 457–462, 1988.

[17] T. Mütschele and R. Kirchheim, “Segregation and diffusion of hydrogen in grain boundaries of palladium,” *Scripta Metallurgica*, vol. 21, no. 2, pp. 135–140, 1987.

[18] R. D. Calder, T. S. Elleman, and K. Verghese, “Grain boundary diffusion of tritium in 304- and 316-stainless steels,” *Journal of Nuclear Materials*, vol. 46, no. 1, pp. 46–52, 1973.

[19] T. Tsuru and R. M. Latanision, “Grain boundary transport of hydrogen in nickel,” *Scripta Metallurgica*, vol. 16, no. 5, pp. 575–578, 1982.

[20] S. M. Lee and J. Y. Lee, “The Trapping and Transport Phenomena of Hydrogen in Nickel,” *Metallurgical Transactions A*, vol. 17, pp. 181–187, 1986.

[21] B. Ladna and H. K. Birnbaum, “SIMS study of hydrogen at the surface and grain boundaries of nickel bicrystals,” *Acta Metallurgica*, vol. 35, no. 10, pp. 2537–2542, 1987.

[22] A. Kimura and H. K. Birnbaum, “Hydrogen induced grain boundary fracture in high purity nickel and its alloys-Enhanced hydrogen diffusion along grain boundaries,” *Acta Metallurgica*, vol. 36, no. 3, pp. 757–766, 1988.

[23] T. M. Harris and M. Latanision, “Grain boundary diffusion of hydrogen in nickel,” *Metallurgical Transactions A*, vol. 22, pp. 351–355, 1991.

[24] G. Palumbo, D. M. Doyle, A. M. El-Sherik, U. Erb, and K. T. Aust, “Intercrystalline hydrogen transport in nanocrystalline nickel,” *Scripta Metallurgica et Materiala*, vol. 25, no. 3, pp. 679–684, 1991.

[25] M. Ichimura, Y. Sasajima, and M. Imabayashi, “Grain boundary effect on diffusion of hydrogen in pure aluminum,” *Materials Transactions, JIM*, vol. 32, no. 12, pp. 1109–1114, 1991.

[26] D. R. Arantes, X. Y. Huang, C. Marte, and R. Kirchheim, “Hydrogen diffusion and permeation in micro- and nanocrystalline nickel,” *Acta Metallurgica Et Materialia*, vol. 41, no. 11, pp. 3215–3222, 1993.

[27] A. Brass and A. Chanfreau, “Accelerated diffusion of hydrogen along grain boundaries in nickel,” *Acta Materialia*, vol. 44, pp. 3823–3831, Sept. 1996.

[28] U. Stuhr, T. Striffler, H. Wipf, H. Natter, B. Wettmann, S. Janssen, R. Hempelmann, and H. Hahn, “An investigation of hydrogen diffusion in nanocrystalline Pd by neutron spectroscopy,” *Journal of Alloys and Compounds*, 1997.

[29] Y. Mine, K. Tachibana, and Z. Horita, “Grain-boundary diffusion and precipitate trapping of hydrogen in ultrafine-grained austenitic stainless steels processed by high-pressure torsion,” *Materials Science and Engineering A*, vol. 528, pp. 8100–8105, 2011.

[30] W. Beck, J. Bockris, J. McBreen, and L. Nanis, “Hydrogen permeation in metals as a function of stress, temperature and dissolved hydrogen concentration,” *Proceedings of the Royal Society of London. Series A. Mathematical and Physical Sciences*, vol. 290, no. 1421, pp. 220–235, 1966.

[31] B. Chew and F. T. Fabling, “The effect of grain boundaries on the low-temperature diffusion of hydrogen in decarburized mild steel,” *Metal Science Journal*, 1972.

[32] V. M. Sidorenko and I. I. Sidorak, “Determination of diffusion characteristics of the volume and boundary components of the flow of hydrogen in polycrystalline metals,” *Soviet Materials Science*, 1975.

[33] V. M. Sidorenko and I. I. Sidorak, “Boundary and volume diffusion of hydrogen in copper, nickel, and iron,” *Soviet Materials Science*, vol. 9, pp. 372–375, 1975.

[34] R. M. Latanision and M. Kurkela, “Hydrogen Permeability and Diffusivity in Nickel and Ni-Base Alloys,” *Corrosion*, vol. 39, no. 5, pp. 174–181, 1983.

[35] J. Yao and J. R. Cahoon, “Theoretical modeling of grain boundary diffusion of hydrogen and its effect on permeation curves,” *Acta Metallurgica Et Materialia*, 1991.

[36] S. Heinze, B. Vuillemin, J. C. Colson, P. Giroux, and D. Leterq, "Relation between grain size and hydrogen diffusion coefficient in an industrial Pd-23% Ag alloy," *Solid State Ionics*, vol. 122, no. 1-4, pp. 51–57, 1999.

[37] A. Oudriss, J. Creus, J. Bouhattate, E. Conforto, C. Berziou, C. Savall, and X. Feaugas, "Grain size and grain-boundary effects on diffusion and trapping of hydrogen in pure nickel," *Acta Materialia*, vol. 60, pp. 6814–6828, Nov. 2012.

[38] A. J. Kumnick and H. H. Johnson, "Hydrogen transport through annealed and deformed armco iron," *Metallurgical transactions*, vol. 5, pp. 1199–1206, May 1974.

[39] W. C. Chiang, C. C. Pu, B. L. Yu, and J. K. Wu, "Hydrogen susceptibility of 17-4 PH stainless steel," *Materials Letters*, vol. 57, no. 16-17, pp. 2485–2488, 2003.

[40] L. W. Tsay, W. C. Lee, R. K. Shiue, and J. K. Wu, "Notch tensile properties of laser-surface-annealed 17-4 PH stainless steel in hydrogen-related environments," *Corrosion Science*, vol. 44, no. 9, pp. 2101–2118, 2002. ISBN: 0010-938X.

[41] M. Alnajjar, F. Christien, C. Bosch, and K. Wolski, "A comparative study of microstructure and hydrogen embrittlement of selective laser melted and wrought 17–4 PH stainless steel," *Materials Science and Engineering A*, vol. 785, p. 139363, 2020.

[42] N. Guennouni, D. Maisonnette, C. Grosjean, E. Andrieu, D. Poquillon, and C. Blanc, "Influence of hydrogen on the stress-relaxation properties of 17-4PH martensitic stainless steel manufactured by laser powder bed fusion," *Materials Science and Engineering A*, vol. 831, p. 142125, 2022.

[43] M. A. V. Devanathan and Z. Stachurski, "The Mechanism of Hydrogen Evolution on Iron in Acid Solutions by Determination of Permeation Rates," *Journal of The Electrochemical Society*, vol. 111, no. 5, pp. 619–623, 1964.

[44] ASTM International, "ASTM G148-97: Standard Practice for Evaluation of Hydrogen Uptake, Permeation, and Transport in Metals by an Electrochemical Technique," 2018.

[45] J. McBreen, L. Nonis, and W. Beck, "A Method for Determination of the Permeation Rate of Hydrogen Through Metal Membranes," *Journal of The Electrochemical Society*, vol. 113, no. 11, p. 1218, 1966.

[46] H. M. Ha, J. H. Ai, and J. R. Scully, "Effects of prior cold work on hydrogen trapping and diffusion in API X-70 line pipe steel during electrochemical charging," *Corrosion*, vol. 70, no. 2, pp. 166–184, 2014.

[47] J. R. Scully and P. J. Moran, "The Influence of Strain on Hydrogen Entry and Transport in a High Strength Steel in Sodium Chloride Solution," *Journal of The Electrochemical Society*, vol. 135, no. 6, pp. 1337–1348, 1988.

[48] T. Zakroczymski, "Adaptation of the electrochemical permeation technique for studying entry, transport and trapping of hydrogen in metals," in *Electrochimica Acta*, 2006. ISSN: 00134686.

[49] J. Crank, *The Mathematics of Diffusion.* Oxford: Oxford University Press, 1975. ISSN: 03064549.

[50] ASTM International, "ASTM A693-22 Standard Specification for Precipitation-Hardening Stainless and Heat-Resisting Steel Plate, Sheet, and Strip," 2016. Place: West Conshohocken, PA.

[51] A. Turnbull, R. B. Hutchings, and D. H. Ferriss, "Modelling of thermal desorption of hydrogen from metals," *Materials Science and Engineering A*, 1997.

[52] F. Iacoviello, J. Galland, and M. Habashi, "A thermal outgassing method (T.O.M.) to measure the hydrogen diffusion coefficients in austenitic, austeno-ferritic and ferritic-perlitic steels," *Corrosion Science*, vol. 40, no. 8, pp. 1281–1293, 1998.

[53] A. Zafra, Z. Harris, C. Sun, and E. Martínez-Pañeda, "Comparison of hydrogen diffusivities measured by electrochemical permeation and temperature-programmed desorption in cold-rolled pure iron," *Journal of Natural Gas Science and Engineering*, vol. 98, 2022. arXiv: 2112.00589.

[54] M. Murayama, Y. Katayama, and K. Hono, "Microstructural evolution in a 17-4 PH stainless steel after aging at 400 °C," *Metallurgical and Materials Transactions A*, vol. 30, pp. 345–353, 1999.

[55] J. Yamabe, J. G. Sezgin, and K. Wada, "Interpretation of complex, tensile-fracture phenomena in precipitation-hardened, martensitic stainless steels, 17-4PH, in presence of hydrogen," *Materials Science and Engineering A*, vol. 823, no. May, p. 141717, 2021. Publisher: Elsevier B.V.

[56] A. Zafra, Z. Harris, E. Korec, and E. Martínez-Pañeda, "On the relative efficacy of electropermeation and isothermal desorption approaches for measuring hydrogen diffusivity," *International Journal of Hydrogen Energy*, vol. 48, no. 3, pp. 1218–1233, 2023. arXiv: 2210.01462.

[57] J. Svoboda, G. Mori, A. Prethaler, and F. D. Fischer, "Determination of trapping parameters and the chemical diffusion coefficient from hydrogen permeation experiments," *Corrosion Science*, vol. 82, pp. 93–100, 2014. Publisher: Elsevier Ltd.

[58] T.-Y. Zhang and Y.-P. Zheng, "Effects of absorption and desorption on hydrogen permeation—I. Theoretical modeling and room temperature verification," *Acta Metallurgica*, vol. 46, no. 14, pp. 5023–5033, 1998.

[59] S. Wach and A. Miodownik, "The diffusion and permeation of H through pure Fe membranes," *Corrosion Science*, vol. 8, pp. 271–279, Jan. 1968.

[60] M. L. Martin, M. J. Connolly, F. W. Delrio, and A. J. Slifka, "Hydrogen embrittlement in ferritic steels," *Applied Physics Reviews*, vol. 7, no. 4, pp. 26–31, 2020. Publisher: AIP Publishing LLC.

[61] J. Lin, F. Chen, F. Liu, D. Xu, J. Gao, and X. Tang, "Hydrogen permeation behavior and hydrogen-induced defects in 316L stainless steels manufactured by additive manufacturing," *Materials Chemistry and Physics*, vol. 250, p. 123038, 2020.

[62] R. Gibala and A. J. Kumnick, "Hydrogen trapping in iron and steels," in *Hydrogen embrittlement and stress corrosion cracking: a Troiano Festschrift*, pp. 61–77, ASM International, 1984.

Chapter 4

Diffusible and Total Hydrogen Concentration Analysis

4.1 Overview

An analysis of diffusible and total hydrogen concentration is performed on wrought and AM 17-4 PH stainless steel using the barnacle cell technique and LECO hydrogen analysis, respectively. The key conclusion drawn from the barnacle cell analysis is that wrought specimens consistently exhibit higher diffusible hydrogen concentrations than AM counterparts over the same range of hydrogen charging overpotentials, indicating that the wrought specimens may have a higher density of reversible hydrogen traps. Relationships between hydrogen concentration and effective diffusivity are examined across different methods. However, LECO hydrogen analysis shows an increase in total hydrogen concentration in the AM specimens compared to the wrought, suggesting that the AM specimens may have a higher density of irreversible trap sites. These results indicate that the increased effective diffusivity found in the AM specimens is derived from a decrease in reversible trapping.

4.2 Background

Characterization of hydrogen concentration in a metallic alloy can provide insight into microstructural hydrogen trapping within the material. The total hydrogen content in an alloy is the sum of hydrogen in the lattice as well as hydrogen bound and trapped in microstructural features.[1] These microstructural features can act as “reversible” or “irreversible” traps depending on the binding energy of hydrogen to the traps.[2, 3] Lower binding energy features are considered reversible traps and the hydrogen in these traps is in equilibrium with lattice hydrogen, consistently lowering the rate of hydrogen diffusion through the material. The sum of lattice and reversibly trapped hydrogen concentration is termed “diffusible” hydrogen, and can be detected through a variety of thermal or electrochemical methods. Features with higher binding energy, or irreversible traps, are not in equilibrium with lattice hydrogen and reduce diffusivity until the traps are saturated.[4, 5] As it takes much more thermal energy to detrap hydrogen from these irreversible traps, methods to measure irreversibly trapped hydrogen tend to be destructive.

Hydrogen concentration has also been theorized to affect diffusion behavior within the same material, i.e. excluding differences in trapping. Kirchheim et al.[6] observed a dependence of effective hydrogen diffusivity on hydrogen concentration in nanocrystalline palladium. The authors speculate that as hydrogen concentration increases, diffusivity also increases due to saturation of low energy sites. When some critical concentration is reached, these low energy sites are all occupied and hydrogen mobility is reduced due to H-H interactions, causing diffusivity to reach a maximum and then decrease as concentration surpasses this critical value.

Interactions with microstructural features also impact the effects of concentration on diffusion. Du et al.[7] performed Kinetic Monte Carlo analyses of the concentration-diffusivity relationship in BCC Fe, specifically examining diffusion along grain boundaries. The authors concluded that, at low concentrations, hydrogen is confined to the grain boundary interface and diffuses slowly compared to the bulk lattice, and as concentration increases, that interface diffusivity may decrease even further due to blockage of available interstitial sites and repulsive H-H interactions. However, as the interface sites reach full coverage, diffusivity actually increases due to the dominance of bulk hydrogen diffusion away from boundaries.

Additionally, even small amounts of mobile hydrogen in the bulk lattice can diffuse to high-stress regions, such as the fracture process zone near a crack tip, and impact fracture behavior.[8] This can be less than 1 ppm with perfect lattice solubility, or 1-2 ppm if reversible trapping is involved. Increased hydrogen concentration can serve to reduce the threshold for crack propagation for internal hydrogen-assisted cracking.[9] For this reason, characterization of hydrogen concentration can provide insight into H-assisted failure.

4.3 Methods

4.3.1 Barnacle Cell Technique

The barnacle cell (BC) hydrogen extraction technique, described by ASTM F1113-87, can be used to measure diffusible hydrogen concentration and characterize hydrogen adsorption behavior as a function of H overpotential.[10–12] This method was adapted from Devanathan-Stachurski permeation, and involves extraction of hydrogen from one side of a fully H-charged specimen. This is achieved by polarizing the specimen to a potential above the reversible hydrogen potential in order to oxidize the exiting hydrogen. The resultant diffusion from the pre-charged specimen can be modeled using a solution to Fick's second law with the following boundary conditions as outlined by Bockris et al.,[13] where C is hydrogen concentration, x is distance into the specimen, L is specimen thickness, and t is time:

1. $\frac{\partial C}{\partial x} = 0$, $x = 0$, $t \geq 0$: There is no concentration gradient at the non-exit surface of the specimen.
2. $C = 0$, $x = L$, $t > 0$: The concentration of hydrogen at the exit surface is zero during extraction.
3. $C = C_0$, $0 < x < L$, $t \leq 0$: Initial H concentration within the specimen is uniform and fixed at a constant value C_0.

These boundary conditions can be used to provide a Laplace transform-based solution to Fick's second law to get diffusible hydrogen concentration $C_{\mathrm{H,diff}}$:[13]

$$C_{\mathrm{H,diff}}(x,t) = C_0 - C_0 \sum_{n=0}^{\infty} (-1)^n \mathrm{erfc} \frac{(2n+1)L - x}{2\sqrt{D_{\mathrm{eff}} t}} - C_0 \sum_{n=0}^{\infty} (-1)^n \mathrm{erfc} \frac{(2n+1)L + x}{2\sqrt{D_{\mathrm{eff}} t}}.$$

This can be used in conjunction with Fick's first law to produce:

$$\frac{J_t}{zF} = C_{\mathrm{H,diff}} \sqrt{\frac{D_{\mathrm{eff}}}{\pi t}} \left(1 - \sum_{n=0}^{\infty} (-1)^n \exp\left[-\frac{(n+1)^2 L^2}{D_{\mathrm{eff}} t} \right] \right),$$

where J_t is the measured oxidation current density, $z = 1$ eq/mol is the charge associated with the H oxidation reaction, F is Faraday's constant, and D_{eff} is hydrogen diffusivity. If $L^2/D_{\mathrm{eff}} t \geq 4$, the first-term solution to this expression can be used, and diffusible hydrogen concentration can be measured:[14]

$$C_{\mathrm{H,diff}} = \frac{J_{\mathrm{t}}}{zF} \left(\frac{D_{\mathrm{eff}}}{\pi t} \right)^{-1/2}. \tag{4.1}$$

The diffusible H content ($C_{\mathrm{H,diff}}$) as a function of applied potential was evaluated via the barnacle cell electrode technique[12] using planar specimens (thickness of 5 mm). Each specimen was hydrogen pre-charged at room temperature for 16 hours in N_2-deaerated 0.1M NaOH on one face using a Hg/$HgSO_4$ electrode at potentials of -1.40V, -1.60V, -1.80V, -2.00V, and -2.20V versus Hg/$HgSO_4$ (a range of -20 mV to -720 mV cathodic to E_{H^+/H_2}). After charging, hydrogen extraction was performed by potentiostatically polarizing the sample for 2 hours at room temperature to -0.60V versus Hg/$HgSO_4$ (780 mV anodic to E_{H+/H_2}). These parameters were chosen to ensure that $L^2/D_{\text{eff}}t \geq 4$; with a specimen thickness of 5 mm, diffusivity between 10^{-8} and 10^{-9} cm^2/s, and an extraction time of two hours, this relationship is valid and the first-term solution can be used. A schematic of the experimental setup and polarization sequence can be seen in Figure 4.1.

$C_{\text{H,diff}}$ was then calculated from Equation 4.1, using the hydrogen diffusivity calculated from the full curve fit analysis of the permeation decay transient as well as the diffusivity from room-temperature isothermal TDS for comparison. The extraction current density was background-corrected, and $C_{\text{H,diff}}$ was then determined from the measured current density at an extraction time of $t = 100$ s corresponding to a linear region within the time-current density relationship. Measurements were repeated on the XY and XZ plane of the AM specimens to observe any anisotropic behavior.

4.3.2 LECO Hydrogen Analysis

Total hydrogen concentration can be examined through destructive methods to guarantee the measurement of irreversibly trapped hydrogen. For this study, LECO H extraction with a LECO 836 ONH Analyzer (4500-5500 W, 1000 A) was used to determine total H concentration of wrought and AM 17-4 PH after electrochemical hydrogen charging. Three ultrahigh purity Ni baskets were used prior to experimentation in order to calibrate the LECO Analyzer and account for drift, and steel pins were used as a reference material. AM and wrought 17-4 PH specimens in the peak-aged and over-aged conditions, approximately 0.35 mm thick, were charged for 1 week at -2.2V versus Hg/HgSO4 and subsequently placed in the Ni baskets within a graphite crucible and rapidly heated until melted in the LECO Analyzer. Total hydrogen gas content was then measured as a function of time using an infrared detector.

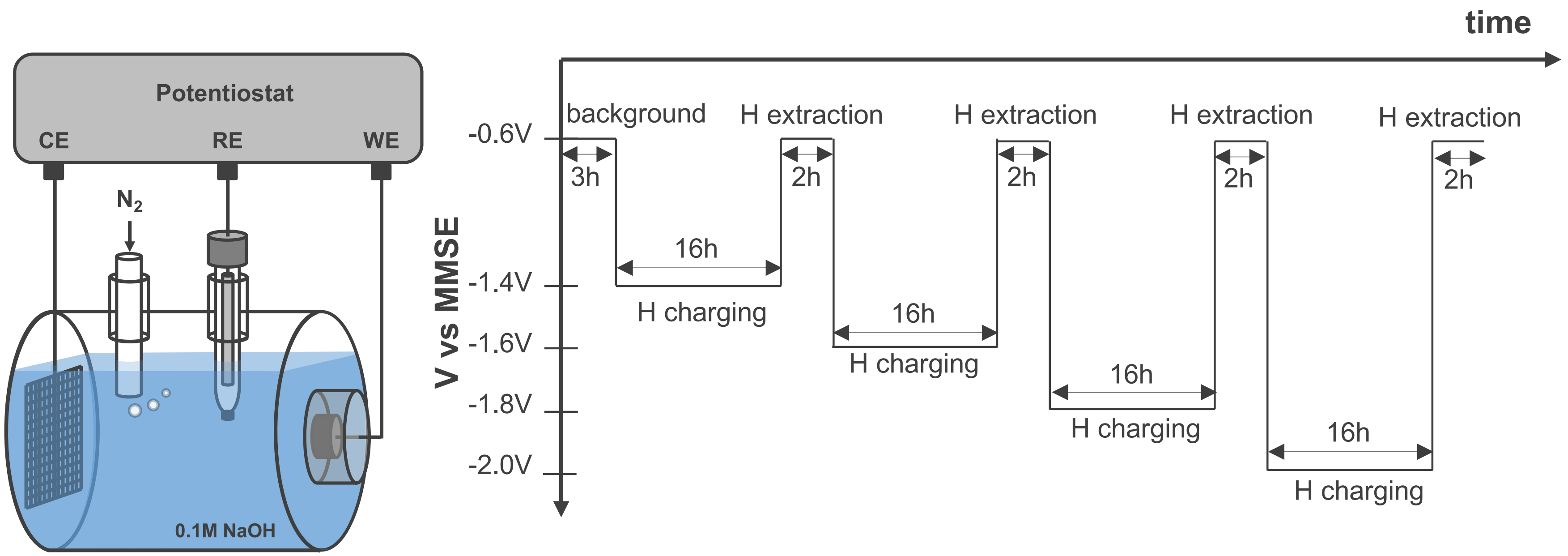

Figure 4.1: (Left) Schematic of the barnacle cell setup, and (right) polarization sequence detailing the potential and time associated with the sequential charging and extraction steps.

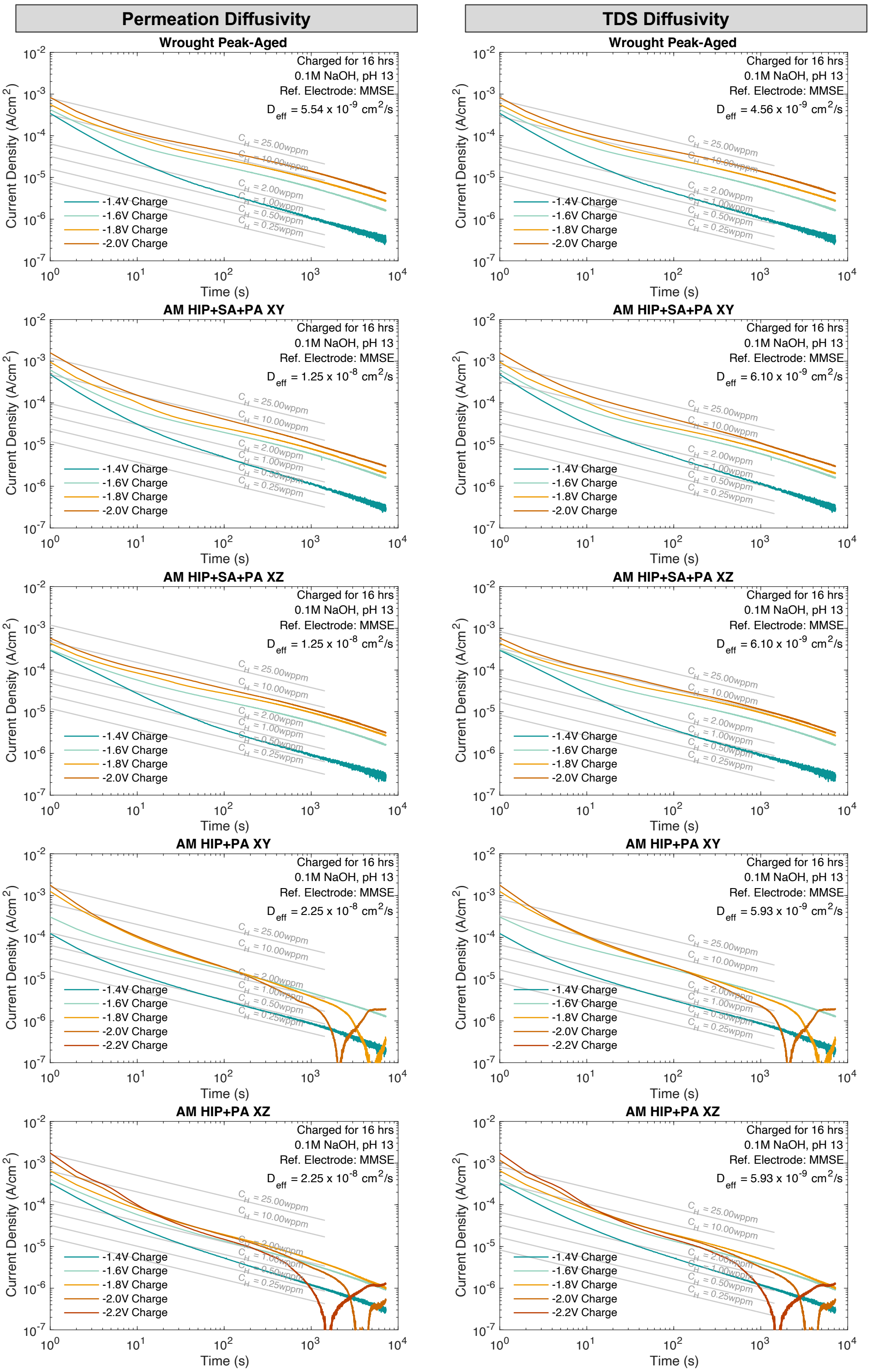

Figure 4.2: Current density versus time for each peak-aged specimen. Theoretical hydrogen concentration values calculated using Equation 4.1 are plotted in gray; calculations using effective diffusivity values from the permeation initial decay (left) and thermal desorption spectroscopy (right) are compared.

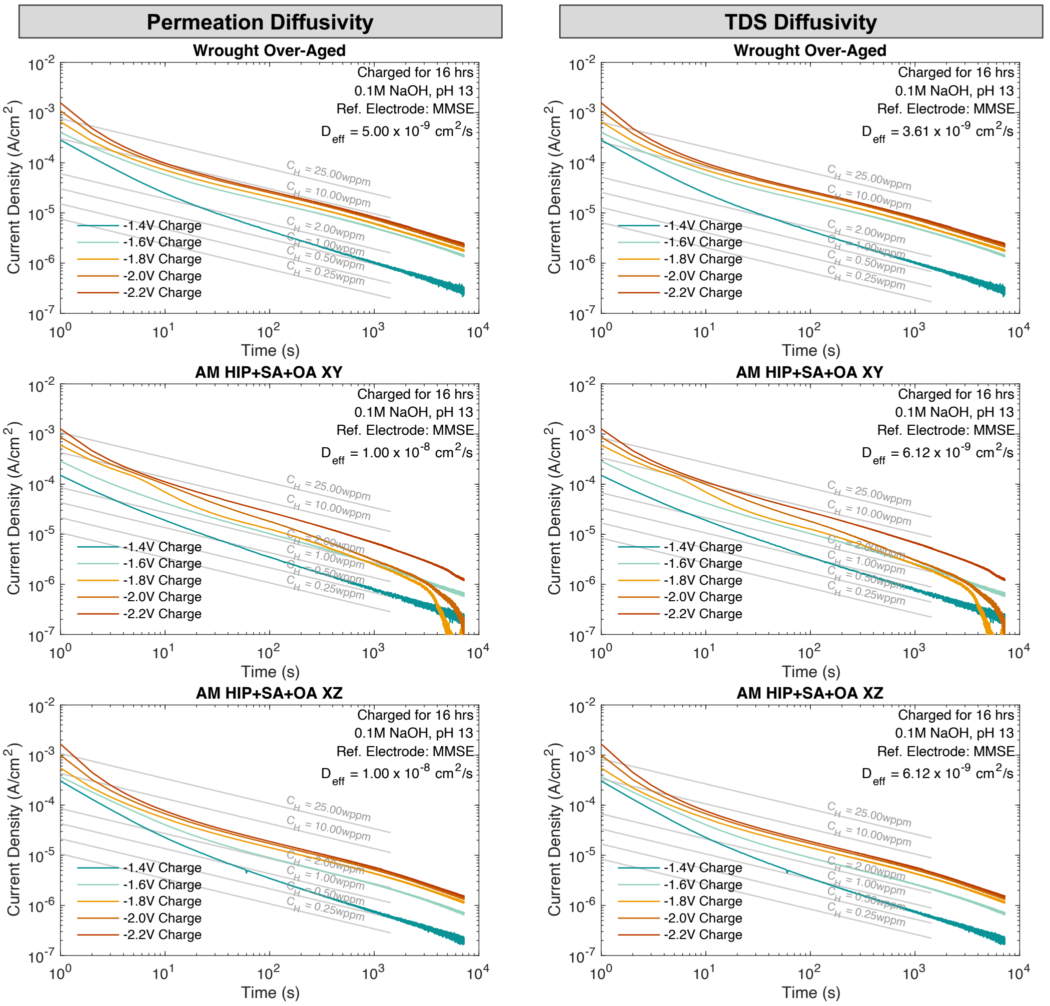

Figure 4.3: Current density versus time for each over-aged specimen. Theoretical hydrogen concentration values calculated using Equation 4.1 are plotted in gray; calculations using effective diffusivity values from the permeation initial decay (left) and thermal desorption spectroscopy (right) are compared.

4.4 Results

The current density versus time curves from each barnacle cell experiment are shown in Figure 4.2 for peak-aged specimens and Figure 4.3 for over-aged specimens. Hypothetical hydrogen concentration values, calculated using Equation 4.1, are overlaid in each plot. These were calculated using two different effective diffusivity values: on the left side of each plot, hydrogen concentration is calculated from the first decay permeation transient diffusivity in order to account for surface and trapping effects, and on the right side, hydrogen concentration is calculated from room-temperature isothermal TDS diffusivity. This comparison allows for a better understanding of the impact of different diffusivity calculation methods.

It can be seen that initial hydrogen concentrations in the first 10 seconds of extraction are slightly elevated, likely due to surface hydrogen artificially increasing current density. However, around 10 seconds after extraction, the current density reaches a constant slope corresponding to a specific hydrogen concentration. It should be noted that the current density corresponding to the -1.4V charge often deviates from its counterparts corresponding to more negative charging potentials; this is attributable to charging at a small overpotential compared to reversible hydrogen, so diffusible hydrogen concentration is very small.

The $C_{\mathrm{H,diff}}$ versus applied potential relationships for AM and wrought 17-4 PH calculated from the barnacle cell experiments at $t = 100$ s post-extraction, near the region of linear slope between time and current density, are shown in Figure 4.4. Results calculated using diffusivity values from permeation and from TDS are compared. As expected from prior literature,[14–16] $C_{\mathrm{H,diff}}$ increases as the applied potential becomes increasingly negative due to the increasing hydrogen overpotential. The HIP+SA+PA and HIP+SA+OA AM materials consistently exhibit a $\sim$2-fold lower $C_{\mathrm{H,diff}}$ relative to their comparable wrought material for a given applied potential. As expected from prior literature on heat treatment effects,[14, 17] $C_{\mathrm{H,diff}}$ is sensitive to the applied post-build heat treatment process, with the non-SA AM material exhibiting a ∼2-fold lower $C_{\mathrm{H,diff}}$ than the HIP+SA+PA AM alloy. Despite the differences in effective diffusivity values between permeation and TDS, the same trend of increased concentration in the wrought specimens is present in barnacle cell results calculated using either diffusivity.

LECO H analysis results, seen in Figure 4.5, show similar total hydrogen content in the over-aged specimens between wrought and AM, but an increase in total hydrogen content from peak-aged wrought to peak-aged AM specimens, contrary to the diffusible hydrogen trend. However, there is a high degree of scatter in much of the data.

4.5 Discussion

Two key conclusions can be drawn from these results. Firstly, the wrought specimens had greater diffusible hydrogen concentrations than the AM specimens, regardless of heat treatment or build direction. Secondly, the peak-aged specimens had the highest diffusible hydrogen concentration in both AM and wrought conditions, followed by the over-aged specimens and lastly by the non-SA peak-aged specimens. These results are examined in the context of hydrogen concentration-effective diffusivity relationships in order to provide insight into trapping behavior.

Barnacle cell hydrogen concentrations calculated using diffusivity from isothermal TDS and from the first decay transient in electrochemical permeation are compared against pertinent effective diffusivity values in Figure 4.6. It can be seen that there is a general decrease in effective diffusivity with increasing hydrogen concentration; this is more apparent when comparing wrought and AM specimens in the same heat treatment condition.

Hydrogen concentration can also be calculated from the Devanathan-Stachurski-type electrochemical permeation experiments described in Section 3.4.1.[18, 19] When the rise

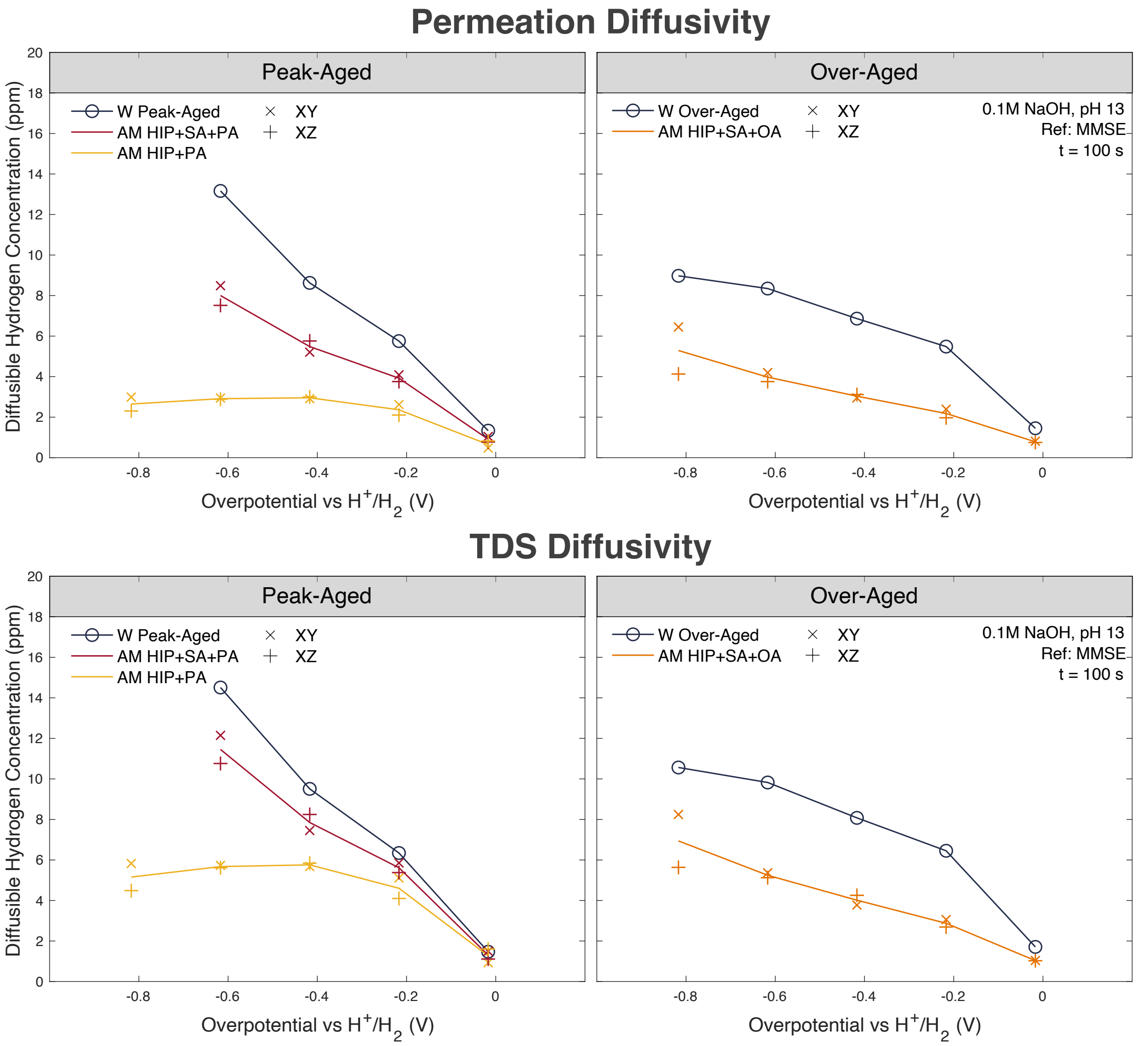

Figure 4.4: Barnacle cell diffusible H concentration for AM and wrought 17-4 PH in the peak-aged and over-aged condition at $t = 100$ s during H extraction. Diffusible H concentration was calculated using diffusivity from permeation (top) and isothermal TDS (bottom). It is notable that diffusible H concentration increases with overpotential, and that wrought 17-4 PH has higher concentration than AM 17-4 PH across all heat treatments.

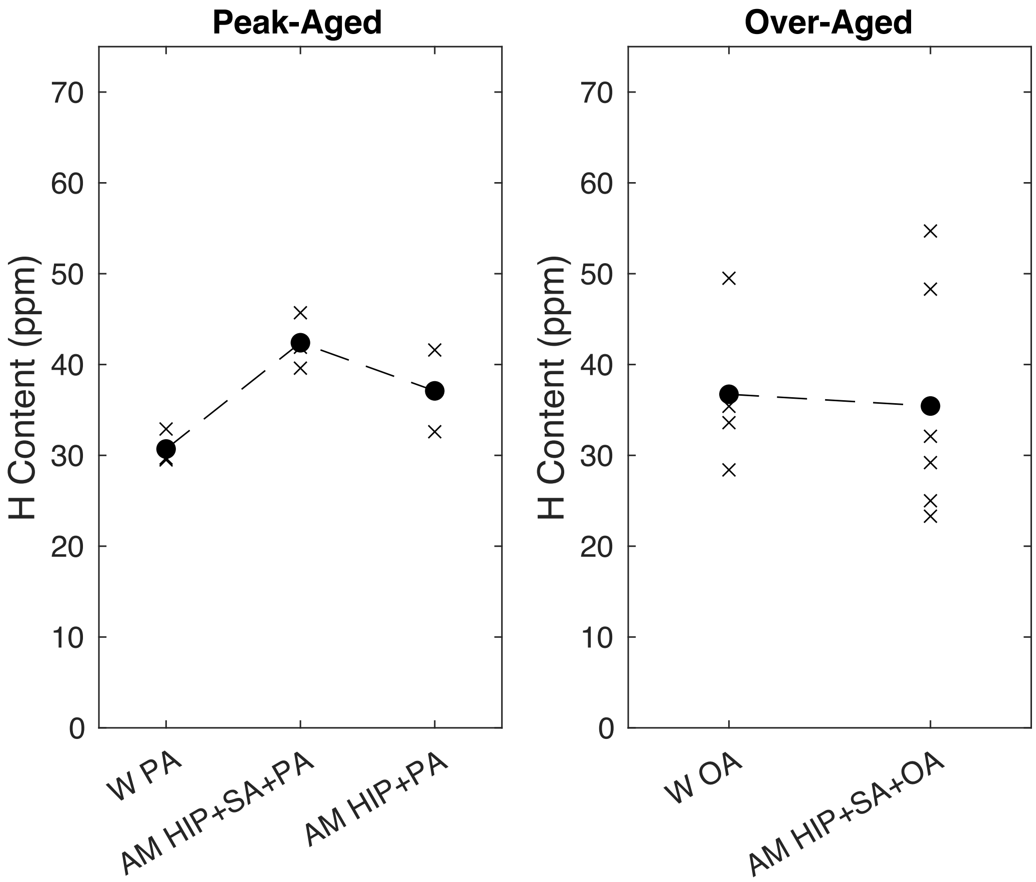

Figure 4.5: LECO hydrogen content for peak-aged (left) and over-aged (right) specimens, with average values represented by black circular symbols.

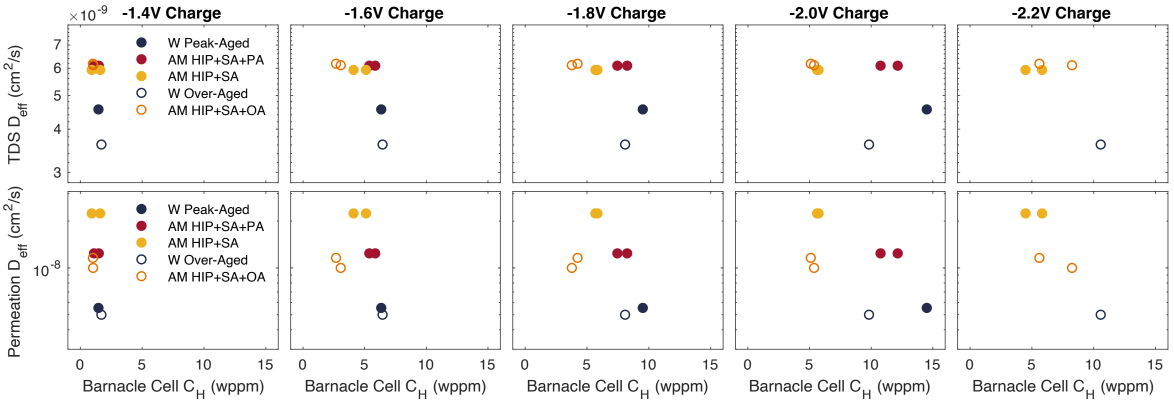

Figure 4.6: Hydrogen concentration versus diffusivity for barnacle cell results calculated using diffusivity from TDS and from permeation.

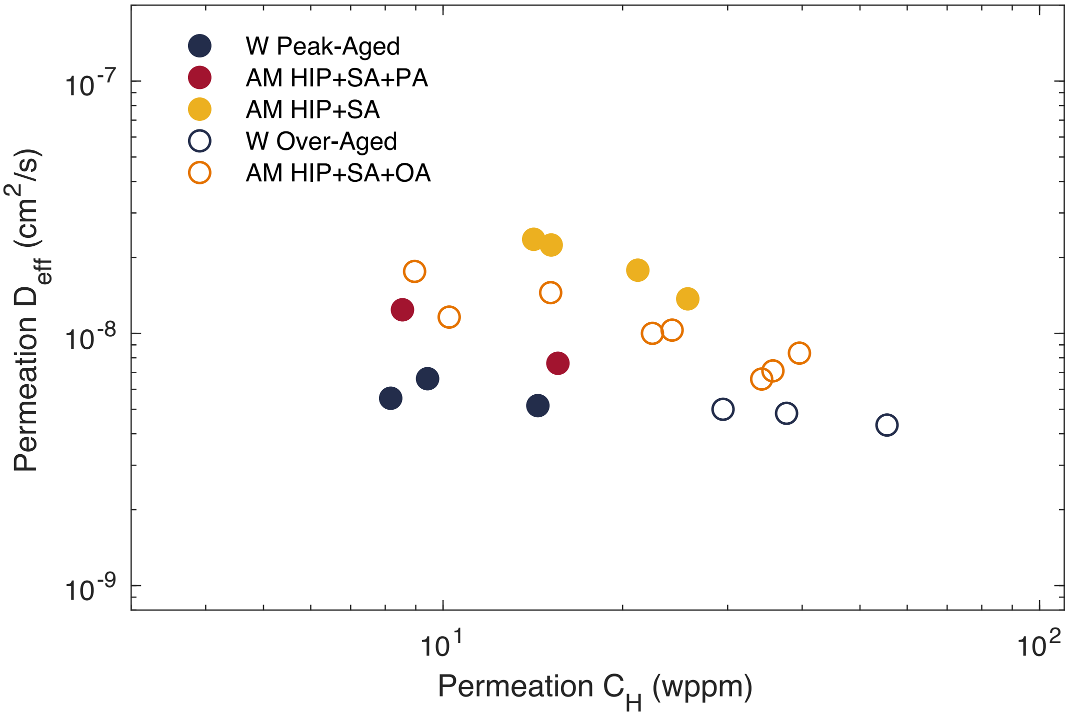

Figure 4.7: Permeation diffusible hydrogen concentration compared to calculated effective diffusivity from the rise and decay transients for each specimen.

transient plateaus at the steady-state H oxidation current density i_∞, the diffusible H concentration can be determined using Equation 4.2:

$$C_{\mathrm{H,diff}} = \frac{i_\infty L}{nFD_{\mathrm{eff}}}, \tag{4.2}$$

in which L is specimen thickness, $n = 1$ is the number of electrons transferred during oxidation, $F = 96500$ coul/equivalent is Faraday's constant, and D_{eff} is the effective diffusivity. The same general increase in hydrogen concentration corresponding to decreasing effective diffusivity can be observed in Figure 4.7, in which electrochemical permeation hydrogen concentration calculated using Equation 4.2 for each permeation curve is compared to effective diffusivity.

This decrease in diffusivity corresponding to increased diffusible hydrogen concentration can also be seen at various temperatures in Figure 4.8, which shows the relationship

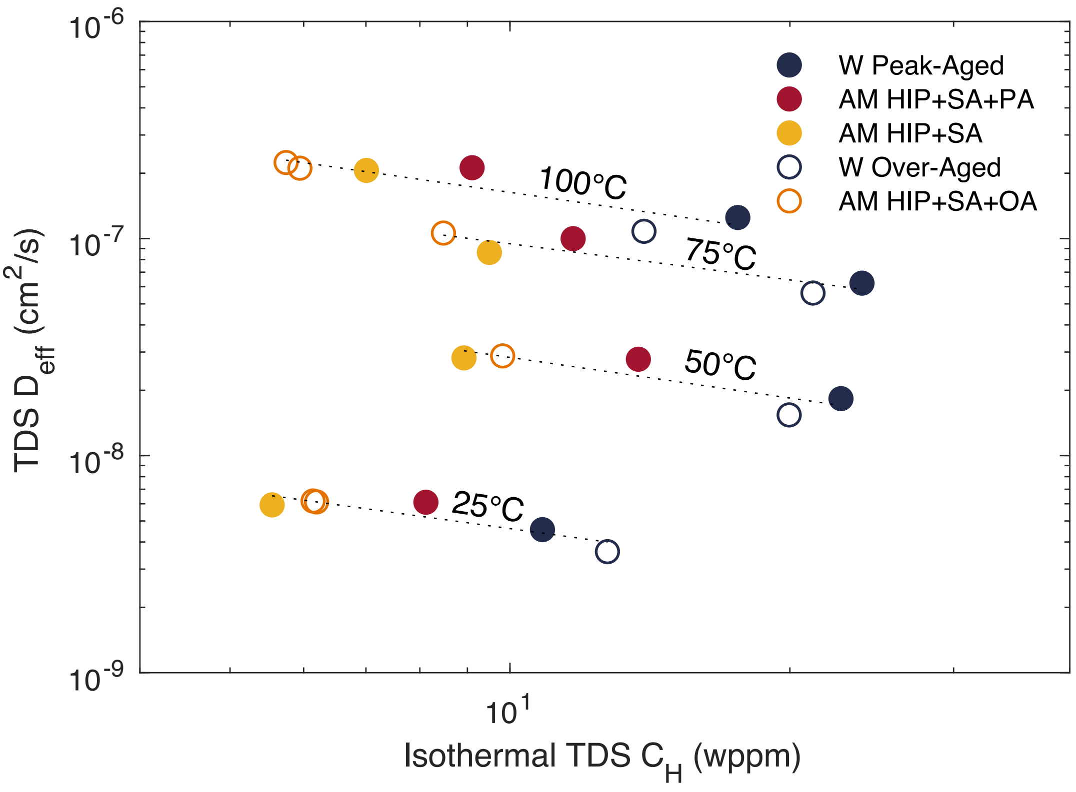

Figure 4.8: Hydrogen concentration versus diffusivity for isothermal TDS at varying temperatures.

between hydrogen concentration and effective diffusivity for each specimen from the isothermal TDS.

Based on the isothermal TDS data, a linear relationship between $\log D_{\text{eff}}$ (in cm^2/s) and $C_{\text{H,diff}}$ (in wppm) can be established at a range of temperatures:

$$\log D_{\text{eff}} = -0.031 C_{\text{H,diff}} - 6.51 \qquad (25^\circ\text{C})$$

$$\log D_{\text{eff}} = -0.019 C_{\text{H,diff}} - 6.86 \qquad (50^\circ\text{C})$$

$$\log D_{\text{eff}} = -0.016 C_{\text{H,diff}} - 7.16 \qquad (75^\circ\text{C})$$

$$\log D_{\text{eff}} = -0.026 C_{\text{H,diff}} - 8.02 \qquad (100^\circ\text{C})$$

The diffusivity-concentration relationship observed in these various experimental methods is likely due to different degrees of reversible trapping between the different alloys; a higher reversible trap density reduces effective diffusivity while simultaneously leading to an increased diffusible hydrogen concentration.[2] Thomas et al.[5] describes the relationship between effective diffusivity, lattice diffusivity D_{L}, perfect-lattice hydrogen concentration C_0, and hydrogen concentration in reversible trap sites $C_{\mathrm{H,rev}}$ at low coverage for a single trap state:

$$\frac{D_{\mathrm{eff}}}{D_{\mathrm{L}}} \approx \frac{C_0}{C_{\mathrm{H,rev}}}.$$

With any increase in reversibly trapped hydrogen concentration due to increased trap density, the ratio of effective diffusivity over lattice diffusivity will be reduced, as observed in this study. This provides a potential explanation for the difference in diffusible hydrogen concentration between wrought and AM specimens, as well as variation between different heat treatments; as diffusible H concentration is higher in the wrought specimens compared to the AM, the corresponding effective diffusivity is lower, indicating a potential increase in reversible trap site density in the wrought specimens.

It should be noted that Thomas et al.,[5] when comparing diffusivity and concentration in AERMET 100 charged at different overpotentials, found an increase in diffusivity with increasing hydrogen concentration within the same specimen, attributed to trap occupancy and H-H interactions. Thus, it is important to acknowledge these competing mechanisms when analyzing hydrogen concentration-diffusivity relationships between different alloys—concentration will increase with a higher density of reversible trap sites, but higher trap occupancies and repulsive interactions may counteract this effect to some degree.

As the total hydrogen concentration ($C_{\mathrm{H,tot}}$) is the sum of the lattice concentration as well as hydrogen concentration in reversible and irreversible traps, irreversibly trapped hydrogen concentration ($C_{\mathrm{H,irr}}$) can be estimated using the following relationship:[5]

$$C_{\mathrm{H,irr}} = C_{\mathrm{H,tot}} - C_{\mathrm{H,diff}}, \tag{4.3}$$

given that $C_{\mathrm{H,diff}}$ represents the sum of lattice and reversibly trapped hydrogen. Thus, irreversibly trapped hydrogen concentration can estimated by subtracting the diffusible hydrogen concentration calculated from barnacle cell or thermal desorption spectroscopy from the total hydrogen concentration calculated from LECO, as shown in Figure 4.9. Though there is a high degree of variability in the LECO results that affects these calculations, a slight increase in irreversibly trapped hydrogen is visible in the AM specimens. This is in contrast with the increased diffusible hydrogen content in the wrought specimens, and suggests some increased degree of irreversible trapping in the AM specimens. One possible microstructural difference that could lead to increased irreversible trapping is the porosity present in the AM specimens but not in the wrought; this is discussed further in subsequent chapters.

4.6 Conclusions

A comprehensive analysis of hydrogen concentration in both wrought and additively manufactured (AM) 17-4 PH stainless steel was performed. Diffusible hydrogen concentration was examined using the barnacle cell technique, and total hydrogen concentration was obtained via LECO hydrogen analysis. The primary observation from the barnacle cell analysis is the increase in diffusible hydrogen concentration in wrought specimens as opposed to their AM counterparts over all applied potentials. This finding remains consistent when concentration is calculated using diffusivity values from both electrochemical permeation and thermal desorption spectroscopy.

The examination of relationships between hydrogen concentration and effective diffusivity across different methods reveals a noteworthy correlation: the increased effective diffusivity found in the AM specimens correlates with the observed decrease in diffusible hydrogen concentration. This can likely be attributed to the effects of reversible trapping.

The LECO analysis shows an elevation in total hydrogen within the AM specimens

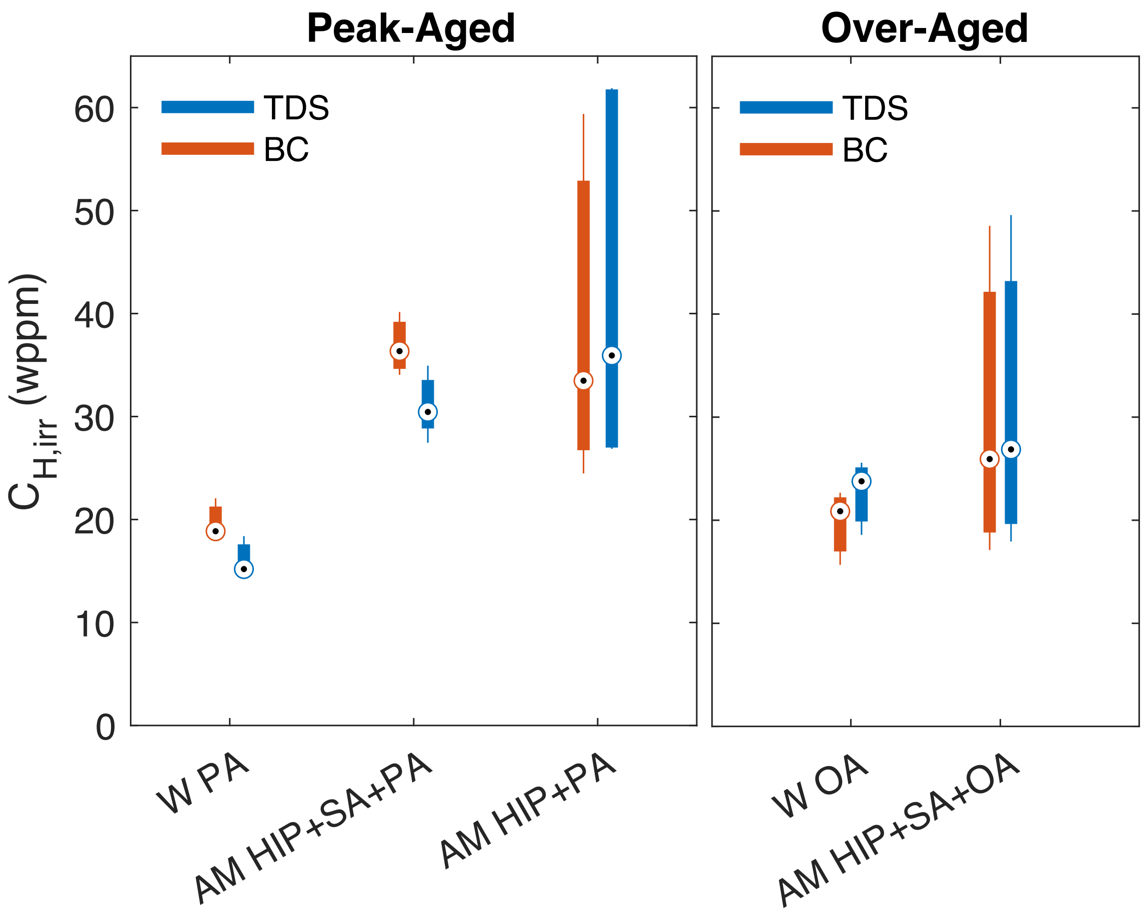

Figure 4.9: Estimated range of irreversibly trapped hydrogen, based on the difference between total hydrogen calculated using LECO and diffusible hydrogen concentration calculated using the barnacle cell (BC) or thermal desorption spectroscopy (TDS) methods.

when compared to the wrought, possibly suggesting a higher density of irreversible hydrogen traps in the AM specimens despite the decrease in reversible trapping. In conclusion, this dual-analysis approach highlights the nuanced relationship between hydrogen concentration and diffusivity in reversible and irreversible traps in wrought and AM 17-4 PH, emphasizing the importance of characterizing hydrogen behavior in additively manufactured alloys.

References

[1] A. H. Krom and A. D. Bakker, “Hydrogen trapping models in steel,” *Metallurgical and Materials Transactions B: Process Metallurgy and Materials Processing Science*, vol. 31, pp. 1475–1482, 2000.

[2] R. A. Oriani, “The diffusion and trapping of hydrogen in steel,” *Acta Metallurgica*, 1970.

[3] A. McNabb and P. K. Foster, “A New Analysis of the Diffusion of Hydrogen in Iron and Ferritic Steels,” *Transactions of the Metallurgical Society of AIME*, 1963.

[4] D. Li, R. P. Gangloff, and J. R. Scully, “Hydrogen Trap States in Ultrahigh-Strength AERMET 100 Steel,” *Metallurgical and Materials Transactions A: Physical Metallurgy and Materials Science*, vol. 35, pp. 849–864, 2004.

[5] R. L. Thomas, D. Li, R. P. Gangloff, and J. R. Scully, “Trap-governed hydrogen diffusivity and uptake capacity in ultrahigh-strength AERMET 100 steel,” *Metallurgical and Materials Transactions A: Physical Metallurgy and Materials Science*, 2002.

[6] R. Kirchheim, T. Mütschele, W. Kieninger, H. Gleiter, R. Birringer, and T. D. Koblé, “Hydrogen in amorphous and nanocrystalline metals,” *Materials Science and Engineering*, vol. 99, no. 1-2, pp. 457–462, 1988.

[7] Y. A. Du, J. Rogal, and R. Drautz, “Diffusion of hydrogen within idealized grains of bcc Fe: A kinetic Monte Carlo study,” *Physical Review B*, vol. 86, p. 174110, Nov. 2012.

[8] A. R. Troiano, “The Role of Hydrogen and Other Interstitials in the Mechanical Behavior of Metals,” *Transactions of the American Society for Metals*, vol. 52, pp. 54–80, 1960.

[9] R. P. Gangloff, “Critical issues in hydrogen assisted cracking of structural alloys,” in *Environment-Induced Cracking of Materials*, pp. 141–165, Elsevier, 2008.

[10] ASTM International, “F 1113 - 87(99) Standard Test Method for Electrochemical Measurement of Diffusible Hydrogen in Steels (Barnacle Electrode),” 1999.

[11] H. Dogan, D. Li, and J. R. Scully, “Controlling hydrogen embrittlement in precharged ultrahigh-strength steels,” *Corrosion*, vol. 63, no. 7, pp. 689–703, 2007.

[12] J. Deluccia and D. Berman, “An Electrochemical Technique to Measure Diffusible Hydrogen in Metals (Barnacle Electrode),” *Electrochemical Corrosion Testing*, vol. 727, pp. 256–274, 1981.

[13] J. Bockris, M. Genshaw, and M. Fullenwider, “The electro-permeation of hydrogen into metals,” *Electrochimica Acta*, vol. 15, pp. 47–60, Jan. 1970.

[14] J. H. Ai, H. M. Ha, R. P. Gangloff, and J. R. Scully, “Hydrogen diffusion and trapping in a precipitation-hardened nickel-copper-aluminum alloy Monel K-500 (UNS N05500),” *Acta Materialia*, vol. 61, no. 9, pp. 3186–3199, 2013. ISBN: 13596454.

[15] Z. D. Harris, K. Guiseva, J. R. Scully, and J. T. Burns, “On the hydrogen environment-assisted cracking resistance of a compositionally complex Co–Ni–Cr–Fe–Mo–Ti alloy,” *Materials Science and Engineering: A*, vol. 802, p. 140601, Jan. 2020.

[16] B. A. Kehler and J. R. Scully, “Predicting the Effect of Applied Potential on Crack Tip Hydrogen in Low-Alloy Martensitic Steels,” *Corrosion 2007*, vol. 64, no. 5, pp. 465–477, 2007.

[17] B. Rincon Troconis, Z. Harris, H. Ha, J. Burns, and J. Scully, “The effect of heat-to-heat variations in metallurgy and hydrogen-metal interactions on the hydrogen embrittlement of Monel K-500,” *Materials Science and Engineering: A*, vol. 703, pp. 533–550, Aug. 2017.

[18] M. A. V. Devanathan and Z. Stachurski, “The Mechanism of Hydrogen Evolution on Iron in Acid Solutions by Determination of Permeation Rates,” *Journal of The Electrochemical Society*, vol. 111, no. 5, pp. 619–623, 1964.

[19] ASTM International, “ASTM G148-97: Standard Practice for Evaluation of Hydrogen Uptake, Permeation, and Transport in Metals by an Electrochemical Technique,” 2018.

Chapter 5

Characterization of Hydrogen Trapping and Transport

5.1 Overview

The objective of this study is to assess and compare microstructural hydrogen trapping in AM and wrought 17-4 PH in order to provide insight on the increased diffusivity and decreased diffusible hydrogen concentration observed in AM 17-4 PH in the context of classical Oriani-type trap theory. Ramp rate thermal desorption spectroscopy (TDS) is used to compare the trap states between wrought and AM specimens. Comparison between microstructural characterization and TDS spectra suggests that the majority of hydrogen is reversibly trapped in low-energy trap sites like high-angle grain boundaries and Cu-rich precipitate interfaces, and that high-energy irreversible trap sites like carbides and low-angle or special grain boundaries only account for a small fraction of trapped hydrogen. Additionally, the absence of a TDS peak unique to AM specimens implies that the submicron porosity in the AM alloy does not function as a significant trap or otherwise cannot be detected as such. As a strong correlation between grain size and effective diffusivity is observed, an Oriani-type trapping model is used as a framework to explore the effects of grain boundary density and binding energy on diffusivity.

5.2 Collaborations

Ramp rate thermal desorption spectroscopy (TDS) experiments were performed by Emilio Martínez-Pañeda and Alfredo Zafra at Imperial College of London.

5.3 Background

Hydrogen can be introduced to a material by a variety of sources, including processing operations and hydrogen-rich environments. Hydrogen uptake can be described by a combination of adsorption ($H_2(g) \rightleftharpoons H_{ads} + H_{ads}$) and absorption ($H_{ads} \rightleftharpoons H_{abs}$) reactions:[1]

$$H_2(g) \rightleftharpoons 2H_{abs}. \tag{5.1}$$

All hydrogen embrittlement theories specify that a critical hydrogen concentration C_{crit} is required to initiate cracking; namely, the extent of H-induced material degradation relies on the amount of hydrogen available.[2–4] The degree of hydrogen embrittlement is dependent on two main factors: the bulk permeability of the material and the degree of hydrogen trapping, both of which affect the amount of hydrogen available to partition to the high triaxial stress field of the fracture process zone.[5]

It is intuitive that increased hydrogen diffusion through a lattice, which mainly occurs via interstitial random-jump migration (perhaps in equilibrium with weakly trapped hydrogen), will intensify the amount of hydrogen present at the triaxial tensile stress field at a crack tip.[6] This ideal or "perfect lattice" diffusion behavior, absent from the effects of trapping, can be described using the ideal lattice diffusivity D_L.[7]

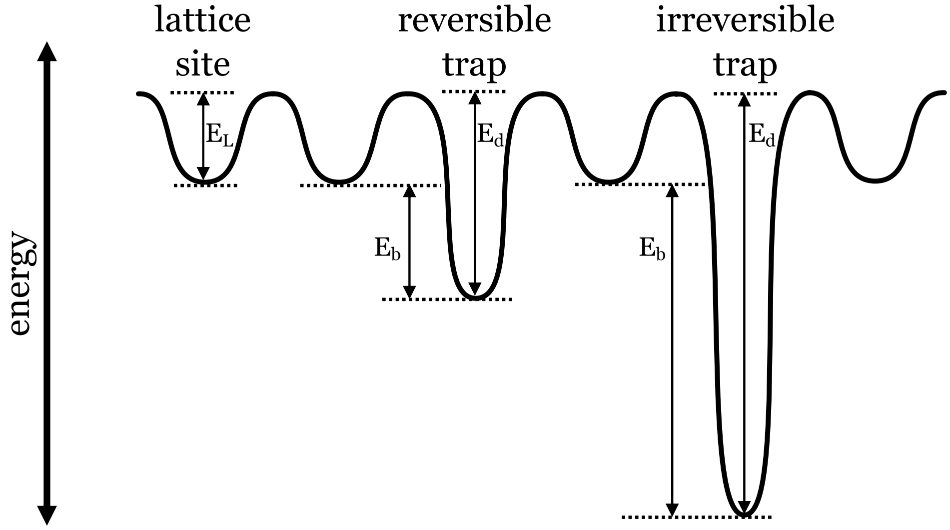

Figure 5.1: Schematic representation of the energies involved in hydrogen trapping. Shown is the energy for occupying an interstitial lattice site (E_L), the binding energy to occupy a trap state (E_b), and the energy required to desorb from a trap state (E_d).

The role of trapping sites on hydrogen behavior is slightly more complex and depends on binding energy as well as the "depth" of the trap, or the energy required for hydrogen to de-trap.[8, 9] "Reversible" traps, which have low trapping strength in comparison to the depth of the energy well, allow for interaction between trapped hydrogen and hydrogen in interstitial lattice sites so equilibrium is maintained. This will increase the effective energy required for hydrogen diffusion, permanently decreasing hydrogen diffusivity through the material to a trap-affected "effective" diffusivity value D_eff. "Irreversible" trapping sites, which have high trapping strength compared to energy well depth (as seen in Figure 5.1), do not allow for any interaction. Therefore, irreversible sites reduce the effective diffusivity of the material only until hydrogen concentration is sufficient to fill the irreversible traps. Both reversible and irreversible traps can reduce hydrogen diffusion through the bulk lattice, but once irreversible traps are filled, they no longer impede hydrogen travel.[10, 11]

Many microstructural inhomogeneities can function as traps, as depicted in the schematic in Figure 5.2, including grain boundaries, inclusions, voids, dislocations, and other defects, as seen in Figure 5.2. As these features often increase material strength by impeding dislocation motion, there has been an observable correlation between high

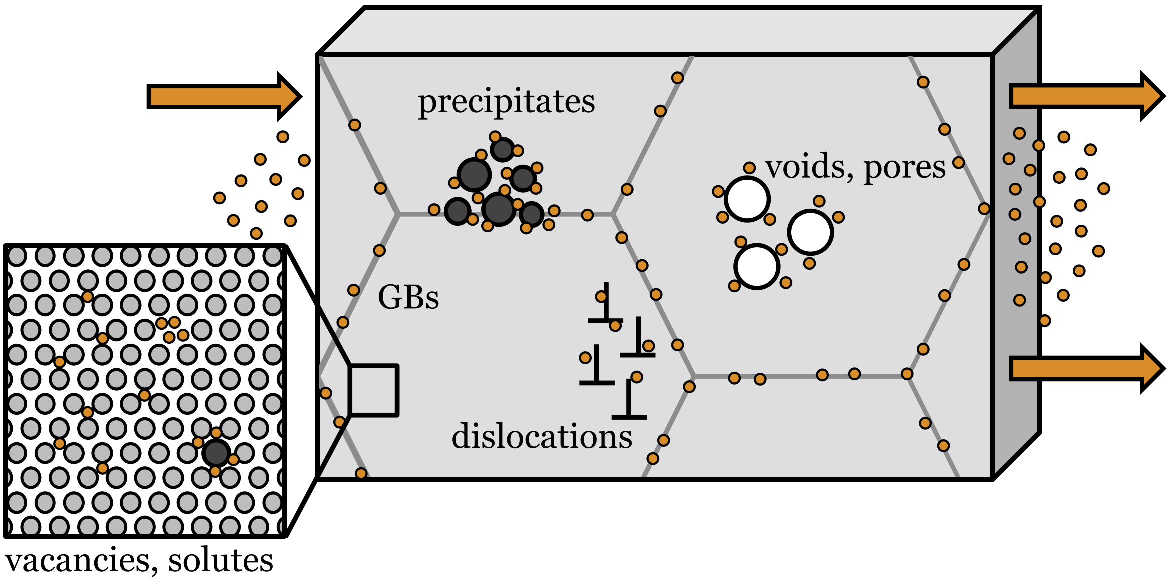

Figure 5.2: Schematic detailing possible hydrogen traps in a metallic alloy, such as point defects, grain boundaries, precipitates, inclusions, dislocations, and voids. Hydrogen is depicted in orange.

tensile strength and a large degree of hydrogen trapping.[6, 12–14]

Traps can have competing effects on hydrogen embrittlement resistance in a metallic alloy.[11] The decrease in effective diffusivity due to trapping can delay the supply of hydrogen to the crack tip zone, thereby temporarily increasing resistance to hydrogen embrittlement. However, a high density or closely connected network of strong, hydrogen-containing trap sites may provide a path for brittle failure to occur. Low-strength traps may also function as hydrogen reservoirs, causing the release of mobile hydrogen which diffuses to nearby cracks and enhances brittle crack growth.[8]

The effective diffusivity value is also influenced by hydrogen “fast paths” or “short circuit paths,” microstructural features such as grain boundaries and dislocations that allow hydrogen to diffuse faster than it would through interstitial random-jump migration in an ideal lattice.[15–18] In particular, there is general disagreement in literature on the impact of grain boundaries on diffusion; several studies attribute an increase in D_{eff} to grain boundaries providing fast diffusion paths,[17, 19–30] whereas other publications report the trapping effects of grain boundaries cause a decrease in D_{eff}.[15, 31–37] It is also important to note that at high coverage of the grain boundaries, the diffusion coefficient may decrease due to attractive hydrogen-hydrogen interaction.[18, 38]

5.4 Methods

5.4.1 Ramp Rate TDS

Hydrogen desorption and trapping can be characterized using "ramp rate" thermal desorption spectroscopy (TDS), which involves steadily increasing the temperature at a constant rate. Each trap site in the metal is characterized by a different binding energy and therefore has a different energy of desorption. Reversible traps have a small binding energy and can function as hydrogen sinks or sources, whereas irreversible traps have a large binding energy and are unlikely to release hydrogen atoms.[39] This deviation in binding energy necessitates the use of a range of temperatures in TDS to allow for the distinction of both reversible and irreversible trap sites.

In steels, the binding energy of a perfect lattice is around 7 kJ/mol and can be assumed to be similar to pure iron.[6] This is smaller than the energy of most trap states, meaning that most steels will have desorption energies dominated by trap state energies.

Observation of a range of trap sites can be achieved using the ramp rate TDS method, which involves a constant rate of increase of temperature over time in the vacuum chamber. As each temperature corresponds to a different trap binding energy, observed desorption "peaks" at certain temperatures can be used to calculate desorption energy for each trap state.[40] Higher temperature peaks indicate higher trap binding energies, and increased peak height suggests a larger amount of trapped hydrogen in the associated site; the total area under each peak will correspond to the total amount of hydrogen desorbed from each trap state.[41] The trap site density is an important component of the diffusible hydrogen concentration $C_{\mathrm{H,diff}}$ calculated in Section 4.4, as seen in the following relationship:[41]

$$C_{\mathrm{H,diff}} = C_{\mathrm{H,L}} + C_{\mathrm{H,T}} = \theta_{\mathrm{L}} N_{\mathrm{L}} + \sum_{i} \theta_{\mathrm{T,i}} N_{\mathrm{T,i}}, \tag{5.2}$$

in which $C_{\mathrm{H,L}}$ is the ideal lattice hydrogen concentration, $C_{\mathrm{H,T}}$ is the concentration of hydrogen in reversible and irreversible traps, θ_{L} is the lattice site fractional coverage, N_{L} is the lattice site density, $\theta_{\mathrm{T,i}}$ is the fractional coverage of trap state i, and $N_{\mathrm{T,i}}$ is the density of trap state i.

Ramp rate TDS measurements display the temperature-specific desorption peaks at which the trap binding energy is reached and hydrogen is excited out of trap states. However, as a material may contain a multitude of trap sites, deconvolution of these peaks is often necessary to find the desorption energy of each trap. This can be a complex and challenging process depending on the material; Wei and Tsuzaki's work with TiC particles in a steel matrix provides a good example of different fits of a single TDS spectrum.[42]

Many desorption energy models are based on the work of Kissinger,[43] which links desorbed hydrogen to activation energy in an Arrhenius relation:

$$\frac{\mathrm{d}x_{\mathrm{H}}}{\mathrm{d}t} = A(1 - x_{\mathrm{H}}) \exp\left(-E_{\mathrm{d}}/RT\right), \tag{5.3}$$

in which x is the fraction of released hydrogen, t is time, A is a material constant, E_{d} is the activation energy for hydrogen desorption, R is the gas constant, and T is absolute temperature. In this analysis, hydrogen diffusion is neglected due to the complexity of modeling lattice diffusion in addition to trapping behavior. This simplification requires careful experimental design in order to minimize the effects of hydrogen diffusion.[44]

Kissinger's model can be used to confirm the assumption that desorption is diffusion-limited (as opposed to surface interaction-limited), which is a necessity in the both the ramp rate and isothermal models. If $\mathrm{d}x/\mathrm{d}t$ and $(1 - x)$ in Equation 5.3 are linearly related, desorption is a first-order process and is limited by hydrogen detrapping and diffusion. However, if $\mathrm{d}x/\mathrm{d}t$ and $(1-x)^2$ are linearly related, then the limiting factor is the surface reaction, which is determined by the desorption of dihydrogen (H_2) instead of H.[11]

The most popular method of analysis is a simplified model outlined by Lee and Lee[45] based on Kissinger's work. By assuming that lattice diffusion can be ignored and instances of hydrogen retrapping are negligible, a model for trapping activation energy was derived from Equation 5.3:

$$-\frac{E_\mathrm{d}}{R} = \frac{\mathrm{d}\ln\left(\phi/T_\mathrm{max}^2\right)}{\mathrm{d}(1/T_\mathrm{max})}, \tag{5.4}$$

in which ϕ is the heating rate and T_max is the temperature at which a hydrogen desorption peak occurs in the TDS spectrum. By performing ramp rate TDS experiments at several different heating rates, it is possible to create a plot of $\ln\left(\phi/T_\mathrm{max}^2\right)$ versus $1/T_\mathrm{max}$ corresponding to a certain peak in the spectra. The slope of this plot can be used to calculate the desorption energy of a specific trap.[46] When several overlapping peaks are present, T_max is commonly obtained by fitting each peak to a Gaussian distribution model, an approach which has been widely successful in literature.[1, 12, 47–57] However, highly asymmetric or skewed spectra can influence the fit and lead to bias in calculated desorption energies.[58] Kirchheim argues that any nonconformity of the peak shape to a Gaussian model may be due to differences in trap energies for one trap type, as well as deviations from the approximated cosinusoidal concentration profile during desorption.[52]

The model outlined by Equation 5.4 is by far the most common approach and is sufficient for the general purpose of this thesis. However, it is important to note that other models have been proposed that account for diffusion and retrapping behaviors. Turnbull et al.,[59] in particular, developed a model that addresses diffusion, detrapping, and retrapping at one or more types of trap sites, as well as accounting for varying trap occupancy. This model is derived from a modification of Fick's second law that better describes low-temperature hydrogen diffusion in steels, taking into account the assumed delay of hydrogen diffusion within the lattice.

More recently, Kirchheim et al.[52] developed both numerical and analytical solutions to describe mono-energetic and multi-energetic trapping energies, as well as those with box-type distributions. Both Kirchheim models account for lattice diffusion and trapping within special lattice sites.

Raina et al.[60] built on Kirchheim's analysis, theorizing that Kissinger's model is only relevant for experiments using slow heating rates on materials with low lattice activation energy, as it neglects diffusion (and therefore specimen thickness effects) and trapping mechanisms and considers hydrogen detrapping the rate limiting step. The Raina model instead employs a non-dimensional numerical solution based on the assumption of local equilibrium between hydrogen atoms at lattice and trap sites to create contour maps of peak temperature with axes of trap density and trap binding energy.

Though these models may be more accurate, their complexity can render them more arduous to use in an experimental research environment with potentially limited gain, as some of the required variables may be difficult or labor-intensive to determine. This is especially relevant when studying emergent materials such as additively manufactured metals, as literature on relevant materials constants may be sparse or non-existent.

Notable simplifications have also been made to the Lee and Lee model. Lee et al.[61] used this model to derive an expression for the desorption energy of a trap at a singular heating rate in a material with several different trapping sites. By assuming the shape of each desorption peak is the same, Lee et al. defined a constant B specific to each trapping site:

$$B = \frac{1}{\phi}\left(\frac{\mathrm{d}x}{\mathrm{d}t}\right)_{\mathrm{max}} \frac{1}{1 - x_{\mathrm{H,max}}}, \tag{5.5}$$

in which $x_{\mathrm{H,max}}$ is the fraction of desorbed hydrogen at the peak maximum. This constant was used to derive an expression for E_{d} based on peak temperature and trap site constant:

$$E_{\mathrm{d}} = RT_{\mathrm{max}}(BT_{\mathrm{max}} - 1). \tag{5.6}$$

Equation 5.6 allows for the calculation of trap state desorption energy without having to consider multiple heating rates, as long as the trapping behavior of the relevant material is already generally understood. Though this is not sufficient for rigorous analysis of novel materials with unknown trapping behavior, it is a useful approximation to confirm the hydrogen trapping behavior of wrought materials or of different build directions in the same material. These trap theories can connect microstructural features to hydrogen behavior and allow for elaboration on differences in bulk hydrogen behavior, such as effective diffusivity and bulk diffusible hydrogen concentration.

Similarly to the isothermal TDS method, ramp rate TDS experiments were performed in collaboration with Emilio Martínez-Pañeda and Alfredo Zafra at Imperial College of London. AM and wrought 17-4 PH specimens of 0.5 mm thickness in the peak-aged and over-aged conditions were electrochemically charged with hydrogen in deaerated 0.6M NaCl at -1.1 V_{SCE} at 55°C. In order for saturation to be achieved, specimens were charged for 24 hours. After a post-charging rest period of 25 minutes to eliminate surface hydrogen, specimens were held in a thermal desorption chamber while the temperature was increased at ramp rates of 2, 5, and 10°C/min up to a maximum temperature of around 800°C.

Peak deconvolution was attempted using MatLab in conjunction with peakfit.m, the peak fitting program developed by Tom O'Haver and available on MatLab Central File Exchange.[62] Peaks were fit to a Gaussian distribution model with linear baseline correction to account for background. The best of 5 fits was chosen based on R^2 value. The peak temperature T_{max} was used in conjunction with Equation 5.4 to calculate activation energy of detrapping, E_{d}. From this, binding energy E_{b} was estimated using:

$$E_{\mathrm{b}} = E_{\mathrm{d}} - E_{\mathrm{L}}, \tag{5.7}$$

where E_{L} is the energy required for interstitial diffusion of hydrogen in the bulk lattice.

5.5 Results

Figure 5.3 shows the ramp rate TDS results for wrought and AM peak-aged and over-aged specimens at 2, 5, and 10°C/min after moving-average smoothing to reduce noise. There is a large initial peak in the results for each specimen corresponding to the desorption of the majority of hydrogen from low-energy reversible trap sites. The inset plots shown in Figure 5.3 represent the small, high-temperature peaks that are not visible with the original scale. Two conclusions can be drawn from this data: (1) the majority of hydrogen is contained in low-temperature reversible traps, and (2) the amount of hydrogen desorbed from the AM specimens is lower than the amount desorbed from the wrought in both peak-aged and over-aged conditions. These results are in agreement with the increased diffusible hydrogen concentration observed via barnacle cell, and suggest an increase in reversibly trapped hydrogen in the wrought specimens.

Potential TDS peaks corresponding to trap sites in the peak-aged and over-aged specimens are labeled in Figures 5.4 and 5.5, respectively. Five peaks can be speculatively identified in the high-temperature region, though the small magnitude and the influence of the tail of the large initial peaks make the small peaks difficult to distinguish. Additionally, at lower ramp rates, these peaks tend to overlap and blend together. The largest peak in the low-temperature region can arguably be deconvoluted into two separate but overlapping peaks, solely based on the visible shoulder on the left-hand side of the peak; the veracity of this claim will be investigated in the following peak fitting analysis.

In order to explore whether the initial large peak consists of two overlapping peaks, a Gaussian fitting analysis is shown in Figure 5.6 for the peak-aged specimens and Figure 5.7 for the over-aged specimens. Each plot includes the raw data, relevant single-peak Gaussian fit, and residuals for the initial large peak. In addition, the goodness of fit (R^2) value and the position, height, width, and area of each fitted peak are displayed on each plot.

There is a clear pattern and a lack of scatter in the residuals for each fit, which may

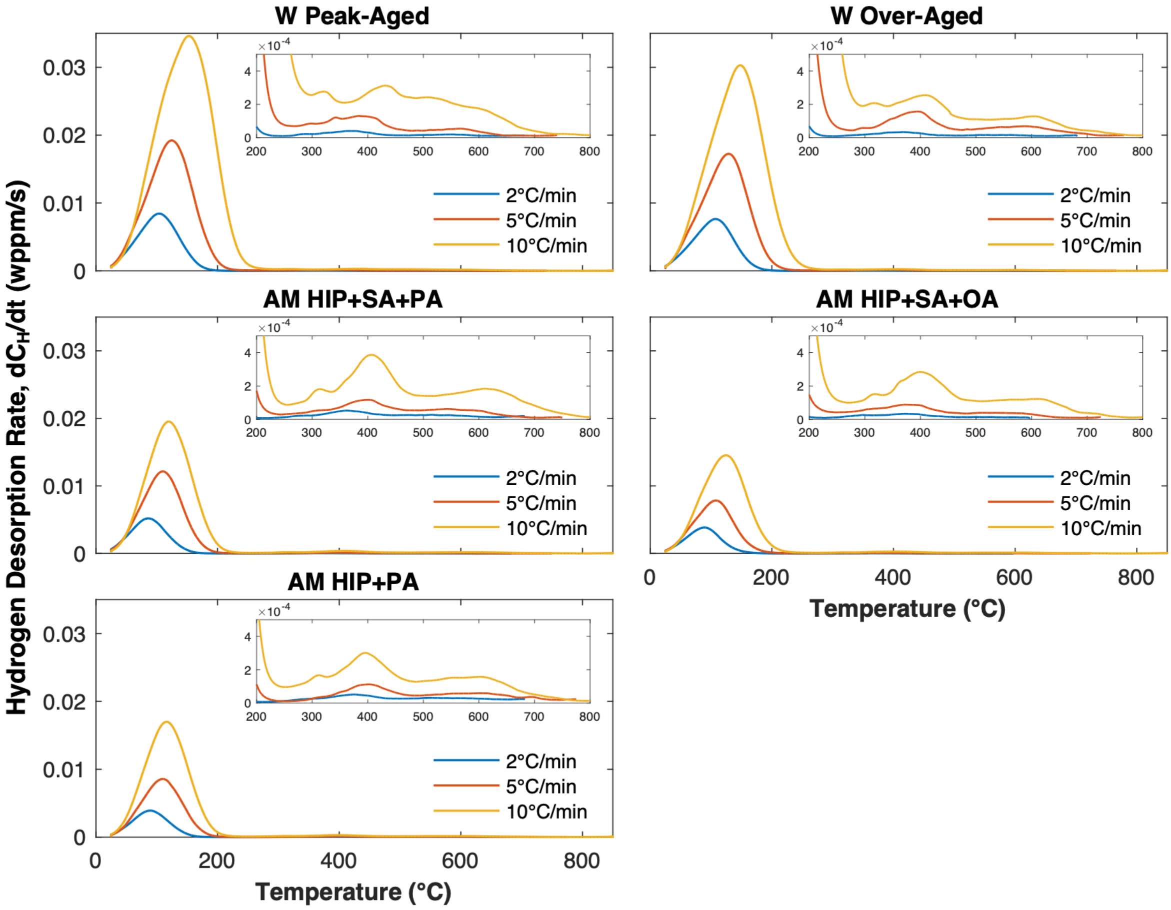

Figure 5.3: Ramp rate TDS data for peak-aged (left) and over-aged (right) wrought and AM 17-4 PH at 2, 5, and 10°C/min. The inset provides a closer look at small, high-temperature peaks not visible in the original scale.

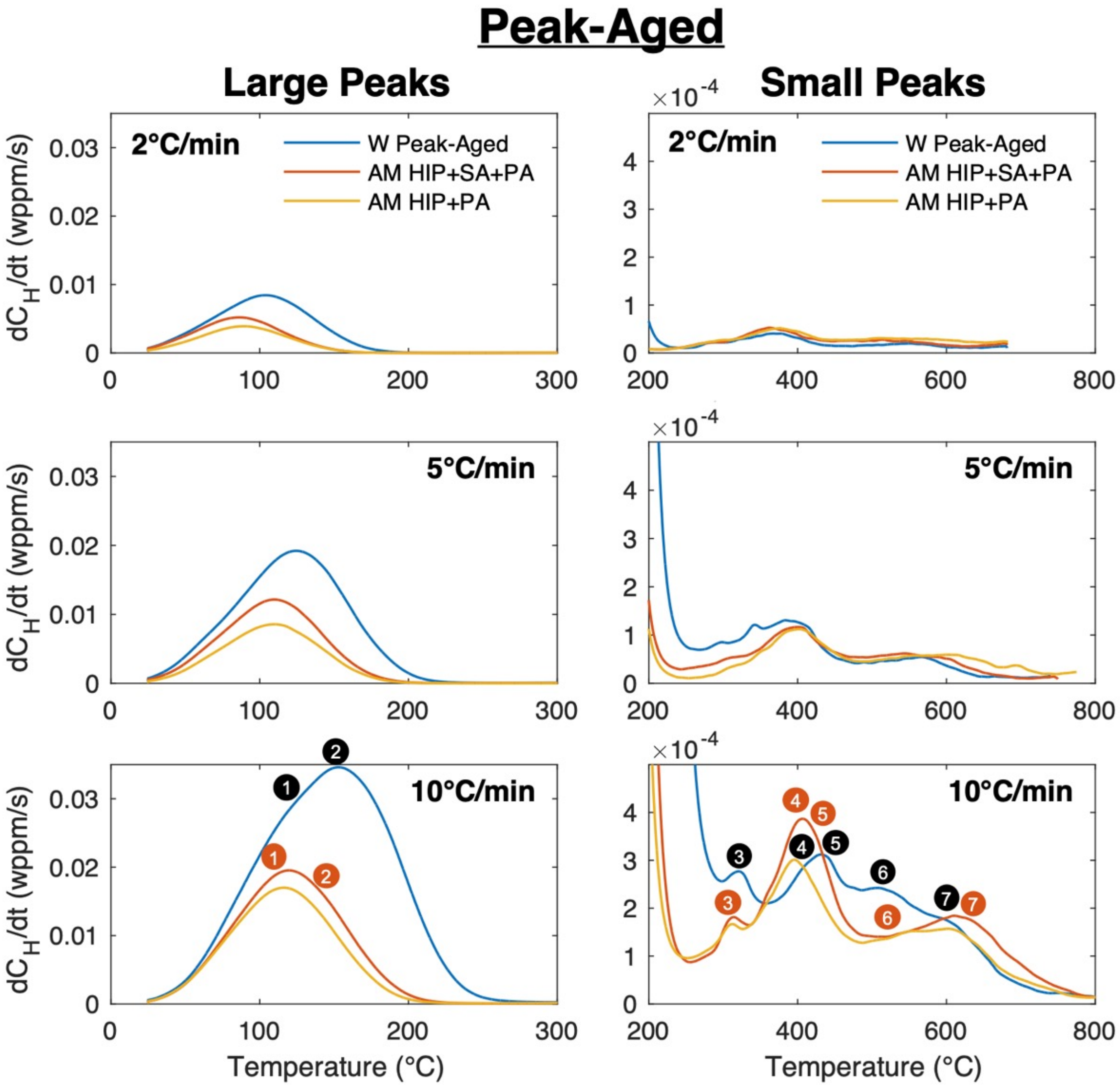

Figure 5.4: Ramp rate TDS results for the peak-aged specimens at 2, 5, and 10°C/min, with the initial large peaks on the left and the smaller high-temperature peaks shown on the right. In the 10°C/min data, each of the 7 possible peaks are labeled for AM and wrought specimens in orange and black, respectively.

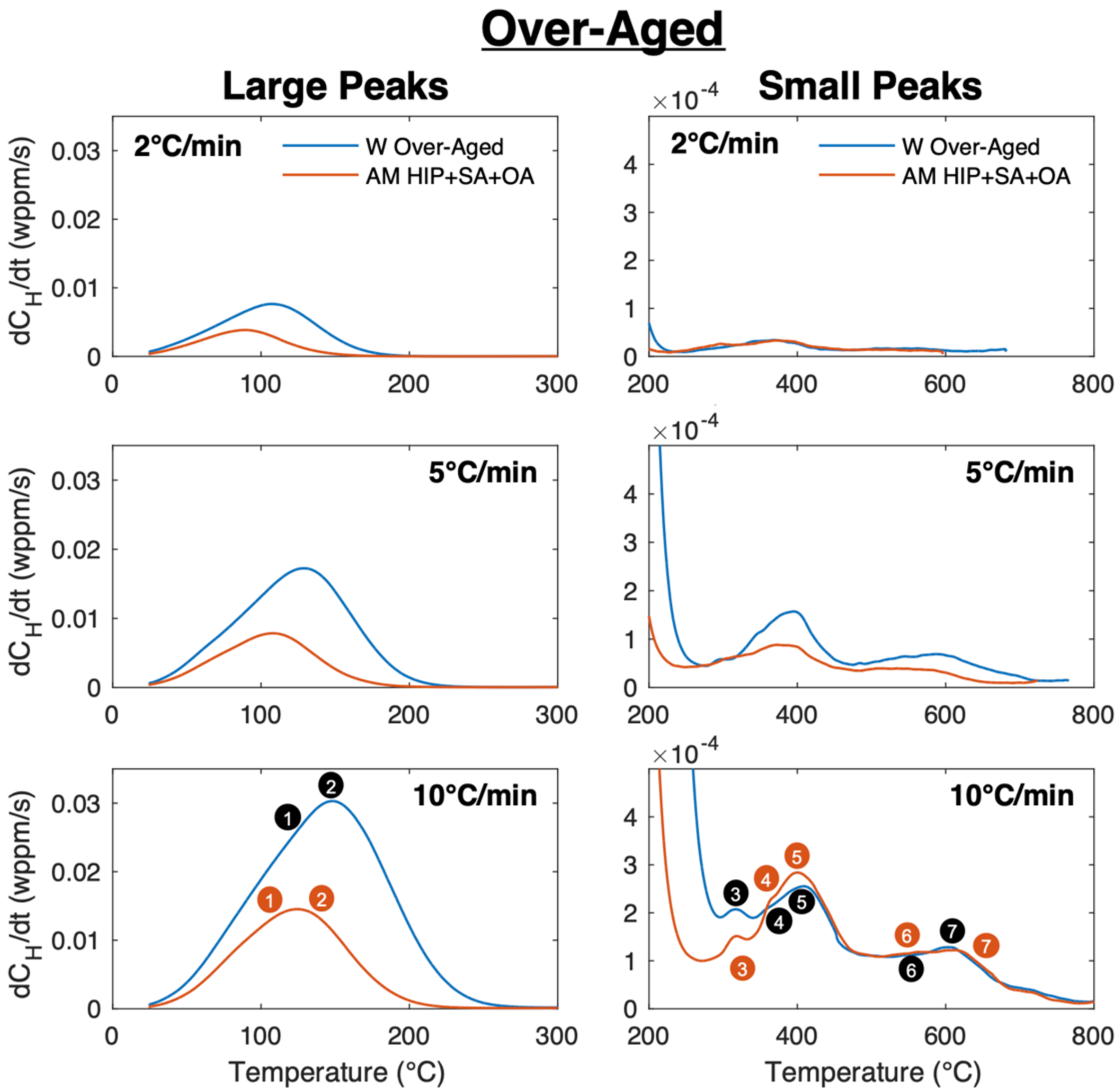

Figure 5.5: Ramp rate TDS results for the over-aged specimens at 2, 5, and 10°C/min, with the initial large peaks on the left and the smaller high-temperature peaks shown on the right. In the 10°C/min data, each of the 7 possible peaks are labeled for AM and wrought specimens in orange and black, respectively.

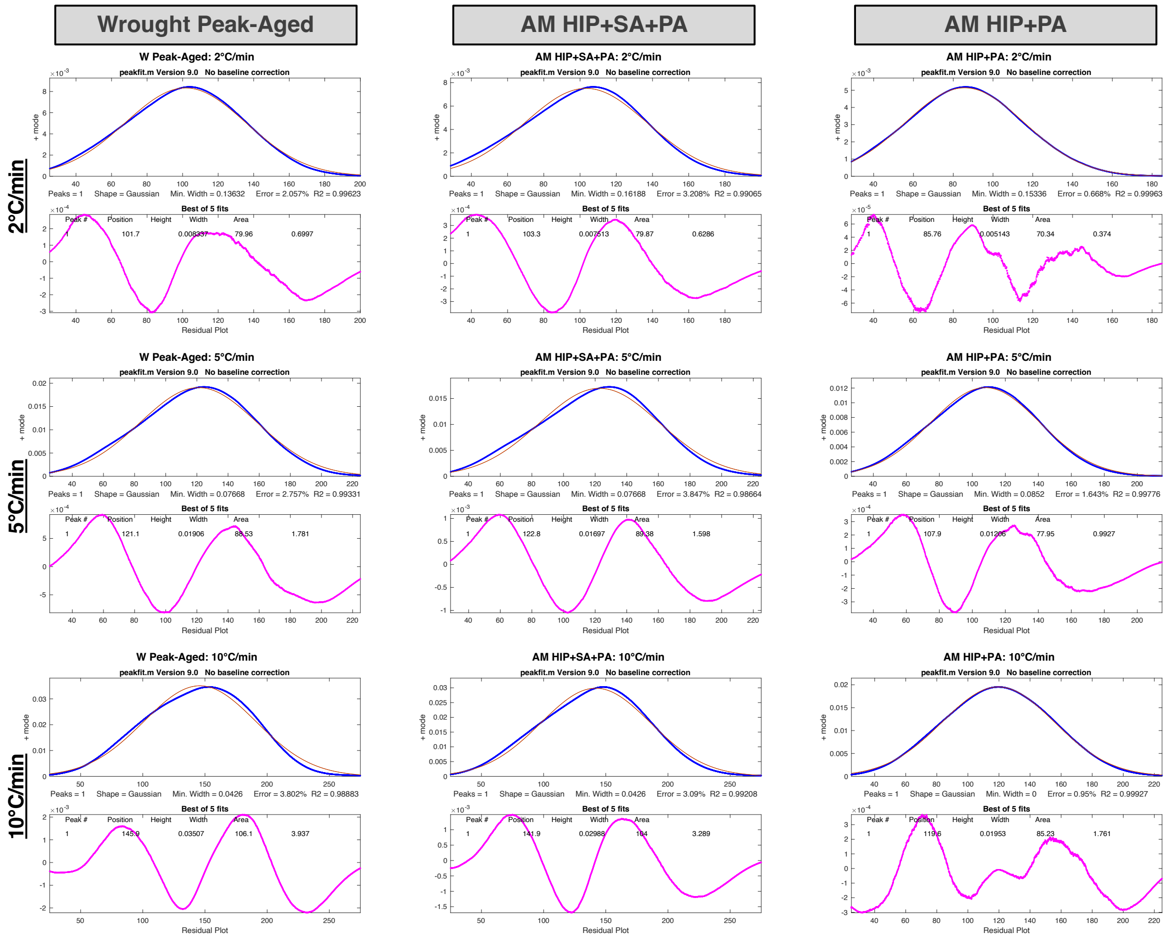

Figure 5.6: Fit of low-temperature peaks of the wrought and AM peak-aged specimens to a single-peak Gaussian model, with raw unsmoothed data shown in blue, fitted peaks in red, and residuals in pink. It can be seen that there are a large amount of concentrated residuals in the single-peak model, indicating a non-optimal fit.

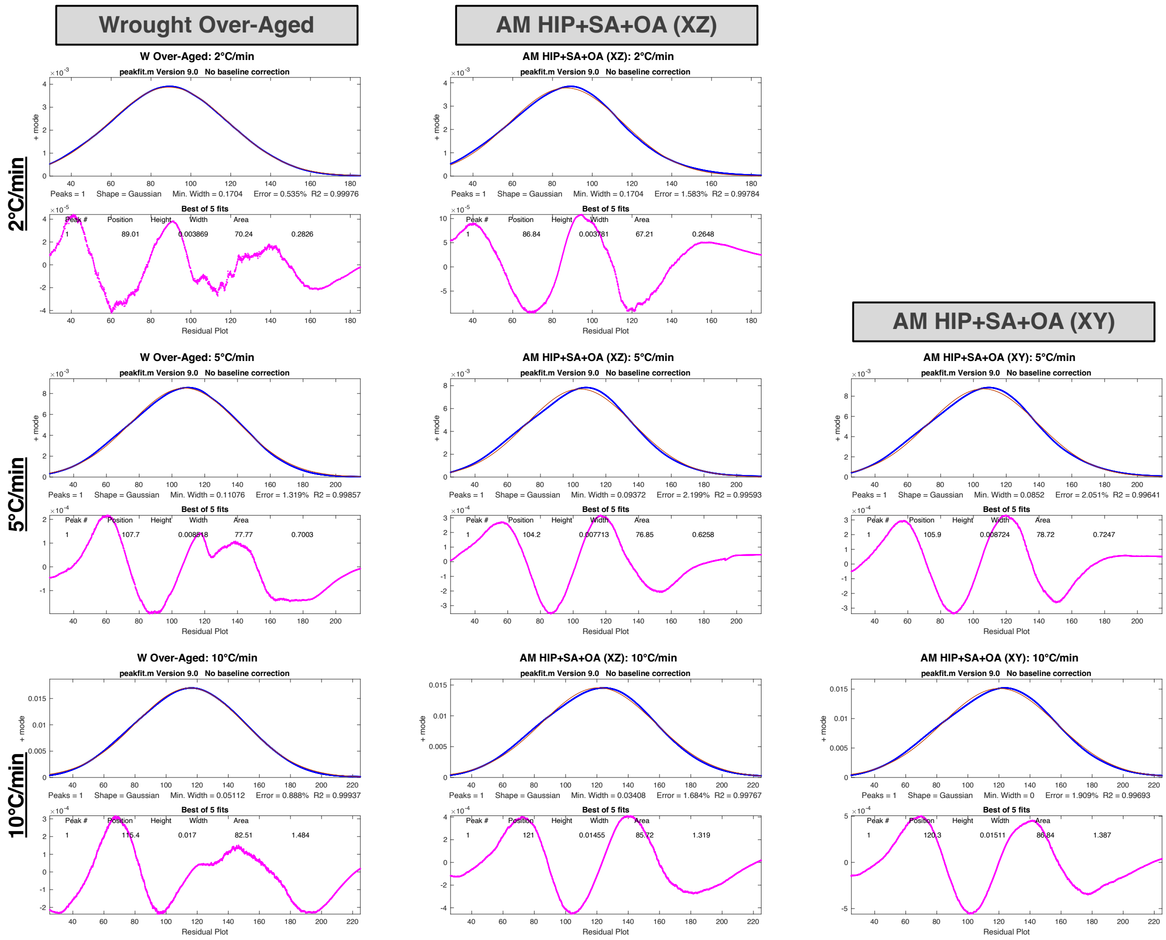

Figure 5.7: Fit of low-temperature peaks of the wrought and AM over-aged specimens to a single-peak Gaussian model, with raw unsmoothed data shown in blue, fitted peaks in red, and residuals in pink. It can be seen that there are a large amount of concentrated residuals in the single-peak model, indicating a non-optimal fit.

indicate that multi-peak fitting is required or possibly that there is a high skew in the spectra so that a symmetrical Gaussian fit is insufficient. Based on the shoulder that can be seen in the initial large peaks, especially on the left side of the curve for the wrought specimens examined at 10°C/min, it is likely that this single peak is actually composed of two overlapping peaks representing two reversible traps. This is demonstrated by the double-peak Gaussian fit analyses shown in Figure 5.8 for the peak-aged specimens and Figure 5.9 for the over-aged specimens. The residuals for each double-peak fit show a higher degree of scatter compared to the single-peak fits, which suggests that the low-temperature spectra do likely consist of two overlapping peaks.

This argument is also bolstered by the apparent rightward shift of the initial peak in the wrought specimen compared to the AM in both heat treatment conditions. Though Wei and Tsuzaki[42] noted that hydrogen concentration can affect site energy, the observed effect is a leftward shift in desorption peaks with increasing hydrogen concentration. The authors attribute this to a decrease in activation energy with increasing H content due to irreversible trap saturation. As the wrought initial peaks show a rightward shift, the difference is more likely due to the presence of multiple peaks instead of an effect of concentration, especially as the specimens in this study were charged to saturation. If there is a low-temperature reversible trap site with a much higher density in the wrought specimen compared to the AM specimen, this would cause the observed rightward shift and the clear increase in concentration in the wrought specimens.

In order to calculate desorption energy E_d, peak temperature (T_max) values for the single-peak and double-peak fits are plotted against $\ln \phi / T_\mathrm{max}^2$ as seen in Figure 5.10. The slope of the linear fit of these data can be related to E_d in accordance with Equation 5.4; desorption energy values for both types of fit are shown in Table 5.1. It should be noted that the desorption energies in the peak-aged wrought specimen are much lower than any other specimen; this is either due to a genuine increase in desorption energy, or simply may be due to a fitting issue based on the prevalence of the shoulder in the 10°C/min

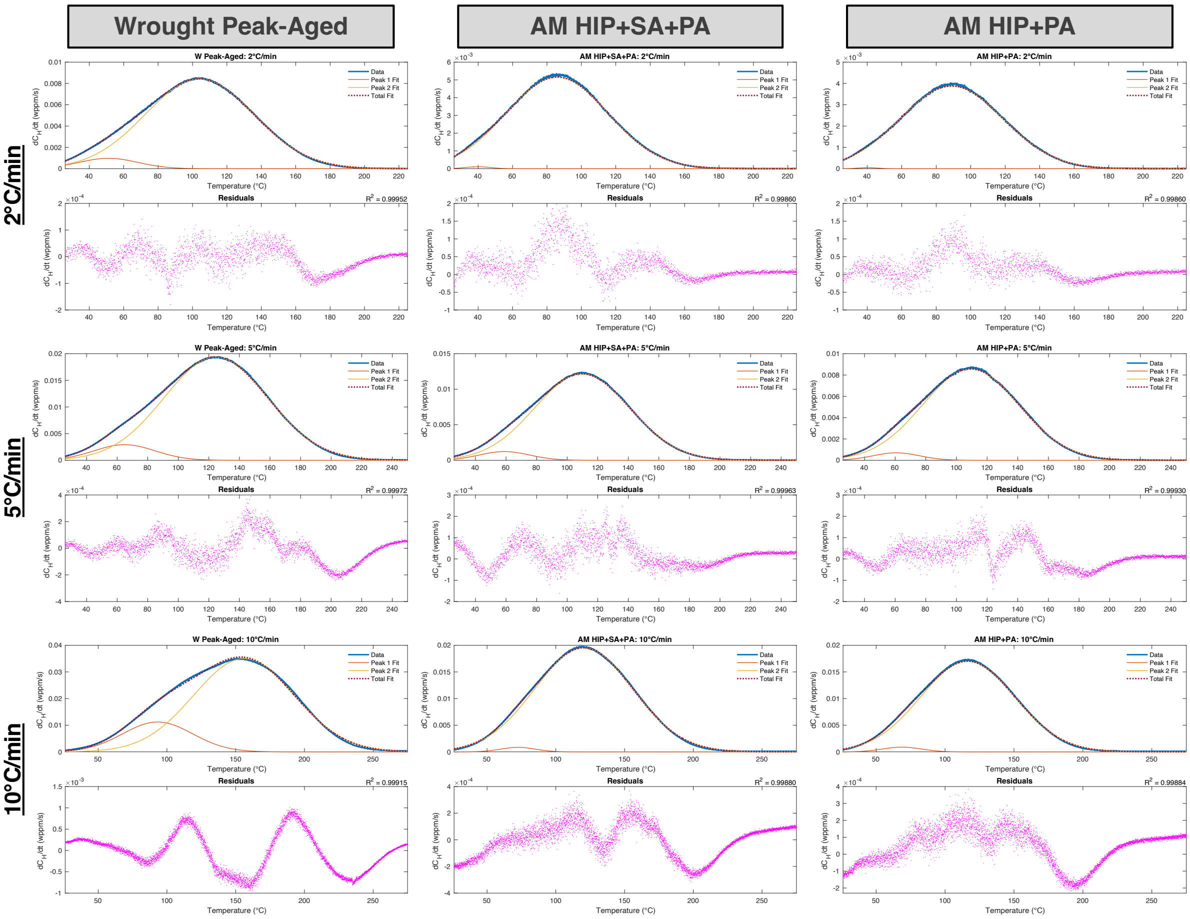

Figure 5.8: Fit of low-temperature peaks of the wrought and AM peak-aged specimens to a double-peak Gaussian model, with raw unsmoothed data shown in blue, fitted peaks in orange and yellow, total fit in red, and residuals in pink. Note the increased scatter of the residuals compared to the single-peak Gaussian model, indicating a more optimal fit.

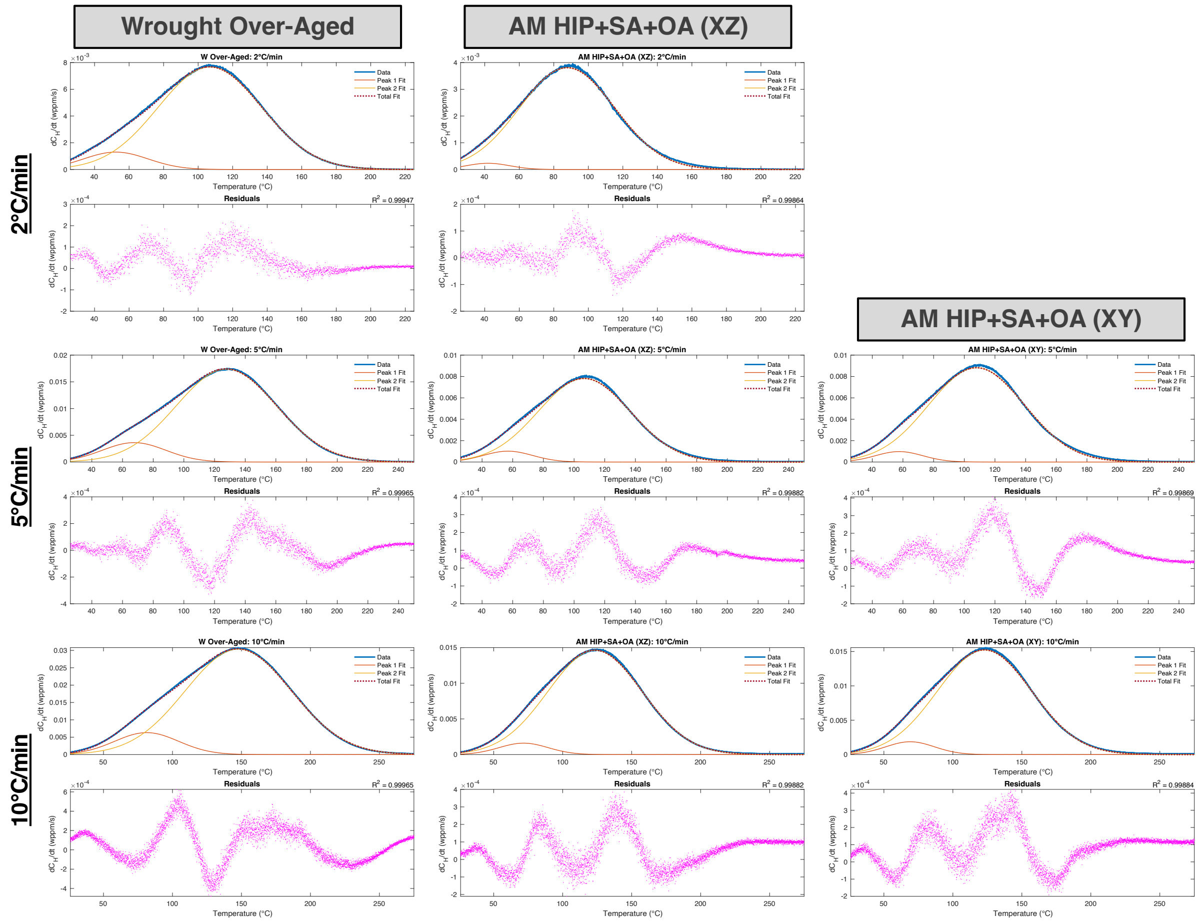

Figure 5.9: Fit of low-temperature peaks of the wrought and AM over-aged specimens to a double-peak Gaussian model, with raw unsmoothed data shown in blue, fitted peaks in orange and yellow, total fit in red, and residuals in pink. Note the increased scatter of the residuals compared to the single-peak Gaussian model, indicating a more optimal fit.

Table 5.1: Desorption energy E_d calculated from the ramp rate TDS analysis shown in Figure 5.10 for both single-peak and double-peak fitting.

Specimen	**Single-Peak E_d (kJ/mol)**	**Double-Peak E_d (kJ/mol)**	
		Peak 1	**Peak 2**
W Peak-Aged	40.7	30.5	34.4
AM HIP+SA+PA	48.3	38.6	46.6
AM HIP+PA	62.0	42.7	58.7
W Over-Aged	47.6	47.7	45.8
AM HIP+SA+OA	49.4	43.4	47.4

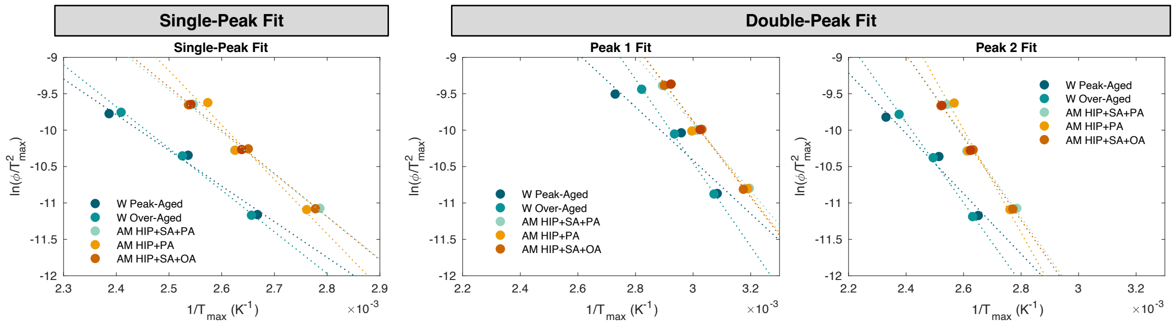

Figure 5.10: Reciprocal peak temperature versus $\ln \phi/T_\mathrm{max}^2$ for the low-temperature spectra for each specimen, with single-peak Gaussian fitting shown on the left and double-peak Gaussian fitting shown on the right. The dotted lines represent linear fits of the data.

spectra, as the wrought peak-aged results align well with the wrought over-aged results in both other ramp rates. In all other specimens, Peak 1 has a desorption energy between 38.6-43.4 kJ/mol, and Peak 2 has a desorption energy between 45.8-58.7 kJ/mol. The activation energy required for lattice diffusion of hydrogen is estimated to be between 4-7 kJ/mol;[63, 64] this can be used to estimate the binding energy based on Equation 5.7. This gives a binding energy range of approximately 31-40 kJ/mol for Peak 1, and 38-55 kJ/mol for Peak 2.

These results are in agreement with several literature-based binding energy values for reversible trap states in iron-based alloys.[65–68] However, it should be emphasized that these deconvolutions are speculative, as there is a high degree of overlap in the two peaks.

Due to the degree of noise and indistinguishability of the smaller peaks at low ramp rates, attempts at a full deconvolution of Peaks 3-7 were unsuccessful. An example of an attempted peak fitting of the high-temperature peaks is shown in Figure 5.11, which depicts a four-peak fit of the high-temperature TDS peaks for the wrought and AM over-aged specimens. The raw data are shown in blue, attempted fits in green, and residuals in pink. The R^2 value of each fit as well as the characteristics of each fitted peak are recorded in each plot. It is clear that the large amount of noise obfuscates the peaks, especially at low ramp rates.

Though rigorous deconvolution could not be achieved, several conclusions can be drawn by simple observation. The most consistent peaks throughout all ramp rates and conditions are Peaks 3, 5, and 7, and there are no peaks in the AM specimens that do not exist in the wrought in either heat treatment. At a ramp rate of 10°C/min, Peak 5 is larger in the AM HIP+SA+PA specimen than in its wrought counterpart, which is slightly shifted rightward; this is also true in the over-aged condition, though the difference is less dramatic and there is no rightward shift in the wrought results. However, this difference is not apparent in the other ramp rates, so this may be simply due to noise and the low magnitude of the results.

5.6 Discussion and Oriani-Type Trapping Model

It is pertinent to consider the microstructural basis of the observed increase in hydrogen diffusivity and decrease in hydrogen concentration in the AM specimens. An increase in D_{eff} in the AM materials can be theoretically attributed to two overarching factors: (1) an increase in hydrogen trapping in the wrought alloys, and/or (2) the presence of a fast diffusion pathway in the AM alloys. In essence, there must exist a microstructural difference between the alloys that either increases the rate of diffusion in the additive material or decreases the rate of diffusion in the wrought. The role of several microstructural features that could potentially affect diffusivity is addressed in this section, and the trapping ability of these features is examined using an Oriani-type trapping model and compared

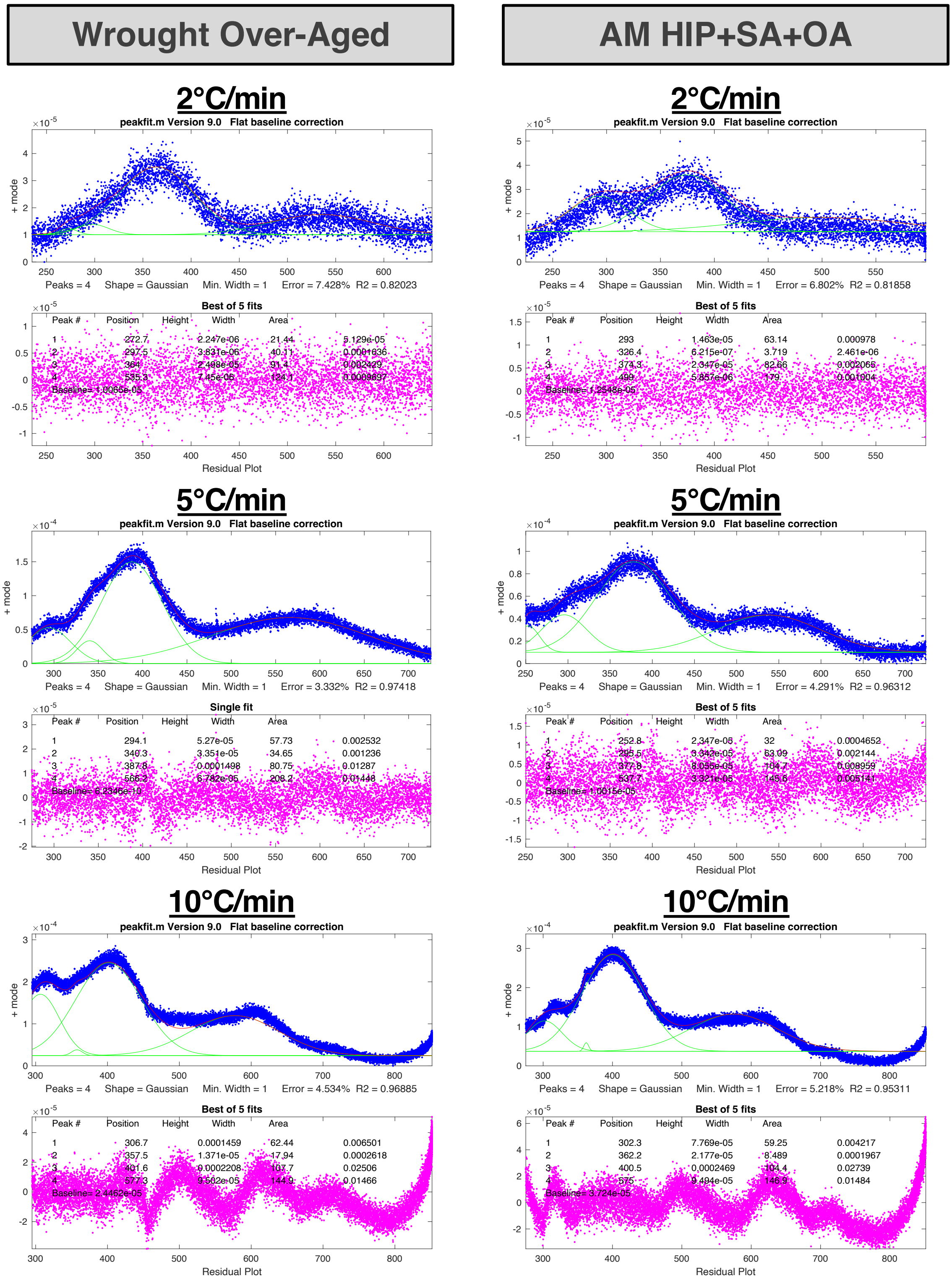

Wrought Over-Aged, 2°C/min:

```
Peaks = 4   Shape = Gaussian   Min. Width = 1   Error = 7.428%  R2 = 0.82023

Best of 5 fits
Peak #      Position     Height     Width        Area
1                272.7              2.247e-06    21.44         5.129e-05
2                297.5              3.831e-06    40.11         0.0001636
3                364                2.498e-05    91.4          0.002429
4                535.3              7.45e-06     124.1         0.0009697
Baseline= 1.0065e-05
```

AM HIP+SA+OA, 2°C/min:

```
Peaks = 4   Shape = Gaussian   Min. Width = 1   Error = 6.802%  R2 = 0.81858

Best of 5 fits
Peak #      Position     Height     Width        Area
1                293                1.463e-05    63.14         0.000978
2                326.4              6.215e-07    3.719         2.461e-06
3                374.3              2.347e-05    82.66         0.002065
4                499                5.857e-06    179           0.001004
Baseline= 1.2548e-05
```

Wrought Over-Aged, 5°C/min:

```
Peaks = 4   Shape = Gaussian   Min. Width = 1   Error = 3.332%  R2 = 0.97418

Single fit
Peak #      Position     Height     Width        Area
1                294.1              5.27e-05     57.73         0.002532
2                340.3              3.351e-05    34.65         0.001236
3                387.8              0.0001498    80.75         0.01287
4                566.2              6.782e-05    208.2         0.01448
Baseline= 6.2346e-10
```

AM HIP+SA+OA, 5°C/min:

```
Peaks = 4   Shape = Gaussian   Min. Width = 1   Error = 4.291%  R2 = 0.96312

Best of 5 fits
Peak #      Position     Height     Width        Area
1                252.8              2.347e-05    32            0.0004652
2                295.5              3.342e-05    63.09         0.002144
3                377.8              8.055e-05    104.7         0.008959
4                537.7              3.321e-05    145.6         0.005141
Baseline= 1.0015e-05
```

Wrought Over-Aged, 10°C/min:

```
Peaks = 4   Shape = Gaussian   Min. Width = 1   Error = 4.534%  R2 = 0.96885

Best of 5 fits
Peak #      Position     Height     Width        Area
1                306.7              0.0001459    62.44         0.006501
2                357.5              1.371e-05    17.94         0.0002618
3                401.6              0.0002208    107.7         0.02506
4                577.3              9.502e-05    144.9         0.01466
Baseline= 2.4462e-05
```

AM HIP+SA+OA, 10°C/min:

```
Peaks = 4   Shape = Gaussian   Min. Width = 1   Error = 5.218%  R2 = 0.95311

Best of 5 fits
Peak #      Position     Height     Width        Area
1                302.3              7.769e-05    59.25         0.004217
2                362.2              2.177e-05    8.489         0.0001967
3                400.5              0.0002469    104.4         0.02739
4                575                9.494e-05    146.9         0.01484
Baseline= 3.724e-05
```

Figure 5.11: Attempted fit of high-temperature peaks in the over-aged specimens to a four-peak Gaussian model, with raw unsmoothed data shown in blue, fitted peaks in green, and residuals in pink. It can be seen that the amount of noise, especially in the slow ramp rate data, obfuscates the high-temperature peaks.

to the ramp rate thermal desorption spectra.

5.6.1 Derivation of Model

The hydrogen trapping model developed by McNabb and Foster[9] and Oriani[8] and updated by Krom and Bakker[69] is commonly used to model trapping in steels. McNabb and Foster proposed a model to describe reversible trapping based on Fick's second law, taking into account the interaction between lattice and trap sites and assuming no interaction between trap sites. This model originates from the premise that total hydrogen concentration is the sum of the hydrogen concentration in trap states ($C_{\mathrm{H,T}}$) and in the lattice ($C_{\mathrm{H,L}}$):

$$C_{\mathrm{H,tot}} = C_{\mathrm{H,T}} + C_{\mathrm{H,L}}. \tag{5.8}$$

Two partial differential equations are outlined to describe lattice H and trapped H concentration:[9]

$$\frac{\partial C_{\mathrm{H,L}}}{\partial t} + N_{\mathrm{T}} \frac{\partial \theta_{\mathrm{T}}}{\partial t} = D_{\mathrm{L}} \frac{\partial^2 C_{\mathrm{H,L}}}{\partial x^2}, \tag{5.9}$$

and

$$\frac{\partial \theta_{\mathrm{T}}}{\partial t} = k C_{\mathrm{H,L}}(1 - \theta_{\mathrm{T}}) - p\theta_{\mathrm{T}}, \tag{5.10}$$

in which $C_{\mathrm{H,L}}$ is the ideal lattice concentration, t is time, N_{T} is the density of traps, θ_{T} is the occupied fraction of available trap sites, D_{L} is the lattice diffusion coefficient, x is location, and k and p are the trapping rate and detrapping rate parameters, respectively. The trapping and detrapping rate parameters are dependent on trapping energy E_{T} as well as trap binding energy E_{b} through the following Arrhenius-type relationships:[1, 9]

$$k = k_0 \exp\left(-\frac{E_{\mathrm{T}}}{RT}\right), \tag{5.11}$$

and

$$p = p_0 \exp\left(-\frac{E_{\mathrm{b}} + E_{\mathrm{T}}}{RT}\right). \tag{5.12}$$

The ratio $\frac{k_0}{p_0}$ can be shown to be constant at low trap occupancy and is inversely proportional to N_{L}.[1, 9]

Oriani expounds on this model by assuming the trap population and the lattice site population are in equilibrium during both static situations and diffusion.[8] This equilibrium between lattice and trap H can be described by equilibrium constant $K = \frac{a_{\mathrm{T}}}{a_{\mathrm{L}}}$, where a_{T} is the H activity in trapping sites and a_{L} is H activity in normal lattice sites. Activity is related to the occupied fraction of available sites θ_i by $a_i = \frac{\theta_i}{1-\theta_i}$, where $a_i = 0$ when $\theta_i \to 0$. Thereby, the equilibrium constant can be related to the occupied fraction of available sites:[1, 8]

$$K = \left(\frac{\theta_{\mathrm{T}}}{1-\theta_{\mathrm{T}}}\right)\left(\frac{\theta_{\mathrm{L}}}{1-\theta_{\mathrm{L}}}\right)^{-1} = \exp\left(-\frac{E_{\mathrm{b}}}{RT}\right). \tag{5.13}$$

Assuming low lattice H concentrations and low occupancy of available trap sites, Oriani relates the concentration of trapped and lattice hydrogen using the number of trap and lattice sites per unit volume (N_{T} and N_{L}, respectively):[1, 8]

$$C_{\mathrm{H,T}} \approx C_{\mathrm{H,L}} \frac{N_{\mathrm{T}}}{N_{\mathrm{L}}} \exp\left(\frac{E_{\mathrm{b}}}{RT}\right). \tag{5.14}$$

This allows the development of a relationship between effective diffusivity and lattice diffusivity by relating lattice and trap H concentrations:

$$D_{\mathrm{eff}} = D_{\mathrm{L}} \frac{C_{\mathrm{H,L}}}{C_{\mathrm{H,L}} + C_{\mathrm{H,T}}(1-\theta_{\mathrm{T}})}, \tag{5.15}$$

which can be arranged into the following expression when a low trap occupancy is assumed:

$$D_{\mathrm{eff}} = \frac{D_{\mathrm{L}}}{1 + \frac{N_{\mathrm{T}}}{N_{\mathrm{L}}} \exp\left(\frac{E_{\mathrm{b}}}{RT}\right)}. \tag{5.16}$$

A theoretical example of the effect of binding energy E_{b} and number of trap sites N_{T} on effective diffusivity, with constant lattice diffusivity and number of lattice sites, can be

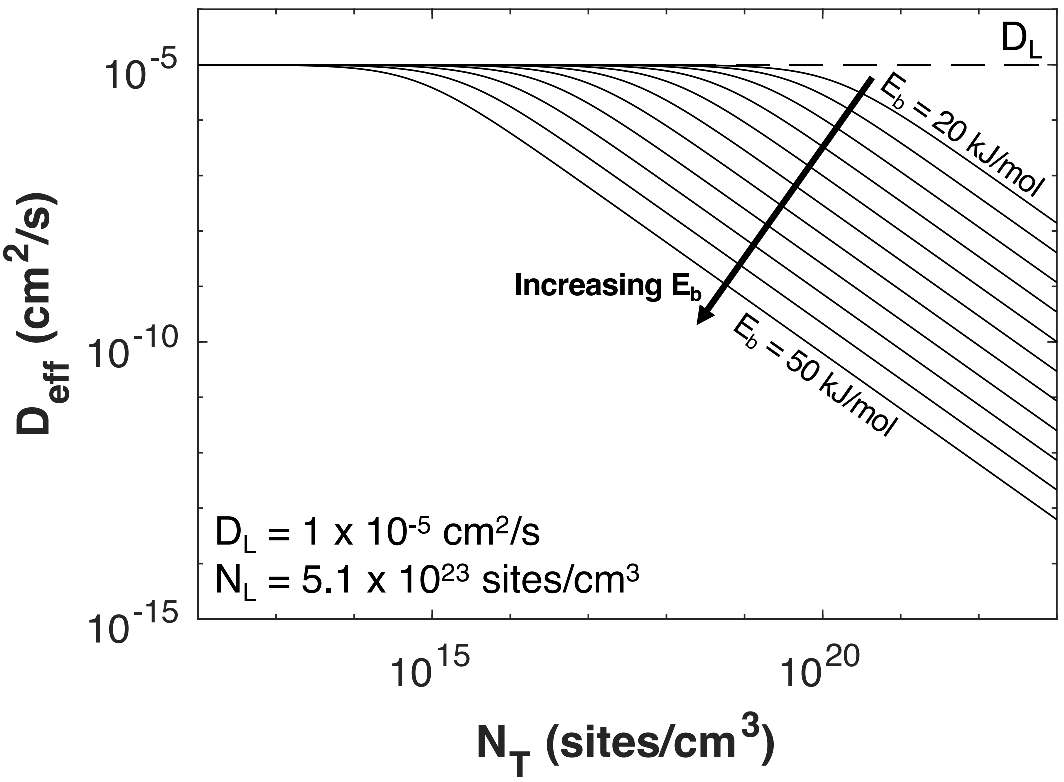

Figure 5.12: Theoretical effects of number of trap sites, effective diffusivity, and binding energy on Oriani trapping with fixed lattice diffusivity and number of lattice sites.

seen in Figure 5.12. It is apparent that a trap site with sufficiently low values of trap density or binding energy will have little effect on diffusivity.

This expression can be used to analyze the influence of multiple traps on effective diffusivity through a summation of the trap term in the denominator, where i denotes the ith type of trap site and n is the total number of trap sites:

$$D_{\text{eff}} = \frac{D_{\text{L}}}{1 + \sum_{i=1}^{n} \frac{N_{\text{T}}^{i}}{N_{\text{L}}} \exp\left(\frac{E_{\text{b}}^{i}}{RT}\right)}. \tag{5.17}$$

If the relevant and quantifiable traps in 17-4 PH are Cu-rich precipitates, NbC-type carbides, dislocations, high-angle grain boundaries, low-angle grain boundaries, and CSL-type grain boundaries, the summation term in the denominator can be expanded to become:

$$\begin{aligned}\sum_{i=1}^{n}\frac{N_{\mathrm{T}}^{i}}{N_{\mathrm{L}}}\exp\left(\frac{E_{\mathrm{b}}^{i}}{RT}\right) = &\frac{N_{\mathrm{T,Cu}}}{N_{\mathrm{L}}}\exp\left(\frac{E_{\mathrm{b,Cu}}}{RT}\right)+\\ &\frac{N_{\mathrm{T,NbC}}}{N_{\mathrm{L}}}\exp\left(\frac{E_{\mathrm{b,NbC}}}{RT}\right)+\\ &\frac{N_{\mathrm{T,dis}}}{N_{\mathrm{L}}}\exp\left(\frac{E_{\mathrm{b,dis}}}{RT}\right)+\\ &\frac{N_{\mathrm{T,HAGB}}}{N_{\mathrm{L}}}\exp\left(\frac{E_{\mathrm{b,HAGB}}}{RT}\right)+\\ &\frac{N_{\mathrm{T,LAGB}}}{N_{\mathrm{L}}}\exp\left(\frac{E_{\mathrm{b,LAGB}}}{RT}\right)+\\ &\frac{N_{\mathrm{T,CSL}}}{N_{\mathrm{L}}}\exp\left(\frac{E_{\mathrm{b,CSL}}}{RT}\right).\end{aligned} \tag{5.18}$$

When this expression is incorporated into Equation 5.17, the effect of each relevant microstructural trap on effective diffusivity can be appraised. However, this requires a quantitative estimation of the number of trap sites and the binding energy corresponding to each trap; this is discussed in the following sections.

5.6.2 Ideal Lattice

Krom and Bakker[69] estimate the number of lattice sites N_{L} based on the characteristics of the host lattice using the following relationship, assuming uniform ideal lattice structure with all interstitial trap sites active (i.e. repulsion between near neighbor hydrogen pairs is not significant enough to prevent total trap site saturation):

$$N_{\mathrm{L}} = \frac{N_{\mathrm{A}}\beta\rho}{A_r}, \tag{5.19}$$

in which N_{A} is Avogadro's number, β is the number of interstitial sites per atom in the unit cell, ρ is the density of the species (in this case, $\rho_{\mathrm{Fe}} = 7.87 \times 10^3$ kg/m^3), and A_r is the atomic weight of the species ($A_{r,\mathrm{Fe}} = 55.8 \times 10^{-3}$ kg/mol). For BCC iron with tetrahedral site occupancy ($\beta = 6$), this gives $N_{\mathrm{L}} = 5.1 \times 10^{29}$ m^{-3} for the number of

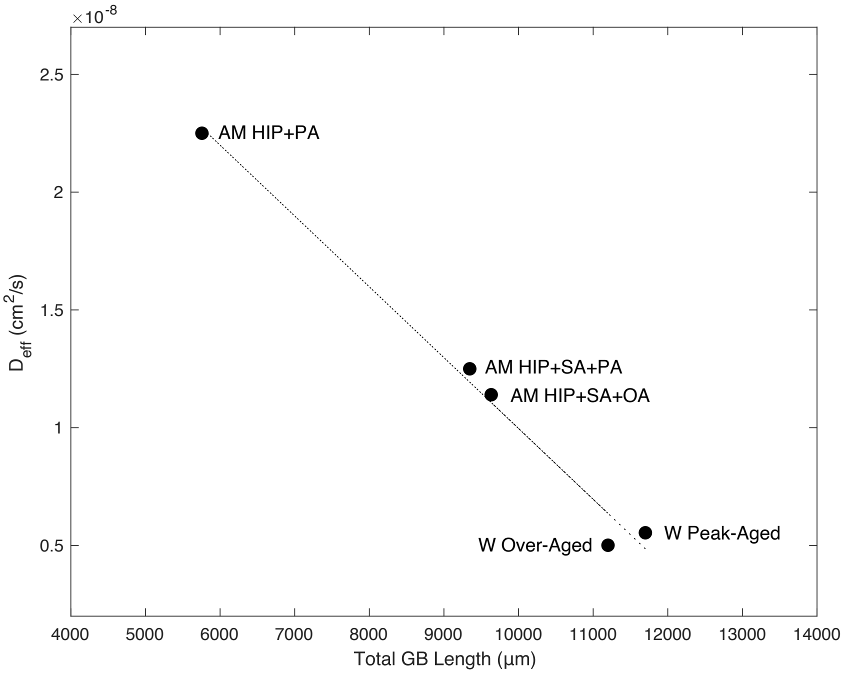

Figure 5.13: Total grain boundary length of each specimen compared to effective diffusivity, calculated using the curve fit of the first decay transient from electrochemical permeation.

lattice sites.[69]

5.6.3 Grain Boundaries

It can be seen in Figure 5.13 that there is a strong inverse correlation between the grain boundary length of each specimen and effective hydrogen diffusivity, which may suggest hydrogen trapping at grain boundaries in 17-4 PH. Hydrogen behavior is often material structure-dependent; though well-connected networks of high-angle grain boundaries have been shown in literature to function as fast diffusion pathways in FCC materials,[15–18] this behavior has not been widely observed in BCC or BCT materials. Hydrogen trapping at grain boundaries in BCC Fe has been predicted through kinetic Monte Carlo simulations[70] as well as density functional theory[71] and molecular dynamics[72–74] energy analyses. Choo and Lee,[75] Ono and Meshii,[76] and Sato and Takai[77] found differences in thermal desorption spectra with varying grain size in pure Fe, suggesting trapping at grain boundaries as well. This conclusion has been supported by several Fe permeation studies where grain size is varied.[31, 65, 78, 79] Grain boundary trapping behavior has also been observed in binary Fe alloys[13, 80, 81] and various body-centered steels.[79, 82–85] Shen et al.[5] theorized that changing heat treatment temperature causes a cross effect in the diffusivity of 17-4 PH—with increasing temperature, both prior austenite grain size and precipitate density increases, leading to a decrease in grain boundary trapping competing with an increase in precipitate trapping.

Additionally, it is well-established that the grain boundary diffusivity depends on the grain boundary character, with low-angle boundaries (those with misorientation angles $< 15°$) and coincident site lattice (CSL) boundaries generally considered to have reduced diffusivities relative to an ideal lattice and their high-angle counterparts.[54, 86, 87] While the low and high-angle boundary length fractions are generally similar across all tested conditions, the $\Sigma3$ CSL boundary length fraction trends appear to correlate with the observed change in D_{eff}. Specifically, the AM alloys have reduced $\Sigma3$ length fractions relative to comparable wrought material, as seen in Figure 5.14. This suggests that the differences in grain boundary character may be contributing to the observed increased D_{eff} in the AM materials, though these differences in grain boundary character are admittedly subtle.

Additionally, triple junctions, or nodes at the intersection of three grain boundaries, have been theorized to increase trapping at the boundary.[88] This is supported by the correlation between effective diffusivity and the fraction of triple junctions as seen in Figure 5.15, calculated by normalizing the number of triple junctions via dividing by the total grain boundary length.

It is also notable that, though intergranular fracture in this material has been shown to occur along PAGBs,[89] there is no correlation between the length fraction of PAGBs and effective diffusivity or grain boundary diffusivity, as seen in Figure 5.16.

Grain boundary trap density can be related to the number of lattice sites N_{L}, Burgers

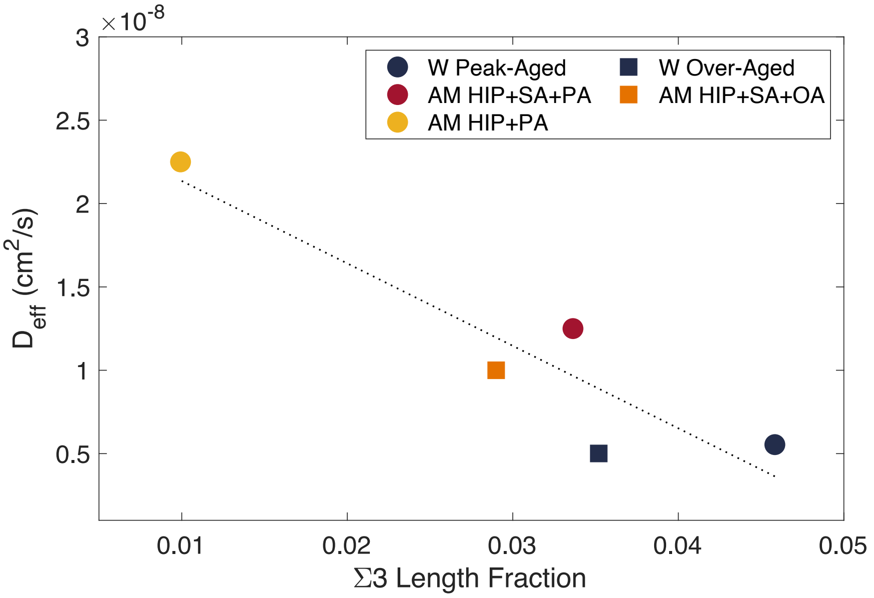

Figure 5.14: Length fraction of $\Sigma3$ CSL grain boundaries compared to effective diffusivity. A mild correlation is observable.

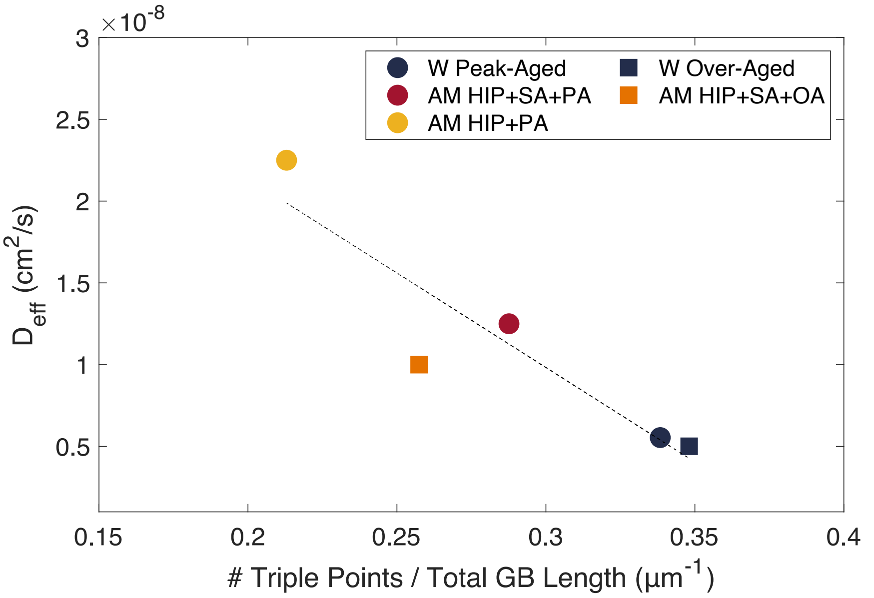

Figure 5.15: Normalized fraction of triple junctions compared to effective diffusivity. A mild correlation is observable.

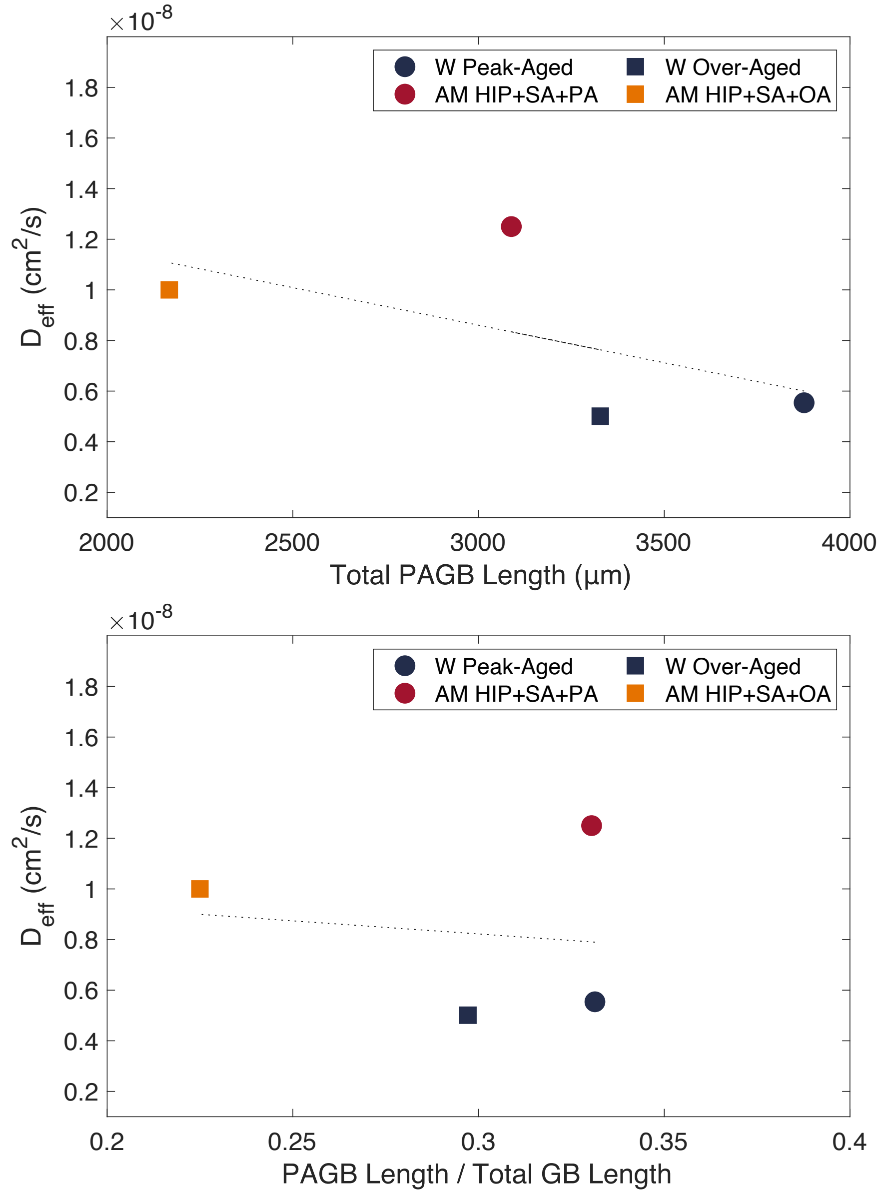

Figure 5.16: Total PAGB length (top) and PAGB length fraction (bottom) compared to effective diffusivity; no significant correlation between diffusion and PAGB length is evident.

vector $\bar{b}$ (0.287 nm for BCC Fe) and average grain size $\bar{d}$ assuming the boundary has a similar trapping capability to that of the lattice but over an interface thickness equal to one burgers vector:[90, 91]

$$N_{\mathrm{T,gb}} = \frac{N_{\mathrm{L}}\bar{b}}{\bar{d}}. \tag{5.20}$$

The number of lattice sites N_{L} is 5.1×10^{23} sites/cm^3 for a BCC lattice with tetrahedral site occupancy.[69] Given the average grain size is between 1 and 4 μm depending on the alloy, this gives a range of $N_{\mathrm{T,gb}}$ values between 4 - 9×10^{19} sites/cm^3. This is higher than some of the reported grain boundary trap density values[65, 92, 93] but similar to the value determined by Fernández-Sousa et al.[94] for 42CrMo4 steel.

There is a wide range of binding energies attributed to grain boundaries in literature, but the majority of studies place the binding energy of high-angle or random grain boundaries somewhere between 25 and 42 kJ/mol.[65–68] This aligns well with the binding energy observed in ramp rate TDS for the initial two low-temperature peaks, possibly indicating that one of the two initial peaks can be attributed to grain boundaries—likely Peak 1, which is visibly larger in the wrought specimens compared to the AM specimens, as would be expected for the grain boundary peak due to the smaller grain size in wrought.

Low-angle and special grain boundaries are more likely to have higher binding energies, depending on the grain boundary type; energies up to 92 kJ/mol have been observed in twist special CSL-type boundaries.[95] It is likely that the substantial fraction of low-angle grain boundaries and $\Sigma 3$ grain boundaries can possibly account for some of the high-temperature trap states seen in ramp rate TDS.

5.6.4 Precipitates

As precipitates in 17-4 PH often function as strong trap sites,[5, 96] comparison of precipitate size and density can provide insight into trapping behavior. The comparable yield strengths between wrought and AM alloys[89] imply some degree of similarity between AM and wrought Cu-rich precipitate characteristics (since the yield strength in 17-4 PH is potently dependent on the precipitate morphology).[97] Indeed, as seen in Section 2.6.3, the total Cu-rich precipitate surface area per unit volume is very similar between the AM and wrought over-aged specimens. However, the marginally finer precipitate size in the wrought specimens increases the surface area-volume ratio, leading to a slightly lower volume density of precipitates compared to the AM specimens. This could be due to the minor difference in copper content between the wrought and AM builds, with the wrought specimen having about 0.5 wt% Cu less than the AM specimen.[89]

It can be argued that the majority of trapping in Cu-rich precipitates occurs at the interface between the precipitate and the martensitic matrix. Schutz et al.[56] observed that the degree of trapping varied with the surface area of Cu-rich precipitates in 17-4 PH even when volume density remained constant, suggesting trapping mainly in the precipitate-matrix interface. Precipitate-matrix interfacial trapping has been previously theorized in literature to exacerbate brittle fracture in peak-aged hydrogen pre-charged 17-4 PH.[98] Thereby, the similarity in surface area in the wrought and AM over-aged 17-4 PH specimens suggests a comparative similarity in the trapping ability of their respective Cu-rich precipitates.

The trapping ability of precipitates can also be influenced by coherency; Yaguchi et al.[99] theorized that incoherent Cu-rich precipitates trap more hydrogen than their coherent counterparts, which have smaller misfit strain than precipitates like TiC and are therefore likely to be weak traps. Similarly, Shutz et al.[56] suggested that the interface between the matrix and Cu-rich precipitates in 17-4 PH acts as a weak trap for fine, semi-coherent precipitates, but as a strong trap for larger, incoherent precipitates.

Though other precipitates are relatively sparse compared to the Cu-rich precipitates, their effect on trapping must be considered as well. Specifically, the increased density and size of NbC-type carbides in the wrought specimens is a likely contributor to increased trapping in the wrought specimens. This can be considered through the lens of Oriani-type

Table 5.2: Surface area density ρ_{SA} and trap site density for Cu-rich precipitates, calculated using Equation 5.21.

Technique	**Specimen**	$\rho_{\mathbf{SA}}$ **(nm^{-1})**	$N_{\mathbf{T}}$ **(cm^{-3})**
HAADF	W OA	4.58×10^{-3}	6.70×10^{20}
	AM HIP+SA+OA	4.21×10^{-3}	6.16×10^{20}
EDS	W OA	4.27×10^{-3}	6.25×10^{20}
	AM HIP+SA+OA	4.49×10^{-3}	6.57×10^{20}

trapping; though the trap density of the carbides is orders of magnitude lower than the density of the copper-rich precipitates or grain boundaries, the reported high trapping energy of NbC in martensitic steel[100] will inflate their contribution to total trapping ability in the alloy.[8] Thermal desorption analysis by Chen et al.[101] suggests that, similar to the incoherent Cu-rich precipitates, hydrogen is likely trapped at the interface between the niobium carbides and the matrix.

Turk et al.[102] developed a model for trap site density of the carbide-matrix interface assuming that the interface had a similar trapping capacity to that of the lattice, but over an interface thickness equal to one burgers vector $\bar{b}$ on the surface of each carbide:

$$N_{\mathrm{T}} = N_{\mathrm{L}}\bar{b}\rho_{\mathrm{SA}}, \tag{5.21}$$

where N_{L} is the number of lattice sites and ρ_{SA} is the surface area density. Turk et al.[102] use the product of carbide surface area and carbide number density to estimate surface area density; in the case of this study, the calculation of surface area density can be seen in Section 2.6.3. The calculated surface area density and trap density for Cu-rich precipitates is shown in Table 5.2.

Little investigation has been performed in literature into the binding energy of Cu-rich precipitates; however, Lin et al.[103] postulates that Cu-rich precipitates in low-carbon martensitic steels have a greater trapping ability compared to dislocations, but do not

Table 5.3: Surface area density ρ_{SA} and trap site density N_{T} for niobium carbides, calculated using Equation 5.21.

Specimen	$\boldsymbol{\rho_{\mathrm{SA}}}$ **(nm^{-1})**	$\boldsymbol{N_{\mathrm{T}}}$ **(cm^{-3})**
W OA	6.6×10^{-3}	7.0×10^{18}
AM HIP+SA+OA	3.8×10^{-3}	5.2×10^{18}

trap as much hydrogen as grain boundaries. This might suggest that Peak 1 corresponds to Cu-rich precipitates, especially as the over-aged specimens and the HIP+PA specimens have larger desorption energies from Peak 1, possibly due to the precipitate coherency. However, it can also be argued that the order-of-magnitude increase in trap density of Cu-rich precipitates compared to grain boundaries may correlate to the much larger relative magnitude of Peak 2. If true, this could indicate that the Cu-rich precipitates actually have slightly increased binding energies compared to grain boundaries. However, it should be noted that this conclusion is dependent on the assumption that these peaks were deconvoluted perfectly, which is uncertain due to the high degree of overlap of the two peaks.

Carbides, in contrast with Cu-rich precipitates, tend to have much higher binding energies. Carbide precipitate interface binding energies ranging from approximately 40-95 kJ/mol have been observed in iron and iron-based alloys.[66, 104–106] Assuming interfacial trapping, the trap density of the large niobium carbides observed in the EBSD analysis can be calculated using Equation 5.21. Based on this analysis, the Nb-type carbides have a trap density two orders of magnitude smaller than the Cu-rich precipitates in the over-aged specimens, as seen in Table 5.3. However, this is still a large surface area fraction relative to other features, and when the high binding energy is considered, it is likely that one of the high-temperature ramp rate TDS peaks can be attributed to these carbides.

5.6.5 Dislocations

The mean and median KAM values of both wrought specimens as well as AM HIP+PA are all extremely similar, whereas AM HIP+SA+PA and AM HIP+SA+OA show a very slight decrease. This suggests that dislocations are not a driving factor in the difference in diffusivity between wrought and AM specimens. This conclusion is supported by literature; Sun et al. postulated that dislocations did not function as a significant trap in high-strength martensitic stainless steels when compared to secondary hardening precipitates.[107]

An experimental value for the dislocation trap density is difficult to obtain without extensive additional characterization. However, due to the low binding energy of dislocations reported in literature as well as the relatively low dislocation density (as seen in Table 5.4) and the similarity in dislocation density between the specimens, it can be argued that an estimation based on literature values is sufficient in this study.

It is possible that a low-temperature TDS peak corresponding to dislocations is concealed within the large initial peak, especially as dislocation density is likely relatively low compared to precipitate and grain boundary interfaces. The 25-minute rest period between electrochemical charging of the specimen and the initiation of ramp rate TDS may have also caused much of the hydrogen reversibly trapped in dislocations to desorb due to the low binding energy of dislocation trap sites.

5.6.6 Pores

One must also consider the potential impact of the observed pores in the AM 17-4 PH with regard to hydrogen trapping. The prevalence of pores in the AM specimens in this study is by no means unique in literature; widespread porosity in L-PBF 17-4 PH has been documented in numerous studies.[114–134] These pores are commonly attributed to entrapped gas, particularly argon, originating from the powder atomization process.[115, 128] Notably, due to the near-zero solubility of argon in iron, these pores are resistant to elimination

Table 5.4: Hydrogen binding energies and trap site densities found in literature for dislocations in iron and iron-based alloys.

Trap Site	E_b **(kJ/mol)**	**Source**	N_T **(sites/cm^3)**	**Source**
Dislocations	18	[108]	5×10^{13} - 5×10^{19}	[69]
	20-30 (screw)	[6]	10^{13} - 10^{20}	[92]
	24.1-29.9	[67]	2.7×10^{16}	[109]
	24.7 (screw)	[110]	4.9×10^{17}	[94]
	26.1 (screw)	[111]	3.3×10^{17}	[112]
	26.8	[75]	4.6×10^{19} (mixed-core)	[93]
	27	[113]	4×10^{20} (screw-core)	[93]
	27.3	[46]	4×10^{20} (elastic)	[93]

through hot isostatic pressing (HIP) or subsequent heat treatments.[117, 124, 135–137]

Though these pores have been linked to reduced ductility[118, 126, 138] and are postulated to exacerbate stress corrosion cracking,[89] there is little reason to believe that they function as strong hydrogen traps in the bulk material. As the pores are likely filled with entrapped gas, hydrogen trapping would occur along the pore-bulk interface, not the pore interior; and as the H-Ar binding energy is relatively weak,[139] it is reasonable to assume that there is not a strong trapping effect along this interface. Additionally, there is no major ramp rate TDS peak that only appears in the AM specimens, which would be the case if hydrogen was detrapped from the pore interface. Lastly, any degree of trapping would reduce hydrogen diffusivity and increase concentration in the additively manufactured 17-4 PH specimens. As the wrought specimens show faster diffusivity and higher concentration than the AM 17-4 PH, any effect of porosity on hydrogen behavior would be outweighed by increased trapping by grain boundaries and precipitates in the wrought counterpart.

5.6.7 Modeling Trapping Behavior

The ultimate purpose of modeling trapping behavior is to provide insight into whether the difference in calculated grain boundary density can account for the observed increase in diffusivity in the wrought specimens. The Oriani trapping model shown in Equation 5.17

Table 5.5: Trap site density N_{T} and binding energy E_{b} for Cu-rich precipitates, dislocations, NbCs, and grain boundaries used in the Oriani trapping model. Lattice diffusivity D_{L} and number of lattice sites N_{L} are also included.

Variable	**W**	**AM**	**Source**
$N_{\mathrm{T,Cu}}$ (sites/cm^3)	6.5×10^{20}	6.4×10^{20}	TEM, EDS
$N_{\mathrm{T,dis}}$ (sites/cm^3)	1.3×10^{17}	1.2×10^{17}	KAM, [92, 94, 112]
$N_{\mathrm{T,NbC}}$ (sites/cm^3)	7.0×10^{18}	5.2×10^{18}	EBSD
$N_{\mathrm{T,GB,tot}}$ (sites/cm^3)	7.9×10^{19}	6.5×10^{19}	EBSD
$N_{\mathrm{T,HAGB}}$ (sites/cm^3)	6.9×10^{19}	5.6×10^{19}	EBSD
$N_{\mathrm{T,LAGB}}$(sites/cm^3)	5.9×10^{18}	6.1×10^{18}	EBSD
$N_{\mathrm{T,CSL}}$ (sites/cm^3)	4.2×10^{18}	3.2×10^{18}	EBSD
$E_{\mathrm{b,Cu}}$ (kJ/mol)	25		TDS
$E_{\mathrm{b,dis}}$ (kJ/mol)	20		[6, 108]
$E_{\mathrm{b,NbC}}$ (kJ/mol)	43		[66]
$E_{\mathrm{b,LAGB}}$ (kJ/mol)	40		[66, 95]
$E_{\mathrm{b,CSL}}$ (kJ/mol)	40		[66, 95]
D_{L} (cm^2/s)	1.0×10^{-5}		[69]
N_{L} (cm^{-3})	5.1×10^{23}		[69]

can be populated with trap densities and energies either calculated using the previously discussed methods or adapted from literature, as seen in Table 5.5. The output of the trapping model based on these input parameters is shown in Figure 5.17, where the number of grain boundary trap sites is varied to calculate effective diffusivity. Because many of these values are estimated or taken from existing studies, this model is not a definitive quantitative analysis, but provides some approximation of the effects of different trap sites.

The first conclusion that can be drawn from this model is that the differences in non-HAGB trap densities and energies do impact the effective diffusivity to some degree, as shown in the variances between the wrought (blue) and AM (red) curves. The sensitivity of this model to changes in binding energy of each feature is examined in Figure 5.18, which shows the effect of a 10% increase in binding energy for LAGBs, CSLs, Cu-rich

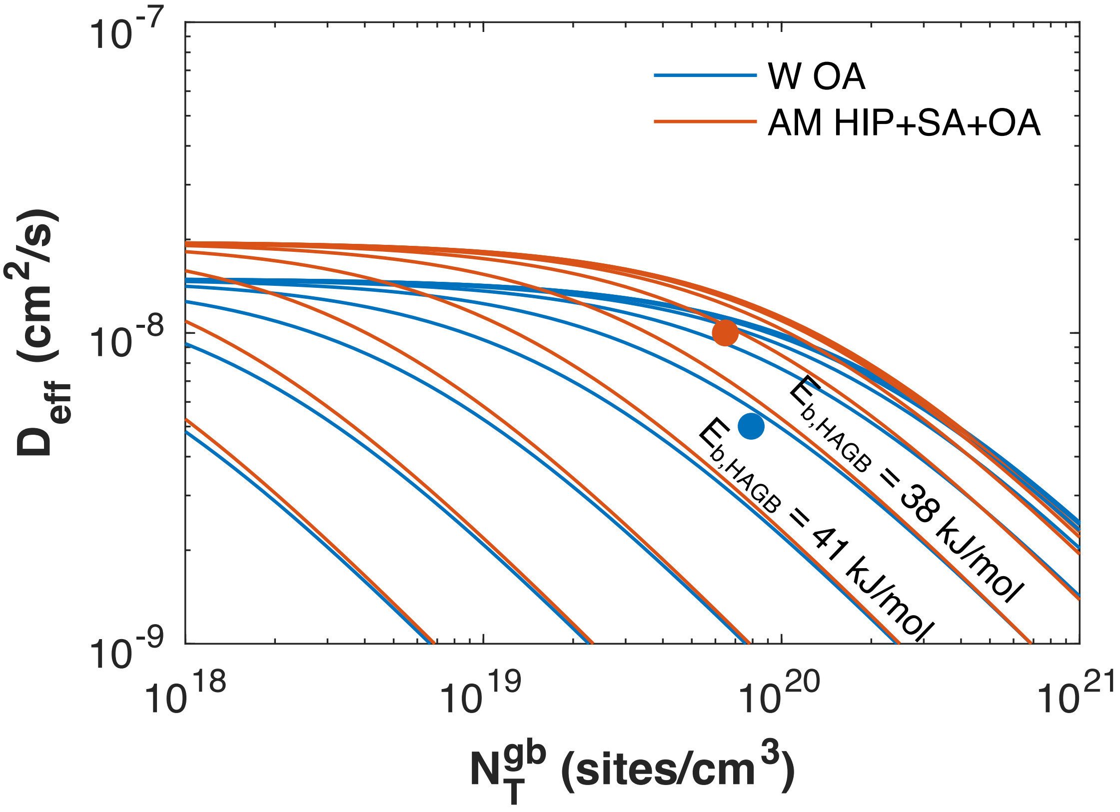

Figure 5.17: Oriani-type trapping model of effective diffusivity over a range of grain boundary trap densities and high-angle grain boundary binding energy values. Experimental results for AM and wrought over-aged specimens are shown with blue and red circular markers, based on first-decay electrochemical permeation diffusivity values as well as grain boundary trap density values calculated from EBSD in Section 5.6.3.

precipitates, dislocations, and NbCs. NbCs have the largest effect on the magnitude of the model, likely due to their relatively high trap density and binding energy values.

Additionally, though this model cannot quantitatively predict binding energy values, it does suggest that the increase in grain boundary density may explain the increase in effective diffusivity in the over-aged specimens if there is a slight increase in grain boundary binding energy in the wrought 17-4 PH compared to its AM counterpart. This could be due to factors like secondary particles along grain boundaries, increased triple junction density, or even thin reverted austenite films along grain boundaries. Further study is needed to fully characterize grain boundary-specific microstructure and nanochemistry to validate this conclusion.

5.7 Conclusions

Ramp rate thermal desorption spectroscopy was employed to compare microstructural hydrogen trap states in wrought and AM specimens in the peak-aged and over-aged conditions. Results show that the majority of hydrogen is trapped in low-energy reversible trap sites, with the wrought specimens in both conditions containing a larger amount of hydrogen trapped in these reversible sites. Comparisons with microstructural characterization suggest that these reversible trap sites likely include Cu-rich precipitates and high-angle grain boundaries, the latter of which are more prevalent in wrought 17-4 PH than AM 17-4 PH. The difference in grain boundary trap density is likely a main contributor to the increased effective diffusivity and decreased diffusible and reversible trapped hydrogen in the AM specimens. Though high-energy irreversible trap sites such as carbides, low-angle grain boundaries, and special grain boundaries likely contain only a small fraction of overall trapped hydrogen, the decrease in niobium carbide trap density in the AM specimens may also slightly contribute to the increased diffusivity and decreased hydrogen concentration. Lastly, as there is no visible desorption peak corresponding to a trap state unique to AM specimens, it can be assumed that the submicron porosity

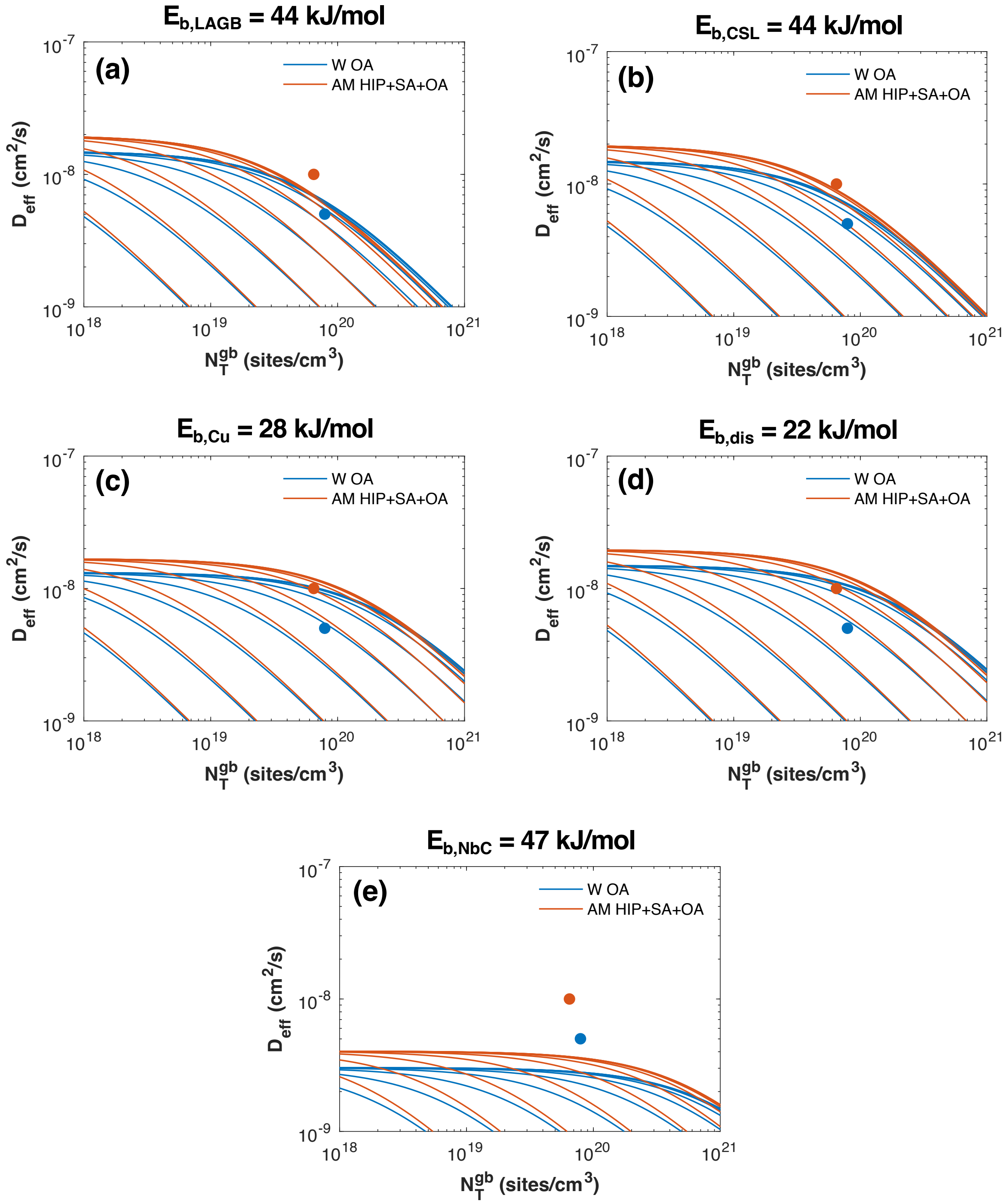

Figure 5.18: Effect of a 10% increase in binding energy of (a) low-angle grain boundaries, (b) special grain boundaries, (c) Cu-rich precipitates, (d) dislocations, and (e) NbC on the Oriani trapping model. A significant effect is noted for LAGBs and NbCs, attributable to their high binding energies and relatively high density.

present only in AM 17-4 PH likely does not function as a significant trap.

The correlation between grain size and effective diffusivity in the over-aged specimens is analyzed using an Oriani-type trapping model to explore if the decrease in grain boundary trap density can account for the increase in diffusivity in AM specimens when all other trap densities and binding energies are set. Results indicate that the increase in effective diffusivity can be tentatively attributed to changes in diffusivity if there is a slight increase in grain boundary binding energy between AM and wrought. Though this may be attributable to factors like triple junctions, future exploration into microstructural features and nanochemistry along the grain boundary is necessary.

References

[1] W. Siegl, *Hydrogen Trapping in Iron and Iron-Based Alloys.* PhD thesis, Montanuniversität Leoben, 2020. ISBN: 0815510276 Publisher: Montan University.

[2] R. P. Gangloff, "Critical issues in hydrogen assisted cracking of structural alloys," in *Environment-Induced Cracking of Materials*, pp. 141–165, Elsevier, 2008.

[3] A. Priyadarshi and R. Balasubramaniam, "On critical hydrogen concentration for hydrogen embrittlement of Fe3Al," *Bulletin of Materials Science*, 2001.

[4] J. O. Bockris and P. K. Subramanyan, "Hydrogen embrittlement and hydrogen traps," *Journal of The Electrochemical Society*, vol. 118, no. 7, pp. 1114–1119, 1971.

[5] S. Shen, X. Li, P. Zhang, Y. Nan, G. Yang, and X. Song, "Effect of solution-treated temperature on hydrogen embrittlement of 17-4 PH stainless steel," *Materials Science and Engineering A*, 2017.

[6] J. P. Hirth, "Effects of hydrogen on the properties of iron and steel," *Metallurgical Transactions A*, vol. 11, pp. 861–890, 1980.

[7] S. Thomas, G. Sundararajan, P. D. White, and N. Birbilis, "The effect of absorbed hydrogen on the corrosion of steels: Review, discussion, and implications," in *Corrosion*, 2017. ISSN: 00109312.

[8] R. A. Oriani, "The diffusion and trapping of hydrogen in steel," *Acta Metallurgica*, 1970.

[9] A. McNabb and P. K. Foster, "A New Analysis of the Diffusion of Hydrogen in Iron and Ferritic Steels," *Transactions of the Metallurgical Society of AIME*, 1963.

[10] D. Li, R. P. Gangloff, and J. R. Scully, "Hydrogen Trap States in Ultrahigh-Strength AERMET 100 Steel," *Metallurgical and Materials Transactions A: Physical Metallurgy and Materials Science*, vol. 35, pp. 849–864, 2004.

[11] R. L. Thomas, D. Li, R. P. Gangloff, and J. R. Scully, "Trap-governed hydrogen diffusivity and uptake capacity in ultrahigh-strength AERMET 100 steel," *Metallurgical and Materials Transactions A: Physical Metallurgy and Materials Science*, 2002.

[12] J. H. Ai, H. M. Ha, R. P. Gangloff, and J. R. Scully, "Hydrogen diffusion and trapping in a precipitation-hardened nickel-copper-aluminum alloy Monel K-500 (UNS N05500)," *Acta Materialia*, vol. 61, no. 9, pp. 3186–3199, 2013. ISBN: 13596454.

[13] T. Asaoka, G. Lapasset, M. Aucouturier, and P. Lacombe, "Observation of hydrogen trapping in Fe-0.15 wt% Ti alloy by high resolution autoradiography," *Corrosion*, vol. 34, no. 2, pp. 39–47, 1978.

[14] A. J. Kumnick and H. H. Johnson, "Deep trapping states for hydrogen in deformed iron," *Acta Metallurgica*, vol. 28, pp. 33–39, 1980.

[15] J. Yao and J. R. Cahoon, "Experimental studies of grain boundary diffusion of hydrogen in metals," *Acta Metallurgica Et Materialia*, vol. 39, no. 1, pp. 119–126, 1991.

[16] H. Magnusson and K. Frisk, "Self-diffusion and impurity diffusion of hydrogen, oxygen, sulphur and phosphorus in copper," tech. rep., Swedish Nuclear Fueland Waste Management Co, Stockholm, Dec. 2013. Publication Title: Swedish Nuclear Waste Management Company Technical Report.

[17] R. Kirchheim, T. Mütschele, W. Kieninger, H. Gleiter, R. Birringer, and T. D. Koblé, "Hydrogen in amorphous and nanocrystalline metals," *Materials Science and Engineering*, vol. 99, no. 1-2, pp. 457–462, 1988.

[18] T. Mütschele and R. Kirchheim, "Segregation and diffusion of hydrogen in grain boundaries of palladium," *Scripta Metallurgica*, vol. 21, no. 2, pp. 135–140, 1987.

[19] R. D. Calder, T. S. Elleman, and K. Verghese, "Grain boundary diffusion of tritium in 304- and 316-stainless steels," *Journal of Nuclear Materials*, vol. 46, no. 1, pp. 46–52, 1973.

[20] A. Brass and A. Chanfreau, "Accelerated diffusion of hydrogen along grain boundaries in nickel," *Acta Materialia*, vol. 44, pp. 3823–3831, Sept. 1996.

[21] U. Stuhr, T. Striffler, H. Wipf, H. Natter, B. Wettmann, S. Janssen, R. Hempelmann, and H. Hahn, "An investigation of hydrogen diffusion in nanocrystalline Pd by neutron spectroscopy," *Journal of Alloys and Compounds*, 1997.

[22] Y. Mine, K. Tachibana, and Z. Horita, "Grain-boundary diffusion and precipitate trapping of hydrogen in ultrafine-grained austenitic stainless steels processed by high-pressure torsion," *Materials Science and Engineering A*, vol. 528, pp. 8100–8105, 2011.

[23] T. Tsuru and R. M. Latanision, "Grain boundary transport of hydrogen in nickel," *Scripta Metallurgica*, vol. 16, no. 5, pp. 575–578, 1982.

[24] S. M. Lee and J. Y. Lee, “The Trapping and Transport Phenomena of Hydrogen in Nickel,” *Metallurgical Transactions A*, vol. 17, pp. 181–187, 1986.

[25] B. Ladna and H. K. Birnbaum, “SIMS study of hydrogen at the surface and grain boundaries of nickel bicrystals,” *Acta Metallurgica*, vol. 35, no. 10, pp. 2537–2542, 1987.

[26] A. Kimura and H. K. Birnbaum, “Hydrogen induced grain boundary fracture in high purity nickel and its alloys-Enhanced hydrogen diffusion along grain boundaries,” *Acta Metallurgica*, vol. 36, no. 3, pp. 757–766, 1988.

[27] T. M. Harris and M. Latanision, “Grain boundary diffusion of hydrogen in nickel,” *Metallurgical Transactions A*, vol. 22, pp. 351–355, 1991.

[28] G. Palumbo, D. M. Doyle, A. M. El-Sherik, U. Erb, and K. T. Aust, “Intercrystalline hydrogen transport in nanocrystalline nickel,” *Scripta Metallurgica et Materiala*, vol. 25, no. 3, pp. 679–684, 1991.

[29] M. Ichimura, Y. Sasajima, and M. Imabayashi, “Grain boundary effect on diffusion of hydrogen in pure aluminum,” *Materials Transactions, JIM*, vol. 32, no. 12, pp. 1109–1114, 1991.

[30] D. R. Arantes, X. Y. Huang, C. Marte, and R. Kirchheim, “Hydrogen diffusion and permeation in micro- and nanocrystalline nickel,” *Acta Metallurgica Et Materialia*, vol. 41, no. 11, pp. 3215–3222, 1993.

[31] W. Beck, J. Bockris, J. McBreen, and L. Nanis, “Hydrogen permeation in metals as a function of stress, temperature and dissolved hydrogen concentration,” *Proceedings of the Royal Society of London. Series A. Mathematical and Physical Sciences*, vol. 290, no. 1421, pp. 220–235, 1966.

[32] B. Chew and F. T. Fabling, “The effect of grain boundaries on the low-temperature diffusion of hydrogen in decarburized mild steel,” *Metal Science Journal*, 1972.

[33] V. M. Sidorenko and I. I. Sidorak, “Determination of diffusion characteristics of the volume and boundary components of the flow of hydrogen in polycrystalline metals,” *Soviet Materials Science*, 1975.

[34] V. M. Sidorenko and I. I. Sidorak, “Boundary and volume diffusion of hydrogen in copper, nickel, and iron,” *Soviet Materials Science*, vol. 9, pp. 372–375, 1975.

[35] R. M. Latanision and M. Kurkela, “Hydrogen Permeability and Diffusivity in Nickel and Ni-Base Alloys,” *Corrosion*, vol. 39, no. 5, pp. 174–181, 1983.

[36] J. Yao and J. R. Cahoon, “Theoretical modeling of grain boundary diffusion of hydrogen and its effect on permeation curves,” *Acta Metallurgica Et Materialia*, 1991.

[37] S. Heinze, B. Vuillemin, J. C. Colson, P. Giroux, and D. Leterq, “Relation between grain size and hydrogen diffusion coefficient in an industrial Pd-23% Ag alloy,” *Solid State Ionics*, vol. 122, no. 1-4, pp. 51–57, 1999.

[38] R. Kirchheim, “Solubility and diffusivity of hydrogen in complex materials,” *Physica Scripta T*, vol. 94, pp. 58–67, 2001.

[39] E. Tal-Gutelmacher, D. Eliezer, and E. Abramov, “Thermal desorption spectroscopy (TDS)-Application in quantitative study of hydrogen evolution and trapping in crystalline and non-crystalline materials,” *Materials Science and Engineering A*, 2007.

[40] Y. Yagodzinskyy, O. Todoshchenko, and S. Papula, “Hydrogen solubility and diffusion in austenitic stainless steels studied with thermal desorption spectroscopy,” in *Steel Research International*, 2011. ISSN: 16113683.

[41] B. A. Kehler, *Modeling and experiments to explain the potential dependency of an UHSS to hydrogen environment assisted cracking.* PhD thesis, University of Virginia, Charlottesville, VA, 2008.

[42] F. G. Wei and K. Tsuzaki, “Quantitative analysis on hydrogen trapping of TiC particles in steel,” *Metallurgical and Materials Transactions A: Physical Metallurgy and Materials Science*, 2006.

[43] H. E. Kissinger, “Variation of peak temperature with heating rate in differential thermal analysis kissinger,” *Journal of Research of the National Bureau of Standards*, vol. 57, no. 4, pp. 217–221, 1956.

[44] K. Verbeken, “Analysing hydrogen in metals: Bulk thermal desorption spectroscopy (TDS) methods,” in *Gaseous Hydrogen Embrittlement of Materials in Energy Technologies: Mechanisms, Modelling and Future Developments*, pp. 27–55, Woodhead Publishing, 2012.

[45] J. Y. Lee and S. M. Lee, “Hydrogen trapping phenomena in metals with B.C.C. and F.C.C. crystals structures by the desorption thermal analysis technique,” *Surface and Coatings Technology*, vol. 28, no. 3-4, pp. 301–314, 1986.

[46] G. A. Young and J. R. Scully, “The diffusion and trapping of hydrogen in high purity aluminum,” *Acta Materialia*, 1998.

[47] M. S. Bhuiyan, H. Toda, Z. Peng, S. Hang, K. Horikawa, K. Uesugi, A. Takeuchi, N. Sakaguchi, and Y. Watanabe, "Combined microtomography, thermal desorption spectroscopy, X-ray diffraction study of hydrogen trapping behavior in 7XXX aluminum alloys," *Materials Science and Engineering A*, vol. 655, pp. 221–228, 2016. Publisher: Elsevier.

[48] L. Cupertino-Malheiros, A. Oudriss, F. Thébault, M. Piette, and X. Feaugas, "Hydrogen Diffusion and Trapping in Low-Alloy Tempered Martensitic Steels," *Metallurgical and Materials Transactions A*, vol. 54, pp. 1159–1173, Apr. 2023.

[49] S. Frappart, A. Oudriss, X. Feaugas, J. Creus, J. Bouhattate, F. Thébault, L. Delattre, and H. Marchebois, "Hydrogen trapping in martensitic steel investigated using electrochemical permeation and thermal desorption spectroscopy," *Scripta Materialia*, vol. 65, no. 10, pp. 859–862, 2011.

[50] H. M. Ha, J. H. Ai, and J. R. Scully, "Effects of prior cold work on hydrogen trapping and diffusion in API X-70 line pipe steel during electrochemical charging," *Corrosion*, vol. 70, no. 2, pp. 166–184, 2014.

[51] T. Izumi and G. Itoh, "Thermal desorption spectroscopy study on the hydrogen trapping states in a pure aluminum," *Materials Transactions*, vol. 52, no. 2, pp. 130–134, 2011.

[52] R. Kirchheim, "Bulk Diffusion-Controlled Thermal Desorption Spectroscopy with Examples for Hydrogen in Iron," *Metallurgical and Materials Transactions A: Physical Metallurgy and Materials Science*, vol. 47, no. 2, pp. 672–696, 2016. Publisher: Springer US ISBN: 1543-1940.

[53] W. Krieger, S. V. Merzlikin, A. Bashir, A. Szczepaniak, H. Springer, and M. Rohwerder, "Spatially resolved localization and characterization of trapped hydrogen in zero to three dimensional defects inside ferritic steel," *Acta Materialia*, vol. 144, pp. 235–244, Feb. 2018.

[54] A. Oudriss, J. Creus, J. Bouhattate, E. Conforto, C. Berziou, C. Savall, and X. Feaugas, "Grain size and grain-boundary effects on diffusion and trapping of hydrogen in pure nickel," *Acta Materialia*, vol. 60, pp. 6814–6828, Nov. 2012.

[55] Y. D. Park, I. S. Maroef, A. Landau, and D. L. Olson, "Retained Austenite as a hydrogen trap in steel welds," *Welding Journal (Miami, Fla)*, vol. 81, no. 2, 2002.

[56] P. Schutz, L. Latu-Romain, F. Martin, Q. Auzoux, J. Adem, Y. Wouters, B. Ravat, and D. Menut, "Onto the role of copper precipitates and reverted austenite on

hydrogen embrittlement in 17-4 PH stainless steel," *Materials Characterization*, vol. 202, p. 113044, Aug. 2023.

[57] K. Wada, J. Yamabe, and H. Matsunaga, "Visualization of trapped hydrogen along grain boundaries and its quantitative contribution to hydrogen-induced intergranular fracture in pure nickel," *Materialia*, vol. 8, p. 100478, Dec. 2019.

[58] A. De Jong and J. Niemantsverdriet, "Thermal desorption analysis: Comparative test of ten commonly applied procedures," *Surface Science*, vol. 233, pp. 355–365, July 1990.

[59] A. Turnbull, R. B. Hutchings, and D. H. Ferriss, "Modelling of thermal desorption of hydrogen from metals," *Materials Science and Engineering A*, 1997.

[60] A. Raina, V. S. Deshpande, and N. A. Fleck, "Analysis of thermal desorption of hydrogen in metallic alloys," *Acta Materialia*, vol. 144, pp. 777–785, 2018. Publisher: Elsevier Ltd.

[61] K. Y. Lee, J. Y. Lee, and D. R. Kim, "A study of hydrogen-trapping phenomena in AISI 5160 spring steel," *Materials Science and Engineering*, vol. 67, no. 2, pp. 213–220, 1984.

[62] T. O'Haver, "peakfit.m," Jan. 2018.

[63] H. Hagi, "Diffusion Coefficient of Hydrogen in Iron without Trapping by Dislocations and Impurities," *Materials Transactions, JIM*, vol. 35, no. 2, pp. 112–117, 1994.

[64] K. Kiuchi and R. McLellan, "The solubility and diffusivity of hydrogen in well-annealed and deformed iron," in *Perspectives in Hydrogen in Metals*, pp. 29–52, Elsevier, 1986.

[65] A. Díaz, A. Zafra, E. Martínez-Pañeda, J. M. Alegre, J. Belzunce, and I. I. Cuesta, "Simulation of hydrogen permeation through pure iron for trapping and surface phenomena characterisation," *Theoretical and Applied Fracture Mechanics*, vol. 110, p. 102818, 2020. Publisher: Elsevier Ltd.

[66] C. Paes de Oliveira, M. Aucouturier, and P. LaCombe, "Hydrogen Trapping in BCC Fe-Cr Alloys (7 ˜ 9.4 Wt% Cr) as Studied by Microautoradiography - Contribution of Carbon-Hydrogen Interaction - Consequences on Hydrogen Cracking," *Corrosion*, vol. 36, no. 2, pp. 53–59, 1980. ISBN: 9788490225370.

[67] G. M. Pressouyre, "A classification of hydrogen traps in steel," *Metallurgical Transactions A*, vol. 10, pp. 1571–1573, Oct. 1979.

[68] I. Bernstein, “The effect of hydrogen on the deformation of iron,” *Scripta Metallurgica*, vol. 8, pp. 343–349, Apr. 1974.

[69] A. H. Krom and A. D. Bakker, “Hydrogen trapping models in steel,” *Metallurgical and Materials Transactions B: Process Metallurgy and Materials Processing Science*, vol. 31, pp. 1475–1482, 2000.

[70] Y. A. Du, J. Rogal, and R. Drautz, “Diffusion of hydrogen within idealized grains of bcc Fe: A kinetic Monte Carlo study,” *Physical Review B*, vol. 86, p. 174110, Nov. 2012.

[71] A. S. Kholtobina, R. Pippan, L. Romaner, D. Scheiber, W. Ecker, and V. I. Razumovskiy, “Hydrogen Trapping in bcc Iron,” *Materials*, vol. 13, p. 2288, May 2020.

[72] S. M. Teus and V. G. Gavriljuk, “Grain-Boundary Diffusion of Hydrogen Atoms in the -Iron,” *Metallofiz. Noveishie Tekhnol*, vol. 36, no. 10, pp. 1399–1410, 2014.

[73] X.-Y. Zhou, J.-H. Zhu, and H.-H. Wu, “Molecular dynamics studies of the grain-size dependent hydrogen diffusion coefficient of nanograined Fe,” *International Journal of Hydrogen Energy*, vol. 46, pp. 5842–5851, Jan. 2021.

[74] S. Teus, V. Mazanko, J.-M. Olive, and V. Gavriljuk, “Grain boundary migration of substitutional and interstitial atoms in -iron,” *Acta Materialia*, vol. 69, pp. 105–113, May 2014.

[75] W. Y. Choo and J. Y. Lee, “Thermal analysis of trapped hydrogen in pure iron,” *Metallurgical Transactions A*, vol. 13, pp. 135–140, Jan. 1982.

[76] K. Ono and M. Meshii, “Hydrogen detrapping from grain boundaries and dislocations in high purity iron,” *Acta Metallurgica et Materialia*, vol. 40, pp. 1357–1364, June 1992.

[77] R. Sato and K. Takai, “Quantitative hydrogen trap states on high-angle grain boundaries and at dislocations in iron,” *Scripta Materialia*, vol. 228, p. 115339, Apr. 2023.

[78] H. Iwaoka, M. Arita, and Z. Horita, “Hydrogen diffusion in ultrafine-grained iron with the body-centered cubic crystal structure,” *Philosophical Magazine Letters*, vol. 97, pp. 158–168, Apr. 2017.

[79] S. L. I. Chan, “Hydrogen trapping ability of steels with different microstructures,” *Journal of the Chinese Institute of Engineers*, vol. 22, no. 1, pp. 43–53, 1999.

[80] Y. Mine, Z. Horita, and Y. Murakami, “Effect of high-pressure torsion on hydrogen trapping in Fe–0.01 mass% C and type 310S austenitic stainless steel,” *Acta Materialia*, vol. 58, pp. 649–657, Jan. 2010.

[81] G. Pressouyre and I. Bernstein, “A kinetic trapping model for hydrogen-induced cracking,” *Acta Metallurgica*, vol. 27, pp. 89–100, Jan. 1979.

[82] T. Das, R. Chakrabarty, J. Song, and S. Yue, “Understanding microstructural influences on hydrogen diffusion characteristics in martensitic steels using finite element analysis (FEA),” *International Journal of Hydrogen Energy*, vol. 47, no. 2, pp. 1343–1357, 2022. Publisher: Hydrogen Energy Publications LLC.

[83] O. Kazum, H. Beladi, and M. B. Kannan, “Hydrogen permeation in twinning-induced plasticity (TWIP) steel,” *International Journal of Hydrogen Energy*, vol. 43, pp. 22685–22693, Dec. 2018.

[84] A. Turk, G. R. Joshi, M. Gintalas, M. Callisti, P. E. Rivera-Díaz-del Castillo, and E. I. Galindo-Nava, “Quantification of hydrogen trapping in multiphase steels: Part I – Point traps in martensite,” *Acta Materialia*, vol. 194, pp. 118–133, Aug. 2020.

[85] K. Takai, J. Seki, and Y. Homma, “Observation of Trapping Sites of Hydrogen and Deuterium in High-Strength Steels by Using Secondary Ion Mass Spectrometry,” *Materials Transactions, JIM*, vol. 36, no. 9, pp. 1134–1139, 1995.

[86] B. Osman Hoch, A. Metsue, J. Bouhattate, and X. Feaugas, “Effects of grain-boundary networks on the macroscopic diffusivity of hydrogen in polycrystalline materials,” *Computational Materials Science*, vol. 97, pp. 276–284, Feb. 2015. Publisher: Elsevier B.V.

[87] X. Zhou, N. Mousseau, and J. Song, “Is Hydrogen Diffusion along Grain Boundaries Fast or Slow? Atomistic Origin and Mechanistic Modeling,” *Physical Review Letters*, vol. 122, p. 215501, May 2019.

[88] N. Yazdipour, A. Haq, K. Muzaka, and E. Pereloma, “2D modelling of the effect of grain size on hydrogen diffusion in X70 steel,” *Computational Materials Science*, vol. 56, pp. 49–57, Apr. 2012.

[89] T. K. Shoemaker, Z. D. Harris, and J. T. Burns, “Comparing Stress Corrosion Cracking Behavior of Additively Manufactured and Wrought 17-4PH Stainless Steel,” *Corrosion*, vol. 78, no. 6, pp. 528–546, 2022.

[90] E. J. Song, D.-W. Suh, and H. Bhadeshia, “Theory for hydrogen desorption in ferritic steel,” *Computational Materials Science*, vol. 79, pp. 36–44, Nov. 2013.

[91] A. Díaz, I. I. Cuesta, E. Martinez-Pañeda, and J. M. Alegre, “Analysis of hydrogen permeation tests considering two different modelling approaches for grain boundary trapping in iron,” *International Journal of Fracture*, vol. 223, pp. 17–35, May 2020.

[92] R. Gibala and A. J. Kumnick, “Hydrogen trapping in iron and steels,” in *Hydrogen embrittlement and stress corrosion cracking: a Troiano Festschrift*, pp. 61–77, ASM International, 1984.

[93] J. R. Scully, J. A. Van Den Avyle, M. J. Cieslak, A. D. Romig, and C. R. Hills, “The influence of palladium on the hydrogen-assisted cracking resistance of PH 13-8 Mo stainless steel,” *Metallurgical Transactions A*, vol. 22, pp. 2429–2444, Oct. 1991.

[94] R. Fernández-Sousa, C. Betegón, and E. Martínez-Pañeda, “Analysis of the influence of microstructural traps on hydrogen assisted fatigue,” *Acta Materialia*, vol. 199, pp. 253–263, 2020. arXiv: 2008.05452.

[95] E. J. McEniry, T. Hickel, and J. Neugebauer, “Hydrogen behaviour at twist {110} grain boundaries in -Fe,” *Philosophical Transactions of the Royal Society A: Mathematical, Physical and Engineering Sciences*, vol. 375, p. 20160402, July 2017.

[96] X. Li, J. Zhang, Q. Fu, E. Akiyama, X. Song, S. Shen, and Q. Li, “Hydrogen embrittlement of high strength steam turbine last stage blade steels: Comparison between PH17-4 steel and PH13-8Mo steel,” *Materials Science and Engineering A*, vol. 742, pp. 353–363, 2019.

[97] C. N. Hsiao, C. S. Chiou, and J. R. Yang, “Aging reactions in a 17-4 PH stainless steel,” *Materials Chemistry and Physics*, vol. 74, pp. 134–142, 2002.

[98] W. C. Chiang, C. C. Pu, B. L. Yu, and J. K. Wu, “Hydrogen susceptibility of 17-4 PH stainless steel,” *Materials Letters*, vol. 57, no. 16-17, pp. 2485–2488, 2003.

[99] H. Yaguchi, T. Kochi, M. Nomura, and T. Watanabe, “Hydrogen Trapping Behavior of Copper Precipitates in Steel,” *Journal of the Japan Institute of Metals*, vol. 71, no. 9, pp. 781–785, 2007.

[100] R. Shi, L. Chen, Z. Wang, X. S. Yang, L. Qiao, and X. Pang, “Quantitative investigation on deep hydrogen trapping in tempered martensitic steel,” *Journal of Alloys and Compounds*, vol. 854, p. 157218, 2021. Publisher: Elsevier B.V.

[101] Y.-S. Chen, H. Lu, J. Liang, A. Rosenthal, H. Liu, G. Sneddon, I. McCarroll, Z. Zhao, W. Li, A. Guo, and J. M. Cairney, “Observation of hydrogen trapping at dislocations, grain boundaries, and precipitates,” *Science*, vol. 367, pp. 171–175, Jan. 2020.

[102] A. Turk, D. San Martín, P. E. Rivera-Díaz-del Castillo, and E. I. Galindo-Nava, "Correlation between vanadium carbide size and hydrogen trapping in ferritic steel," *Scripta Materialia*, vol. 152, pp. 112–116, July 2018.

[103] J. Lin, F. Chen, F. Liu, D. Xu, J. Gao, and X. Tang, "Hydrogen permeation behavior and hydrogen-induced defects in 316L stainless steels manufactured by additive manufacturing," *Materials Chemistry and Physics*, vol. 250, p. 123038, 2020.

[104] F. G. Wei and K. Tsuzaki, "Hydrogen absorption of incoherent TiC particles in iron from environment at high temperatures," *Metallurgical and Materials Transactions A*, vol. 35, pp. 3155–3163, Oct. 2004.

[105] I. Bernstein and G. Pressouyre, "The Role of Traps in the Microstructural Control of Hydrogen Embrittlement of Steels," Tech. Rep. 036-099-17, Carnegie-Mellon University, 1985.

[106] G. M. Pressouyre and I. M. Bernstein, "A quantitative analysis of hydrogen trapping," *Metallurgical Transactions A*, vol. 9, pp. 1571–1580, Nov. 1978.

[107] H. Sun, W. Lv, Y. Yang, D. Li, L. Yan, X. Pang, Y. He, and K. Gao, "Optimizing the hydrogen embrittlement resistance by tuning the structures of Cu-rich nanoprecipitates in high strength martensite stainless steels," *Acta Materialia*, vol. 246, p. 118722, Mar. 2023.

[108] P. Novak, R. Yuan, B. Somerday, P. Sofronis, and R. Ritchie, "A statistical, physical-based, micro-mechanical model of hydrogen-induced intergranular fracture in steel," *Journal of the Mechanics and Physics of Solids*, vol. 58, pp. 206–226, Feb. 2010.

[109] A. J. Kumnick and H. H. Johnson, "Hydrogen transport through annealed and deformed armco iron," *Metallurgical transactions*, vol. 5, pp. 1199–1206, May 1974.

[110] M. Itakura, H. Kaburaki, M. Yamaguchi, and T. Okita, "The effect of hydrogen atoms on the screw dislocation mobility in bcc iron: A first-principles study," *Acta Materialia*, vol. 61, pp. 6857–6867, Oct. 2013.

[111] Y. Zhao and G. Lu, "QM/MM study of dislocation—hydrogen/helium interactions in -Fe," *Modelling and Simulation in Materials Science and Engineering*, vol. 19, p. 065004, Sept. 2011.

[112] A. Nagao, M. Dadfarnia, B. P. Somerday, P. Sofronis, and R. O. Ritchie, "Hydrogen-enhanced-plasticity mediated decohesion for hydrogen-induced intergranular and "quasi-cleavage" fracture of lath martensitic steels," *Journal of the Mechanics and Physics of Solids*, vol. 112, pp. 403–430, Mar. 2018.

[113] M. Enomoto, D. Hirakami, and T. Tarui, “Thermal Desorption Analysis of Hydrogen in High Strength Martensitic Steels,” *Metallurgical and Materials Transactions A*, vol. 43, pp. 572–581, Feb. 2012.

[114] L. Carneiro, B. Jalalahmadi, A. Ashtekar, and Y. Jiang, “Cyclic deformation and fatigue behavior of additively manufactured 17–4 PH stainless steel,” *International Journal of Fatigue*, vol. 123, pp. 22–30, 2019.

[115] A. Kudzal, B. McWilliams, C. Hofmeister, F. Kellogg, J. Yu, J. Taggart-Scarff, and J. Liang, “Effect of scan pattern on the microstructure and mechanical properties of Powder Bed Fusion additive manufactured 17-4 stainless steel,” *Materials and Design*, vol. 133, pp. 205–215, 2017.

[116] M. Mahmoudi, A. Elwany, A. Yadollahi, S. M. Thompson, L. Bian, and N. Shamsaei, “Mechanical properties and microstructural characterization of selective laser melted 17-4 PH stainless steel,” *Rapid Prototyping Journal*, vol. 23, pp. 280–294, Mar. 2017.

[117] M. Alnajjar, F. Christien, V. Barnier, C. Bosch, K. Wolski, A. D. Fortes, and M. Telling, “Influence of microstructure and manganese sulfides on corrosion resistance of selective laser melted 17-4 PH stainless steel in acidic chloride medium,” *Corrosion Science*, vol. 168, p. 108585, May 2020.

[118] U. Ali, R. Esmaeilizadeh, F. Ahmed, D. Sarker, W. Muhammad, A. Keshavarzkermani, Y. Mahmoodkhani, E. Marzbanrad, and E. Toyserkani, “Identification and characterization of spatter particles and their effect on surface roughness, density and mechanical response of 17-4 PH stainless steel laser powder-bed fusion parts,” *Materials Science and Engineering: A*, vol. 756, pp. 98–107, May 2019.

[119] P. Auguste, A. Mauduit, L. Fouquet, and S. Pillot, “Study on 17-4 PH stainless steel produced by selective laser melting,” *UPB Scientific Bulletin*, vol. 80, no. 4, pp. 197–210, 2018.

[120] S. Dobson, S. Vunnam, D. Frankel, C. Sudbrack, and T. Starr, “Powder variation and mechanical properties for SLM 17-4 PH stainless steel,” in *Proceedings of the 30th Annual International Solid Freeform Fabrication Symposium – An Additive Manufacturing Conference*, University of Texas at Austin, 2019.

[121] Z. Hu, H. Zhu, H. Zhang, and X. Zeng, “Experimental investigation on selective laser melting of 17-4PH stainless steel,” *Optics & Laser Technology*, vol. 87, pp. 17–25, Jan. 2017.

[122] H. Irrinki, J. S. D. Jangam, S. Pasebani, S. Badwe, J. Stitzel, K. Kate, O. Gulsoy, and S. V. Atre, “Effects of particle characteristics on the microstructure and mechanical properties of 17-4 PH stainless steel fabricated by laser-powder bed fusion,” *Powder Technology*, vol. 331, pp. 192–203, May 2018.

[123] P. G. Jerrard, L. Hao, and K. E. Evans, “Experimental investigation into selective laser melting of austenitic and martensitic stainless steel powder mixtures,” *Proceedings of the Institution of Mechanical Engineers, Part B: Journal of Engineering Manufacture*, vol. 223, no. 11, pp. 1409–1416, 2009.

[124] R. Molaei, A. Fatemi, and N. Phan, “Multiaxial fatigue of LB-PBF additive manufactured 17–4 PH stainless steel including the effects of surface roughness and HIP treatment and comparisons with the wrought alloy,” *International Journal of Fatigue*, vol. 137, p. 105646, Aug. 2020.

[125] P. Nezhadfar, K. Anderson-Wedge, S. Daniewicz, N. Phan, S. Shao, and N. Shamsaei, “Improved high cycle fatigue performance of additively manufactured 17-4 PH stainless steel via in-process refining micro-/defect-structure,” *Additive Manufacturing*, vol. 36, p. 101604, Dec. 2020.

[126] A. Poudel, A. Soltani-Tehrani, S. Shao, and N. Shamsaei, “Effect of powder characteristics on tensile properties of additively manufactured 17-4 PH stainless steel,” in *Proceedings of the 32nd Annual International Solid Freeform Fabrication Symposium*, University of Texas at Austin, 2021.

[127] S. Romano, P. Nezhadfar, N. Shamsaei, M. Seifi, and S. Beretta, “High cycle fatigue behavior and life prediction for additively manufactured 17-4 PH stainless steel: Effect of sub-surface porosity and surface roughness,” *Theoretical and Applied Fracture Mechanics*, vol. 106, p. 102477, Apr. 2020.

[128] R. F. Schaller, J. M. Taylor, J. Rodelas, and E. J. Schindelholz, “Corrosion Properties of Powder Bed Fusion Additively Manufactured 17-4 PH Stainless Steel,” *CORROSION*, vol. 73, pp. 796–807, July 2017.

[129] R. Shrestha, N. Shamsaei, M. Seifi, and N. Phan, “An investigation into specimen property to part performance relationships for laser beam powder bed fusion additive manufacturing,” *Additive Manufacturing*, vol. 29, p. 100807, Oct. 2019.

[130] A. Soltani-Tehrani, J. Pegues, and N. Shamsaei, “Fatigue behavior of additively manufactured 17-4 PH stainless steel: The effects of part location and powder re-use,” *Additive Manufacturing*, vol. 36, p. 101398, Dec. 2020.

[131] Y. Sun, R. J. Hebert, and M. Aindow, "Non-metallic inclusions in 17-4PH stainless steel parts produced by selective laser melting," *Materials & Design*, vol. 140, pp. 153–162, Feb. 2018.

[132] J. S. Weaver, J. Whiting, V. Tondare, C. Beauchamp, M. Peltz, J. Tarr, T. Q. Phan, and M. A. Donmez, "The effects of particle size distribution on the rheological properties of the powder and the mechanical properties of additively manufactured 17-4 PH stainless steel," *Additive Manufacturing*, vol. 39, p. 101851, Mar. 2021.

[133] A. Yadollahi, M. Mahmoudi, A. Elwany, H. Doude, L. Bian, and J. C. Newman, "Effects of crack orientation and heat treatment on fatigue-crack-growth behavior of AM 17-4 PH stainless steel," *Engineering Fracture Mechanics*, vol. 226, p. 106874, Mar. 2020.

[134] A. Yadollahi, N. Shamsaei, S. M. Thompson, A. Elwany, and L. Bian, "Effects of building orientation and heat treatment on fatigue behavior of selective laser melted 17-4 PH stainless steel," *International Journal of Fatigue*, vol. 94, pp. 218–235, 2017.

[135] P. Nezhadfar, E. Burford, K. Anderson-Wedge, B. Zhang, S. Shao, S. Daniewicz, and N. Shamsaei, "Fatigue crack growth behavior of additively manufactured 17-4 PH stainless steel: Effects of build orientation and microstructure," *International Journal of Fatigue*, vol. 123, pp. 168–179, June 2019.

[136] S. Tammas-Williams, P. Withers, I. Todd, and P. Prangnell, "Porosity regrowth during heat treatment of hot isostatically pressed additively manufactured titanium components," *Scripta Materialia*, vol. 122, pp. 72–76, Sept. 2016.

[137] G. Wegmann, R. Gerling, and F. P. Schimansky, "Temperature induced porosity in hot isostatically pressed gamma titanium aluminide alloy powders," *Acta Materialia*, vol. 51, pp. 741–752, Feb. 2003.

[138] T. LeBrun, T. Nakamoto, K. Horikawa, and H. Kobayashi, "Effect of retained austenite on subsequent thermal processing and resultant mechanical properties of selective laser melted 17-4 PH stainless steel," *Materials and Design*, vol. 81, pp. 44–53, 2015. Publisher: Elsevier Ltd.

[139] P. Zhang, J. Ding, D. Sun, and J. Zhao, "First-principles study of noble gas atoms in bcc Fe," *Journal of Nuclear Materials*, vol. 492, pp. 134–141, Aug. 2017.

Chapter 6

Modeling of Grain Boundary-Hydrogen Interactions

6.1 Overview

A review of literature since 1955 on grain boundary hydrogen diffusion in different alloys is provided. Though there is little consensus on the influence of hydrogen concentration, grain boundary type, and features like dislocations and triple junctions on hydrogen trapping and mobility, this literature review reveals a prevailing theme: the dependence of grain boundary diffusion behavior on alloy structure. Grain boundaries in face-centered (FCC) alloys commonly provide fast pathways for diffusion, whereas their body-centered cubic or tetragonal (BCC/BCT) often have relatively slow diffusion along grain boundaries. This is attributable to the difference in packing factor in FCC and BCC/BCT alloys; the close-packed FCC lattice leads to slow bulk diffusion, causing a dominance of diffusion along grain boundaries. This behavior is also speculated to be dependent on grain boundary type, with short circuit diffusion linked to well-connected networks of high-angle grain boundaries in FCC alloys. The Hashin-Shtrikman upper bound is employed to characterize the grain boundary diffusion behavior of the studied wrought and AM 17-4 PH alloys. This model suggests that grain boundary characteristics are similar enough in wrought and AM 17-4 PH such that no short-circuit diffusion along grain boundaries can be interpreted to account for the rapid effective diffusivity in AM specimens. A slight increase in grain boundary diffusivity in the AM specimens seen in the model is discussed.

6.2 State of Literature on Grain Boundary Hydrogen Diffusion

Though a good understanding of diffusion along grain boundaries is vital to characterizing hydrogen-microstructure interactions, the precise nature of grain boundary diffusion is frequently a controversial topic in literature. There is often disagreement on the effects of concentration and grain boundary type, as well as features such as dislocations and triple junctions, on the trapping and mobility of hydrogen. However, there is a significant amount of evidence in literature that the role of grain boundaries as fast pathways for diffusion is dependent on the structure of the alloy, with short-circuit grain boundary diffusion reported almost exclusively for face-centered alloys as opposed to their body-centered counterparts. A review of relevant literature to date is presented to provide insight into notable findings regarding grain boundary diffusion and its dependence on structure and other pertinent factors. Table 6.1 and Table 6.2 provide summaries of selected literature addressing face-centered and body-centered alloys, respectively.

6.2.1 Face-Centered Materials

Ni and Ni-Based Alloys

Nickel and nickel-based alloys are the focal point of the majority of literature addressing grain boundary-hydrogen interactions in FCC materials. Numerous studies have documented accelerated diffusion along grain boundaries in nickel and nickel alloys using a variety of investigative methods, though there is not universal consensus on the effects of hydrogen concentration and grain boundary type.

Both electrochemical and gaseous hydrogen permeation have been employed to explore hydrogen diffusion along grain boundaries in nickel. Early permeation breakthroughs and small increases in short-time permeation current density have been linked to heightened grain boundary diffusivity in pure Ni.[1] Tsuru and Latanision[2] combined electrochemical permeation with iron microprobe analyses to study hydrogen-grain boundary interactions in cold-rolled pure Ni, theorizing that the observed increase in short-time permeation rate and higher hydrogen concentration at grain boundaries indicates that grain boundary diffusivity exceeds lattice diffusivity.

Hydrogen permeation has also been used to quantify the grain boundary diffusivity coefficient. Harris and Latanision[3] adapted the following model developed by Hart[4] to predict grain boundary diffusivity D_{gb} from effective diffusivity D_{eff} and ideal lattice diffusivity D_{L}:

$$D_{\mathrm{eff}} = D_{\mathrm{gb}} s f_{\mathrm{gb}} + D_{\mathrm{L}}(1 - f_{\mathrm{gb}}), \tag{6.1}$$

where s is a concentration-based segregation coefficient and f_{gb} is the volume fraction of grain boundaries. The segregation coefficient can be expressed in terms of binding energy E_{b} between a lattice site and a grain boundary site, following an Arrhenius-type relationship:

$$s = s_0 \exp\left(\frac{E_{\mathrm{b}}}{RT}\right), \tag{6.2}$$

where s_0 is a pre-exponential factor, R is the gas constant, and T is temperature. By estimating grain boundary volume fraction, binding energy, and lattice diffusivity, Harris and Latanision calculated grain boundary diffusivity over a range of segregation coefficients and concluded that grain boundary diffusivity is at least 40 times greater than lattice diffusivity in the electrodeposited fine-grained Ni.

In a more recent study, Wang et al.[5] investigated the gas permeation behavior of polycrystalline Ni, reporting a comparable increase in D_{gb} compared to D_{L} using the same model. However, Brass and Chanfreau[6] applied the Hart model to compare electrochemical permeation behavior of single-crystal, small-grain, and large-grain Ni, and concluded that grain boundary diffusivity is around 2-7 times greater than lattice diffusivity—notably smaller than the difference observed by Wang et al. and Harris and Latanision. This discrepancy is speculatively credited to reversible hydrogen trapping reducing the observed intergranular diffusivity.

This increase in diffusion along grain boundaries in nickel has been corroborated by other experimental and modeling methods. Lee and Lee[7, 8] used thermal desorption analyses to compare hydrogen content in pre-charged single-crystal and polycrystalline nickel, attributing a small but reproducible increase in hydrogen content early in the spectra to short-circuit grain boundary diffusion. Molecular dynamics simulations by Szpunar et al.[9] reported an order of magnitude increase in diffusion along [100] $\Sigma5$, $\Sigma13$, and $\Sigma17$ grain boundaries relative to lattice diffusion. Jothi et al.[10] employed a coupled Monte Carlo and finite element model to compare micro-polycrystalline and nano-polycrystalline Ni, also reporting an increase in hydrogen diffusion in the nano-polycrystalline material due to fast grain boundary diffusion.

This enhanced grain boundary diffusion observed in nickel is often reported to be grain boundary type-dependent. Through a combination of microstructural characterization, electrochemical permeation, and thermal desorption spectroscopy, Oudriss et al.[11] demonstrated that high-angle grain boundaries (HAGBs) are the main culprit behind fast-path diffusion due to their disordered structure. However, low-misorientation or special grain boundaries act as stronger traps, counteracting the short-circuit diffusion effect. This conclusion was supported by kMC simulations by Zhou et al.,[12] who concluded that fast diffusion occurs along a well-connected network of HAGBs, whereas low-angle grain boundaries (LAGBs) act as barriers to diffusion.

There are numerous studies addressing hydrogen diffusion effects of specific special grain boundary types and orientations. Through deuterium SIMS analysis, Ladna and Birnbaum[13, 14] observed accelerated diffusivity along high-energy ($\Sigma 9$) symmetrical tilt boundaries, but not along low-energy ($\Sigma 11$) symmetrical tilt boundaries. First principles density function theory calculations by Di Stefano et al.[15] suggest that symmetric tilt $\Sigma 3$ grain boundaries don't serve as strong traps and can inhibit hydrogen diffusion, whereas symmetric tilt $\Sigma 5$ grain boundaries strongly trap hydrogen and provide channels for diffusion twice as fast as lattice diffusion. Molecular dynamics simulations by Zhou et al.[16] support the combination of strong trapping and accelerated diffusion in $\Sigma 5$ and $\Sigma 11$ grain boundaries, and conclude that $\Sigma 3$ grain boundaries have little effect on diffusivity unless interstitials are present.

The effect of grain boundary structure on diffusivity was theorized to be related to the density of packing of Ni atoms within grain boundaries by Marte and Kirchheim,[17] based on permeation of nickel produced by galvanic plating versus annealed nanocrystalline Ni. Similarly, Li et al.[18] hypothesized that special grain boundary diffusion behavior is dependent on energy and excess volume, based on analysis combining molecular dynamics modeling, thermal desorption spectroscopy, and hydrogen permeation. The authors argued that certain high energy or excess volume special grain boundaries, such as $\Sigma 11(332)$ and $\Sigma 5(210)$, experience a directional 3-4 order of magnitude increase in diffusion relative to the lattice, while other directions of these special grain boundaries act to trap hydrogen. Similar orientation-dependent diffusion behavior has been observed in other studies; Wang et al.[5] found that grain boundary orientation strongly affected diffusivity based on gas permeation of directionally solidified Ni.

The difference in diffusion behavior between different grain boundary types may imply that the degree of hydrogen trapping is grain boundary type-dependent in nickel and nickel alloys, a conclusion that is corroborated by several studies.[19] Angelo et al.[20] modeled hydrogen trapping in various defects in nickel using the embedded atom method, concluding that hydrogen segregates strongly to $\Sigma3(112)$, $\Sigma9(221)$, and $\Sigma11(113)$ tilt boundaries, with the $\Sigma9$ boundary having a higher trap site energy than its counterparts due to its volume. A SIMS study by Oudriss et al.[21] indicates that the concentration profile across a grain boundary may depend on grain boundary type, with gaps in the concentration profile across the boundary occurring at random grain boundaries that act as fast paths. Alternatively, special grain boundaries with stronger trapping ability are theorized to have an unbroken H concentration across the boundary. However, Wada et al.[22] did not find any apparent difference in the trapping abilities of special and random grain boundaries in a SIMS analysis.

Grain boundary diffusivity has also been postulated to depend on hydrogen concentration in nickel as evidenced by Arantes et al.,[23] who used electrochemical permeation to compare microcrystalline and nanocrystalline Ni. At high hydrogen concentrations, the authors theorized that the increased hydrogen flux and faster diffusivity in the nanocrystalline Ni indicate increased diffusivity and hydrogen concentration along the grain boundaries. However, at low hydrogen concentrations, the diffusivity value was actually observed to be lower in the nanocrystalline Ni than in its microcrystalline counterpart. This was attributed to saturation of low-energy sites, leading to occupation of high-energy sites as hydrogen concentration increases. This conclusion is also supported by Yao and Cahoon,[24] who postulated that at a low hydrogen concentration, grain boundary diffusion of hydrogen is effectively stopped.

There has also been discussion regarding the role of dislocations in hydrogen diffusion along grain boundaries in nickel. Louthan et al.[25] hypothesize that their observed increase in deuterium permeability in pure nickel after cold-working is due to faster diffusivity along grain boundaries; however, they argue that this increase is caused by dislocation substructures acting as short-circuit diffusion paths. This conclusion is maintained by Tseng et al.,[26] who observed silver decoration in dislocations and certain grain boundary sections in commercial pure Ni. It is noted by the authors that this experimental method cannot be used to observe hydrogen in the lattice, and therefore no conclusion about diffusivity in the grain boundary can be made. However, in the study performed by Lee and Lee using thermal analysis to compare cold-rolled and annealed Ni, the authors directly disagree with the conclusion drawn by Louthan et al,[8] arguing that fast path diffusion would be observable in the early transient region of the cold-rolled specimen. They state instead that dislocations act as very weak hydrogen traps in Ni, with lower trap activation energy than that of bulk diffusion.

Triple junctions, or intersections of three or more grain boundaries, may also play a role in grain boundary diffusion in nickel. Palumbo et al.[1] observed multiple early permeation breakthrough events in nanocrystalline Ni, credited to fast diffusion in both grain boundaries and triple junctions. Oudriss et al.[11] attributed this fast diffusion through triple junctions to an excess of free volume. As triple junction density inherently depends on grain size, this produces a strong grain-size dependence of diffusivity. In a separate study, Oudriss et al.[21] proposed that fast diffusion through grain boundaries and triple junctions may compete with irreversible trapping in geometrically necessary dislocations (GNDs) depending on grain size. Short-circuit grain boundary diffusion will increase effective diffusivity in coarser-grained microstructures, but as grain size falls below a critical size (in the 10s of microns), trapping by GNDs begins to dominate, limiting and eventually reducing effective diffusivity. However, if grain size is decreased to the sub-micron region, fast diffusion through triple junctions can counteract this GND trapping.

The grain boundary diffusion behavior has also been shown to affect hydrogen embrittlement kinetics; Kimura and Birnbaum[27] attributed the unexpectedly rapid intergranular embrittlement of nickel to grain boundary diffusivity being about two times faster than lattice diffusivity.

It should be noted that not all literature is in agreement with the idea of short-circuit diffusion along random grain boundaries in nickel; Hurley et al.[28] did not find a difference in experimental deuterium TDS spectra between single-crystal and polycrystalline nickel-based alloy Inconel 600, concluding that grain boundaries do not affect hydrogen transport. Ma et al.[29] examined directionally solidified polycrystalline Ni using scanning Kelvin probe force microscopy, concluding that random grain boundaries do not act as fast paths and that coherent $\Sigma 3$ grain boundaries accelerate diffusion. Additionally, secondary inclusions and precipitates along grain boundaries in Ni-based alloys can reduce diffusivity along the grain boundary; carbides have been theorized to counteract fast diffusion along the grain boundary in HR6W[30] and Inconel 625.[31]

Pd and Pd-Based Alloys

Though fewer studies exist on hydrogen diffusion in the grain boundaries of palladium and its alloys, the same increase in diffusivity along grain boundaries has been observed. Additionally, the existing body of literature includes some of the landmark analyses of hydrogen concentration dependency. Mütschele and Kirchheim in 1987 and Kirchheim et al. in 1988 linked an increase in diffusivity in nanocrystalline Pd with an increase in concentration, positing the existence of a critical hydrogen concentration value at which the diffusivity of nanocrystalline palladium exceeds the diffusivity of single-crystalline Pd.[32, 33] This increase was attributed to the occupation of higher energy sites, which decreases the average activation energy of H diffusion and therefore increases hydrogen diffusivity.

Iwaoka et al.[34] used electrochemical hydrogen permeation to compare diffusion in ultrafine-grained and coarse-grained Pd, finding rapid diffusion in ultrafine-grained Pd compared to its coarse-grained counterpart. It is also worth noting that the ultrafine-grained and coarse-grained Pd had similar dislocation density, and that, though hydrogen concentration and diffusivity increase concurrently as observed in Kirchheim et al., activation energy does not decrease with hydrogen concentration as would be expected in Kirchheim's theory. Iwaoka et al. attributed this difference to the effects of the fraction of disordered structure; the random grain boundaries can be likened to amorphous regions, but H atoms jump both through the disordered region in the grain boundaries and also between grain boundary sites and lattice sites.

Al and Al-Based Alloys

Like other FCC alloys, aluminum and its alloys have demonstrated an increased grain boundary diffusivity. This has notably been observed through local spatial techniques; Saitoh et al.[35] used tritium electron microautoradiography to observe H distribution in Al, concluding based on the lack of Ag in the observed high-angle grain boundary that HAGBs have minimal trapping power and act as a path for short-circuit diffusion. Larignon et al.[36] employed SIMS and Kelvin probe force microscopy to examine hydrogen in grain and subgrain boundaries of Al 2024, reporting trapping and subsequent fast diffusion along the boundaries. Bhuiyan et al.[37] argued that grain boundaries actually trap less hydrogen than dislocations in Al 7150, though the trap occupancy in these boundaries increases with hydrogen concentration. Though there is disagreement in the trapping ability of grain boundaries between these studies, there is a consistent observation of short-circuit diffusion.

Limited investigation has been made into specific grain boundary types in aluminum. Kinetic Monte Carlo simulations by Pedersen and Jónsson[38] showed a slight increase in diffusion parallel to the $\Sigma 5$ boundary, with diffusion blocked across the boundary; however, tilt grain boundaries and twist + tilt grain boundaries were perceived to slow hydrogen diffusion.

Additionally, though triple junctions in nickel have been theorized to accelerate diffusion, Ichimura et al.[39] posited that trapping by triple junctions may actually reduce diffusion along grain boundaries based on thermal desorption diffusivity measurements of aluminum specimens with various grain sizes. Ichimura et al. proposed a "grain boundary cross effect" based on competing mechanisms of triple junction trapping and grain boundary fast diffusion, hypothesizing that diffusivity will increase with decreasing grain size up to a certain critical grain diameter, at which point a critical number of triple junctions is reached. Any further decrease of grain size would only enhance the trapping by triple junctions, causing a drastic decrease in diffusivity as the fast diffusion is outweighed by trapping at the junctions.

Fe and Fe-Based Alloys

Fast diffusion in the grain boundaries of FCC iron alloys and austenitic steels has been commonly observed as well, often directly through tracer methods. Abraham et al.[40] explored permeation of tritium in grain boundaries of 304L through autoradiography, observing rapid diffusion along grain boundaries. More recently, Tanaka et al.[41] used TOF-SIMS to directly observe grain boundary diffusion of deuterium in single-phase FCC Fe-30Ni, indicating fast path diffusion.

Dramatic increases in grain boundary diffusion have been observed in austenitic stainless steels. One of the most extreme differences between bulk and grain boundary diffusion was suggested by Calder et al.,[42] who measured the tritium concentration profile in 304 and 316 stainless steels. The authors calculated grain boundary diffusivity using several models based on the tritium concentration, and reported a grain boundary diffusivity eight orders of magnitude higher than bulk. A multiple-order of magnitude increase has also been observed elsewhere; Dieudonné et al.[43] employed SIMS to examine deuterium diffusion in austenitic Fe-Mn-C steels and attributed a tail in the deuterium curve to short-circuit diffusion in grain boundaries, calculating that diffusivity in grain boundaries to be 4 orders of magnitude faster than that seen in the bulk.

Though the extent of research into different types of grain boundaries has not been as thorough compared to materials like nickel, GB-type dependencies similar to those observed in other FCC alloys have been reported. Density functional theory energy analysis performed by He et al.[44] on $\Sigma3[\bar{1}10](111)$, $\Sigma5[\bar{1}00](021)$, and $\Sigma9[110](2\bar{2}1)$ grain boundaries in γ-Fe found that the $\Sigma 3$ and $\Sigma 5$ grain boundaries can slow diffusion in all directions, whereas $\Sigma 9$ grain boundaries can enhance grain boundary diffusion along the boundary.

Iron naturally has a BCC structure at room temperature and often requires alloying to attain an FCC structure at room temperature, so Fe-based FCC alloys often have a large degree of inclusions and defects that affect hydrogen diffusion. However, increased grain boundary diffusivity has still been observed after accounting for trapping effects; Mine et al.[45] still observed enhanced H diffusivity through type 660 and 310S stainless steels after grain refinement through HPT after using an Oriani-type model to account for trapping due to higher dislocation density from HPT processing. In 310S, a nearly linear increase in diffusivity was observed with decreasing grain size after the Oriani model was employed. However, this trend was not linear in 660, speculatively due to the effects of η-Ni_3Ti precipitates.

Lee et al.[46] used permeation to observe diffusivity in Cantor HEA, 316L, and 304. The 304 and 316L alloys had similar grain sizes, more than twice that of the Cantor HEA alloy. However, 316L and Cantor had similar H concentration and effective diffusivity values, whereas the 304 showed comparatively slower diffusivity. Therefore, the difference in diffusivity could not be explained by grain size alone. The authors attributed the slower D_{eff} in 304 to dislocations and twins caused by martensite transformation during hydrogen permeation.

Triple junctions in Fe-based alloys have also been discussed. Similar to the work by Ichimura et al.[39] in aluminum, Yazdipour et al.[47] observed a grain boundary cross effect in X70 steel that was annealed to reduce grain size. As grain size decreased, diffusivity increased until a certain critical value was reached, after which there was a rapid decrease in diffusivity attributed to trapping by triple junctions. Yazdipour et al. compared experimental results to a finite difference model, concluding that hydrogen trapping at triple junctions and nodes increases with reduced grain size. However, it should be noted that other microstructural features, such as dislocations, were not analyzed in this study.

Also similar to other FCC metals, there is little consensus on the effects of dislocations in the context of grain boundary diffusion in FCC Fe-based alloys. It is widely understood that dislocations act as hydrogen traps, and thereby are often believed to impede fast diffusion. However, based on observed plastic deformation induced by hydrogen charging of Fe-36Ni, Mogilny et al.[48] proposed that the origin of increased hydrogen flux along grain boundaries is due to sliding dislocations, not an actual acceleration of diffusion of interstitials within the boundary.

There has also been some consideration of diffusion rate dependency; Lin et al.[49] investigated hydrogen permeation in AM and cold-rolled 316L and found that diffusivity was higher in the AM specimen, attributed to sub-grain boundaries acting as fast paths. Lin et al. also speculated that hydrogen diffusion behavior was diffusion rate-dependent, theorizing that grain boundaries only act as the main diffusion path at low diffusion rates. It should be noted that the authors define high and low diffusion rates using current density instead of the traditionally used effective diffusivity.

6.2.2 Body-Centered Materials

Fe and Binary Fe Alloys

Unlike face-centered alloys, the more open structure of body-centered alloys contributes to relatively fast lattice diffusion; consequently, increased diffusivity along grain boundaries is not commonly reported. This is evidenced by numerous studies detailing increased effective diffusivity through coarser microstructure in BCC iron. Beck et al.[51] observed that single crystal permeation diffusivity is 30% higher than polycrystalline diffusivity in Armco Fe; similarly, Iwaoka et al.[52] found that permeation diffusivity in HPT-process fine-grained iron is reduced compared to diffusivity in coarser-grained annealed iron. This was attributed to a reduction in diffusivity along the grain boundaries due to the high rate of lattice diffusion as well as hydrogen atom interactions. Slow grain boundary diffusion

Table 6.1: Summary of selected literature addressing grain boundary-hydrogen interactions in FCC alloys.

Alloy	GB Type	GB Diffusion	Methods	Evidence	Source
Ni and Ni-Based Alloys					
Nickel	Unspecified	Accelerated	Permeation	Cold working vs. diffusivity	[25]
	Unspecified	Accelerated	Permeation, ion microprobe	Short-time permeation rate, H conc. at GBs	[2]
	Unspecified	Accelerated	TDS	Single vs. polycrystalline TDS peak area	[8]
	Unspecified	Accelerated	Fracture	Fit of GB fracture ratio vs. charge time	[27]
	Unspecified	GB type-dependent	Permeation, silver dec.	More Ag (higher perm) along GBs	[26]
	Unspecified	Slowed	Permeation, silver dec.	No Ag along GBs, no grain size effect on perm.	[24]
	Unspecified	Accelerated	Permeation	Grain size vs. D_{eff}	[3]
	Unspecified	Accelerated	Permeation	Breakthrough events in perm.	[1]
	Unspecified	Accelerated	Permeation	Grain size vs. D_{eff}	[23]
	Unspecified	Accelerated	Permeation	Grain size vs. D_{eff}	[6]
	Unspecified	GB type-dependent	Permeation	Grain size vs. D_{eff}	[17]
	Unspecified	Accelerated	Permeation	Grain size vs. D_{eff}	[50]
	Unspecified	Accelerated	Permeation	Grain size vs. D_{eff}	[5]
	$\Sigma9$, $\Sigma11$	GB type-dependent	Deut. SIMS	SIMS deuterium segregation at GBs	[13]
	$\Sigma9$, $\Sigma11$	GB type-dependent	Deut. SIMS	SIMS deuterium segregation at GBs	[14]
	$\Sigma3$, $\Sigma9$, $\Sigma11$	Slowed	Embedded atom model	Simulation of trapping energies	[20]
	$\Sigma5$, $\Sigma13$, $\Sigma17$	Accelerated	Molecular dynamics	D_{gb} calculated via mean-square displacement	[9]
	HAGBs, LAGBs, special GBs	GB type-dependent	Permeation, TDS	Grain size vs. D_{eff}, GB type TDS results	[11]
	$\Sigma3$, $\Sigma5$	GB type-dependent	DFT	DFT GB energy analysis	[15]
	LAGB, HAGB	Accelerated	Monte Carlo, FEA	MC-FE trap model	[10]
	random, special $\Sigma3^n$	GB type-dependent	SIMS	SIMS map + EBSD comparison	[21]
	Coherent $\Sigma3$ twin, random	GB type-dependent	SKPFM	Observed hydrogen breakthrough in GBs	[29]
	$\Sigma3$, $\Sigma5$, $\Sigma11$	GB type-dependent	Molecular dynamics	MD GB energy analysis	[16]
	Special, random	GB type-dependent	TDS, SIMS	SIMS map, TDS peak analysis	[22]
	$\Sigma3$, $\Sigma5$, $\Sigma11$, $\Sigma25$, $\Sigma41$	GB type-dependent	Kinetic Monte Carlo	kMC GB energy analysis	[12]
	$\Sigma3$, $\Sigma9$, $\Sigma11$, $\Sigma57$, $\Sigma171$, $\Sigma451$	GB type-dependent	Molecular dynamics	MD GB energy analysis	[19]
	$\Sigma3$, $\Sigma5$, $\Sigma11$	GB type-dependent	TDS, permeation, MD	MD GB energy analysis, grain size vs. D_{eff}	[18]
HR6W	Unspecified	Accelerated	TDS	Grain size vs. D_{eff}	[30]
Inconel 600	Unspecified	No effect of GB	TDS	Grain size vs. D_{eff}	[28]
Inconel 625	Unspecified	Accelerated	Permeation, TDS	Grain size vs. D_{eff}	[31]
Pd and Pd-Based Alloys					
Pd	Unspecified	Conc.-dependent	Permeation	Single vs polycrystalline C_{H} vs. D_{eff}	[32]
	HAGB, LAGB	GB type-dependent	Permeation	Grain size vs. D_{eff}	[34]
Pd-Si	Unspecified	Conc.-dependent	Electrochem. techniques	Single vs polycrystalline C_{H} vs. D_{eff}	[33]
Al and Al-Based Alloys					
Al	Unspecified	Accelerated	TDS	Grain size vs. D_{eff}	[39]
	$\Sigma5$ twist/tilt/twist+tilt	GB type-dependent	Monte Carlo, DFT	kMC atomic interaction simulation	[38]
Al 2024	Unspecified	Accelerated	SIMS, KFM	SIMS map, KFM signal map	[36]
Al, Al-4Cu, Al-1Mg2Si	HAGB	Accelerated	Microautoradiography	No Ag in HAGB	[35]
Fe and Fe-Based Alloys					
γ-Fe	$\Sigma3$, $\Sigma5$, $\Sigma9$	GB type-dependent	DFT	DFT GB energy analysis	[44]
Fe-30Ni	Unspecified	Accelerated	Ga-FIB-TOF-SIMS	High intensity at GBs	[41]
Fe-36Ni	Unspecified	Accelerated via dislocs.	XRD	Texture/dislocation increase after charging	[48]
Fe-Mn-C steels	Unspecified	Accelerated	SIMS	SIMS concentration profiles	[43]
304, 316	Unspecified	Accelerated	Tritium conc. profiles	Tritium diffusion coefficient	[42]
304L	Unspecified	Accelerated	Autoradiography	Tritium at GBs	[40]
304L, 316L, Cantor	Unspecified	Accelerated	Permeation	Grain size vs. D_{eff}	[46]
316L	Unspecified	Accelerated	Permeation	Grain size vs. D_{eff}	[49]
660, 310S	Unspecified	Accelerated	TDS	Grain size vs. D_{eff}	[45]
X70	Unspecified	Accelerated	Permeation, Finite diff	Grain size vs. D_{eff}	[47]

has also been reported by Addach et al.,[53] who varied specimen thickness below a certain small value (0.5-2 mm) to reduce the influence of grain boundaries on bulk diffusivity. It was found that permeation diffusivity in iron increased with decreasing specimen thickness, implying an obstruction of diffusion from grain boundaries.

Slow grain boundary diffusivity has been observed in modeling studies as well. Autoradiography of iron was combined with molecular dynamics energy and enthalpy analyses by Teus et al.,[54, 55] who found that the activation enthalpy of hydrogen migration in the grain boundary is higher than in bulk iron, leading to a reduction in grain boundary diffusivity. Díaz et al.[56] found model-experimental agreement between permeation and finite element analysis examination of iron with different grain sizes, consistently noting increased diffusion correlating to finer grain size. Zhou et al.[57] performed a molecular dynamics analysis on nanograined Fe with different grain sizes and found that the segregation energies of grain boundaries in iron are much higher than the bulk, assuming low hydrogen concentration. Zhou et al. also concluded that triple junctions act as stronger traps than grain boundaries.

Thermal desorption has been employed to quantify activation energies for grain boundary binding and detrapping in iron, though the range of published values is wide. Choo and Lee[58] examined the effects of different grain boundary densities on thermal desorption of iron, studying the trapping behavior of grain boundaries through variations in TDS spectra correlating to grain size. The authors estimated an activation energy of 17.2 kJ/mol for desorption from grain boundary trap sites. However, Ono and Meshii[59] calculated a binding energy of 49.2 kJ/mol using a similar method of thermal desorption of Fe with different grain sizes. Even accounting for the migration energy of hydrogen through the lattice, this is much larger than that observed by Choo and Lee. Sato and Takai[60] reported a similar activation energy for high-angle grain boundaries in iron, quantified by eliminating any low-angle grain boundaries so that thermal desorption analysis could be performed solely on high-angle grain boundaries.. The spectra associated with these grain boundaries occurred at 85°C, corresponding to an activation energy of 43.7 kJ/mol.

Despite the absence of reported short-circuit diffusion along grain boundaries, it should be noted that similarly to the FCC alloys, grain boundary type has been theorized to affect the degree of trapping. However, the precise nature of this relationship is controversial. For example, increased trapping ability of high-angle grain boundaries compared to their low-angle counterparts has been reported in electrochemical permeation and silver decoration studies.[61, 62] Martinez-Madrid et al.[61] argued that the increase in energy and distortion corresponding to high-angle grain boundaries causes an increase in trapping ability compared to their low-angle counterparts. However, autoradiography studies on Fe-Ti alloys published by Asaoka et al.[63] and Pressouyre and Bernstein[64] both reported high-angle grain boundaries acting as poorer traps than their low-angle counterparts. Little investigation has been performed into special grain boundaries, though Kholtobina et al.[65] predicted a slight reduction in trapping energy at tilt $\Sigma3$ and $\Sigma5$ boundaries compared to twist $\Sigma5$ boundaries through density functional theory analysis.

Asaoka et al.[63] also found that carbides can have a strong effect on hydrogen behavior near the grain boundaries. This is supported by the thermal desorption and autoradiography work of Paes de Oliviera et al.,[66] who attributed trapping at Fe-Cr grain boundaries to the presence of carbon at the interface.

Concentration dependency has also been observed in BCC iron and its alloys. Kinetic Monte Carlo simulations from Du et al.[67] found that, at low concentrations, hydrogen is confined to the grain boundary interface, leading to a low effective diffusivity due to slow diffusion along the boundaries. As concentration increases, the available interstitial sites are filled, and the effect of grain boundaries on diffusivity is reduced. Additionally, molecular dynamics simulations performed by Yang et al.[68] on a <111> symmetric tilt grain boundary found anisotropic diffusion behavior, with fast travel at low hydrogen concentrations and impeded diffusion at high hydrogen concentrations.

Lastly, it should be noted that high temperatures may affect this observed behavior, as seen in the 1955 study by Haynes and Smoluchowski[69] on the effect of grain boundary angle on hydrogen penetration in Fe-3Si using autoradiography above 769°C. Below a certain grain boundary misorientation, there was no observed preference for grain boundary diffusion over lattice diffusion; however, the authors did report the existence of some intermediate grain boundary angle at which grain boundary diffusivity exceeds that of the lattice at these high temperatures, based on measurements of penetration depth. Additionally, Hagi et al.[70] found that, while single-crystal iron followed an Arrhenius-type temperature-diffusivity trend, the polycrystalline iron diverged from this trend at around 260 K due to low-energy trapping. This may indicate that, above this temperature, the trapping effect at grain boundaries is negated and any reduction of diffusivity due to grain boundaries is eliminated.

Body-Centered Steels

Similar to BCC iron and Fe-based alloys, there is little evidence of enhanced diffusion along grain boundaries in body-centered steels. This has been shown in a variety of steels. Danford[71] found that increased grain boundary density in 4340 steel led to a higher hydrogen concentration, indicating grain boundary trapping. Likewise, Turk et al.[72] compared martensitic DP800 stainless steel with different grain sizes through permeation and TDS, reporting lower diffusivity in finer-grained specimens. It should be noted that tempered specimens with different dislocation densities had the same diffusivity value, leading Turk et al. to conclude that dislocations have limited effects on trapping.

Though the trapping ability of grain boundaries in alloys like precipitation-hardening stainless steels and AerMet 100 is commonly reported, the microstructural complexity of these alloys often makes it difficult to draw any direct conclusions about interactions between hydrogen and specific features. Tsay et al.[73] theorized based on changes in permeation diffusivity of 17-4 PH that grain boundaries act as the main hydrogen trap in the over-aged condition, but that precipitates are the main trap in the peak-aged condition. Alternatively, Shen et al.[74] proposed that raising heat treatment temperature caused opposing effects in 17-4 PH due to simultaneous grain coarsening reducing the slow grain boundary diffusion effect, and increased precipitation causing more trapping.

Li et al.[75] investigated hydrogen trap states in AerMet100 using thermal desorption, theorizing that grain boundaries act as strong traps, though there was difficulty distinguishing the desorption peak associated with grain boundaries from the effects of mixed dislocation cores and martensite interfaces. This difficulty is often encountered in thermal desorption analysis of hydrogen in steels, which may explain the wide variation of trap behavior attributed to grain boundaries in literature. Grain boundaries have been characterized as reversible, low-temperature traps in high-strength steels;[76, 77] however, high-angle grain boundaries have also been theorized to act as irreversible traps.[78]

These effects may also rely on concentration and grain boundary type. Das et al.[79] postulated that grain boundary trapping ability in martensitic stainless steels is concentration-dependent based on finite element analysis, arguing that high angle grain boundaries act as the primary traps at low hydrogen concentrations, whereas dislocations are more prominent at high concentrations.

The amount of carbon in specific alloys also may be an important factor in grain boundary diffusivity. The previously discussed work of Paes de Oliviera et al.[66] on Fe-Cr aligns well with literature on mild or low-carbon steels; Chew and Fabling[80] observed similar diffusivities in decarburized mild steel with different grain sizes, indicating minimal trapping or slowing of diffusion along grain boundaries. Additionally, Luu and Wu[81] and Ichitani and Kanno[82] both reported uniform silver along grain boundaries in hydrogen microprint analysis of mild and medium-carbon steels, concluding that diffusivity along grain boundaries is likely similar to lattice diffusivity.

Table 6.2: Summary of selected literature addressing grain boundary-hydrogen interactions in BCC/BCT alloys.

Alloy	**GB Type**	**GB Diffusion**	**Methods**	**Evidence**	**Source**
Fe and Binary Fe Alloys					
Iron	Unspecified	No effect of GB	Permeation	Grain size vs. D_{eff}	[51]
	Unspecified	Slowed	Permeation	Single vs polycrystalline D_{eff}	[70]
	Unspecified	Slowed	TDS	GB influence on TDS peak	[58]
	Unspecified	Slowed	TDS	GB influence on TDS peak	[59]
	Unspecified	Slowed	Permeation	Thickness vs. D_{eff}	[53]
	Unspecified	Slowed	Permeation, FEA	Grain size vs. D_{eff}, model-exp agreement	[56]
	Unspecified	Slowed	Molecular dynamics	MD GB energy analysis	[57]
	HAGB	Slowed	L-TDS	GB influence on TDS peak	[60]
	HAGB, LAGB	Slowed	Electrochem. charging	Occluded H vs. grain size	[61]
	HAGB, LAGB	Slowed	Ag decoration	Ag segregation on GBs	[62]
	HAGB, LAGB, special	Slowed	Permeation	Grain size vs. D_{eff}	[52]
	$\Sigma5$	Slowed	Kinetic Monte Carlo	kMC simulation	[67]
	$\Sigma3$, $\Sigma5$	Slowed	DFT	DFT GB energy analysis	[65]
	$\Sigma35$, $\Sigma17$, $\Sigma25$	Slowed	Molecular dynamics	MD GB enthalpy analysis	[55]
	$\Sigma5$	Slowed	Autoradiography, MD	MD GB energy analysis; grain size vs. D_{eff}	[54]
	S19	Conc.-dependent	Molecular dynamics	MD GB energy analysis	[68]
Fe-0.15Ti	Unspecified	Slowed	Microautoradiography	C segregation vs. D_{eff}	[63]
Fe-3Si	HAGB, LAGB, special	GB type-dependent	Autoradiography	Angle vs. GB penetration	[69]
Fe-Cr	Unspecified	Slowed	TDS, autoradiography	Ag segregation on GBs	[66]
Fe-Ti	HAGB, LAGB	Slowed	Charging + etching	Grain size vs. damage	[64]
Body-Centered Steels					
17-4 PH	Unspecified	Slowed	Permeation, SSRT	Literature comparison	[73]
	Unspecified	Slowed	Permeation, SSRT	PAG size/precip. ratio vs. D_{eff}	[74]
4340	Unspecified	Slowed	LECO, charging	Grain size vs. charging current	[71]
Mild steel	Unspecified	No effect of GB	TDS	Grain size vs. D_{eff}	[80]
	Unspecified	No effect of GB	Permeation, H microprint	Uniform Ag along GBs in HMT	[82]
Mild and med-C steel	Unspecified	No effect of GB	Permeation, H microprint	Uniform Ag along GBs in HMT	[81]
AERMET 100	Unspecified	Slowed	TDS	Similar E_{b} as literature	[75]
Cr-Mo steel	Unspecified	Slowed	Autoradiography, TDS	Ag segregation on GBs	[83]
DP800	Unspecified	Slowed	Permeation, TDS	Grain size vs. D_{eff}	[72]
High strength SS	Unspecified	Slowed	TDS, SIMS	Deuterium segregation at GBs, TDS peak	[76]
Maraging steel	Unspecified	Slowed	Autoradiography	Ag segregation on GBs	[84]
Martensitic SS	HAGB	Conc.-dependent	FEA	Model-lit agreement	[79]

6.2.3 Comparative Studies

There have been few published studies comparing hydrogen-grain boundary interactions in FCC and BCC metals, and there is little agreement in the findings. Though enhanced H diffusion in grain boundaries of FCC alloys has been widely observed, there is not universal agreement on this topic; Sidorenko and Sidorak report that grain boundary diffusivity is slower than the lattice diffusivity in nickel, and postulate that hydrogen is more mobile in grain boundaries in BCC structures (iron).[85] However, it should be noted that the lattice diffusivities found for Cu and Ni in this paper are much faster than often found in literature. In contrast, Lee and Lee reviewed and compared thermal analyses for several BCC and FCC alloys, concluding that grain boundaries in FCC structures act as fast paths for hydrogen, with minimal effect from dislocations.[7]

Mine et al. used hydrogen gas charging and TDS to compare hydrogen concentration of both BCC Fe-0.01C and austenitic 310S stainless steel before and after grain refinement via HPT processing.[86] The authors found a linear relationship between dislocation density and H content in the 310S, concluding that little hydrogen is trapped by the grain boundaries in 310S. However, this relationship was not linear in the Fe-0.01C BCC alloy, indicating trapping in both grain boundaries and dislocations. Though this study does not address diffusion along grain boundaries, it should be noted that the increased hydrogen trapping by grain boundaries in the BCC alloy can slow diffusivity and increase H content.

In sequential electrochemical permeation studies on diffusion in ultrafine-grained FCC Pd and BCC Fe, Iwaoka et al.[34, 52] observed opposing trends in diffusivity when varying grain size. Reducing grain size through high-pressure torsion increased diffusivity in the Pd, but decreased the diffusivity in Fe. This was ascribed to a lower hydrogen solubility in Fe compared to Pd, causing hydrogen to accumulate in grain boundaries and resulting in H-H interactions slowing down grain boundary diffusion. Additionally, the fast rate of lattice diffusion through the BCC alloy was speculated to contribute to this phenomenon.

Kazum et al.[87] compared hydrogen permeation of an austenitic TWIP steel and a ferritic mild steel. The average grain size of the TWIP steel was about an order of magnitude smaller than that of the mild steel. Ferritic alloys tend to have increased hydrogen diffusivity compared to austenitic alloys (as would be expected due to the more open BCC structure), but an increased diffusivity was observed in the austenitic TWIP steel compared to the mild steel. The authors attribute this to fast grain boundary diffusion in the TWIP steel; this is supported by the observed shorter breakthrough time and lower permeation rate.

Several modeling studies have also been published comparing hydrogen interactions with specific grain boundary types in FCC and BCC materials. Du et al. performed a first principles analysis comparing hydrogen interactions in certain representative "dense" and "open" grain boundaries in BCC and FCC Fe. The specific grain boundary types modeled were $\Sigma3[1\bar{1}0](112)$ (dense) and $\Sigma5[001](310)$ (open) in BCC, and $\Sigma3[1\bar{1}10](111)$ (dense) and $\Sigma11[1\bar{1}0](113)$ (open) in FCC.[88] Du et al. concluded that none of these grain boundaries act as short circuit diffusion pathways for hydrogen, but that diffusion along the open grain boundaries ($\Sigma5$ BCC and $\Sigma11$ FCC) occurs preferentially along the grain boundary plane. Additionally, Du et al. found that all of the examined grain boundaries act as hydrogen traps.

Liu and Gong, in a 2021 first principles study comparing diffusion through a BCC $\Sigma3(112)$ grain boundary and FCC $\Sigma3(111)$ grain boundary in PdCu, similarly observe trapping in BCC grain boundaries, though they state that it is more difficult for hydrogen to segregate to the FCC grain boundaries due to higher binding energy.[89] However, unlike Du et al., Liu and Gong conclude that the FCC $\Sigma3(111)$ grain boundaries accelerate diffusion, whereas the BCC $\Sigma3(112)$ grain boundaries slow diffusion. The authors also examine directional grain boundary diffusion, arguing that diffusion across the $\Sigma3(112)$ grain boundary is easier than diffusion along the grain boundary, whereas there is little difference in diffusion along and across the FCC $\Sigma3(111)$ grain boundary.

6.2.4 Discussion

This investigation into literature on hydrogen-grain boundary interactions in face-centered and body-centered alloys reveals a general trend of accelerated grain boundary diffusion in FCC materials. The nature of this accelerated diffusion is linked to grain boundary type, with high-angle grain boundaries often acting as favorable paths for hydrogen diffusion. Additionally, the presence of low-angle special grain boundaries introduces complexity to the trapping behavior, further influencing the overall diffusion dynamics. Accelerated diffusion has been observed along $\Sigma5$ grain boundaries as well as $\Sigma9$ and $\Sigma11$ grain boundaries, though these observations are not universal; some studies report that fast-path diffusion primarily occurs along a well-connected network of high-angle grain boundaries due to their disordered structure.

BCC and BCT alloys demonstrate notably different behaviors from FCC alloys. The more open structure of body-centered alloys contributes to fast lattice diffusion and relatively slower grain boundary diffusion. This is evidenced by experimental studies comparing diffusivity of alloys with various grain sizes, as well as modeling studies indicating higher activation enthalpy for hydrogen migration along grain boundaries compared to bulk diffusion. There is little agreement on the role of different grain boundaries in the obstruction of diffusion in these alloys; high-angle grain boundaries have been portrayed as both stronger and weaker traps than their low-angle counterparts. This may also be influenced by temperature, as the trapping ability of grain boundaries may be negated at high temperatures.

The difference in trapping and diffusion of varying grain boundary types tends to be attributed to the degree of disorder in the grain boundary structure, the associated energy, or the amount of excess volume. It would follow that, if a face-centered lattice has a higher associated energy of migration than a body-centered lattice, this would result in the observed preferential diffusion along grain boundaries with lower energies or higher excess volumes. It can be argued this difference is less determined by differences in grain

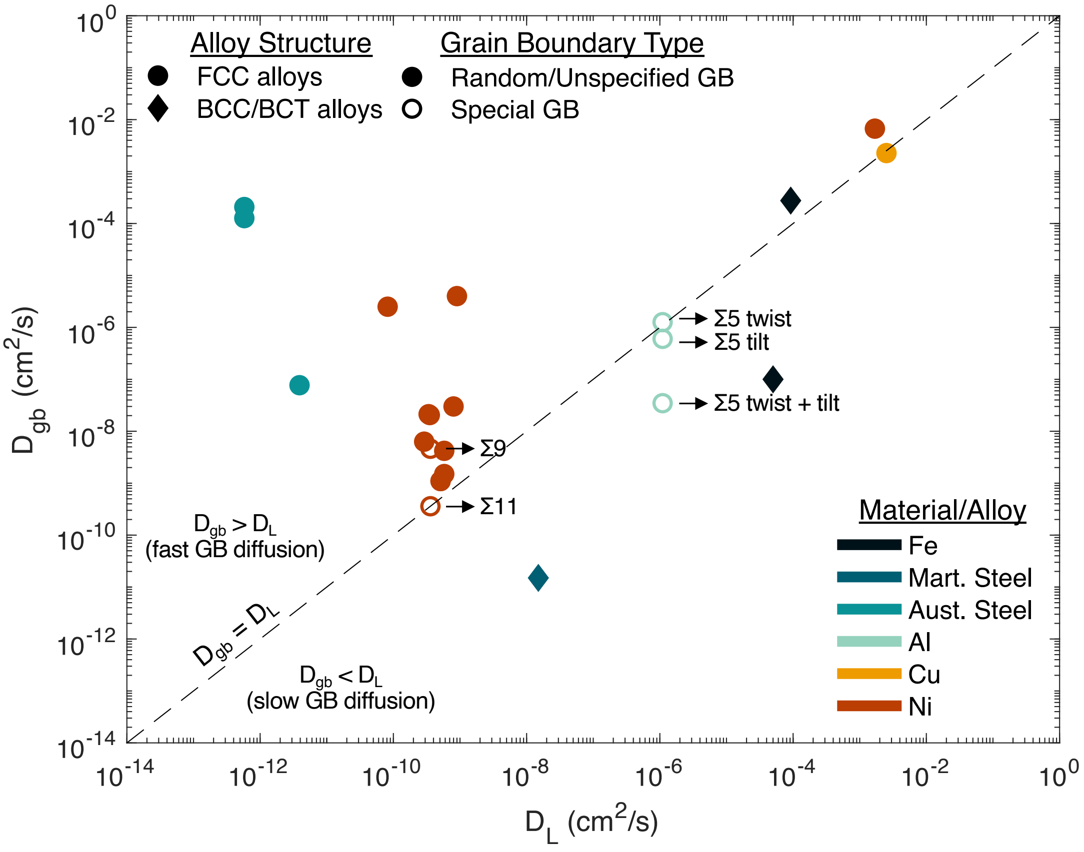

Figure 6.1: Published values of lattice and grain boundary diffusivity from literature.[1–3, 5, 6, 11, 13, 14, 27, 38, 85] The alloy structure and grain boundary type are denoted, and the regions of slow or fast grain boundary diffusion compared to lattice diffusion are labeled.

boundary structure and openness between face- and body-centered materials, but instead is determined by the lattice structure itself. This can be evidenced by the comparison of studies reporting both lattice and grain boundary diffusivity is shown in Figure 6.1. It can be seen that the majority of studies on FCC alloys show enhanced grain boundary diffusion, with the exception of those looking at specific special grain boundaries. While there are notably fewer studies on body-centered alloys, the majority report reduced grain boundary diffusivity compared to lattice diffusivity.

Hydrogen concentration has been noted as a critical factor influencing grain boundary diffusivity, as enhanced impedance of grain boundary diffusion in both BCC and FCC alloys has been reported at low hydrogen concentrations. The increase in diffusivity with concentration has been attributed to the saturation of low-energy sites.

The role of dislocations is a controversial topic in studies on face-centered alloys, with dislocations speculated to act as fast diffusion paths in some studies on FCC alloys and hydrogen traps in others. However, little evidence of enhanced dislocation diffusion in body-centered alloys has been presented in literature to date. Triple junctions have also been theorized to enhance this fast grain boundary behavior in nickel, but studies on FCC aluminum and both face- and body-centered iron alloys have reported the opposite conclusion.

6.3 Grain Boundary Network Diffusion Modeling

In order to examine the differences in effective diffusivity between the AM and the wrought 17-4 PH specimens, it is important to understand the diffusion behavior along the grain boundary. The models used to approximate grain boundary network diffusion often depend on the estimated rate of grain boundary diffusivity compared to bulk lattice diffusivity. If grain boundary diffusivity is slow compared to diffusion in the bulk, the effective diffusivity can often be modeled using a composite-type framework.[90] The purpose of these composite models is to effectively homogenize the theoretical material microstructure as an equivalent continuous medium; these often treat the microstructure as a two-phase system, with one phase being the grain interior and the other being the grain boundary. Though these models are useful approximations, it is important to note that they cannot account for microstructural complexity.

For systems with relatively fast diffusion along grain boundaries, the basic composite models often are sufficient if it can be assumed that (1) the overwhelming majority of grain boundaries consist of one type, or (2) there is little contrast between diffusivity values along the different types of grain boundaries.[91] However, when these conditions do not apply—especially when only one grain boundary type acts as a fast path for diffusion—fractal analysis or percolation theory is often employed to approximate diffusion along a grain boundary network where connectivity must be evaluated.[90–98] These analyses depend on the grain boundary fraction consisting of susceptible fast pathways, often high-angle grain boundaries. Given a certain fraction, there can be assumed a sufficient connected pathway of these grain boundaries to provide a fast path for diffusion across the specimen. Schematics of idealized composite and percolation diffusion behavior can be seen in Figure 6.2.

As discussed in the literature review contained in the previous section, the BCT structure of 17-4 PH is likely to have slow grain boundary diffusivity. However, there is still a vital question as to whether this grain boundary diffusivity is different in the AM and wrought specimens, and if this contributes to the difference in effective diffusivity. As the BCT 17-4 PH is more likely to display composite behavior due to its body-centered structure, the relationship between grain boundary density and effective diffusivity can be modeled using the Hashin-Shtrikman upper bound for two-phase materials to provide insight into diffusivity along grain boundaries:[91, 99]

$$D_{\mathrm{eff}} = D_{\mathrm{gb}} + \frac{1 - f_{\mathrm{gb}}}{\frac{1}{D_{\mathrm{L}} - D_{\mathrm{gb}}} + \frac{f_{\mathrm{gb}}}{2D_{\mathrm{gb}}}}, \tag{6.3}$$

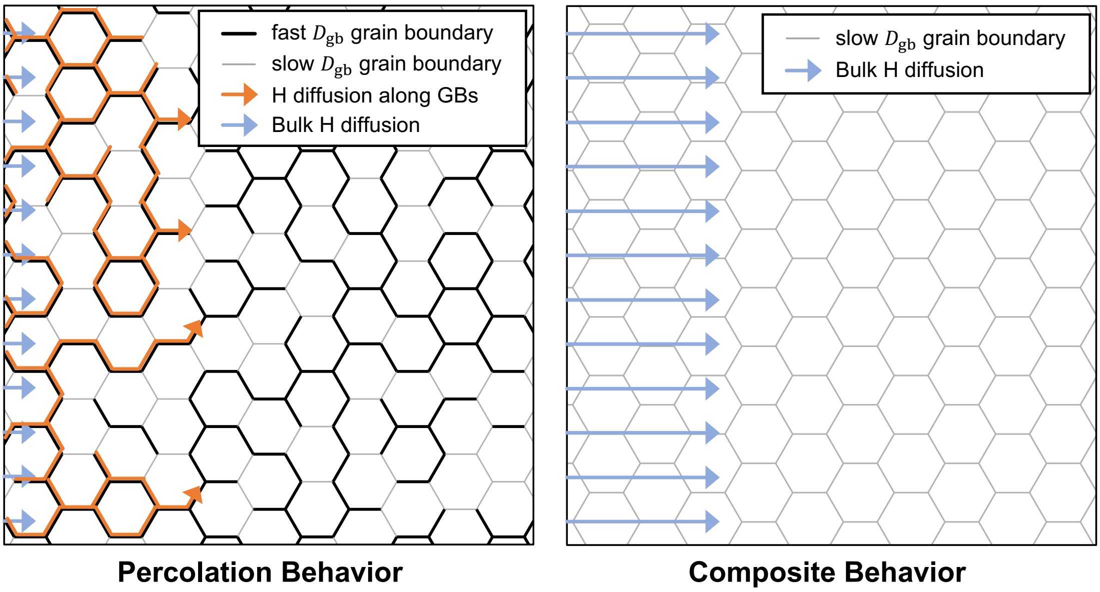

Figure 6.2: (Left) A schematic of percolation behavior in a material containing a well-connected network of short circuit grain boundaries. Fast diffusion can be observed. (Right) A schematic of composite behavior in a material containing no short circuit grain boundaries.

where D_{eff} is effective diffusivity as determined by permeation, D_{gb} is the grain boundary diffusivity, D_{L} is the ideal lattice diffusivity, and f_{gb} is the area fraction of grain boundaries in the material. This model represents the microstructure as a two-phase composite material, with one phase being grain boundaries and the other being the bulk grain interior. The bound is reached when the geometry can be approximated by spheres embedded in a matrix; in this case, the grain interior is embodied by the spheres, and the grain boundaries are the matrix phase. It should be noted that this model does not account for differences in grain boundary type, but solely provides insight into diffusivity based on the total grain boundary network. As the vast majority of grain boundaries are high-angle in all examined specimens, this model is relevant in this system.

The sensitivity of this model to grain boundary fraction and effective diffusivity can be seen in Figure 6.3. It can be concluded that the grain boundary fraction affects only the magnitude of the curve—namely, reducing grain boundary fraction increases the degree to which grain boundary diffusivity fluctuates based on lattice diffusivity—whereas changing

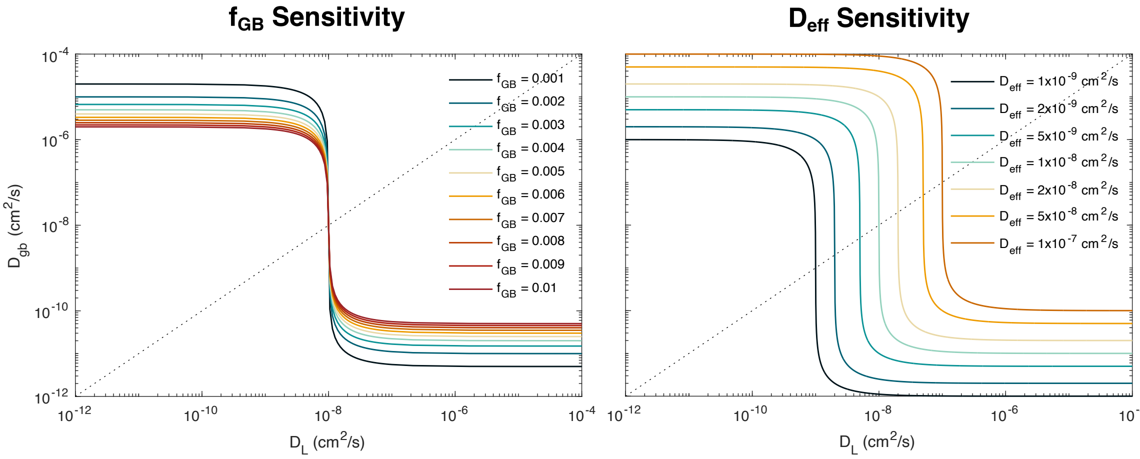

Figure 6.3: Sensitivity of the Hashin-Shtrikman model to grain boundary fraction f_{GB} (left) and effective hydrogen diffusivity D_{eff} (right).

effective diffusivity transposes the curve diagonally along the line at which $D_{\mathrm{gb}} = D_{\mathrm{L}}$.

The sensitivity effects of both variables are intuitive given some thought. Firstly, reducing the density of grain boundaries in a material without changing the effective diffusivity implies that the grain boundaries must have a greater effect, and therefore will have greater variations in grain boundary diffusivity. A suitable analogy for this is comparing two simple circuits with the same measured resistance, one consisting of wire type A and wire type B in series, and the other consisting of wire type A and wire type C in series. Assume that wire type A has a specified known resistance different from both type B and type C. It is logical that if the A+B circuit consists of 90% A and 10% B, and the A+C circuit consists of 99% A and 1% C, the difference between A and C must be greater than the difference between A and B for the two circuits to have the same resistance. In this analogy, lattice diffusion can be thought of as akin to wire A resistance, with grain boundaries represented by wires B and C.

Additionally, changing the effective diffusivity will change the point of intersection of the curve along the line where $D_{\mathrm{gb}} = D_{\mathrm{L}}$. This can be understood knowing that this model is a composite model, so if the lattice diffusivity is the same as the grain boundary diffusivity, than both will equal the effective diffusivity ($D_{\mathrm{eff}} = D_{\mathrm{gb}} = D_{\mathrm{L}}$). Therefore, changing the effective diffusivity will transpose the curve along that line of equal grain boundary and lattice diffusion values.

Table 6.3: Literature lattice diffusivity values for various martensitic steels.

Material	**Method**	$D_{\mathbf{L}}$ **(cm^2/s)**	**Reference**
Fe-C-Cr martensitic steel	Permeation	1.1×10^{-5}	[100]
Fe-C-Mo martensitic steel	Permeation	1.45×10^{-5}	[101]
X65, F22 steel	Permeation	1-3 $\times 10^{-6}$	[102]
42CrMo4 steel	Permeation	8×10^{-6}	[103]
X65 steel	Permeation	1.6×10^{-6}	[104]
AerMet 100	Isothermal TDS	1.3×10^{-7}	[75]

To evaluate the grain boundary diffusivity of the relevant alloys using this model, lattice diffusivity D_{L} can be assumed to be comparable to or moderately slower than the diffusivity of pure iron, as impurities and other defects in the steel lattice may effectively slow lattice diffusion.[100–105] Literature values for lattice diffusivities of various steels can be found in Table 6.3.

To approximate f_{gb}, the total grain boundary length was multiplied by the average grain boundary width. This width was assumed to be around 2 nm based on measurements from TEM micrographs; this value is in good agreement with grain boundary widths for BCC alloys reported in literature.[106] As D_{eff} and f_{gb} are known and fixed, D_{gb} can be calculated for a range of D_{L} values for each AM and wrought 17-4 PH specimen as seen in Figure 6.4. When lattice diffusivity is estimated from Table 6.3, the resultant D_{gb} (a function of D_{eff} and f_{gb}) provides insight as to whether the grain boundaries are acting as a short circuit or "fast path" for hydrogen (if $D_{\mathrm{gb}} > D_{\mathrm{L}}$) or if hydrogen diffusion is slowed by grain boundaries (if $D_{\mathrm{gb}} < D_{\mathrm{L}}$).

Grain boundary diffusivities are several orders of magnitude lower than the range of lattice diffusivities found in literature, possibly indicating slow diffusion or trapping behavior along grain boundaries. This is in good agreement with the permeation results—if short-circuit diffusion was occurring through a fast-path grain boundary network in

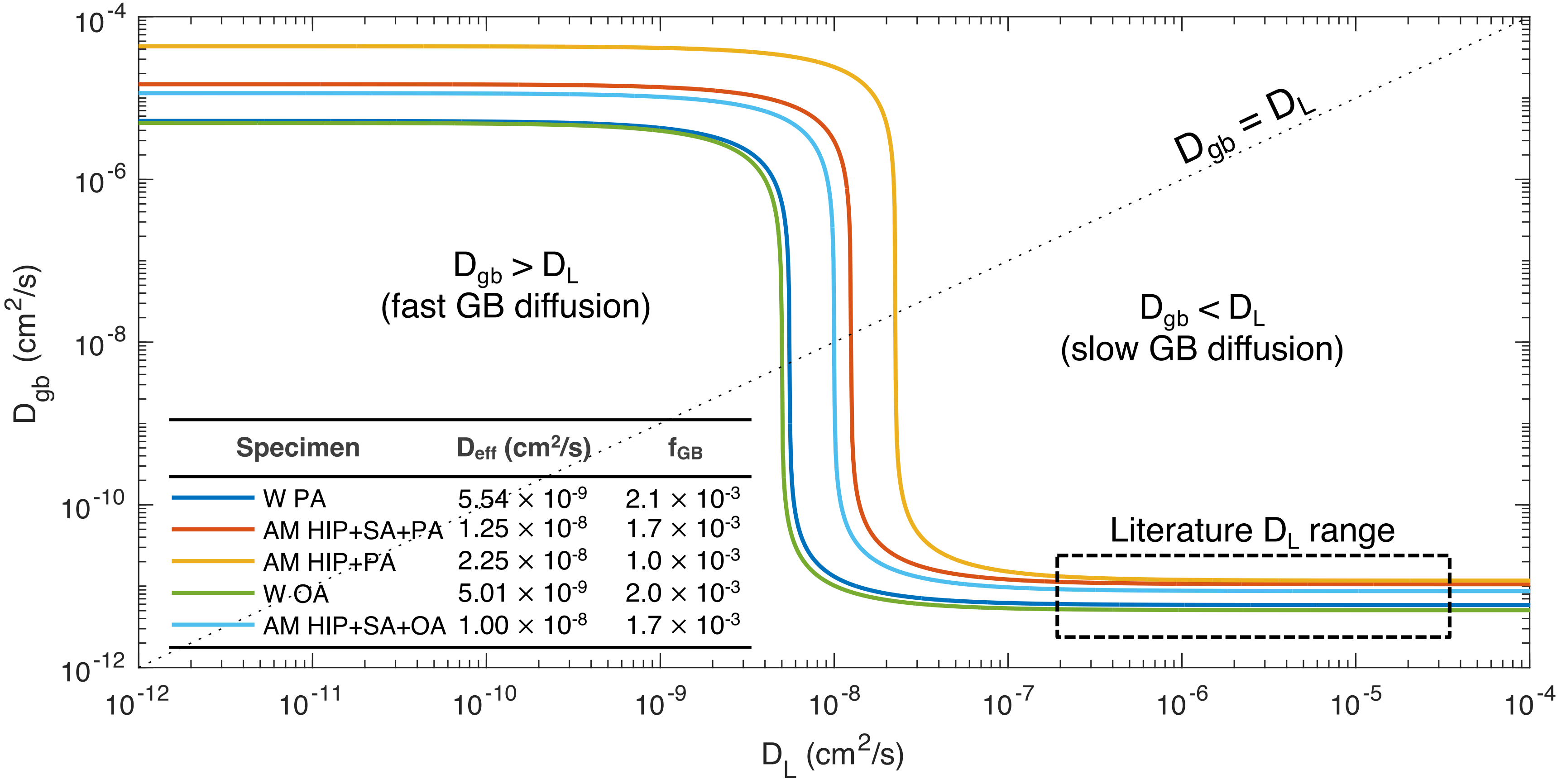

Figure 6.4: The solution to the Hashin-Shtrikman superior bound for each specimen. The range of literature lattice diffusivity values for various steels is marked (see Table 6.3).

the materials characterized in this study, it is likely that initial permeation hydrogen breakthrough in the wrought specimens would occur before breakthrough in the AM specimens due to the increased prevalence of grain boundaries in wrought. However, as seen in Section 3.5.1, the additive material shows consistently shorter breakthrough times, implying that there is no short-circuit behavior along well-connected grain boundaries.

In addition, grain boundary diffusivities are not uniform; the wrought specimens have slightly slower grain boundary diffusivities at the same lattice diffusivities than their AM counterparts. This may be attributable to several factors. The first and most important factor is the increase of special grain boundaries, specifically $\Sigma 3$ CSL grain boundaries, in the wrought specimens. This is likely to slow diffusivity along grain boundaries, leading to the observed differences. Secondly, features such as precipitate segregation along the grain boundary as well as triple junctions at grain boundary intersections have been theorized to increase trapping at the boundary.[47, 73] In that line of thought, it is likely that trapping effects are exacerbated by the observed Cu-rich decoration along grain boundaries in over-aged material, as well as the increased density of triple junctions in the wrought specimens due to smaller grain size. It is also possible that there exists a thin film of retained or reverted austenite along the grain boundaries; this would be beneficial to explore in future studies.

These relate to the assumptions inherent in this model, which simplifies a complex microstructure down to a two-phase system. When examining the results of this model, it must be understood that inclusions or precipitates along grain boundaries, as well as differences in grain boundary structure, will affect the calculated grain boundary diffusivity. This means that the D_{gb} values calculated from this model do not represent a ”pure” grain boundary diffusivity, free from the influence of microstructural features along the boundary. However, this does not diminish the usefulness of this model in analyzing the comparative diffusion rate between the lattice and the grain boundaries, as features like inclusions or precipitates will, in practice, slow hydrogen diffusion along the boundaries.

6.4 Conclusions

A comprehensive literature review of grain boundary diffusivity in face-centered and body-centered alloys has been conducted. Though there is disagreement on the specific role of grain boundary type, concentration effects, and the impact of features such as dislocations and triple junctions, there is almost universal agreement on the following phenomenon: enhanced diffusion along grain boundaries has been observed in FCC alloys, but not in BCC or BCT alloys. This can be attributed at least in part to the open lattice structure of body-centered materials, which allows for rapid diffusion in the lattice. The grain boundary diffusion behavior of the wrought and AM 17-4 PH studied in this thesis was characterized using the Hashin-Shtrikman upper bound. Based on the model, it is likely that there is slow grain boundary behavior in both wrought and AM alloys, so it is unlikely that short-circuit diffusion is responsible for the difference in diffusivity between the wrought and AM specimens. The significance of this analysis to crack growth behavior is addressed in the following chapter.

References

[1] G. Palumbo, D. M. Doyle, A. M. El-Sherik, U. Erb, and K. T. Aust, “Intercrystalline hydrogen transport in nanocrystalline nickel,” *Scripta Metallurgica et Materiala*, vol. 25, no. 3, pp. 679–684, 1991.

[2] T. Tsuru and R. M. Latanision, “Grain boundary transport of hydrogen in nickel,” *Scripta Metallurgica*, vol. 16, no. 5, pp. 575–578, 1982.

[3] T. M. Harris and M. Latanision, “Grain boundary diffusion of hydrogen in nickel,” *Metallurgical Transactions A*, vol. 22, pp. 351–355, 1991.

[4] E. Hart, “On the role of dislocations in bulk diffusion,” *Acta Metallurgica*, vol. 5, p. 597, Oct. 1957.

[5] Y. Wang, L. Xiong, and S. Liu, “Rapid Hydrogen Transportation Along Grain Boundary in Nickel,” *Acta Metallurgica Sinica (English Letters)*, vol. 27, pp. 615–620, Aug. 2014.

[6] A. Brass and A. Chanfreau, “Accelerated diffusion of hydrogen along grain boundaries in nickel,” *Acta Materialia*, vol. 44, pp. 3823–3831, Sept. 1996.

[7] J. Y. Lee and S. M. Lee, “Hydrogen trapping phenomena in metals with B.C.C. and F.C.C. crystals structures by the desorption thermal analysis technique,” *Surface and Coatings Technology*, vol. 28, no. 3-4, pp. 301–314, 1986.

[8] S. M. Lee and J. Y. Lee, “The Trapping and Transport Phenomena of Hydrogen in Nickel,” *Metallurgical Transactions A*, vol. 17, pp. 181–187, 1986.

[9] B. Szpunar, L. J. Lewis, I. Swainson, and U. Erb, “Thermal expansion and hydrogen diffusion in nanocrystalline nickel,” *Physical Review B*, vol. 60, pp. 10107–10113, Oct. 1999. Publisher: American Physical Society.

[10] S. Jothi, T. Croft, L. Wright, A. Turnbull, and S. Brown, “Multi-phase modelling of intergranular hydrogen segregation/trapping for hydrogen embrittlement,” *International Journal of Hydrogen Energy*, vol. 40, pp. 15105–15123, Nov. 2015.

[11] A. Oudriss, J. Creus, J. Bouhattate, E. Conforto, C. Berziou, C. Savall, and X. Feaugas, “Grain size and grain-boundary effects on diffusion and trapping of hydrogen in pure nickel,” *Acta Materialia*, vol. 60, pp. 6814–6828, Nov. 2012.

[12] X. Zhou, N. Mousseau, and J. Song, “Is Hydrogen Diffusion along Grain Boundaries Fast or Slow? Atomistic Origin and Mechanistic Modeling,” *Physical Review Letters*, vol. 122, p. 215501, May 2019.

[13] B. Ladna and H. K. Birnbaum, “SIMS study of hydrogen at the surface and grain boundaries of nickel bicrystals,” *Acta Metallurgica*, vol. 35, no. 10, pp. 2537–2542, 1987.

[14] H. K. Birnbaum, B. Ladna, and A. Kimura, “Hydrogen segregation and diffusion at grain boundaries,” *Le Journal de Physique Colloques*, vol. 49, pp. C5–397–C5–401, Oct. 1988.

[15] D. Di Stefano, M. Mrovec, and C. Elsässer, “First-principles investigation of hydrogen trapping and diffusion at grain boundaries in nickel,” *Acta Materialia*, vol. 98, pp. 306–312, Oct. 2015.

[16] X. W. Zhou, R. Dingreville, and R. A. Karnesky, “Molecular dynamics studies of irradiation effects on hydrogen isotope diffusion through nickel crystals and grain boundaries,” *Physical Chemistry Chemical Physics*, vol. 20, no. 1, pp. 520–534, 2018.

[17] C. Marte and R. Kirchheim, “Hydrogen diffusion in nanocrystalline nickel indicating a structural change within the grain boundaries after annealing,” *Scripta Materialia*, vol. 37, pp. 1171–1175, Oct. 1997.

[18] J. Li, A. Hallil, A. Metsue, A. Oudriss, J. Bouhattate, and X. Feaugas, “Antagonist effects of grain boundaries between the trapping process and the fast diffusion path in nickel bicrystals,” *Scientific Reports*, vol. 11, p. 15533, July 2021.

[19] J. Li, C. Lu, L. Pei, C. Zhang, and R. Wang, “Hydrogen-modified interaction between lattice dislocations and grain boundaries by atomistic modelling,” *International Journal of Hydrogen Energy*, vol. 45, pp. 9174–9187, Mar. 2020.

[20] J. E. Angelo, N. R. Moody, and M. I. Baskes, “Trapping of hydrogen to lattice defects in nickel,” *Modelling and Simulation in Materials Science and Engineering*, vol. 3, pp. 289–307, 1995.

[21] A. Oudriss, S. Le Guernic, Z. Wang, B. Osman Hoch, J. Bouhattate, E. Conforto, Z. Zhu, D. Li, and X. Feaugas, “Meso-scale anisotropic hydrogen segregation near grain-boundaries in polycrystalline nickel characterized by EBSD/SIMS,” *Materials Letters*, vol. 165, pp. 217–222, Feb. 2016.

[22] K. Wada, J. Yamabe, and H. Matsunaga, “Visualization of trapped hydrogen along grain boundaries and its quantitative contribution to hydrogen-induced intergranular fracture in pure nickel,” *Materialia*, vol. 8, p. 100478, Dec. 2019.

[23] D. R. Arantes, X. Y. Huang, C. Marte, and R. Kirchheim, "Hydrogen diffusion and permeation in micro- and nanocrystalline nickel," *Acta Metallurgica Et Materialia*, vol. 41, no. 11, pp. 3215–3222, 1993.

[24] J. Yao and J. R. Cahoon, "Experimental studies of grain boundary diffusion of hydrogen in metals," *Acta Metallurgica Et Materialia*, vol. 39, no. 1, pp. 119–126, 1991.

[25] M. Louthan, J. Donovan, and G. Caskey, "Hydrogen diffusion and trapping in nickel," *Acta Metallurgica*, vol. 23, pp. 745–749, June 1975.

[26] D. Tseng, Q. Long, and K. Tangri, "Detection of hydrogen permeation on the microscopic scale in nickel," *Scripta Metallurgica*, vol. 22, pp. 649–652, Jan. 1988.

[27] A. Kimura and H. K. Birnbaum, "Hydrogen induced grain boundary fracture in high purity nickel and its alloys-Enhanced hydrogen diffusion along grain boundaries," *Acta Metallurgica*, vol. 36, no. 3, pp. 757–766, 1988.

[28] C. Hurley, F. Martin, L. Marchetti, J. Chêne, C. Blanc, and E. Andrieu, "Role of grain boundaries in the diffusion of hydrogen in nickel base alloy 600: Study coupling thermal desorption mass spectroscopy with numerical simulation," *International Journal of Hydrogen Energy*, vol. 41, pp. 17145–17153, Oct. 2016.

[29] Z. X. Ma, X. L. Xiong, L. N. Zhang, Z. H. Zhang, Y. Yan, and Y. J. Su, "Experimental study on the diffusion of hydrogen along individual grain boundaries in nickel," *Electrochemistry Communications*, vol. 92, pp. 24–28, July 2018.

[30] A. Turk, D. Bombač, J. Jelita Rydel, M. Zietara, P. E. Rivera-Díaz-del Castillo, and E. I. Galindo-Nava, "Grain boundary carbides as hydrogen diffusion barrier in a Fe-Ni alloy: A thermal desorption and modelling study," *Materials & Design*, vol. 160, pp. 985–998, Dec. 2018.

[31] X. Lu, T. Depover, and R. Johnsen, "Evaluation of hydrogen diffusion and trapping in nickel Alloy 625 by thermal desorption spectroscopy," *International Journal of Hydrogen Energy*, vol. 47, pp. 31673–31683, Aug. 2022.

[32] T. Mütschele and R. Kirchheim, "Segregation and diffusion of hydrogen in grain boundaries of palladium," *Scripta Metallurgica*, vol. 21, no. 2, pp. 135–140, 1987.

[33] R. Kirchheim, T. Mütschele, W. Kieninger, H. Gleiter, R. Birringer, and T. D. Koblé, "Hydrogen in amorphous and nanocrystalline metals," *Materials Science and Engineering*, vol. 99, no. 1-2, pp. 457–462, 1988.

[34] H. Iwaoka, M. Arita, and Z. Horita, "Hydrogen diffusion in ultrafine-grained palladium: Roles of dislocations and grain boundaries," *Acta Materialia*, vol. 107, pp. 168–177, 2016.

[35] H. Saitoh, Y. Iijima, and K. Hirano, "Behaviour of hydrogen in pure aluminium, Al-4 mass% Cu and Al-1 mass% Mg2Si alloys studied by tritium electron microautoradiography," *Journal of Materials Science*, vol. 29, pp. 5739–5744, Nov. 1994.

[36] C. Larignon, J. Alexis, E. Andrieu, L. Lacroix, G. Odemer, and C. Blanc, "Combined Kelvin probe force microscopy and secondary ion mass spectrometry for hydrogen detection in corroded 2024 aluminium alloy," *Electrochimica Acta*, vol. 110, pp. 484–490, 2013.

[37] M. S. Bhuiyan, H. Toda, Z. Peng, S. Hang, K. Horikawa, K. Uesugi, A. Takeuchi, N. Sakaguchi, and Y. Watanabe, "Combined microtomography, thermal desorption spectroscopy, X-ray diffraction study of hydrogen trapping behavior in 7XXX aluminum alloys," *Materials Science and Engineering A*, vol. 655, pp. 221–228, 2016. Publisher: Elsevier.

[38] A. Pedersen and H. Jónsson, "Simulations of hydrogen diffusion at grain boundaries in aluminum," *Acta Materialia*, vol. 57, pp. 4036–4045, Aug. 2009.

[39] M. Ichimura, Y. Sasajima, and M. Imabayashi, "Grain boundary effect on diffusion of hydrogen in pure aluminum," *Materials Transactions, JIM*, vol. 32, no. 12, pp. 1109–1114, 1991.

[40] P. Abraham, T. Elleman, and K. Verghese, "Diffusion and trapping of tritium in grainboundaries of 304L stainless steel," *Journal of Nuclear Materials*, vol. 73, pp. 77–88, Apr. 1978.

[41] T. Tanaka, K. Kawakami, and S.-i. Hayashi, "Visualization of deuterium flux and grain boundary diffusion in duplex stainless steel and Fe–30 % Ni alloy, using secondary ion mass spectrometry equipped with a Ga focused ion beam," *Journal of Materials Science*, vol. 49, pp. 3928–3935, June 2014.

[42] R. D. Calder, T. S. Elleman, and K. Verghese, "Grain boundary diffusion of tritium in 304- and 316-stainless steels," *Journal of Nuclear Materials*, vol. 46, no. 1, pp. 46–52, 1973.

[43] T. Dieudonné, L. Marchetti, F. Jomard, M. Wery, J. Chêne, C. Allely, P. Cugy, and C. Scott, “SIMS analysis of deuterium absorption and diffusion in austenitic Fe-Mn-C steels,” *Defect and Diffusion Forum*, vol. 323-325, pp. 477–483, Apr. 2012.

[44] Y. He, Y. Su, H. Yu, and C. Chen, “First-principles study of hydrogen trapping and diffusion at grain boundaries in -Fe,” *International Journal of Hydrogen Energy*, vol. 46, pp. 7589–7600, Feb. 2021.

[45] Y. Mine, K. Tachibana, and Z. Horita, “Grain-boundary diffusion and precipitate trapping of hydrogen in ultrafine-grained austenitic stainless steels processed by high-pressure torsion,” *Materials Science and Engineering A*, vol. 528, pp. 8100–8105, 2011.

[46] J. Lee, C. Park, H. Park, and N. Kang, “Effective hydrogen diffusion coefficient for CoCrFeMnNi high-entropy alloy and microstructural behaviors after hydrogen permeation,” *International Journal of Hydrogen Energy*, vol. 45, no. 16, pp. 10227–10232, 2020.

[47] N. Yazdipour, A. Haq, K. Muzaka, and E. Pereloma, “2D modelling of the effect of grain size on hydrogen diffusion in X70 steel,” *Computational Materials Science*, vol. 56, pp. 49–57, Apr. 2012.

[48] G. Mogilny, V. Shyvaniuk, S. Teus, L. Ivaskevich, and V. Gavriljuk, “On a mechanism for enhanced hydrogen flux along grain boundaries in metals,” *Acta Materialia*, vol. 194, pp. 516–521, Aug. 2020.

[49] J. Lin, F. Chen, F. Liu, D. Xu, J. Gao, and X. Tang, “Hydrogen permeation behavior and hydrogen-induced defects in 316L stainless steels manufactured by additive manufacturing,” *Materials Chemistry and Physics*, vol. 250, p. 123038, 2020.

[50] A. Oudriss, J. Creus, J. Bouhattate, C. Savall, B. Peraudeau, and X. Feaugas, “The diffusion and trapping of hydrogen along the grain boundaries in polycrystalline nickel,” *Scripta Materialia*, vol. 66, pp. 37–40, Jan. 2012.

[51] W. Beck, J. Bockris, J. McBreen, and L. Nanis, “Hydrogen permeation in metals as a function of stress, temperature and dissolved hydrogen concentration,” *Proceedings of the Royal Society of London. Series A. Mathematical and Physical Sciences*, vol. 290, no. 1421, pp. 220–235, 1966.

[52] H. Iwaoka, M. Arita, and Z. Horita, “Hydrogen diffusion in ultrafine-grained iron with the body-centered cubic crystal structure,” *Philosophical Magazine Letters*, vol. 97, pp. 158–168, Apr. 2017.

[53] H. Addach, P. Berçot, M. Rezrazi, and J. Takadoum, “Study of the electrochemical permeation of hydrogen in iron,” *Corrosion Science*, vol. 51, pp. 263–267, Feb. 2009.

[54] S. Teus, V. Mazanko, J.-M. Olive, and V. Gavriljuk, “Grain boundary migration of substitutional and interstitial atoms in -iron,” *Acta Materialia*, vol. 69, pp. 105–113, May 2014.

[55] S. M. Teus and V. G. Gavriljuk, “Grain-Boundary Diffusion of Hydrogen Atoms in the -Iron,” *Metallofiz. Noveishie Tekhnol*, vol. 36, no. 10, pp. 1399–1410, 2014.

[56] A. Díaz, A. Zafra, E. Martínez-Pañeda, J. M. Alegre, J. Belzunce, and I. I. Cuesta, “Simulation of hydrogen permeation through pure iron for trapping and surface phenomena characterisation,” *Theoretical and Applied Fracture Mechanics*, vol. 110, p. 102818, 2020. Publisher: Elsevier Ltd.

[57] X.-Y. Zhou, J.-H. Zhu, and H.-H. Wu, “Molecular dynamics studies of the grain-size dependent hydrogen diffusion coefficient of nanograined Fe,” *International Journal of Hydrogen Energy*, vol. 46, pp. 5842–5851, Jan. 2021.

[58] W. Y. Choo and J. Y. Lee, “Thermal analysis of trapped hydrogen in pure iron,” *Metallurgical Transactions A*, vol. 13, pp. 135–140, Jan. 1982.

[59] K. Ono and M. Meshii, “Hydrogen detrapping from grain boundaries and dislocations in high purity iron,” *Acta Metallurgica et Materialia*, vol. 40, pp. 1357–1364, June 1992.

[60] R. Sato and K. Takai, “Quantitative hydrogen trap states on high-angle grain boundaries and at dislocations in iron,” *Scripta Materialia*, vol. 228, p. 115339, Apr. 2023.

[61] M. Martinez-Madrid, S. L. I. Chan, and J. A. Charles, “Hydrogen occlusivity and embrittlement in iron – effect of grain structure and cold work,” *Materials Science and Technology*, vol. 1, pp. 454–460, June 1985.

[62] M. Koyama, D. Yamasaki, T. Nagashima, C. C. Tasan, and K. Tsuzaki, “In situ observations of silver-decoration evolution under hydrogen permeation: Effects of grain boundary misorientation on hydrogen flux in pure iron,” *Scripta Materialia*, vol. 129, pp. 48–51, Mar. 2017.

[63] T. Asaoka, G. Lapasset, M. Aucouturier, and P. Lacombe, “Observation of hydrogen trapping in Fe-0.15 wt% Ti alloy by high resolution autoradiography,” *Corrosion*, vol. 34, no. 2, pp. 39–47, 1978.

[64] G. Pressouyre and I. Bernstein, "A kinetic trapping model for hydrogen-induced cracking," *Acta Metallurgica*, vol. 27, pp. 89–100, Jan. 1979.

[65] A. S. Kholtobina, R. Pippan, L. Romaner, D. Scheiber, W. Ecker, and V. I. Razumovskiy, "Hydrogen Trapping in bcc Iron," *Materials*, vol. 13, p. 2288, May 2020.

[66] C. Paes de Oliveira, M. Aucouturier, and P. LaCombe, "Hydrogen Trapping in BCC Fe-Cr Alloys (7 ˜ 9.4 Wt% Cr) as Studied by Microautoradiography - Contribution of Carbon-Hydrogen Interaction - Consequences on Hydrogen Cracking," *Corrosion*, vol. 36, no. 2, pp. 53–59, 1980. ISBN: 9788490225370.

[67] Y. A. Du, J. Rogal, and R. Drautz, "Diffusion of hydrogen within idealized grains of bcc Fe: A kinetic Monte Carlo study," *Physical Review B*, vol. 86, p. 174110, Nov. 2012.

[68] S. Yang, S.-H. Yun, and T. Oda, "Molecular dynamics simulation on stability and diffusivity of hydrogen around a symmetric tilt grain boundary in bcc-Fe," *Fusion Engineering and Design*, vol. 131, pp. 105–110, June 2018.

[69] C. Haynes and R. Smoluchowski, "Grain boundary diffusion in a body-centered cubic lattice," *Acta Metallurgica*, vol. 3, pp. 130–134, Mar. 1955.

[70] H. Hagi, Y. Hayashi, and N. Ohtani, "Diffusion Coefficient of Hydrogen in Pure Iron between 230 and 300 K," *Transactions of the Japan Institute of Metals*, vol. 20, no. 7, pp. 349–357, 1979.

[71] M. D. Danford, "Hydrogen Trapping and the Interaction of Hydrogen With Metals," Tech. Rep. NASA-TP-2744, 1987.

[72] A. Turk, G. R. Joshi, M. Gintalas, M. Callisti, P. E. Rivera-Díaz-del Castillo, and E. I. Galindo-Nava, "Quantification of hydrogen trapping in multiphase steels: Part I – Point traps in martensite," *Acta Materialia*, vol. 194, pp. 118–133, Aug. 2020.

[73] L. W. Tsay, W. C. Lee, R. K. Shiue, and J. K. Wu, "Notch tensile properties of laser-surface-annealed 17-4 PH stainless steel in hydrogen-related environments," *Corrosion Science*, vol. 44, no. 9, pp. 2101–2118, 2002. ISBN: 0010-938X.

[74] S. Shen, X. Li, P. Zhang, Y. Nan, G. Yang, and X. Song, "Effect of solution-treated temperature on hydrogen embrittlement of 17-4 PH stainless steel," *Materials Science and Engineering A*, 2017.

[75] D. Li, R. P. Gangloff, and J. R. Scully, “Hydrogen Trap States in Ultrahigh-Strength AERMET 100 Steel,” *Metallurgical and Materials Transactions A: Physical Metallurgy and Materials Science*, vol. 35, pp. 849–864, 2004.

[76] K. Takai, J. Seki, and Y. Homma, “Observation of Trapping Sites of Hydrogen and Deuterium in High-Strength Steels by Using Secondary Ion Mass Spectrometry,” *Materials Transactions, JIM*, vol. 36, no. 9, pp. 1134–1139, 1995.

[77] T. Depover, A. Laureys, D. P. Escobar, E. Van den Eeckhout, E. Wallaert, and K. Verbeken, “Understanding the interaction between a steel microstructure and hydrogen,” *Materials*, vol. 11, no. 5, p. 698, 2018.

[78] R. Shi, L. Chen, Z. Wang, X. S. Yang, L. Qiao, and X. Pang, “Quantitative investigation on deep hydrogen trapping in tempered martensitic steel,” *Journal of Alloys and Compounds*, vol. 854, p. 157218, 2021. Publisher: Elsevier B.V.

[79] T. Das, R. Chakrabarty, J. Song, and S. Yue, “Understanding microstructural influences on hydrogen diffusion characteristics in martensitic steels using finite element analysis (FEA),” *International Journal of Hydrogen Energy*, vol. 47, no. 2, pp. 1343–1357, 2022. Publisher: Hydrogen Energy Publications LLC.

[80] B. Chew and F. T. Fabling, “The effect of grain boundaries on the low-temperature diffusion of hydrogen in decarburized mild steel,” *Metal Science Journal*, 1972.

[81] W. Luu and J. Wu, “The influence of microstructure on hydrogen transport in carbon steels,” *Corrosion Science*, vol. 38, pp. 239–245, Feb. 1996.

[82] K. Ichitani and M. Kanno, “Visualization of hydrogen diffusion in steels by high sensitivity hydrogen microprint technique,” *Science and Technology of Advanced Materials*, vol. 4, pp. 545–551, Jan. 2003.

[83] G. Katano, K. Ueyama, and M. Mori, “Observation of hydrogen distribution in high-strength steel,” *Journal of Materials Science*, vol. 36, pp. 2277–2286, 2001.

[84] M. Aucouturier, G. Lapasset, and T. Asaoka, “Direct observation of hydrogen entrapment,” *Metallography*, vol. 11, pp. 5–21, Jan. 1978.

[85] V. M. Sidorenko and I. I. Sidorak, “Boundary and volume diffusion of hydrogen in copper, nickel, and iron,” *Soviet Materials Science*, vol. 9, pp. 372–375, 1975.

[86] Y. Mine, Z. Horita, and Y. Murakami, “Effect of high-pressure torsion on hydrogen trapping in Fe–0.01 mass% C and type 310S austenitic stainless steel,” *Acta Materialia*, vol. 58, pp. 649–657, Jan. 2010.

[87] O. Kazum, H. Beladi, and M. B. Kannan, “Hydrogen permeation in twinning-induced plasticity (TWIP) steel,” *International Journal of Hydrogen Energy*, vol. 43, pp. 22685–22693, Dec. 2018.

[88] Y. A. Du, L. Ismer, J. Rogal, T. Hickel, J. Neugebauer, and R. Drautz, “First-principles study on the interaction of H interstitials with grain boundaries in - and -Fe,” *Physical Review B*, vol. 84, p. 144121, Oct. 2011.

[89] L. C. Liu and H. R. Gong, “Hydrogen solubility and diffusivity at 3 grain boundary of PdCu,” *RSC Advances*, vol. 11, no. 22, pp. 13644–13652, 2021.

[90] B. Osman Hoch, *Modelling of hydrogen diffusion in heterogeneous materials: implications of the grain boundary connectivity.* PhD thesis, Université de La Rochelle, 2015.

[91] Y. Chen and C. A. Schuh, “Diffusion on grain boundary networks: Percolation theory and effective medium approximations,” *Acta Materialia*, vol. 54, no. 18, pp. 4709–4720, 2006.

[92] S. Kobayashi, T. Maruyama, S. Tsurekawa, and T. Watanabe, “Grain boundary engineering based on fractal analysis for control of segregation-induced intergranular brittle fracture in polycrystalline nickel,” *Acta Materialia*, vol. 60, pp. 6200–6212, Oct. 2012.

[93] Z. Harris, *Elucidating Microstructural Contributions to Hydrogen Embrittlement Susceptibility in Ni-base Alloys.* PhD thesis, University of Virginia, Dec. 2018.

[94] J. Sayet, B. O. Hoch, A. Oudriss, J. Bouhattate, and X. Feaugas, “Multi-scale approach to hydrogen diffusion in FCC polycrystalline structure with binary classification of grain boundaries in continuum model,” *Materials Today Communications*, vol. 34, p. 105021, 2023. Publisher: Elsevier.

[95] B. Osman Hoch, A. Metsue, J. Bouhattate, and X. Feaugas, “Effects of grain-boundary networks on the macroscopic diffusivity of hydrogen in polycrystalline materials,” *Computational Materials Science*, vol. 97, pp. 276–284, Feb. 2015. Publisher: Elsevier B.V.

[96] M. Frary and C. A. Schuh, “Connectivity and percolation behaviour of grain boundary networks in three dimensions,” *Philosophical Magazine*, vol. 85, pp. 1123–1143, Apr. 2005.

[97] S. Bechtle, M. Kumar, B. Somerday, M. Launey, and R. Ritchie, "Grain-boundary engineering markedly reduces susceptibility to intergranular hydrogen embrittlement in metallic materials," *Acta Materialia*, vol. 57, pp. 4148–4157, Aug. 2009.

[98] N. A. Rutter, B. A. Glowacki, and J. E. Evetts, "Percolation modelling for highly aligned polycrystalline superconducting tapes," *Superconductor Science and Technology*, vol. 13, pp. L25–L30, Nov. 2000.

[99] E. Legrand, J. Bouhattate, X. Feaugas, S. Touzain, H. Garmestani, M. Khaleel, and D. Li, "Numerical analysis of the influence of scale effects and microstructure on hydrogen diffusion in polycrystalline aggregates," *Computational Materials Science*, vol. 71, pp. 1–9, Apr. 2013.

[100] S. Frappart, X. Feaugas, J. Creus, F. Thebault, L. Delattre, and H. Marchebois, "Hydrogen solubility, diffusivity and trapping in a tempered Fe–C–Cr martensitic steel under various mechanical stress states," *Materials Science and Engineering: A*, vol. 534, pp. 384–393, Feb. 2012.

[101] S. Frappart, X. Feaugas, J. Creus, F. Thebault, L. Delattre, and H. Marchebois, "Study of the hydrogen diffusion and segregation into Fe–C–Mo martensitic HSLA steel using electrochemical permeation test," *Journal of Physics and Chemistry of Solids*, vol. 71, pp. 1467–1479, Oct. 2010.

[102] E. Fallahmohammadi, F. Bolzoni, and L. Lazzari, "Measurement of lattice and apparent diffusion coefficient of hydrogen in X65 and F22 pipeline steels," *International Journal of Hydrogen Energy*, vol. 38, pp. 2531–2543, Feb. 2013. Publisher: Elsevier Ltd.

[103] A. Zafra, J. Belzunce, and C. Rodríguez, "Hydrogen diffusion and trapping in 42CrMo4 quenched and tempered steel: Influence of quenching temperature and plastic deformation," *Materials Chemistry and Physics*, vol. 255, p. 123599, Nov. 2020.

[104] E. Koren, C. M. H. Hagen, D. Wang, X. Lu, R. Johnsen, and J. Yamabe, "Experimental comparison of gaseous and electrochemical hydrogen charging in X65 pipeline steel using the permeation technique," *Corrosion Science*, vol. 215, p. 111025, May 2023.

[105] A. J. Kumnick and H. H. Johnson, "Hydrogen transport through annealed and deformed armco iron," *Metallurgical transactions*, vol. 5, pp. 1199–1206, May 1974.

[106] B. Fultz and H. N. Frase, “Grain boundaries of nanocrystalline materials – their widths, compositions, and internal structures,” *Hyperfine Interactions*, vol. 130, pp. 91–108, 2000.

Chapter 7

Relation to Environmentally-Assisted Cracking Kinetics

7.1 Overview

The role of experimentally determined and observed hydrogen materials interactions in determining hydrogen environmentally assisted cracking (HEAC) resistance in the context of crack growth kinetics is explored. This is accomplished through the evaluation of previously measured HEAC kinetics as a function of the measured diffusible hydrogen concentration. The agreement of diffusible hydrogen concentration-dependent crack growth rate with an existing model for H-affected stage II cracking is assessed. The impact of effective hydrogen diffusivity and critical diffusible hydrogen concentration on the increased HEAC susceptibility of AM 17-4 PH in the peak-aged and over-aged conditions is discussed. Results indicate that increased crack growth kinetics in the AM alloys can be attributed primarily to the reduced critical diffusible hydrogen concentration required for cracking, with a minor contribution from the increased effective diffusivity in

AM 17-4 PH.

7.2 Collaborations

The role of experimentally determined and observed hydrogen materials interactions in determining hydrogen environmentally assisted cracking (HEAC) resistance in the context of crack growth kinetics is explored. This is accomplished through the evaluation of previously measured HEAC kinetics as a function of the measured diffusible hydrogen concentration. The agreement of diffusible hydrogen concentration-dependent crack growth rate with an existing model for H-affected stage II cracking is assessed. The impact of effective hydrogen diffusivity and critical diffusible hydrogen concentration on the increased HEAC susceptibility of AM 17-4 PH in the peak-aged and over-aged conditions is discussed. Results indicate that increased crack growth kinetics in the AM alloys can be attributed primarily to the reduced critical diffusible hydrogen concentration required for cracking, with a minor contribution from the increased effective diffusivity in AM 17-4 PH.

7.3 Background

The hydrogen behavior analysis performed in the previous chapters of this thesis can be applied to better understand the increased hydrogen environmentally-assisted cracking (HEAC) susceptibility of AM 17-4 PH observed by Shoemaker et al.,[1] who measured 5- to 10-fold increases in crack growth rate for peak-aged and over-aged AM 17-4 PH compared to wrought 17-4 PH with comparable strengths. SCC experiments were conducted at constant stress intensity (K) loads ranging from 30 to 40 MPa$\sqrt{\text{m}}$ for specimens immersed in 0.6 M NaCl and polarized to potentials between -0.2 and -1.4 V_{SCE} relative to wrought 17-4 PH with comparable strengths. These results have been reproduced in Figure 7.1.

As shown by Shoemaker et al., crack growth rate shows dependence on applied potential,

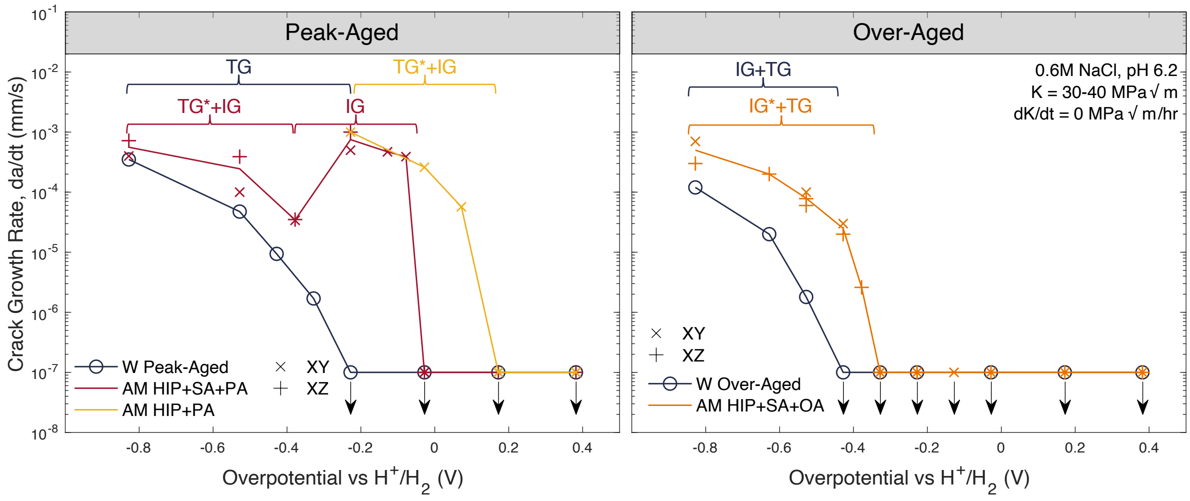

Figure 7.1: Data from Shoemaker et al.[1] on constant K HEAC crack growth rate as a function of overpotential in AM and wrought 17-4 PH in the peak-aged (left) and over-aged (right) conditions. Intergranular (IG) and transgranular (TG) fracture modes for each condition are marked, with the primary mode of fracture denoted by an asterisk. The downward arrows represent the non-susceptible region with no crack growth.

with increased susceptibility to SCC at increasingly cathodic potential. Two overarching initial conclusions can be drawn from these data: (1) the cathodic potential accompanying the initiation of stage II SCC susceptibility, or the "takeoff potential" is lower in the AM 17-4 PH specimens than in their wrought counterpart in both aging conditions, and (2) at the same cathodic potential, crack growth rate is higher in the AM specimens compared to wrought in both conditions. The AM HIP+PA specimens have the least cathodic takeoff potential, around 200 mV less cathodic than that of AM HIP+SA+PA, though crack growth rate between -0.2V and 0V was largely similar between the two. The over-aged AM specimens also exhibited a less cathodic takeoff potential and faster crack growth rates than their wrought counterparts, though the difference is less dramatic than in the peak-aged.

In essence, these stress corrosion cracking data show the increased susceptibility of AM 17-4 PH to environmentally-assisted cracking. As even small differences in microstructure can impact environmentally-assisted cracking (EAC) behavior,[2–4] the marked difference between AM and wrought microstructure observed both in this study and in literature[5–15] is likely the culprit; however, the precise microstructural factors contributing to this susceptibility are still uncertain. The submicron porosity and oxide inclusions in AM 17-4 PH observed by Shoemaker et al.[1] were theorized to degrade boundary fracture toughness and thereby increase EAC susceptibility.

Fractography by Shoemaker et al.[1] revealed differences in fracture morphology between each specimen. Peak-aged wrought 17-4 PH displayed exclusively transgranular (TG) fracture, with branching observed at the most cathodic overpotentials. In comparison, the AM HIP+SA+PA and AM HIP+PA specimens both showed mixed intergranular (IG) and TG cracking, with AM HIP+PA exhibiting primarily TG fracture at all potentials. At an overpotential between -0.2 and -0.4V, the AM HIP+SA+PA specimen actually exhibits a transition between mostly IG fracture to a mixed fracture mode dominated by TG fracture, corresponding to the reduced crack growth rate seen in Figure 7.1. The over-aged wrought and AM specimens both showed mixed but primarily IG fracture. The wrought specimen displayed L-T plane fissuring at the most cathodic potential, whereas the AM HIP+SA+OA specimens showed branching at the most cathodic potential.

The differences in fracture morphology are attributed by Shoemaker et al.[1] to variations in the Griffith fracture toughness of the interface k_{IG} and stress-enhanced hydrogen concentration $C_{\mathrm{H}\sigma}$ between different fracture paths, based on the following interface decohesion-based model for stress corrosion cracking proposed by Gerberich[16] and modified by Harris et al.[2] and Burns et al.:[17]

$$K_{\mathrm{TH}} = \frac{1}{\beta'} \left[\frac{([k_{\mathrm{IG}} + \sum_{i=0}^{n} \beta_i C_i] - \alpha C_{\mathrm{H}\sigma})^2}{\alpha'' \sigma_{\mathrm{ys}}} \right], \tag{7.1}$$

in which K_{TH} is the threshold stress intensity for the onset of subcritical crack growth at a certain interface, α is a weighting factor defining the deleterious effects of hydrogen concentration on Griffith toughness, σ_{ys} is the yield strength of the alloy, and α'' and β' are constants derived through a dislocation shielding model of crack tip elastic stress.

The summation term $\sum_{i=0}^{n} \beta_i C_i$ is used by Shoemaker et al.[1] to account for the effects of trace impurities along the fracture path interface on Griffith toughness, with β_i being the weighting factor and C_i being the local concentration of trace impurity i.

This framework is analyzed by the authors with respect to the Ritchie-Knott-Rice (RKR) paradigm of crack advance, which models crack advance as a result of exceeding critical local failure criteria over a critical distance x_{crit} ahead of the crack tip.[18, 19] This demonstrates a reliance of crack advance on crack path-specific microstructural features, and the authors postulate that the difference in crack path can be attributed to variations in Griffith fracture toughness k_{IG} and weighted stress-affected hydrogen concentration $\alpha C_{\text{H}\sigma}$ between different fracture pathways based on these microstructural features. Thereby, the transition in dominant fracture mode in AM HIP+SA+PA from IG to TG with increasingly cathodic potential can be explained by different rates of reduction in interface failure stress for different boundary types (specifically, prior austenite grain (PAG) boundaries and martensite boundaries) as local H content increases. Shoemaker et al.[1] argues that the interface failure stress of the martensite boundaries in the AM peak-aged specimen must decrease more quickly when compared to the PAG boundaries, causing a cross-over at a certain critical H content; in comparison, the PAG and martensite boundaries in the wrought peak-aged specimen likely decrease at similar rates as H concentration increases, so no change is observed in fracture mode.

These prior analyses focus on local failure criteria and the impact of microstructural features; however, the potential differences in hydrogen-metal interactions and their influence on crack growth kinetics are not considered.

The effect of hydrogen on EAC behavior has been described through the Gerberich model, which relates threshold stress intensity to hydrogen concentration.[16, 20, 21] Beyond this framework, stress corrosion cracking can be directly correlated to hydrogen behavior through its relationship with effective diffusivity and hydrogen concentration. One notable example is Lee and Gangloff's model relating stress corrosion cracking (SCC) stage II crack growth rate $\left(\frac{\mathrm{d}a}{\mathrm{d}t}\right)_{\mathrm{II}}$ directly to hydrogen diffusivity and concentration.[22] This originated from a solution to Fick's second law, considering the scenario of a plane infinite source of hydrogen diffusing into a semi-infinite medium, given the following boundary conditions describing hydrogen concentration C:

1. $C = C_0$, $x = 0$, $t > 0$: Initial H concentration at the boundary is uniform and fixed at a constant value C_0.
2. $C = 0$, $x > 0$, $t = 0$: Initial H concentration in the medium is zero.

Fick's second law can then be solved to find the concentration $C(x,t)$ at any point x or time t:[23]

$$C(x,t) = C_0 \left[1 - \mathrm{erf}\left(\frac{x}{2\sqrt{D_{\mathrm{eff}}t}}\right)\right], \tag{7.2}$$

where D_{eff} is effective hydrogen diffusivity. This can be rearranged to isolate distance x over time t:

$$\frac{x}{t} = \frac{4D_{\mathrm{eff}}}{x}\left[\mathrm{erf}^{-1}\left(1 - \frac{C(x,t)}{C_0}\right)\right]^2.$$

If hydrogen concentration at the boundary is assumed to be equivalent to diffusible hydrogen concentration (i.e., the effects of irreversible trapping are negligible), this can be expressed as

$$\frac{x}{t} = \frac{4D_{\mathrm{eff}}}{x}\left[\mathrm{erf}^{-1}\left(1 - \frac{C(x,t)}{C_{\mathrm{H,diff}}}\right)\right]^2. \tag{7.3}$$

This can be applied to hydrogen-assisted cracking if one assumes that hydrogen charging of a cracked specimen can be approximated as diffusion of hydrogen a plane infinite source into a plane infinite specimen with the same boundary conditions as listed above, assuming diffusivity is independent of stress and hydrogen concentration.[24] However, a modification of the concentration variables is necessary in order to account for the effects of the stress field in the fracture process zone on hydrogen concentration.

Stress-affected hydrogen concentration $C_{\mathrm{H}\sigma}$ at any point x within a stress field can be expressed using a Boltzmann distribution function, assuming that $C_{\mathrm{H,diff}}$ is representative of bulk hydrogen concentration:[25]

$$C_{\mathrm{H}\sigma} = C_{\mathrm{H,diff}} \exp\left(\frac{U}{k_{\mathrm{B}}T}\right),$$

where k_{B} is the Boltzmann constant, T is temperature, and the interaction U controlling solute segregation in a stress field is given by the basic thermodynamic relationship between work, pressure, and volume change $U = p_\sigma \Delta V$, where p_σ is the pressure tensor of the stress field and ΔV is the change in atomic volume of a solute atom. This leads to:

$$C_{\mathrm{H}\sigma} = C_{\mathrm{H,diff}} \exp\left(\frac{p_\sigma \Delta V}{k_{\mathrm{B}}T}\right).$$

The pressure and volume terms can be defined in terms of hydrostatic stress $p_\sigma = \frac{\sigma_{\mathrm{H}}}{3}$ and the change in partial molar volume $\bar{V}_{\mathrm{H}} = N_{\mathrm{A}}\Delta V$, respectively, knowing that Boltzmann constant k_{B} is related to ideal gas constant R and Avogadro's number N_{A} through $k_{\mathrm{B}} = \frac{R}{N_{\mathrm{A}}}$:[26]

$$C_{\mathrm{H}\sigma} = C_{\mathrm{H,diff}} \exp\left(\frac{\sigma_{\mathrm{H}} \bar{V}_{\mathrm{H}}}{3RT}\right). \tag{7.4}$$

This assumes that the movement of hydrogen into the fracture process zone is not also driven by elastic-plastic stress field region in front of the process zone. [i]

If $C_{\mathrm{H,diff}}$ and $C(x,t)$ in Equation 7.3 are modified to incorporate the results of stress, this can provide a model of hydrogen concentration near a fracture process zone:

$$\frac{x}{t} = \frac{4D_{\mathrm{eff}}}{x}\left[\mathrm{erf}^{-1}\left(1 - \frac{C_{\mathrm{H}\sigma}(x,t)}{C_{\mathrm{H}\sigma}}\right)\right]^2, \tag{7.5}$$

where $C_{\mathrm{H}\sigma}$ is representative of stress-affected bulk hydrogen concentration. If it is assumed that stage II crack advance is triggered when stress-affected hydrogen concentration

---

[i] If this is the case, this expression can be updated to include that external force acting on the system:[27]

$$C'_{\mathrm{H}\sigma} = C_{\mathrm{H}\sigma} \exp\left(\frac{H_{\mathrm{b}}}{RT}\right) = C_{\mathrm{H,diff}} \exp\left(\frac{\sigma_{\mathrm{H}} \bar{V}_{\mathrm{H}}}{3RT}\right) \exp\left(\frac{H_{\mathrm{b}}}{RT}\right),$$

where $C'_{\mathrm{H}\sigma}$ is the updated hydrogen concentration at the trap site and H_{b} is binding energy.

reaches a critical value $C_{\mathrm{H}\sigma-\mathrm{crit}}$ at a certain critical distance x_{crit} ahead of the crack tip surface after time Δt:[27]

$$\left(\frac{\mathrm{d}a}{\mathrm{d}t}\right)_{\mathrm{II}} = \frac{x_{\mathrm{crit}}}{\Delta t}, \tag{7.6}$$

then Equation 7.5 can be updated to incorporate stage II crack growth rate, given that $C_{\mathrm{H}\sigma}(x_{\mathrm{crit}}, t) = C_{\mathrm{H}\sigma-\mathrm{crit}}$:[28]

$$\left(\frac{\mathrm{d}a}{\mathrm{d}t}\right)_{\mathrm{II}} = \frac{4D_{\mathrm{eff}}}{x_{\mathrm{crit}}}\left[\mathrm{erf}^{-1}\left(1-\frac{C_{\mathrm{H}\sigma-\mathrm{crit}}}{C_{\mathrm{H}\sigma}}\right)\right]^{2}, \tag{7.7}$$

as described by Lee and Gangloff.[22] The relationship between $C_{\mathrm{H}\sigma}$ and diffusible hydrogen concentration described by Equation 7.4 can also be incorporated into the stage II crack growth rate model:

$$\left(\frac{\mathrm{d}a}{\mathrm{d}t}\right)_{\mathrm{II}} = \frac{4D_{\mathrm{eff}}}{x_{\mathrm{crit}}}\left[\mathrm{erf}^{-1}\left(1-\frac{C_{\mathrm{H,diff\text{-}crit}}\exp\left(\frac{\sigma_{\mathrm{H}}\bar{V}_{\mathrm{H}}}{3RT}\right)}{C_{\mathrm{H,diff}}\exp\left(\frac{\sigma_{\mathrm{H}}\bar{V}_{\mathrm{H}}}{3RT}\right)}\right)\right]^{2},$$

if $C_{\mathrm{H,diff\text{-}crit}}$ is the critical diffusible hydrogen concentration corresponding to $C_{\mathrm{H}\sigma-\mathrm{crit}}$. Within a single material, hydrostatic stress and partial molar volume will be constant and cancel out, giving:

$$\left(\frac{\mathrm{d}a}{\mathrm{d}t}\right)_{\mathrm{II}} = \frac{4D_{\mathrm{eff}}}{x_{\mathrm{crit}}}\left[\mathrm{erf}^{-1}\left(1-\frac{C_{\mathrm{H,diff\text{-}crit}}}{C_{\mathrm{H,diff}}}\right)\right]^{2}. \tag{7.8}$$

If the binding energy related to the elastic-plastic stress field region in front of the process zone is also assumed to be constant within a single alloy, this relationship is also valid if the elastic-plastic stress field is not neglected.

Based on this interpretation of Lee and Gangloff's framework, crack growth rate is dependent on effective diffusivity, the critical length parameter, the diffusible hydrogen concentration in the material, and the diffusible hydrogen concentration corresponding to crack propagation. Both effective diffusivity and diffusible hydrogen concentration have been experimentally determined as described in Chapters 3 and 4, respectively. If diffusible hydrogen concentration can be correlated to the corresponding experimentally determined crack growth rates based on similar charging conditions, the $C_{\mathrm{H,diff}}$-dependent crack growth rate can be fit to Equation 7.8, and both the length parameter and the critical diffusible hydrogen concentration can be estimated.

These relationships demonstrate the importance of considering H interactions when characterizing cracking behavior in steels. If environmentally-assisted crack growth kinetics can be sufficiently described by this model, it is evident that an understanding of hydrogen diffusion and concentration within the microstructure is indispensable.

7.4 Comparison of Hydrogen Interactions and HEAC Behavior

7.4.1 Coupling Hydrogen Concentration and Stage II Crack Growth Rate

Mechanistically, it is useful to evaluate the observed hydrogen-metal interactions in the context of existing EAC growth rate kinetics for these alloys.[1] Therefore, the measured EAC growth rates (at K between 30-40 MPa$\sqrt{\mathrm{m}}$) for each tested AM and wrought alloy are plotted as a function of barnacle cell $C_{\mathrm{H,diff}}$ in Figure 7.2. This was achieved through conversion to hydrogen overpotential from potential versus saturated calomel and Hg/$HgSO_4$ electrodes for stage II crack growth rate and barnacle cell, respectively, accounting for solution pH.[29] The data were then interpolated to match hydrogen overpotential values.

The usual relationship of crack growth rate increasing with hydrogen concentration and exhibiting a threshold is observed. This comparison provides two key insights: (1) when cracking is observed, the measured crack growth rate for the AM alloy is always increased relative to comparable wrought material at a given $C_{\mathrm{H,diff}}$; and (2) the critical

$C_{\mathrm{H,diff}}$ at the onset of cracking is significantly increased for the wrought alloys relative to the comparable AM condition.

7.4.2 Modeling of Hydrogen-Dependent EAC Behavior

The data shown in Figure 7.2 can be used alongside proposed models for K_{TH} to identify the causal factors responsible for the lower EAC resistance of AM 17-4 PH. In general, phenomenological models for the onset and propagation of EAC[2, 16, 17, 30] suggest that increased EAC susceptibility is linked to three overarching variables: (1) yield strength, (2) hydrogen-metal interactions, and (3) alloy microstructure. It should be noted that these variables often do not act independently of each other; for example, hydrogen-metal interactions are dependent on microstructural features. Critically, the yield strengths of these alloys are nominally similar;[1] therefore, the increased EAC susceptibility of the AM materials is most likely driven by differences in the latter two contributions. However, a comparison of these models with the measured hydrogen-metal interactions suggests that, while the increased diffusivity in the AM specimens certainly contributes to the increased crack growth rate, the difference in diffusivity cannot fully explain the observed differences in EAC behavior. Recall Lee and Gangloff's HEAC stage II crack growth rate model, shown in Equation 7.7 and reproduced here:[22]

$$\left(\frac{\mathrm{d}a}{\mathrm{d}t}\right)_{\mathrm{II}} = \frac{4D_{\mathrm{eff}}}{x_{\mathrm{crit}}}\left[\mathrm{erf}^{-1}\left(1-\frac{C_{\mathrm{H}\sigma\text{-crit}}}{C_{\mathrm{H}\sigma}}\right)\right]^2 .$$

Clearly, the ~3- to 5-fold increase in effective diffusivity does not account for the entirety of the 10 to 20-fold increase in $\left(\frac{\mathrm{d}a}{\mathrm{d}t}\right)_{\mathrm{II}}$. This is evidenced in Figure 7.3, which compares effective diffusivity and stage II crack growth rate, with charging hydrogen overpotential denoted by the colormap and the theoretical ratios of critical versus observed stress-affected hydrogen concentration $\left(\frac{C_{\mathrm{H}\sigma\text{-crit}}}{C_{\mathrm{H}\sigma}}\right)$ depicted by dashed lines. If the increase in effective diffusivity was sufficient to account for the increased crack growth rate, then the diffusivity-crack growth rate results at similar overpotentials would lie along one

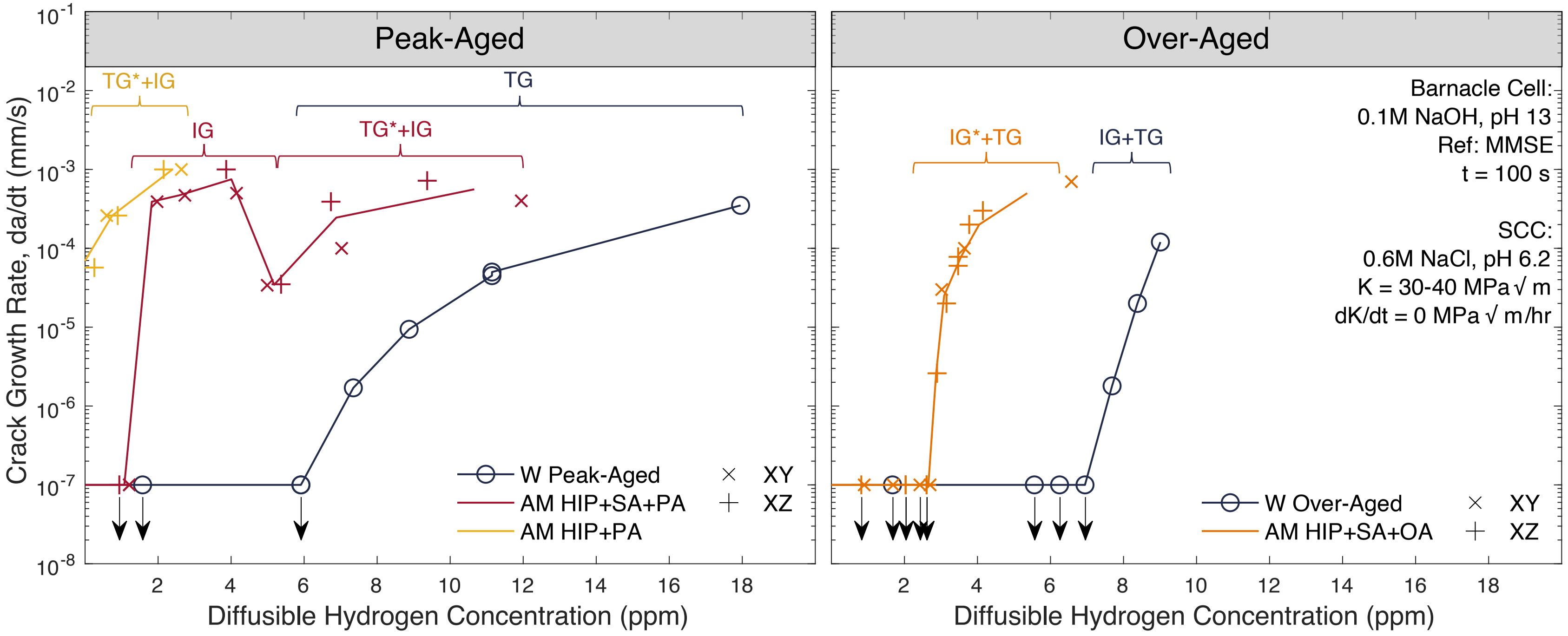

Figure 7.2: Barnacle cell hydrogen concentration plotted against HEAC crack growth rate results from Shoemaker et al.[1] for the peak-aged and over-aged heat treatment conditions. The regions of intergranular (IG) and transgranular (TG) crack growth for the AM HIP+SA conditions are labeled; dominant morphologies are labeled with an asterisk (*).

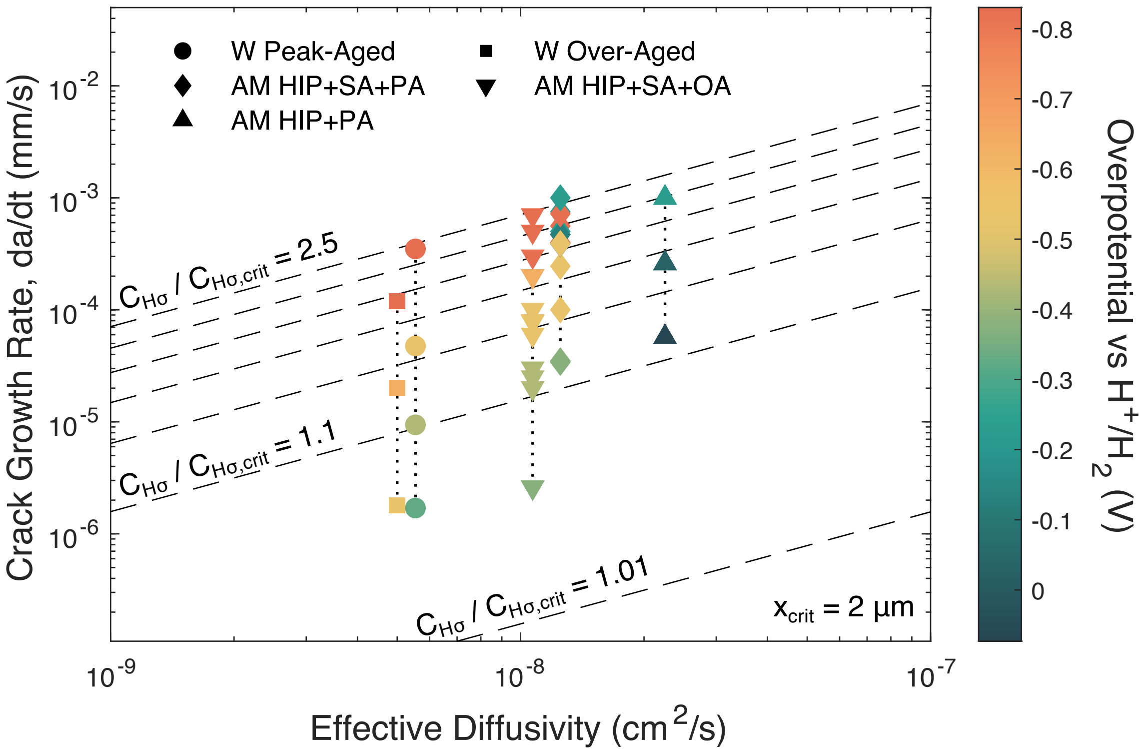

Figure 7.3: The range of stage II crack growth rates versus effective hydrogen diffusivity for each specimen, with a colormap denoting the hydrogen overpotential corresponding to each measured crack growth rate. Theoretical $\frac{C_{\mathrm{H}\sigma\text{-crit}}}{C_{\mathrm{H}\sigma}}$ values, calculated using Equation 7.7, are labeled with dashed lines.

theoretical $\frac{C_{\mathrm{H}\sigma\text{-crit}}}{C_{\mathrm{H}\sigma}}$ line. However, it is clear that crack growth rate increases beyond the slope of the concentration ratio lines, indicating that crack growth rate is also influenced by factors such as critical length and hydrogen concentration.

As such, it is necessary to consider the impact of the other terms in the model on crack growth rate. For example, a decrease in x_{crit} or critical stress-enhanced hydrogen concentration value, $C_{\mathrm{H}\sigma\text{-crit}}$, may increase crack growth rate derived from the model at a given $C_{\mathrm{H}\sigma}$. In order to assess the applicability of Lee and Gangloff's model in this scenario, the stress-enhanced hydrogen concentration terms must be estimated using experimentally obtained hydrogen concentration values. The dependence of crack growth rate on $C_{\mathrm{H}\sigma}$ can be approximated using the reversible trap-affected, potential-dependent hydrogen concentration $C_{\mathrm{H,diff}}$ via the relationship outlined in Equation 7.8 and reproduced here:

$$\left(\frac{\mathrm{d}a}{\mathrm{d}t}\right)_{\mathrm{II}} = \frac{4D_{\mathrm{eff}}}{x_{\mathrm{crit}}}\left[\mathrm{erf}^{-1}\left(1 - \frac{C_{\mathrm{H,diff\text{-}crit}}}{C_{\mathrm{H,diff}}}\right)\right]^2,$$

where $C_{\mathrm{H,diff\text{-}crit}}$ is the critical diffusible H concentration value corresponding to crack initiation. This allows for experimental $C_{\mathrm{H,diff}}$ versus crack growth rate curves to be fit to this stage II crack growth rate model, as seen in Figure 7.4. Effective diffusivity in the fit was set to the permeation decay curve fit values from Section 3.5.1 and $C_{\mathrm{H,diff\text{-}crit}}$ was bounded using the diffusible hydrogen concentration values corresponding to crack initiation as seen in Figure 7.2.

The value of x_{crit} in this fit is on the same length scale as values found in literature.[31] The critical length parameter is contingent on the interaction between crack-tip stress and local microstructural features such as hydrogen-affected dislocation structures.[3, 16, 22] It might be expected for the AM alloys to experience a reduction in x_{crit} due to microstructural variations like voids acting to preinitiate cracks and reduce the critical length required for crack propagation, which would be in agreement with the increased HEAC susceptibility.[1] Though there is a slight reduction in x_{crit} in the peak-aged condition, the reverse is true in the over-aged condition, suggesting that x_{crit} in this analysis may not have a strong dependence on the microstructural differences between wrought and AM specimens. As several of the specimen conditions have few data points for crack growth rate, a fit sensitivity analysis was performed to observe the scope of fits based on possible x_{crit} values and the potential $C_{\mathrm{H,diff\text{-}crit}}$ range, as shown in Figure 7.5. For each x_{crit} value in this analysis (depicted using different colors), the fit may vary based on the $C_{\mathrm{H,diff\text{-}crit}}$ value, so the range of $C_{\mathrm{H,diff\text{-}crit}}$) is reflected in the width of each band. This fit sensitivity analysis shows a high degree of overlap between fits with adjacent x_{crit} values, so it can be argued that the observed differences in x_{crit} may be a result of uncertainty.

The observed similarity in x_{crit} between different specimens in this study indicates that

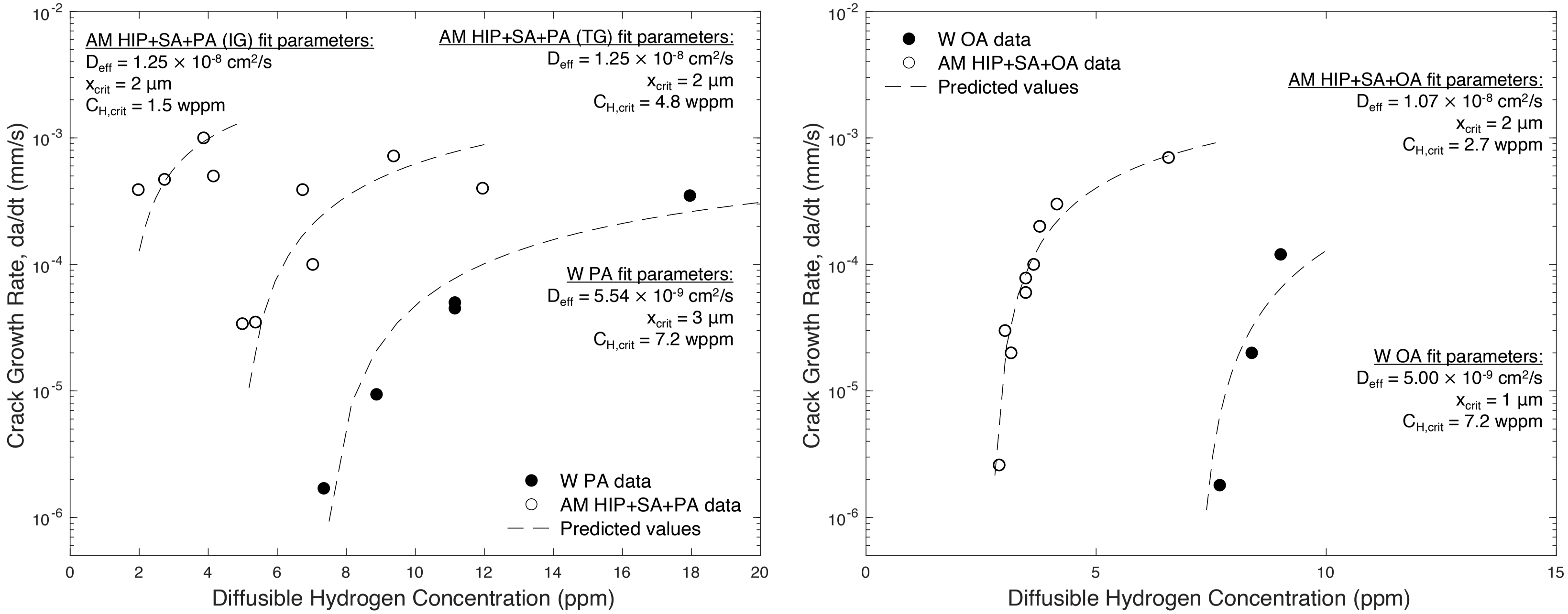

Figure 7.4: Fit of Equation 7.8 to the barnacle cell diffusible hydrogen concentration versus HEAC crack growth rate[1] data for peak-aged (left) and over-aged (right) specimens. Note that two separate fits have been performed for AM HIP+SA+PA, as the fracture method changes from intergranular to primarily transgranular as hydrogen concentration increases.

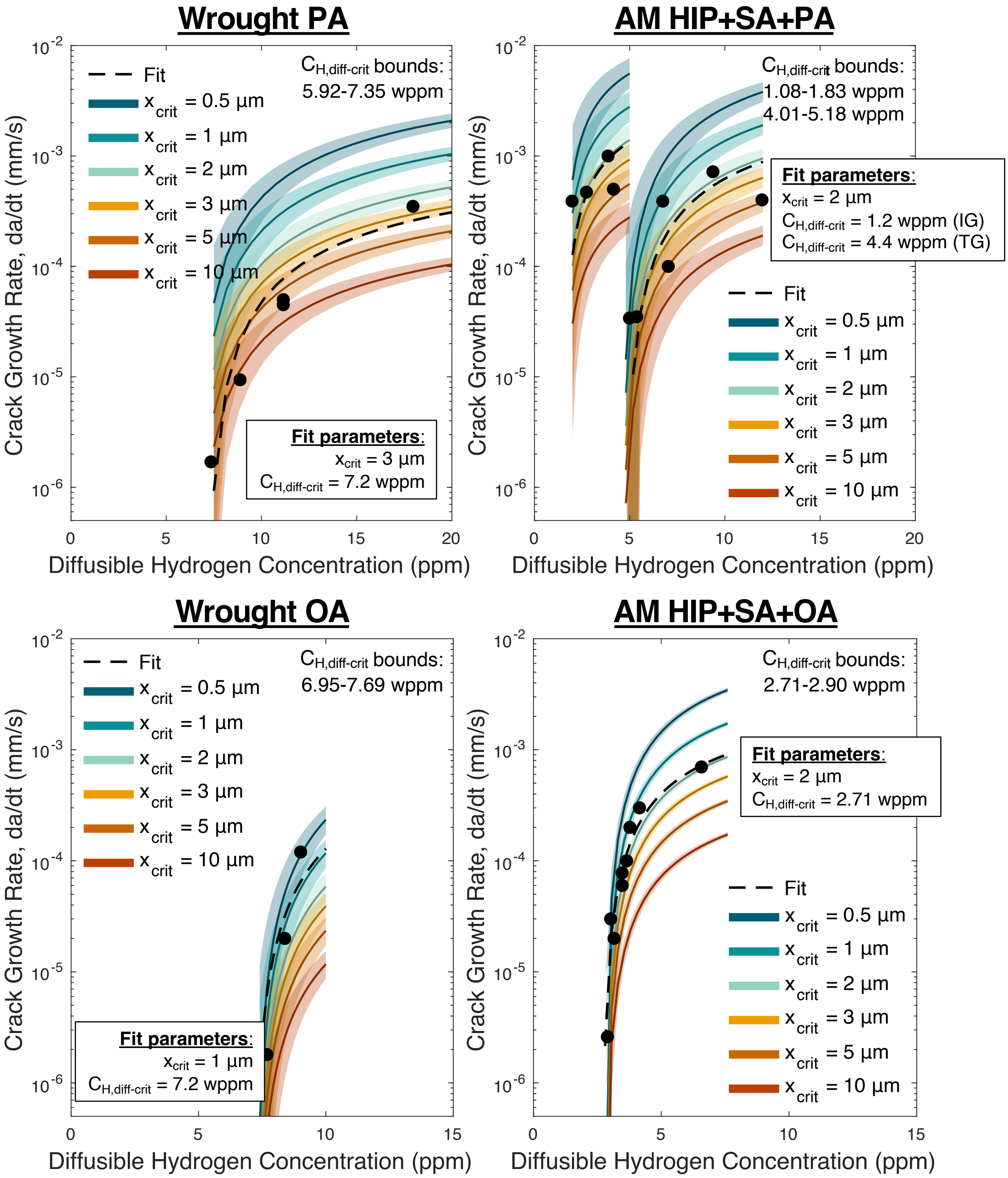

Figure 7.5: Fit sensitivity analyses for the Lee-Gangloff fits. Each colored band represents a different x_{crit} fit value, and the width of each band represents the range of $C_{\text{H,diff-crit}}$ values that can be used in the fit.

the difference in crack growth kinetics may instead be attributable to the difference in diffusible critical hydrogen concentration. This represents a modification in the failure criteria between the AM and wrought specimens, implying a dependency of EAC behavior on the interplay between microstructure and stress-affected hydrogen concentration. Despite its usefulness, a shortcoming of the Lee-Gangloff framework is that several different possible failure criteria are described with a single parameter, $C_{\mathrm{H,diff\text{-}crit}}$. Within this framework, a decrease in critical stress-affected hydrogen concentration can originate from variations in sensitivity to hydrogen (defined by weighted stress-affected hydrogen concentration $\alpha C_{\mathrm{H}\sigma}$) between different fracture pathways, as well as lower intrinsic toughness k_{IG} of fracture pathways due to microstructural factors such as porosity or trace impurities (described by $k_{\mathrm{IG}} + \sum_{i=0}^{n} \beta_i C_i$). Additionally, as $C_{\mathrm{H,diff}}$ is related to $C_{\mathrm{H}\sigma}$ through crack tip hydrostatic stress σ_{H}, it is possible that variations in σ_{H} between materials can affect critical hydrogen values as well. The crack tip σ_{H} is expected to be between 3 and 20 times the tensile yield strength σ_{YS} depending on shielding mechanisms at the crack tip.[3] Due to these complexities, it is clear that this analysis is most useful when employed in conjunction with other models, such as the Gerberich framework, to enable further deconvolution of different criteria.

Another notable assumption made in the Lee-Gangloff framework is the applicability of bulk diffusivity, D_{eff}, to hydrogen diffusion near the crack tip. As effective diffusivity is dependent on lattice diffusion and trapping, this assumption is only valid if local lattice diffusivity and trap effects reflect that of the bulk. If there are substantial effects of local trap states (e.g. geometrically necessary dislocations), strain gradient plasticity, or fast diffusion along grain boundaries adjacent to the fracture process zone, the local hydrogen diffusion near the crack tip can be strongly affected.[32, 33] It can be seen in the D_{eff} sensitivity analyses in Figure 7.6 that even small changes to the effective diffusivity used in the Lee-Gangloff analysis can greatly impact the resulting fit. This provides an impetus for future exploration into the validity of using bulk effective diffusivity in

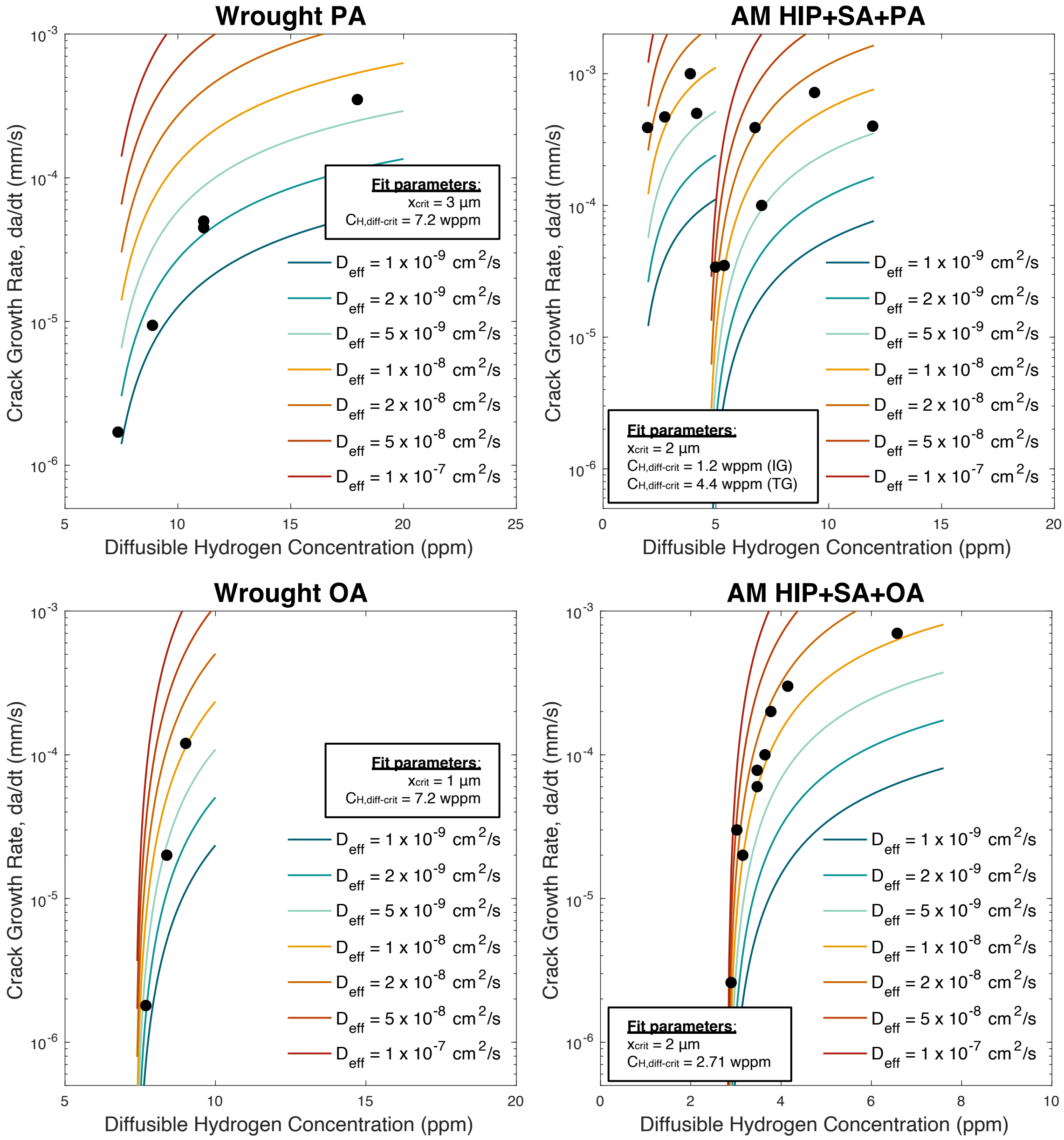

Figure 7.6: D_{eff} sensitivity analyses for the Lee-Gangloff fits, holding x_{crit} and $C_{\text{H,diff-crit}}$ constant and varying effective diffusivity.

this model, and an examination of the effects of strain and local microstructure on the diffusivity near the crack tip.

As such, it follows that alloy microstructure must play a critical role in increasing the EAC susceptibility of AM 17-4 PH. This speculation is also consistent with the observation of the onset of EAC at lower $C_{\mathrm{H,diff}}$, shown in Figure 7.2, and demonstrates the need for further study to understand the microstructural origins of the enhanced EAC susceptibility of AM 17-4 PH. For example, differences in impurity segregation to grain boundaries or the widespread sub-micrometer porosity and oxide inclusions could play an important role in the EAC behavior of AM 17-4 PH.[1] Follow-on analyses are currently ongoing to interrogate the relationship between these microstructural factors and EAC, which will be reported in future studies.

7.5 Conclusions

The important role of alloy microstructure in determining the EAC resistance of AM versus wrought 17-4 PH is confirmed via evaluation of the measured $C_{\mathrm{H,diff}}$ as a function of applied potential in the context of previously measured EAC kinetics. The critical diffusible hydrogen concentration at the onset of crack growth was determined for each alloy. Diffusible hydrogen concentration-dependent HEAC data were fitted to an existing model for crack tip hydrogen-affected stage II crack growth rate kinetics, providing deeper insight into H behavior at the crack tip. Though the increased diffusivity in the AM specimens can account for some of the increased crack growth rate, both the experimental comparison and the Lee-Gangloff model fit suggest a dependence of stage II crack growth kinetics on critical diffusible hydrogen concentration. Specifically, results demonstrate that the critical diffusible hydrogen concentration required for crack advancement in the wrought alloys is notably increased relative to AM 17-4 PH, suggesting that hydrogen concentration near the crack tip represents the dominant failure criteria. However, further study is needed to understand the precise metallurgical factors governing the differences in both hydrogen-metal interactions and EAC susceptibility of AM 17-4 PH.

References

[1] T. K. Shoemaker, Z. D. Harris, and J. T. Burns, “Comparing Stress Corrosion Cracking Behavior of Additively Manufactured and Wrought 17-4PH Stainless Steel,” *Corrosion*, vol. 78, no. 6, pp. 528–546, 2022.

[2] Z. D. Harris, J. D. Dolph, G. L. Pioszak, B. C. Rincon Troconis, J. R. Scully, and J. T. Burns, “The Effect of Microstructural Variation on the Hydrogen Environment-Assisted Cracking of Monel K-500,” *Metallurgical and Materials Transactions A*, vol. 47, no. 7, pp. 3488–3510, 2016. Publisher: Springer US.

[3] R. P. Gangloff, H. M. Ha, J. T. Burns, and J. R. Scully, “Measurement and Modeling of Hydrogen Environment-Assisted Cracking in Monel K-500,” *Metallurgical and Materials Transactions A*, vol. 45, pp. 3814–3834, Aug. 2014. Publisher: Springer US.

[4] Z. D. Harris and J. T. Burns, “The effect of isothermal heat treatment on hydrogen environment-assisted cracking susceptibility in Monel K-500,” *Materials Science and Engineering: A*, vol. 764, p. 138249, Sept. 2019.

[5] T. DebRoy, H. L. Wei, J. S. Zuback, T. Mukherjee, J. W. Elmer, J. O. Milewski, A. M. Beese, A. Wilson-Heid, A. De, and W. Zhang, “Additive manufacturing of metallic components – Process, structure and properties,” *Progress in Materials Science*, vol. 92, pp. 112–224, 2018. ISBN: 9188720411.

[6] S. Gorsse, C. Hutchinson, M. Gouné, and R. Banerjee, “Additive manufacturing of metals: a brief review of the characteristic microstructures and properties of steels, Ti-6Al-4V and high-entropy alloys,” *Science and Technology of Advanced Materials*, vol. 18, no. 1, pp. 584–610, 2017.

[7] M. R. Stoudt, R. E. Ricker, E. A. Lass, and L. E. Levine, “Influence of Postbuild Microstructure on the Electrochemical Behavior of Additively Manufactured 17-4 PH Stainless Steel,” *JOM*, vol. 69, no. 3, pp. 506–515, 2017. ISBN: 1047-4838.

[8] M. K. Alam, A. Edrisy, J. Urbanic, and J. Pineault, “Microhardness and stress analysis of laser-cladded AISI 420 martensitic stainless steel,” *Journal of Materials Engineering and Performance*, vol. 26, pp. 1076–1084, 2017.

[9] T. M. Chiu, M. Mahmoudi, W. Dai, A. Elwany, H. Liang, and H. Castaneda, “Corrosion assessment of Ti-6Al-4V fabricated using laser powder-bed fusion additive manufacturing,” *Electrochimica Acta*, vol. 279, pp. 143–151, 2018.

[10] R. Li, J. Liu, Y. Shi, M. Du, and Z. Xie, “316L stainless steel with gradient porosity fabricated by selective laser melting,” *Journal of Materials Engineering and Performance*, vol. 19, pp. 666–671, 2010.

[11] J. J. Marattukalam, A. K. Singh, S. Datta, M. Das, V. K. Balla, S. Bontha, and S. K. Kalpathy, “Microstructure and corrosion behavior of laser processed NiTi alloy,” *Materials Science and Engineering C*, vol. 57, pp. 309–313, 2015.

[12] K. G. Prashanth, S. Scudino, T. Maity, J. Das, and J. Eckert, “Is the energy density a reliable parameter for materials synthesis by selective laser melting?,” *Materials Research Letters*, 2017.

[13] R. I. Revilla, J. Liang, S. Godet, and I. De Graeve, “Local Corrosion Behavior of Additive Manufactured AlSiMg Alloy Assessed by SEM and SKPFM,” *Journal of The Electrochemical Society*, 2017.

[14] G. Sander, S. Thomas, V. Cruz, M. Jurg, N. Birbilis, X. Gao, M. Brameld, and C. R. Hutchinson, “On The Corrosion and Metastable Pitting Characteristics of 316L Stainless Steel Produced by Selective Laser Melting,” *Journal of The Electrochemical Society*, 2017.

[15] Y. Shang, Y. Yuan, D. Li, Y. Li, and J. Chen, “Effects of scanning speed on in vitro biocompatibility of 316L stainless steel parts elaborated by selective laser melting,” *International Journal of Advanced Manufacturing Technology*, 2017.

[16] W. Gerberich, *Modeling hydrogen induced damage mechanisms in metals.* Woodhead Publishing Limited, 2012. Publication Title: Gaseous Hydrogen Embrittlement of Materials in Energy Technologies: Mechanisms, Modelling and Future Developments.

[17] J. T. Burns, Z. D. Harris, J. D. Dolph, and R. P. Gangloff, “Measurement and modeling of hydrogen environment-assisted cracking in a Ni-Cu-Al-Ti superalloy,” *Metallurgical and Materials Transactions A*, vol. 47, no. 3, pp. 990–997, 2016. Publisher: Springer US ISBN: 1166101533.

[18] R. Ritchie, J. Knott, and J. Rice, “On the relationship between critical tensile stress and fracture toughness in mild steel,” *Journal of the Mechanics and Physics of Solids*, vol. 21, pp. 395–410, Nov. 1973.

[19] Z. Harris, *Elucidating Microstructural Contributions to Hydrogen Embrittlement Susceptibility in Ni-base Alloys.* PhD thesis, University of Virginia, Dec. 2018.

[20] B. A. Kehler, *Modeling and experiments to explain the potential dependency of an UHSS to hydrogen environment assisted cracking.* PhD thesis, University of Virginia, Charlottesville, VA, 2008.

[21] R. L. S. Thomas, J. R. Scully, and R. P. Gangloff, “Internal Hydrogen Embrittlement of Ultrahigh-Strength AERMET 100 Steel,” *Metallurgical and Materials Transactions A: Physical Metallurgy and Materials Science*, vol. 34, no. 2, pp. 327–344, 2003.

[22] Y. Lee and R. P. Gangloff, “Measurement and modeling of hydrogen environment-assisted cracking of ultra-high-strength steel,” *Metallurgical and Materials Transactions A: Physical Metallurgy and Materials Science*, vol. 38, pp. 2174–2190, 2007.

[23] J. Crank, *The Mathematics of Diffusion.* Oxford: Oxford University Press, 1975. ISSN: 03064549.

[24] P. Doig and G. T. Jones, “A model for the initiation of hydrogen embrittlement cracking at notches in gaseous hydrogen environments,” *Metallurgical Transactions A*, vol. 8, pp. 1993–1998, 1977.

[25] W. A. Tiller and R. Schrieffer, “A hydrogen pump for stress corrosion cracking,” *Scripta Metallurgica*, vol. 4, pp. 57–61, Jan. 1970.

[26] W. W. Gerberich and Y. T. Chen, “Hydrogen-controlled cracking-An approach to threshold stress intensity,” *Metallurgical Transactions A*, vol. 6, no. 2, pp. 271–278, 1975.

[27] W. W. Gerberich, T. Livne, X. F. Chen, and M. Kaczorowski, “Crack growth from internal hydrogen—temperature and microstructural effects in 4340 steel,” *Metallurgical Transactions A*, vol. 19, pp. 1319–1334, May 1988.

[28] M. Hall and D. Symons, “Hydrogen assisted creep fracture model for low pential stress corrosion cracking of Ni-Cr-Fe alloys,” in *Chemistry and Electrochemistry of Stress Corrosion Cracking: A Symposium Honoring the Contributions of R.W. Staehle* (R. Jones, ed.), (Warrendale, PA), pp. 447–467, The Minerals, Metals, and Materials Society [TMS], 2001.

[29] P. A. Schweitzer, *Fundamentals of corrosion: mechanisms, causes, and preventative methods.* Corrosion technology, Boca Raton, FL: CRC Press, 2010. OCLC: ocn156818649.

[30] K. N. Akhurst and T. J. Baker, “The threshold stress intensity for hydrogen-induced crack growth,” *Metallurgical Transactions A*, vol. 12, pp. 1059–1070, June 1981.

[31] R. P. Gangloff, “Hydrogen Assisted Cracking of High Strength Alloys,” in *Comprehensive Structural Integrity* (I. Milne, R. O. Ritchie, and B. Karihaloo, eds.), vol. 6, pp. 31–101, New York, NY: Elsevier Science, 2003.

[32] J. R. Scully and P. J. Moran, “The Influence of Strain on Hydrogen Entry and Transport in a High Strength Steel in Sodium Chloride Solution,” *Journal of The Electrochemical Society*, vol. 135, no. 6, pp. 1337–1348, 1988.

[33] E. Martínez-Pañeda, S. Del Busto, C. Niordson, and C. Betegón, “Strain gradient plasticity modeling of hydrogen diffusion to the crack tip,” *International Journal of Hydrogen Energy*, vol. 41, pp. 10265–10274, June 2016.

Chapter 8

Conclusions and Recommendations for Future Work

8.1 Summary and Conclusions

The aim of this work is to characterize hydrogen behavior in additively manufactured (AM) 17-4 PH stainless steel compared to its compositionally equivalent matched-strength wrought counterpart. This has been achieved through an analysis of the influence of microstructure on bulk hydrogen interactions, as well as an investigation into the role of these hydrogen interactions in the increased environmentally-assisted cracking susceptibility of AM 17-4 PH. The conclusions from each of the relevant areas of interest are as follows:

Characterization of bulk hydrogen behavior

The bulk hydrogen analysis indicated significant differences between bulk hydrogen interactions in wrought and AM 17-4 PH. Through both electrochemical and thermal methods, it was determined that effective hydrogen diffusivity is faster the AM specimens compared to the wrought specimens in both peak-aged and over-aged conditions. This conclusion is consistent with existing literature on diffusion in additively manufactured alloys. Electrochemical and thermal techniques were also employed to analyze hydrogen concentration, with the AM specimens showing consistently decreased diffusible hydrogen concentrations compared to the wrought. However, the AM specimens exhibited higher total hydrogen concentrations than the wrought specimens.

Between all analysis methods, there was a correlation between increased effective diffusivity and decreased diffusible hydrogen concentration in the AM alloys, which implies a decrease in the degree of reversible trapping. Based on the existence of a break point in temperature-diffusivity relationships in all alloys, as well as an increase in magnitude of secondary permeation transients compared to the initial permeation transients, reversible trapping is likely to have a significant impact on effective diffusivity. Additionally, the increased total hydrogen concentration in the AM specimens suggests a possible higher density of irreversible trap states.

Microstructural trapping analysis

Microstructural trap states in wrought and AM specimens in the peak-aged and over-aged conditions were analyzed using ramp rate thermal desorption spectroscopy, revealing that low-energy reversible trap sites contained the majority of trapped hydrogen. It is notable that the wrought specimens contained a larger amount of reversibly trapped hydrogen than the AM specimens in all heat treatment conditions. Several high-temperature desorption peaks corresponding to high-energy irreversible trap states were observed.

These desorption peaks were compared to the extensive microstructural characterization performed on AM and wrought 17-4 PH; this analysis encompassed features such as phase composition, precipitate type and morphology, grain size, grain boundary type, and dislocation density. Key microstructural differences include increased grain size and slightly reduced niobium carbide size and density in the AM specimens, as well as slightly lower dislocation density in the AM specimens that were solution-annealed. Comparisons of thermal desorption spectra, characterization results, and existing literature suggest that the major reversible hydrogen traps are comprised of Cu-rich precipitates and high-angle grain boundaries. Reversible trapping via grain boundaries likely accounts for the decrease in diffusible hydrogen concentration and increase in effective diffusivity seen in the AM specimens, which have coarser grains than their wrought counterparts. The prevalence of Cu-rich precipitates in both alloys may also explain the large magnitude of the initial reversible peak. Based on binding energy values from literature, it is likely that the high-energy irreversible traps consist of microstructural features such as carbides, low-angle grain boundaries, and special grain boundaries. Lastly, the absence of a visible desorption peak corresponding to a trap state unique to AM specimens insinuates that the submicron porosity in AM 17-4 PH does not act as a significant trap.

These results suggest that coarser grain size is the main factor behind the increased diffusivity and decreased diffusible hydrogen concentration in AM 17-4 PH. This is further explored using an Oriani-type trapping model to account for density and binding energy of each trap state based on literature values and microstructural characterization. It can be seen that grain size may account for these changes in diffusivity if grain boundary binding energy is slightly higher in the wrought specimens compared to the AM specimens.

The assumption that grain boundaries impede hydrogen diffusion is supported by a thorough literature review detailing the dependence of grain boundary diffusivity on alloy structure. A Hashin-Shtrikman upper bound two-phase composite analysis of grain boundary diffusion is used to reinforce this conclusion and show that short-circuit diffusion is unlikely to be responsible for any differences in diffusivity in this alloy. It should also be noted that the wrought specimens in the Hashin-Shtrikman model show slightly reduced grain boundary diffusivity compared to the AM specimens; this is in line with the increased wrought grain boundary binding energy observed in the Oriani analysis, and may possibly be attributable to differences in grain boundary character or factors like triple junctions.

Relating hydrogen and environmentally-assisted cracking kinetics

The influence of hydrogen interactions on the environmentally-assisted cracking resistance of AM and wrought 17-4 PH is emphasized through an analysis of previously measured EAC kinetics compared to the observed diffusible hydrogen concentration at matching applied potentials. These data were fit to the Lee-Gangloff framework of stage II stress corrosion crack (SCC) growth rate using previously measured bulk hydrogen diffusivity and diffusible hydrogen concentration in order to provide insight on the mechanisms affecting crack growth kinetics.

While the increased diffusivity in AM specimens can account for a portion of the observed increase in crack growth rate, both the experimental concentration-crack growth rate comparison and the application of the Lee-Gangloff model suggest that EAC kinetics are contingent on the critical diffusible hydrogen concentration, as there is a substantial increase in the critical diffusible hydrogen concentration required for crack advancement in wrought alloys compared to AM 17-4 PH.

In conclusion, this comprehensive investigation provides valuable insights into the hydrogen behavior and microstructure of AM 17-4 PH stainless steel. The observed differences in hydrogen-microstructure interactions between wrought and AM specimens demonstrate that a thorough understanding of these factors is required to mitigate environmentally-assisted cracking susceptibility in additively manufactured alloys.

8.2 Recommendations for Future Work

Recommendations for future work are as follows:

- Though an in-depth examination of microstructure at different length scales was performed in this work, further exploration into the grain boundary-specific microstructure and nanochemistry would be beneficial. Specifically, characterization of precipitate or secondary phase segregation to grain boundaries as well as a thorough search for thin-film retained or reverted austenite would provide insight into the precise differences of grain boundary trapping and diffusion of hydrogen between wrought and AM specimens.
- Future study regarding the relationship between microstructural features and hydrogen EAC susceptibility would improve the current understanding of hydrogen behavior near the crack tip. One possible next step is exploring the differences in hydrogen trapping near the fracture process zone in pre-cracked AM and wrought 17-4 PH, especially concerning the trapping or repartitioning effects of stress fields around pores.
- The Lee-Gangloff framework employed in the EAC kinetics analysis relies upon the assumption that bulk effective diffusivity is sufficient to describe diffusion near the fracture process zone (FPZ). However, further investigation into the veracity of this assumption would be beneficial, especially when considering rapid diffusion along grain boundaries in the context of intergranular fracture. Though this may be a laborious undertaking, the development of a model accounting for the effects of the stress field ahead of the FPZ as well as local microstructural effects on diffusion near the crack tip would greatly assist in improving the current understanding of the relationship between local hydrogen behavior and crack growth kinetics.
- Contextualization of the AM microstructure-property relationships discussed in this work in terms of additive manufacturing and processing parameters would provide a better insight into the processing-microstructure-properties relationship. Manipulation of processing parameters to reduce grain size and increase hydrogen trap density in the AM specimens may reduce the susceptibility of AM 17-4 PH

to hydrogen environmentally-assisted cracking, and further investigation into increasing microstructural trapping to improve cracking behavior while retaining good mechanical properties will help move collective understanding forward towards the development of safe and long-lasting AM 17-4 PH for commercial usage.